Atomic Number and Gamma-ray Measurements from Neutron-induced Fission at the ILL and n_ToF

A thesis submitted to the University of Manchester for the degree of Doctor of Philosophy in the Faculty of Science and Engineering

2020

Nikolay V. Sosnin

Department of Physics and Astronomy in the School of Natural Sciences
The University of Manchester

Blank page

Contents

Word count: 41,662

Blank page

List of Figures

Blank page

List of Tables

Blank page

Abbreviations

2E2v	**2** **E**nergy **2** **v**elocity
BD	**B**ragg **D**etector
BLOB	**B**inary **L**arge **OB**ject
BRGF	Bragg arm Frisch grid on STEFF
BRGG	Bragg arm anodes on STEFF
CASTOR	**C**ERN **A**dvanced **STOR**age
CSEWG	**C**ross **S**ection **E**valuation **W**orking **G**roup
DANCE	**D**etector for **A**dvanced **N**eutron **C**apture **E**xperiments
EAR1, EAR2	**E**xperimental **AR**ea 1 or 2
ENDF	**E**valuated **N**uclear **D**ata **F**ile
FALSTAFF	**F**our **A**rm c**L**over for the **ST**udy of **A**ctinide **F**ission **F**ragments
FEB	**F**ission **E**vent **B**uilder
FF	**F**ission **F**ragment
FIAB	Bragg FiFI arm anodes on STEFF
FIAH	Hipps FiFI arm anodes on STEFF
FiFI	**Fi**ssion **F**ragment **I**dentification
FISB	Bragg FiFI arm Frisch grid on STEFF
FISH	Hipps FiFI arm Frisch grid on STEFF
HIPF	Hipps arm Frisch grid on STEFF
HIPS	Hipps arm anodes on STEFF
IAEA	**I**nternational **A**tomic **E**nergy **A**gency
ICM	**I**ntranuclear **C**ascade **M**odel
ILL	**I**nstitut **L**aue-**L**angevin
JEFF	**J**oint **E**uropean **F**ission **F**usion (Library)
LDM	**L**iquid **D**rop **M**odel

MCP	**M**icro**c**hannel **P**late
MWD	**M**oving **W**indow **D**econvolution
MWPC	**M**ulti**w**ire **P**roportional **C**ounter
NEA	**N**uclear **E**nergy **A**gency
NNDC	**N**ational **N**uclear **D**ata **C**enter
n_ToF	**N**eutron **T**ime-**o**f-**F**light
PES	**P**otential **E**nergy **S**urface
PFG	**P**rompt **F**ission **G**amma
PFN	**P**rompt **F**ission **N**eutron
PKUP	Pick-up, n_ToF proton beam intensity monitor
PS	**P**roton **S**ynchrotron
PSA	**P**ulse-**S**hape **A**nalysis
SCM	**S**hell **C**orrection **M**ethod
SEE	**S**econdary **E**lectron **E**mission
SPIDER	**SP**ectrometer for **I**on **DE**termination in fission **R**esearch
STEFF	**S**pec**t**rometer for **E**xotic **F**ission **F**ragments
ToF	**T**ime-**o**f-**F**light
VERDI	**VE**locity fo**R** **D**irect particle **I**dentification

Abstract

The STEFF spectrometer was used at the Neutron Time-of-Flight facility (n_ToF) at CERN in 2016 to perform a 30-day long experimental campaign of measurements of fission fragments and gamma rays produced in ^{235}U fission for a wide range of incident neutron energies. A pipeline for reading, correlating and database deposition of the experimental data from this experimental campaign as well as for future STEFF campaigns at n_ToF has been constructed. The pipeline resulted in 70-fold data size reduction to an experimental database that can be fully processed in ≈7 hours.

The collected gamma-ray data acquired using NaI and $LaBr_3$ detectors have been analyzed in the <1 eV neutron energy range and compared to prior STEFF ^{235}U fission gamma-ray measurements. A method for correcting NaI signal amplitudes for n_ToF-specific effects, such as rates and pulse types, based on fission gamma-ray spectrum shape has been developed. The correcting factors were the greatest for the dedicated proton pulses at neutron energies of ≈0.06 eV, increasing signal amplitude by approximately a factor of 2. Corrections to $LaBr_3$ signals have also been considered and performed based on count rates, with the the largest correcting factors reducing signal amplitude by ≈15%. The corrected and calibrated energy spectra and calculated fold distributions have been prepared for extraction of gamma-ray multiplicity, average energy and total energy in thermal and epithermal fission of ^{235}U.

An experiment was conducted at the Lohengrin mass spectrometer at Institut Laue-Langevin, France, using a FiFI spectrometer for measurement of masses and atomic numbers of selected ^{235}U fission fragments. The details of the experiment and the data analysis are presented, and a method for calibrating Bragg detectors for atomic number extraction is proposed. The method is based on amplitudes, derivatives and risetimes of signals produced by fission fragments in isobutane fill gas. The extracted signal properties were used in conjunction with known fragment masses and energies to produce functional forms based on powers of fragment velocities and average atomic numbers. Furthermore, a comparison with simulations produced in SRIM-2013 was performed, assessing the accuracy of the simulations.

Declaration of Authorship

I, Nikolay V. Sosnin , confirm that no portion of the work referred to in the thesis has been submitted in support of an application for another degree or qualification of this or any other university or other institute of learning.

Copyright statement

"You know what uranium is, right? It's this thing called nuclear weapons. And other things. Like lots of things are done with uranium. Including some bad things. But nobody talks about that."

Donald J. Trump

Acknowledgements

I would like to thank Dr. Gavin Smith for his great supervision, invaluable insights and support throughout my PhD work and the opportunity to take part in the weird world of fission physics. I am very thankful to Dr. Toby Wright for never failing to provide great advice all the times I have needed help and for all the adventures in various places around the planet. I am very grateful to Andy Macfarlane for both the remarkable skills in all the experimental work that went into my PhD, all the help teaching me how not to perish in a lab, and great company on experiments.

This project has benefited from funding through the Advanced Fuel Cycle Program from the BEIS Nuclear Innovation Program, as well the STFC UK Nuclear Data Network (UKNDN).

I would further like to thank the collaborations at ILL and n_ToF that I have had the privilege of participating in. The expertise of Ulli Köster has been critical in making sense of the Lohengrin spectra and ensuring my own understanding of the fission studies at ILL. The n_ToF collaboration (and particularly Michi) have also rescued me many times when I needed help with getting to grips with either the data or the analysis of the STEFF campaign. My time at CERN has been very productive and very fun, thanks to the n_ToF family.

It has been a great pleasure working with the University of Manchester Nuclear Physics group, and I would like to thank the staff (Jon Billowes in particular for introducing me to nuclear physics), the postdocs (particularly Ben Pietras in particular for all the ROOT help, great advice and equally great times), and the PhD students. It has been a great collective to be a part of. I would also like to thank Bob Chapman (although not part of the Manchester group anymore) for rescuing me many times throughout my life as a nuclear physicist.

I would particularly like to thank my family for showing me support that's been nothing short of amazing. There aren't words enough to express my gratitude.

And of course a huge thank you to *Dr*. Helen Barker for being there for me in any and all times. It has been absolutely breathtaking.

Blank page

Chapter 1

Introduction

The process of nuclear fission has been studied in great detail since its first observation in 1938 [1] and identification as a new reaction type in 1939 [2]. Studies of fission have rapidly extended past purely scientific interest to include practical applications. The great energy yield of nuclear fission was recognized, and the first nuclear reactor was built in 1942, called Chicago Pile 1 (CP-1) [3]. In 1954, the first commercial nuclear reactor in Obninsk, Russia, was connected to the grid and produced electricity [4]. Currently there are ≈440 nuclear reactors operating around the world producing around 10% of the world's electricity [5]. Moreover, a new generation of reactors, Generation IV, is an active area of current research [6] with the aim of increasing reactor efficiency and reducing waste production. Various reactor designs rely on different neutron energies to maintain fission and produce energy. Of the six proposed reactor designs comprising Generation IV, only two reactors operate in the thermal (0.025 eV) neutron energy range [7], which is typical for the earlier reactor generations. Inside thermal-reactor cores, fission neutrons, which are produced at MeV energies (referred to as fast neutrons), require moderation to reduce their energy to the thermal range [8]. Fast neutron reactors, on the other hand, do not require moderators, and therefore can be made more compact. Furthermore, fast neutrons can induce fission in a considerably larger number of actinides than thermal neutrons (more details on this are presented in the next chapter of this work), thus broadening the range of useful nuclear fuels and reducing the amount of long-lived actinide waste products (or even eliminating the pre-existing actinide waste) [9]. These advantages result in prominence of the fast reactor designs in the upcoming reactor generation, and subsequently the need for new nuclear data for fission induced by neutrons at a wide energy range for a broad range of fissioning nuclei.

Nuclear data are compilations of information concerning nuclear structure and decays. Various databases store experimental, simulated or theoretically calculated information on nuclear species, reactions, emitted radiations, and particle interaction properties.

Such databases require information inputs in order to address the current needs of the nuclear industry, medicine and science. As data are added to the databases, they undergo a process called evaluation, whereby the candidate results are compared to the pre-existing database information and their merits inform how much the prior data are adjusted to reflect the new results. The evaluation process begins with publication of the data, which are then assessed by evaluators, who examine the methodology used for producing the data, devise correction factors which may be required to compare the new data with the pre-existing ones, investigate the uncertainties and then adjust the current standards to reflect the decided contribution by the final corrected new data. Many databases exist focusing on different data sources and information types, but of particular interest to this work are the ENDF/B library [10] maintained by the National Nuclear Data Center (NNDC) Cross Section Evaluation Working Group (CSEWG) formatted in the Evaluated Nuclear Data File (ENDF) format developed by the International Atomic Energy Agency (IAEA), and the Joint Evaluated Fission and Fusion (JEFF) library [11], maintained by the Nuclear Energy Agency (NEA). ENDF/B library's latest release is ENDF/B-VIII.0 and the latest release of JEFF is JEFF-3.3.

Approximately 10% of the energy in a typical reactor core is released through gamma rays which propagate out of the core and contribute to total heating [12]. Of the 10% gamma ray energy release in the core, 40% is accounted for by prompt fission gamma rays (PFG) [12], i.e. gamma rays emitted by fission fragments before they undergo beta decay. For this reason NEA has issued a high priority request for information on neutron-induced prompt fission gamma ray energy and multiplicity with a precision of 7.5%, as well as information on the gamma-ray spectrum shape in the energy range of 0-10 MeV [13]. The required precision addressed by the NEA request has already been achieved for fission gamma ray energy, total energy and multiplicity in ^{235}U [14] and ^{241}Pu [15]. ^{235}U is a nucleus of particular interest, since it is a common fuel for reactors. Gamma ray multiplicities and energies have been measured for this particular nucleus several times before, predominantly for thermal-neutron-induced fission, and the results of these studies are presented in Table 1.1. While the results in Ref. [14] fulfil the requirements of the NEA request, these results are also in considerable disagreement with the previous measurements.

TABLE 1.1: Summary of the results of the previous measurements of average and total gamma-ray energies and multiplicities for fission of ^{235}U. Note, that the Makii *et al.* measurement has a different minimum gamma-ray energy threshold from others (1 MeV compared to 100-150 keV for other measurements).

Cited work	Neutron energy range	Average total energy (MeV)	Average γ-ray energy (MeV)	Average multiplicity
Peelle *et al.*, 1971 [16]	Thermal	6.51±0.30	0.97±0.05	6.70±0.30
Pleasonton *et al.*, 1972 [17]	Thermal	6.43±0.30	0.99±0.07	6.51±0.30
Verbinski *et al.*, 1973 [18]	Thermal	7.18±0.26	0.96	7.45±0.35
Oberstedt *et al.*, 2013 [14]	Thermal	6.92±0.09	0.85±0.02	8.19±0.11
DANCE, 2015 [19]	Thermal-100 keV	8.35±0.40	-	7.35±0.35
STEFF, 2014 [20]	Thermal	8.40±0.26	1.08±0.03	7.74±0.12
STEFF, 2015 [21]	Thermal-1 eV	9.00±0.10	1.42±0.05	6.30±0.20
Makii *et al.*, 2019 [22]	Thermal	4.07±0.07	1.78±0.05	2.29±0.05
ENDF/B-VIII.0, 2018 [10]	Thermal	7.28	0.85	8.58

The Peelle *et al.* and Pleasonton *et al.* measurements are believed to have suffered from an incomplete separation of prompt fission neutrons from the gamma-rays [18]. The measurement by Verbinski *et al.* was affected by complications in the spectrum unfolding procedure, resulting in higher uncertainties. Oberstedt *et al.* measurements were conducted using two $LaBr_3$(Ce), two $CeBr_3$ and one $LaCl_3$(Ce) crystals performing individual measurements, compared to all the the previous results which used NaI(Tl) crystals. The use of detectors with faster timing and better energy resolution, coupled with the overall agreement between three crystal types, leads to greater confidence in this set of measurements, as reflected by its greater influence in the ENDF/B-VIII.0 release, as opposed to its predecessor, the ENDF/B-VII.0 release [23]. Detector for Advanced Neutron Capture Experiments (DANCE) collaboration work is the first set of published PFG properties obtained by multiple gamma-ray detectors performing measurements in coincidence, since DANCE array is composed of 140 BaF_2 crystals. Due to the complexity of the set-up, the results could be affected by improper unfolding, which was the reason for the average gamma-ray energy not being reported. The 4 fissioning nuclide measurements (^{235}U, ^{239,241}Pu and ^{252}Cf) reported in the PFG campaign by DANCE [19], resulted in 20% underestimation of multiplicity and subsequent 20% overestimation of energy compared to the established data. A recent set of measurements have been performed by H. Makii *et al.* [22] investigating high-energy part of the ^{235}U gamma-ray spectrum in thermal fission, and the results of this work are listed alongside the previous works in Table 1.1, however they only apply for a gamma-ray energy cut of 1 MeV$\leq E_\gamma \leq$6 MeV. Within the confines of the high-energy gamma-ray cut, the results by Makii *et al.* and Oberstedt *et al.* agree with each other, but not with Peele *et al.* or Verbinski *et al.* The results of previous STEFF measurements listed in Table 1.1 are

discussed in greater detail in Chapters 5 and 6 of this work.

As suggested above, one of the aims of the ongoing work with the SpecTrometer for Exotic Fission Fragments (STEFF) is to address the discrepancies of the prior results for gamma-ray data. Moreover, the latest STEFF measurements span beyond thermal fission, an energy range where the majority of the prior measurements have been conducted. Since Generation IV proposes three fast-neutron reactor designs [7] (and a further design that can be constructed to operate in either thermal or fast mode), further measurements of PFG produced in fission at neutron energies beyond thermal would be beneficial to the nuclear industry as well as to fundamental fission studies.

STEFF is a two-energy two-velocity (2E2v) fission fragment spectrometer. It performs parallel measurements of each of the two fission fragments produced in binary fission. Moreover, STEFF provides gamma-ray information from an array of 12 scintillators, the types of which varied between STEFF experiments. Two campaigns of fission product measurements in ^{235}U have been conducted in 2015 and 2016 at the Neutron Time-of-Flight (n_ToF) facility at CERN for a wide range of incident neutron energies. A further STEFF experiment took place in 2018, aimed at measuring ^{239}Pu fission properties. Due to its broad neutron energy spectrum, the n_ToF facility is suitable for measurements needed to address the data needs at neutron energies above thermal, as well as for addressing the existing discrepancies in the thermal measurements. Prior to deployment at n_ToF, STEFF has been used at Institut Laue-Langevin (ILL) in Grenoble in 2014 to perform measurements of exclusively thermal neutron-induced fission of ^{235}U, and the results of this measurement as well as prior results from STEFF measurements at n_ToF are shown in Table 1.1. There is an evident disagreement between the extracted gamma-ray data for the two facilities, indicating the need for an investigation of STEFF behaviour in the n_ToF environment to ensure that detector response is understood. Treatment of data resulting from STEFF measurements at n_ToF in 2016 and a subsequent investigation of gamma-ray spectra measured at n_ToF with reference to the work performed at ILL [20] are addressed in this thesis with the aim of validating STEFF measurements for future studies of fission of various fissioning nuclei at a range of incident neutron energies.

A significant benefit of STEFF compared to prior measurements of fission gamma-rays is the availability of correlated fission fragment mass and kinetic energy measurements. In order to aid the analysis of STEFF data on fission fragments, characterization of a Fission Fragment Identification (FiFI) chamber has been performed in 2016 at the Lohengrin mass spectrometer at ILL. The characterization process is needed to help refine techniques for Bragg detector data analysis, specifically fission fragment charge extraction, and provide information on the Bragg detector response to varying fragment masses

and charges. Fission fragment atomic number has been a difficult quantity to measure throughout the history of fission studies, and would constitute a valuable observable for STEFF measurements, and a possible method of addressing charge measurements is discussed in this work based on the data measured at Lohengrin.

This work summarizes developments in the handling of data and analysis from the 2016 STEFF experimental run, as well as the process and the results of FiFI characterization. Firstly, an introduction of some important characteristics of nuclear fission is provided in Chapter 2. The structure of all the detectors used on STEFF with a particular focus on gas-filled detectors is then described in Chapter 3. Details of the FiFI experiment at ILL and the subsequent analysis are summarized next in Chapter 4. STEFF ^{235}U campaign details and data processing are addressed in Chapter 5 and the analysis of the results is presented in Chapter 6. Concluding remarks and further STEFF work are presented in Chapter 7.

Blank page

Chapter 2

Nuclear Fission

Nuclear fission is a process observed in a variety of nuclei ranging from $^{178}_{78}$Pt [24] up to $^{284}_{114}$Fl [25], with theoretical investigations ongoing into even heavier exotic nuclei produced in supernovae, such as calculations over a large range of nuclides spanning from $^{250}_{90}$Pt to $^{294}_{100}$Fm [26]. During fission, a nucleus splits into two or more nuclei, called fission fragments. This process was first observed by O. Hahn and F. Strassman in 1938 [1], when they bombarded uranium (Z=92) with neutrons, hoping to synthesize neptunium (Z=93) via beta-decay of the compound nucleus, and identified barium (Z=56) in a sample of uranium. The following year, L. Meitner and O.R. Frisch correctly interpreted this observation as separation of a nucleus into two fragments and provided a description of the process based on an analogy to a charged incompressible liquid drop [2]. Further work on the Liquid Drop Model (LDM) of the fission process was published the same year by N. Bohr and J. Wheeler [27].

2.1 Liquid Drop Model

The LDM description of a nucleus is based on C.F. von Weizsäcker's Semi-Empirical Mass Formula (SEMF) [28], given in Equation (2.1). The formula describes the binding energy E_b of a nucleus of mass A with proton number Z and neutron number N as [8]

$$E_b = a_v A - a_s A^{2/3} - a_c \frac{Z^2}{A^{1/3}} - a_a \frac{(A-2Z)^2}{A} - \delta(A,Z), \tag{2.1}$$

for

$$\delta = \begin{cases} +a_p A^{-3/4} & \text{if } Z \text{ and } N \text{ are even,} \\ -a_p A^{-3/4} & \text{if } Z \text{ and } N \text{ are odd,} \\ 0 & \text{if } A \text{ is odd.} \end{cases} \tag{2.2}$$

The SEMF features five terms multiplied by parameters a_i, which are fitted based on the experimental data. The first term is the volume term, which represents binding within the volume of a nucleus. However, nucleons on the surface of a nucleus have fewer neighbours binding them, therefore the volume term is reduced by the surface term. The attractive force between nucleons is opposed by the Coulomb repulsion of the protons. For this reason, binding is further reduced by the Coulomb term. However, a nucleus with any number of neutrons will be bound according to the terms introduced in the formula so far. The next term, the asymmetry term, is added to the formula to account for that. This term arises from modeling the nucleus as a volume of Fermi gas, rather than a liquid drop [29]. A state in a Fermi gas can be occupied by two protons and two neutrons by the Pauli Exclusion Principle. Therefore, by this model, if there is a difference in the number of protons and neutrons, the 'excess' particles will occupy higher energy states, increasing the total energy. The last term is the pairing term, which describes an increase in the binding energy observed in nuclei with paired nucleons.

As the nucleus stretches during the fission process, changes in surface and Coulomb terms dominate the other three parts of Equation 2.1 [30]. For an elliptically-stretched nucleus with eccentricity ϵ, the deformation energy E_{def} is defined as

$$E_{def}(\epsilon) = E_c(\epsilon) + E_s(\epsilon) - E_c(0) - E_s(0), \tag{2.3}$$

where E_c and E_s are surface and Coulomb energies. By considering only quadrupole deformations in a multipole expansion of nuclear shape, and using substitutions

$$E_s(\epsilon) \simeq E_s(0)\left(1 + \frac{2}{5}a_{20}^2\right) \tag{2.4}$$

and

$$E_c(\epsilon) \simeq E_s(0)\left(1 - \frac{2}{5}a_{20}^2\right), \tag{2.5}$$

for quadrupole term coefficient a_{20}, Bohr and Wheeler have defined the fissility parameter x as

$$x = \frac{E_c(0)}{2E_s(0)}. \tag{2.6}$$

The fissility parameter describes the stability of a nucleus against fission and is proportional to Z^2/A, with $x = 1$ for $Z^2/A \approx 50$ [30]. Nuclei with $x > 1$ are predicted to be unbound to increasing deformation leading to fission. Such nuclei would have $Z \sim 120$ [31], but no such nuclei have been observed to date. Spontaneous fission occurs instead due to tunneling of fragments through the fission barrier. ^{235}U, which is the focus of this work, has $x \approx 0.36$ [31], and ^{252}Cf, a nucleus that undergoes spontaneous fission $\sim 3\%$ of the time [32], has $x \approx 0.76$ [33], which is considerably lower than the $x = 1$ recipe for spontaneous fission prescribed by LDM.

The fissility parameter inconsistencies with the behaviour of fissile nuclei show that the LDM picture of fission is incomplete. The inconsistencies extend beyond fissility. LDM predicts that all stable nuclei have spherical ground states, which contradicts observations [30]. Moreover, equilibrium shapes above $x > 0.39$ in LDM are stable against reflection-asymmetric distortions. This is also not the case, since actinide nuclei fission predominantly asymmetrically (although symmetric fission becomes pronounced in actinides for high excitation energies, such as for 14-MeV incident neutrons on ^{235}U in Ref. [34], and is the dominant fission mode for many nuclei lighter or heavier than actinides, such as ^{210}Po [35] or ^{258}Rf [36]). LDM predicts a simple fission barrier with a single maximum, however observation of fission isomer states [37], i.e. isomers with unusually short half-lives for spontaneous fission [8], contradicts this prediction. The isomeric states suggest additional structure in the fission barrier, not accounted for in the LDM. These inaccurate predictions of the LDM are attributed to the model's collective nature, which ignores single-particle effects.

2.2 The Shell Correction Method

The nuclear shell model considers individual nucleons moving in a common potential, comprised of a central spherical potential and a spin-orbit term [8]. The nucleons inside the potential can occupy quantized states, called shells. The shell model was extended to include deformed potentials by Nilsson [38], and Strutinsky [39] combined the independent particle approach with collective description of the LDM to form the Shell Correction Method (SCM). Binding energies in the SCM are defined as

$$E_b = E_{LDM} + \delta U + \delta P, \tag{2.7}$$

where

$$\delta U = U - \widetilde{U} = 2\sum_{\nu} E_\nu n_\nu - 2\int_{-\infty}^{\widetilde{\lambda}} E\widetilde{g}(E)dE \tag{2.8}$$

and

$$\delta P = P - \widetilde{P}. \tag{2.9}$$

The corrections are applied to the LDM binding energy E_{LDM}. The effect of the corrections for a typical actinide nucleus is shown in Figure 2.1. The δU term is a correction that accounts for shell structure. It is defined as the difference between the total energy associated with all the occupied shells of a nucleus and a distribution of energy averaged over a major shell. The shell model term is the sum of shell energies E_ν times the corresponding shell occupancy n_ν. The uniform nucleus term is the integral over energy of the uniform distribution $\widetilde{g}(E)$ from $-\infty$ up to a chemical potential $\widetilde{\lambda}$, i.e. the energy needed to remove a nucleon from the nucleus. δP is the pairing term, P is the pairing energy for nucleons near the Fermi surface (i.e. the most energetic occupied shell), and $\widetilde{P}$ is the average pairing energy contained in the pairing term of the LDM [40]. The two correction terms are summed separately for neutrons and protons.

The SCM approach correctly reproduces the shape of the observed fission double-humped barrier, however it overestimates the height of both the initial deformation hump and the fission potential for the fission isomer produced through deformation [30]. Nonetheless, SCM provides insight into the interplay of the single-particle and collective effects during the nuclear fission process.

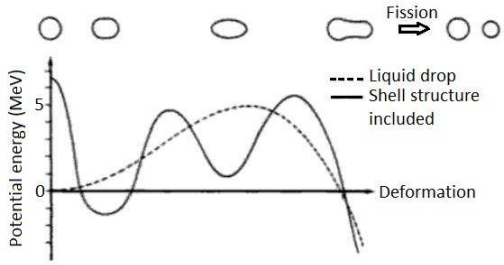

FIGURE 2.1: A schematic comparison of fission barrier potentials for a typical actinide nucleus as predicted by the Liquid Drop Model with and without shell structure corrections, adapted from [30]. A diagram of the shape of the fissioning nucleus corresponding to different stages of fission is included.

Calculations using the SCM and derived models are typically performed over a set of nuclear deformation parameters, as discussed in work by P. Möller *et al.* [41]. Such calculations result in potential energy surfaces (PES) showing all the potential paths fission process of a particular nucleus can take, i.e. binary or ternary/quaternary, symmetric or asymmetric etc. PES plots clearly show path of minimum potential with associated barriers for various nuclear processes, making extraction of features of fission dynamics possible through calculation of inertial parameters, described in more detail in Ref. [42]. An example of a PES plot is shown in Figure 2.2.

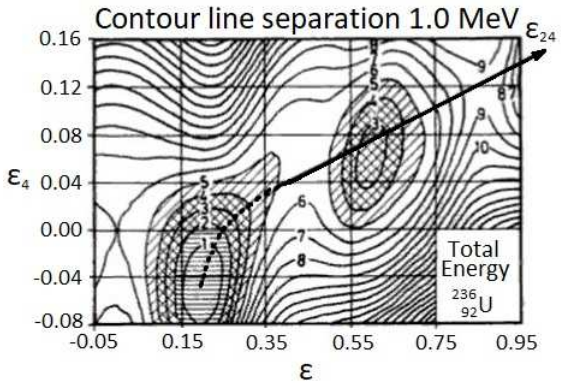

FIGURE 2.2: Potential energy surface of ^{236}U described in terms of quadrupole and hexadecapole deformation parameters, ϵ and ϵ_4 respectively. ϵ_{24} indicates the 'static path to fission', i.e. the deformations nucleus is the most likely to undergo during the fission process. Adapted from [43].

2.3 Fission Cross-section

Fission can be spontaneous, as in the case of ^{252}Cf discussed above, or particle-induced, as was the case for the uranium samples used by Hahn and Strassman. While ^{235}U fission is typically neutron-induced inside reactors (as neutrons are not hindered by the nuclear Coulomb barrier), experiments have been done using other methods of inducing fission, such as photon-induced fission (or 'photofission') [44], electron-induced fission (or 'electrofission') [45], proton-induced fission [46] or Coulomb excitation (Coulex) induced fission [47]. Neutrino-induced fission has also been proposed as a mechanism behind abundances of elements involved in the *r*-process for nuclei heated by the neutrino flux in supernovae ejecta [48]. STEFF, however, has so far been used only for measurements of neutron-induced fission following commissioning with ^{252}Cf.

Figure 2.3 shows a plot of fission cross-section for neutron-induced fission of ^{235}U as a function of incident neutron energy. The cross-section is typically divided into several sections based on the features it exhibits: smooth decay in the thermal and epithermal neutron region (0.025 eV - ∼0.2 eV) [31], resolved resonance region (∼0.2 eV - ∼10 keV),

unresolved resonance region (∼10 keV - ∼6 MeV) and multichance fission region ($\gtrapprox$6 MeV).

The cross-section roughly follows $^1/_v$ decay (evident at thermal and epithermal incident neutron energies), a relationship that suggests that the probability of neutron absorption and, consequently, fission largely depends on the amount of time the neutron spends in the volume of a nucleus [49]. When the binding energy and kinetic energy of the incident neutron are equal to the energy of some excited state in the compound nucleus, a sharp increase in the cross-section associated with a resonance appears. As the incident neutron energy grows, the spacing between resonances becomes comparable to the widths of the states corresponding to the resonances, and the resonances become unresolved, producing a relatively smooth cross-section as a function of energy. At excitation energies about ∼6 MeV [50] the compound nucleus $^{236}U^*$ excitation is greater than the binding energy of a neutron, which may then be emitted, and the resulting $^{235}U^*$ nucleus can still undergo fission. Fission following single neutron emission is called 'first-chance' fission, an effect that causes a cross-section increase seen in ≥6 MeV energy range due to contribution from fission of the excited post-evaporation nucleus. Similarly, fission following two-neutron emission is called 'second-chance' fission. In the case of the ^{235}U nucleus, it has been investigated as a fissioning nucleus in the 5^{th} chance fission scenario of ^{240}U [51].

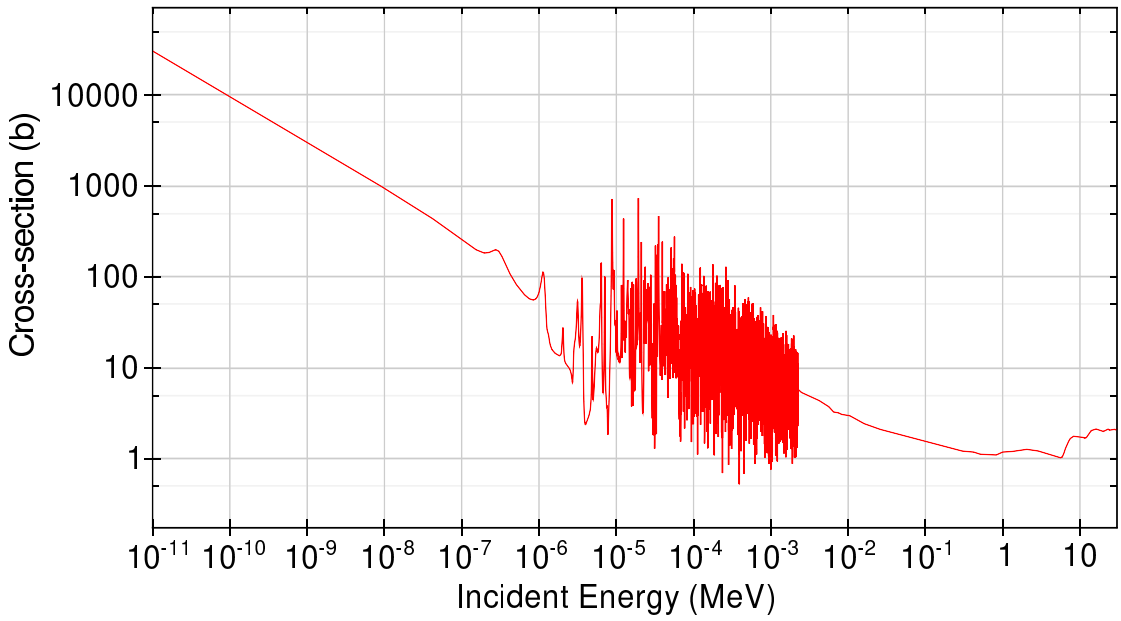

FIGURE 2.3: Cross-section of ^{235}U(n,f) reaction in barns as a function of incident neutron energy, taken from JEFF3.3 release [11]. At neutron energies below ∼0.2 eV, in the thermal and epithermal regions, the fission cross-section decreases following $^1/_v$ dependence. At higher neutron energies, above ∼0.2 eV and below ∼10 keV, the neutrons are in the ^{235}U resolved resonance region, where cross-section features sharp peaks due to neutron energies coinciding with the ^{236}U* energy levels. The energy levels overlap at energies greater than ∼10 keV and form a continuum in the cross-section, known as the unresolved resonance region. At energies greater than ∼6 MeV, the compound nucleus is excited to energies above neutron separation. This region is known as the multi-chance fission region, a name given to it due to compound nucleus undergoing fission following emission of one or more neutrons.

2.4 Fission Products

The fission process is very diverse and results in a range of product particles. A typical fission event produces two fission fragments (FF), accompanied by a number of neutrons and gamma rays. Ternary fission, i.e. fission that produces three fragments, is also a possibility and occurs at a rate of about 0.3% of all fission for ^{235}U [52], producing an alpha particle as a third fragment in 90% of such events [53]. The alpha particle is then ejected at a ∼90°angle to the paths of the two larger fragments. A proposed exotic case of ternary fission called 'colinear ternary fission' produces light nuclei through formation of two fragments, where one of them forms in a highly-deformed configuration and undergoes a secondary fission-like rupture [54], with the resulting fragment distribution featuring two lighter fragments moving in one direction and another, heavier fragment going in the opposite direction. Quaternary fission, division of a nucleus into 4 fragments, has also been experimentally observed at a rate of 1:10^6 fissions [55]. Much like in ternary fission, the additional fragments (as compared to binary fission) are typically light nuclei,

predominantly alphas. This work, however, concentrates on the most common binary fission, and the word 'fission' refers to binary fission by default throughout the work.

2.4.1 Fission fragments

The two FFs produced in binary fission of actinides are predominantly asymmetric in mass. Figure 2.4 shows the FF mass distribution for a number of parent nuclei. Heavy fragment mass distributions are consistently peaked around the $Z = 50$, $N = 82$ double-shell closure, indicating the importance of shell effects in the fission process.

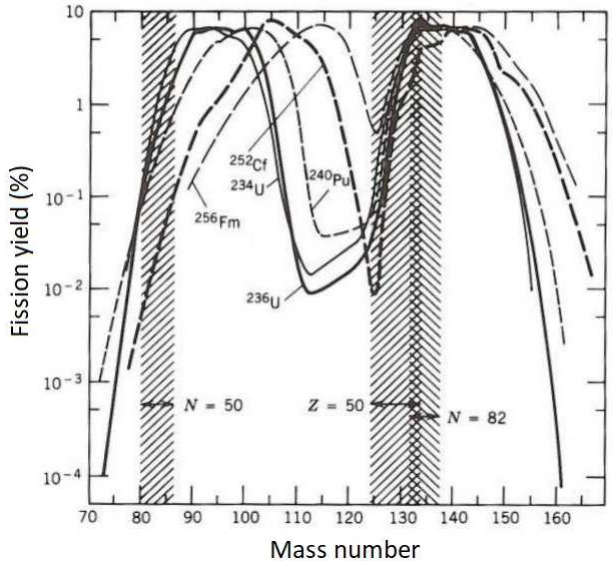

FIGURE 2.4: Mass distributions of fission fragments produced in fission of ^{234,236}U, ^{240}Pu, ^{252}Cf, [56] and ^{256}Fm [57]. One noteworthy feature of the mass distributions presented is the consistency of the heavy fragment masses, centering around the $Z = 50$, $N = 82$ shell closure.

There are other shell closures involved in describing the mass distributions of fission fragments. An observed increase in the $A = 140$ yield of heavy fragments, shown in Fig. 2.4 above, is typically attributed to the $N = 88$ deformed shell closure [58]. The $Z = 28$ and $N = 50$ shell closures contribute to increased yield in $A = 70$ light fragments in highly-asymmetric fission [59] and in colinear ternary fission [60], and $Z = 2$, $N = 2$ closures explain the prevalence of alphas forming in the neck region during ternary/quaternary fission.

A general description of scission configurations and the resulting fission fragment mass, shape and kinetic energy distributions in binary fission was formulated by U. Brosa *et al* [61] in terms of neck length between the two fragments. Scission configurations, often called Brosa modes, are grouped into several types. The original publication suggests four modes, Standard I, Standard II, super-short and super-long, however a fifth mode, Standard III, has since been identified [62]. A schematic representation of

the modes is shown in Fig. 2.5 with Standard modes combined into one. The standard modes are all asymmetric and correspond to the scission configurations built on the shell closures described above: the Standard I mode corresponds to the $Z = 50$, $N = 82$ heavy fragment configuration, Standard II to the $N = 88$ deformed shell, and Standard III to the $Z = 28$, $N = 50$ closure. The super-short and super-long modes are both symmetrical. The shape and kinetic energy properties of the fission fragments are interrelated and arise naturally from the Brosa modes: if the mode's neck is longer, the fragments are further apart, which implies less Coulomb repulsion between them. In such a situation, the fragments would separate with lower kinetic energies, leaving more energy for their excitation, deformation and possible subsequent neutron and gamma emission. As Fig. 2.5 shows, for super-short mode, fragments tend to be more oblate, and, conversely, in super-long mode they tend to be more prolate.

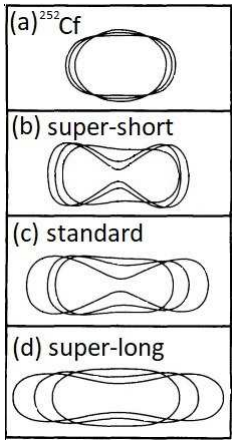

FIGURE 2.5: A schematic representation of Brosa modes, adapted from [61]. Panel (a) shows a ^{252}Cf nucleus as it stretches into a fission isomer. Fission isomer then tunnels through the second barrier and undergoes scission process, which Brosa *et al* described in terms of scission modes dependent on the length of the neck between the nascent fragments: super-short (shown in panel (b), Standard I and II (grouped into a single standard mode in panel (c)) and super-long (shown in panel (d)).

Fission fragments are typically produced in a neutron-rich configuration, since stable nuclei around and below the $Z = 50$ shell closure have a lower neutron-to-proton ratio than actinide nuclei [63]. Thus, when ^{235}U (proton-to-neutron ratio 143:92≈1.55) undergoes fission, the resulting fragments have an excess of neutrons, explaining the neutron emission taking place as described above. After the excitation energy has been expended, the nuclei undergo β^- decay and the resulting nuclei are referred to as 'fission products' (as opposed to 'fission fragments'), and their production time (order of seconds [8]) lies outside the timescales of measurements performed using the detectors on STEFF (slow heavy fission fragment time-of-flight in STEFF is ≈120 ns).

2.4.2 Neutrons

The kinetic energy of the two fragments in binary fission typically takes away ∼80% of the binding energy available from fission. The other ∼20% takes the form of fragment excitation energy and is subsequently distributed between neutron and gamma-ray emission from the fragments [8]. Neutrons are typically emitted from moving fragments $\approx 10^{-18}$ s after scission [64] and appear forward-focused in the laboratory frame of reference due to kinematic boost from the fragments. However, an earlier emission of neutrons perpendicularly to the axis of fission from the neck of a scissioning nucleus has been a long-standing subject of interest [64] [65] [66] [67] and estimated to account for ≥10% of prompt fission neutrons [64]. Such neutrons have not been experimentally confirmed, and a recent prompt fission neutron measurement by A. Göök *et al* [68] for ^{235}U fission induced by 0.26 eV - 45 keV neutrons appears to contradict prior experimental suggestions for the existence of scission neutrons in that energy region.

Since it takes several MeV to separate a neutron from a nucleus, prompt fission neutron (PFN) emission occurs while there is sufficient energy available for the process. The number of prompt neutrons emitted is known as the neutron multiplicity, denoted ν. Averaged multiplicity for light fragments has been measured to be $\bar{\nu}_{LF} \approx 1.42$, and $\bar{\nu}_{HF} \approx 1.00$ for heavy fragments [68]. Further delayed neutrons may be emitted following beta decay of the fragments [69]. Typical PFN energy distribution is shown in Fig. 2.6 and average PFN multiplicity as a function of FF mass is shown in Fig. 2.7.

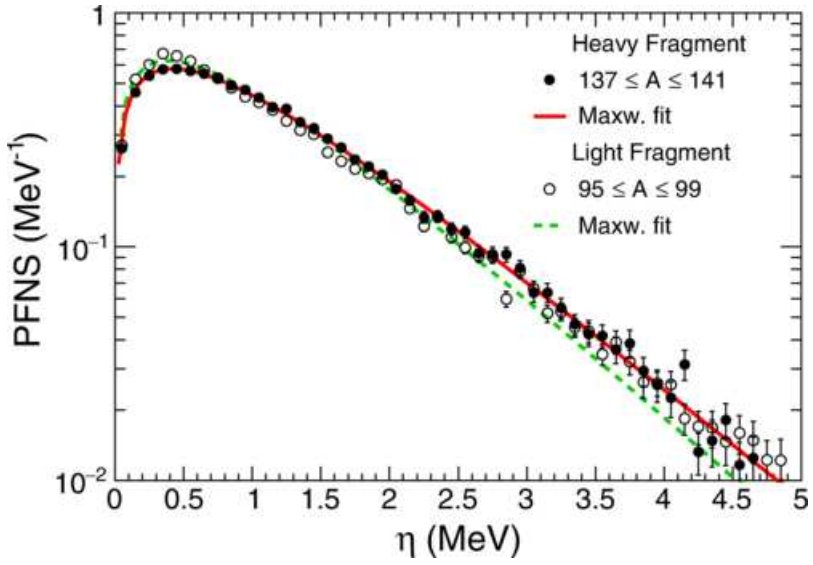

FIGURE 2.6: Prompt fission neutron energy spectrum, showing the measured prompt neutron energy η distribution in the centre-of-mass frame in ^{235}U fission for light fragments (in white) and heavy fragments (in black) [68]. Also shown are Maxwellian fits to the distribution: dashed green lines for light fragments and solid red line for heavy fragments.

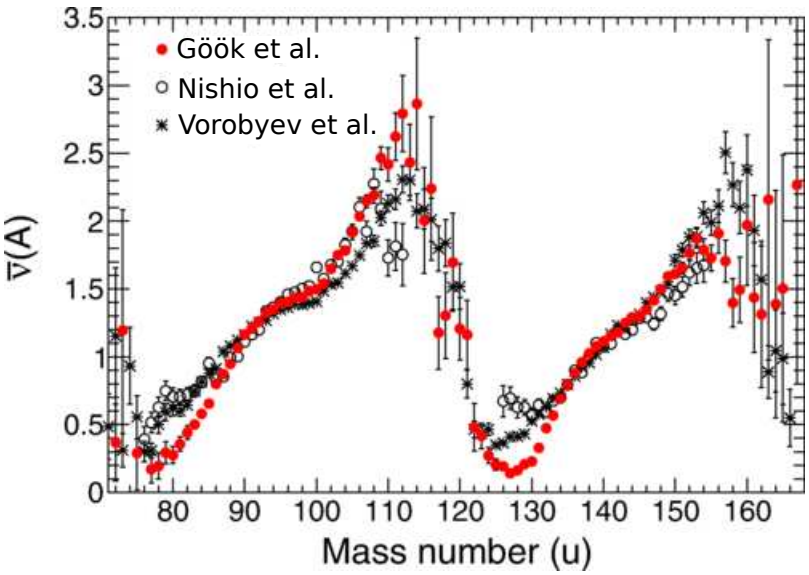

FIGURE 2.7: Average multiplicity spectrum of measured PFN from ^{235}U fission as a function of FF mass, adapted from [68]. The results are compared to previous measurements by Nishio *et al.* [70] and Vorobyev *et al.* [71]. The spectrum exhibits a shape often referred to as 'sawtooth', whereby as light and heavy fragment sides of the spectrum increase in mass and the heavy fragment moves further from $Z = 50, N = 82$ shell closures, more neutrons are available for evaporation.

2.4.3 Gamma rays

Once the available excitation energy approaches neutron separation energy, gamma emission competes with neutron emission depending on the spins and parities of the states the nucleus occupies at this stage [72]. Once excitation energy is expended to levels below the neutron separation threshold, fission fragments emit high-energy statistical gamma rays until they decay to an yrast state. Subsequent decays take place through gamma emission via series of states with the lowest spin for a given available excitation, i.e. yrast line gamma ray emission, until the nucleus reaches the ground state [69]. Collectively, these fission gamma rays are referred to as prompt fission gammas (PFG), as opposed to delayed gamma rays originating from long-lived isomers or following beta decay of the fragments. Figure 2.8 shows the stages described above for binary fission of a ^{248}Cm nucleus. Fig. 2.9 shows PFG spectra (PFGS) as measured by Oberstedt *et al.* [14] and Verbinski *et al.* [18], along with the PFGS in the ENDF/B-VII.1 release [23]. PFGS show the energy distribution and relative yield of PFG. Measurements of PFGS in correlation with fission fragments is the aim of the STEFF experiments conducted to date.

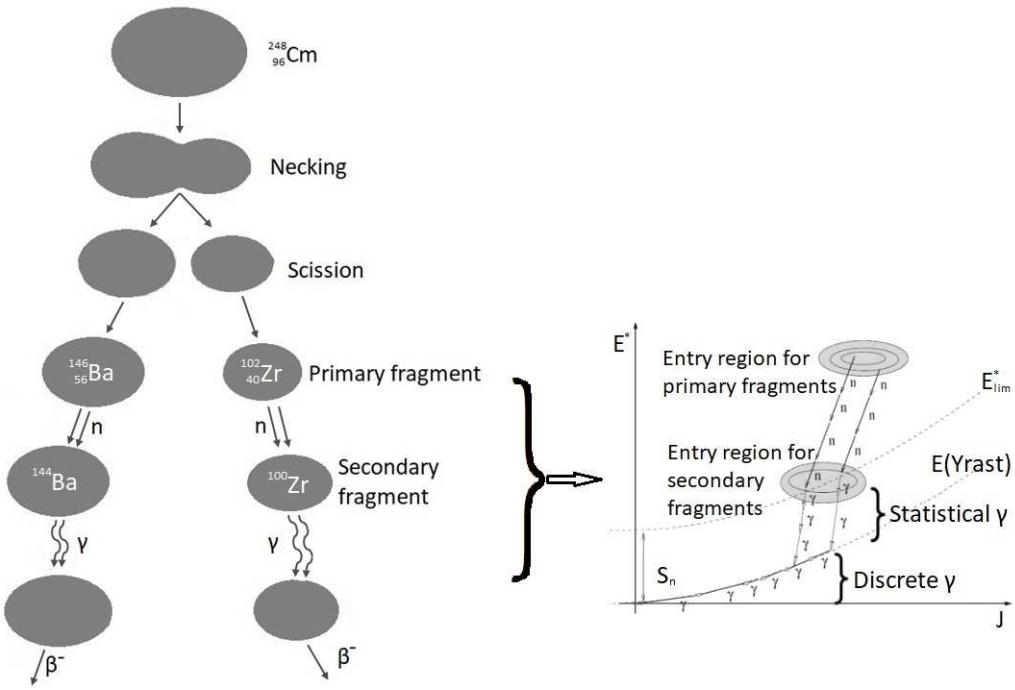

FIGURE 2.8: A timeline of several significant stages during binary fission of a ^{248}Cm nucleus adapted from [69]. The parent nucleus divides into two fission fragments which emit neutrons. Subsequent de-excitation of the fission products takes place by gamma decay. Lastly, fission fragments undergo several beta-decays. The fragment de-excitation process is describe in greater detail in the insert, which was adapted from [73]. The insert shows a schematic representation of the primary and secondary fragment excitation energy E^* dissipation against fragment spin J. The fragments de-excite via neutron emission until their excitation is re-educed to an energy limit E^*_{lim}, which is less than the neutron separation energy S_n. The fragments then de-excite from the high-spin region via statistical decays until they reach the yrast line at energy E(Yrast) and de-excite via discrete yrast decays.

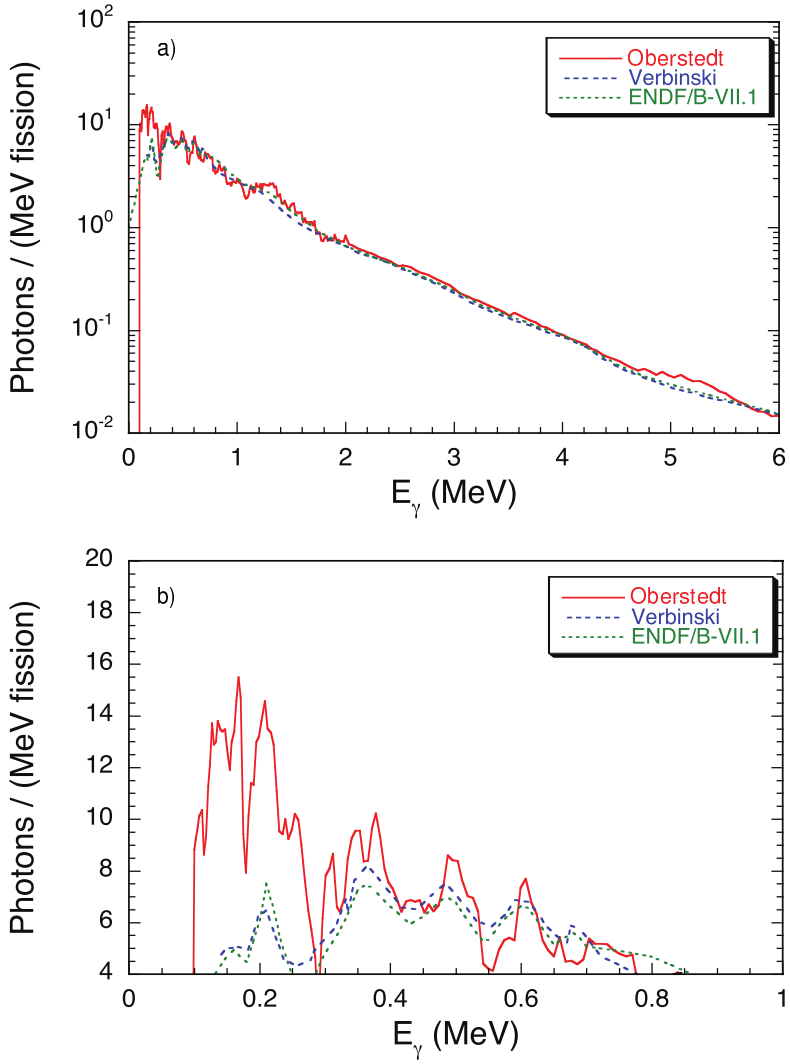

FIGURE 2.9: Comparative results of PFGS measurements by Oberstedt *et al.* [14], Verbinski *et al.* [18] and ENDF/B-VII.1 [23]. The top panel a) shows the full measured gamma-ray energy range, while bottom panel b) shows only the lower-energy part of the spectrum. Adapted from [14].

Blank page

Chapter 3

STEFF

3.1 STEFF

STEFF was constructed at the University of Manchester in the late 2000's with the aim of conducting PFG measurements to address the data needs of the nuclear industry and fundamental nuclear science. The spectrometer was conceived based on a pre-existing experimental set-up, where an HPGe array was used in conjunction with an ionization chamber to perform nuclear structure measurements based on gamma-ray spectroscopy, such as isomeric states identified in ^{94}Rb fragments produced through ^{235}U fission [74]. Gas-filled detectors were developed and tested on several occasions [75] [20] at Lohengrin in a similar fashion to the experiment discussed in Chapter 4 of this work. Two ionization chambers were coupled to a NaI scintillator array forming STEFF, which had its debut in fission studies at the PF1B neutron guide at ILL in 2013 [76]. The experiment consisted of measurements of PFG and both FF formed in binary thermal neutron-induced fission of ^{235}U. Since that experiment, STEFF underwent a number of modifications. The upgrades include addition of two secondary 1E1v arms, changes to the time-of-flight detectors, upgrades to NaI detectors and changing some NaI crystals to $LaBr_3$. The diagram of the current layout of the spectrometer is presented in Fig. 3.1.

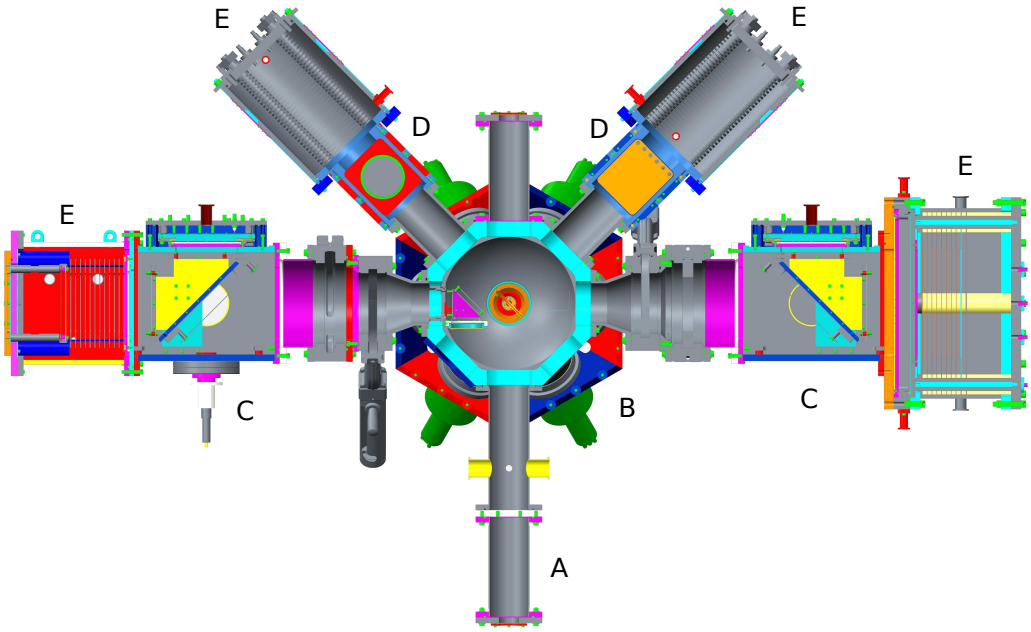

FIGURE 3.1: False-colour diagram of the STEFF spectrometer with labeled sections [77]. Letter A indicates the neutron beam entry point. Letter B denotes the central chamber, which contains the fissile material target (in orange), the START detector (in purple) and an array of scintillators (in green). Letter C shows the positions of the two MWPC STOP detectors on the main arms of STEFF (left arm is Bragg, right arm is Hipps). D indicates the position of the MCP STOPs in the FiFI arms. Lastly, E shows the positions of the four gas-filled detectors.

In the diagram, the main features of STEFF are indicated in false colour and with letters. The beam line, indicated by letter A, enters STEFF from below and exits at the top, allowing the neutrons that did not interact with the target to travel to the beam dump. The target is positioned inside the central chamber, denoted with letter B, The target mount can rotate at certain angular increments; there have been several such target mounts used with different rotational capabilities. Next to the target sits the START detector used for starting the timing of the FF ToF through the main two arms of STEFF. The START detector sits on the Bragg arm of STEFF, which is on the left in the diagram. Around the central chamber are 12 slots for scintillator detectors. Passive tungsten shields surround the scintillator slots to reduce detector-to-detector scattering. The scintillators are mainly 4×5 in. NaI(Tl) detectors with a geometric efficiency of 30%, but individual or clustered $LaBr_3$(Ce) scintillators have also been used. STEFF has four arms attached to the central chamber; the two arms that are opposite each other around the target are called Bragg and Hipps and form the 2E2v section of STEFF. The other two arms are called FiFI Bragg and FiFI Hipps, these arms perform measurements of only one of the two fission FFs in an event. Each of the arms has a STOP detector: the two main arms' STOPs are MWPC assemblies (marked with letter C) and the FiFI arm STOPS are microchannel plate (MCP) assemblies (marked with letter D). All arms end in gas-filled chambers, which are denoted with letter E.

3.1.1 2-Energy 2-velocity Measurements

The main arms of STEFF rely on the 2E2v technique, whereby both FF from binary fission have their velocities and kinetic energies measured in parallel. Since FF travel at velocities of a few percent of the speed of light, their kinetic energy can be approximated using the classical kinetic energy formula

$$E_k = \frac{Av^2}{2}, \tag{3.1}$$

where A is the FF mass following neutron emission and v is velocity. Measurements of kinetic energy and velocity, therefore, permit a calculation of FF mass. In principle, given sufficient mass resolution, measuring the two FF masses allows one to calculate the number of prompt neutrons emitted during fission, although the current mass resolution of STEFF ($\pm$4 amu) is insufficient for this purpose.

Other 2E2v devices have been previously constructed for fission experiments. The first such device was Cosi Fan Tutte [78], which was constructed and operated at ILL in Grenoble, France. This spectrometer attained a great time resolution of 100 ps for velocity measurements and a very good energy resolution of $\approx$500 keV for light fragments, which led to its capability of resolving individual FF masses. Cosi Fan Tutte, however, had very low geometric efficiency, which has been estimated to be at most 0.1% [79], which led to its disuse. Several other 2E2v spectrometers were built following the proof of principle by Cosi Fan Tutte. Besides STEFF, there are three other spectrometers: VERDI (VElocity foR Direct particle Identification) [80], SPIDER (SPectrometer for Ion DEtermination in fission Research) [81], and FALSTAFF (Four Arm cLover for the STudy of Actinide Fission Fragments) [82]. VERDI spectrometer has two silicon detector arms, which are currently being investigated for plasma delay time effects whereby electron-ion plasma formed in Si delays signal registration by the anode [83]. SPIDER spectrometer is ionization chamber-based and is being upgraded from two arms to sixteen in order to form a new spectrometer called MegaSPIDER [84]. FALSTAFF is planned to have two ionization chamber-based arms, only one of which is completed and is currently being tested [85].

3.1.2 START

STEFF START detector is one of the two sets of timing detectors required for measuring the FF ToF in the main arms of STEFF. START detector is positioned 15 cm from the target center covering $\approx$0.37 sr [86], and comprises three main components that share a

mount. The full assembly is shown in Fig. 3.2. The main mechanism of START timing is the emission of electrons from a thin foil, called Secondary Electron Emission (SEE) foil, which is made of aluminium evaporated onto a 0.2 μm formvar film and is held at a -1.75 kV potential. The aluminium layer has a thickness of 10$\pm$1 μg cm^{-2}. The electron emission may occur as the FF passes through the foil and interacts with the atomic electrons in it. Alternatively, the emission can be spontaneous, producing a background of false signals. When a fragment ejects electrons from a foil, a large number of them will be forward-scattered, however some of them may be backscattered instead (for light fragments, 95 forward-focused electrons have been measured in Ref. [87], compared to 38 backward-focused electrons). A measurement has been performed on foils identical to the START foils [88] using α particles in order to estimate the number of the electrons emitted at backwards angles per incident α. The resulting value of 1.1$\pm$0.2 electrons is in agreement with previously measurement by Pferdekämper and Clerc [87] performed for carbon foils. The investigation in Ref. [88] did not make electron emission measurements for FF, however Pferdekämper and Clerc observed backward emission of 38 electrons for light fragments and 40 for heavy fragments, with the majority of the electrons having the energy of less than 230 eV.

The backscattered electrons in the START detector enter the space between the foil and the electrostatic mirror, which consists of two wire grids separated by 1 cm. The wires have a diameter of 20 μm thick and a pitch of 2 mm, resulting in a transparency of 90% [77]. A potential of -3.5 kV is applied across the gap between the grids in order to deflect the electrons into the MCP assembly, which consists of two Hamamatsu F1942-04 MCPs [89] in a chevron configuration. The MCPs are $\approx$1 mm-thick lead-doped glass plates with $\approx$25 μm-wide tubular channels, which extend from one side of the plate to the other at an angle to the surface. The channels are angled to ensure the interaction of any electrons entering the MCP with the channel walls. A voltage is of -4.8 kV is applied across the MCPs, accelerating the electrons which enter it in order to cause ejection of secondary electrons in the collisions with the walls. The chevron arrangement of the two MCP plates means that the channels in the first MCP are arranged at a different angle to the channels in the second MCP, so that the electrons leaving the first MCP will restart the collisions upon entering the second plate, while also reducing the slow component of the signal caused by electrons ejected through scattering of resulting ions. This process repeats until the electrons leave the second MCP and are registered by the anode as a timing signal. The collisions in the MCPs multiply the number of electrons by a factor of $\approx 10^6$. The STOP detectors in the FiFI arms have an identical arrangement to the START detector.

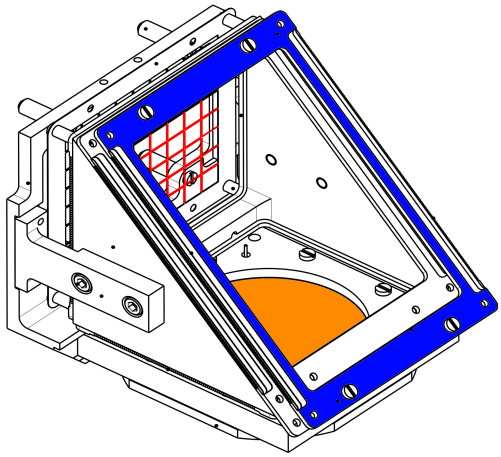

FIGURE 3.2: A false-colour diagram of the START detector assembly. Shown in red is the metal grid that supports the timing foil. The support mount that holds the thin wire grid of the electrostatic mirror is in blue. In orange is the position of the MCP.

3.1.3 Scintillators

As mentioned previously, STEFF gamma-ray measurements are performed using some combination of NaI(Tl) and $LaBr_3$(Ce) inorganic scintillation detectors. The scintillators are arranged in two rings surrounding the target and containing 6 scintillator slots each. The scintillators are all angled at 45° relative to the horizontal plane, spaced at 60° relative to each other and are positioned 20 cm away from the center of the chamber. Both of the scintillator types function in similar ways, which are thoroughly described in Ref. [90]. The general principle behind these detectors lies in conversion of the incident gamma-ray energy into visible scintillation light. This is done by means of a crystal whose electrons are promoted to conduction band by an interaction with an incident gamma ray via Compton scattering or photoelectric effect. If the electron was to be re-absorbed by a resulting hole, the photon could be re-absorbed or its energy would be too high for photomultiplier tubes to function efficiently, so an activator material is added to the crystal at a fraction of ∼0.1%. The addition of the activator material introduces levels into the forbidden gap of the crystal electronic band structure. The sites with activator material then become very favorable for electron de-excitation, which is done in smaller increments producing visible scintillation light (maximum wavelength of NaI scintillation light is 415 nm [91] and 380 nm for $LaBr_3$ [92]). Moreover, since the resulting photons are not produced with energies that match the majority of the electronic levels of the crystal, there is very little self-absorption of the scintillation light by the crystal.

Scintillation light may travel to the photocathode attached to the photomultiplier tube (PMT) or alternatively towards the sides of the crystal. Typical NaI crystals are surrounded with MgO powder to reflect the visible photons to ensure maximum flux at the

photocathode [90]. For a properly-chosen photocathode material, once the visible light impinges on the photocathode, it will be absorbed and an electron will be emitted. The geometry of the photocathode is such, that the electrons are focused towards a series of dynodes. A potential across the multiplication region that the dynodes occupy will accelerate the electrons, which will scatter off or inside the dynode and eject secondary electrons. The multiplied current of secondary electrons will then be accelerated towards further dynodes and the process will repeat. The final current for *Scionix Ltd.* PMTs used on STEFF is typically multiplied by a factor of $>10^5$ over a series of 10 dynodes [93]. The current is finally collected at the anode and forms a signal of amplitude proportional to the original gamma-ray energy for a properly configured scintillation setup.

For NaI(Tl) (sodium iodide) and $LaBr_3$(Ce) (lanthanum bromide) scintillators, the principal performance differences lie in the timing and the energy resolutions of the two detectors and stem from the difference in electron structure and its decay time. Greater Z of the constituent elements in a $LaBr_3$ crystal means that there are more electrons with various pathways through the band gap available for excitation and subsequent scintillation (typical $LaBr_3$ scintillation photon yield is 65 per keV of incident gamma energy [92], while the same value is 38 for NaI [91]), which contributes to a considerable improvement in the energy resolution ($\sim$3% for 661-keV ^{137}Cs gamma ray, compared to $\sim$7% in NaI [91]). The primary reason for the improved resolution of the $LaBr_3$ compared to NaI, however, lies in the light yield non-proportionality of the two scintillator types [94]. Light yield non-proportionality is a factor that varies depending on the incident gamma-ray energy and, as the name suggests, describes the linearity of the of scintillation light yield for each gamma-ray energy. Non-proportionality arises in scintillators from various complicated interactions of photons and electrons inside the crystal that affect the detector response, such as formation of Auger electrons, δ rays, excitons, etc. [95]. The reduction of the contribution of these properties is discussed in Ref. [94], and measurements with a ^{137}Cs source in Ref. [95] show a factor of two reduction in non-proportionality for $LaBr_3$ compared to NaI crystals. $LaBr_3$ timing resolution is also improved compared to NaI crystals, and primary decay time is $\sim$20 ns in $LaBr_3$ [96] [92] and $\sim$250 ns in NaI [96] [91]. A spectrum comparing the response of the two detector types to that of HPGe for a mix of standard calibration sources in shown below in Fig. 3.3.

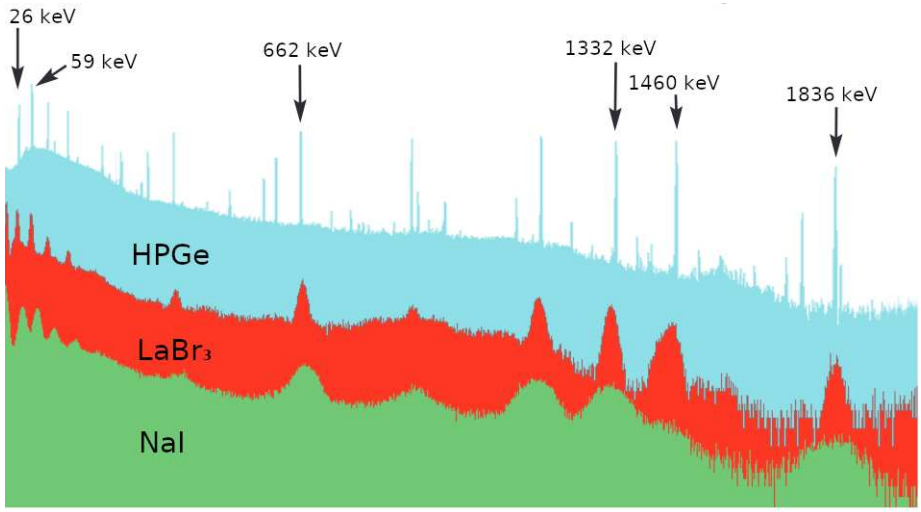

FIGURE 3.3: Spectra collected by HPGe, $LaBr_3$(Ce) and NaI(Tl) detectors for a mix of standard calibration sources demonstrating differing energy resolutions [96].

Despite the advantages presented by the smaller crystal, the trade-off in replacing NaI crystals with $LaBr_3$ arises through reduced geometric efficiency, which combines poorly with the efficiency problems associated with 2E2v technique. The NaI detectors on STEFF have a diameter of 127 mm and a length of 102 mm, while the $LaBr_3$ used in ^{235}U measurements was a block with a 55×55 mm face and a 110 mm length. Replacement of one NaI crystal on STEFF with 1 $LaBr_3$ crystal resulted in geometric efficiency for gamma rays reducing from ≈ 30% to ≈ 28% [21]. Smaller size also implies lower likelihood of re-absorption of a scattered gamma-ray. A comparison of Compton events from 661-keV gamma rays from a calibration ^{137}Cs source for the two crystal types is show in Fig. 3.4. Furthermore, $LaBr_3$ crystals produce a gamma-ray background due to the internal activity of natural lanthanum. Natural lanthanum is 0.09% ^{138}La, which has a half-life of 10^{11} years against β^+ decay to ^{138}Ba with a branching ratio of ≈66% or β^- decay to ^{138}Ce with a branching ratio of ≈34%. The former results in a gamma-ray of 1436 keV followed by a ^{138}Ba X-ray of 32 keV, the latter results in a gamma ray with an energy of 789 keV [97]. These two gamma rays form background in experiments involving natural lanthanum scintillators, which has to be accounted for, although these transitions also may be beneficial by serving as an additional calibration source.

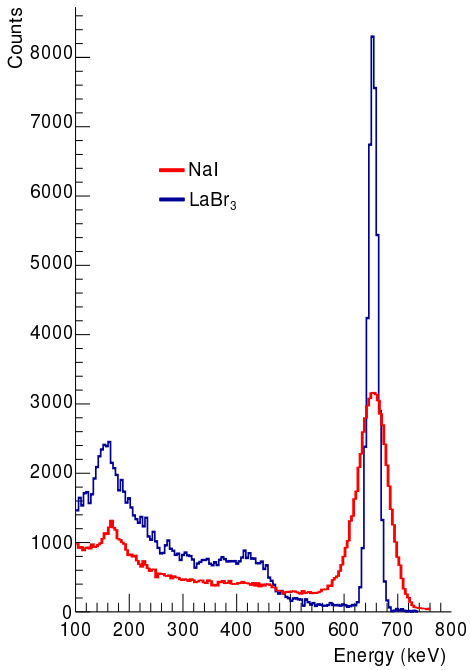

FIGURE 3.4: A comparison of the responses of $LaBr_3$(Ce) (in blue) and NaI(Tl) (in red) scintillators to a standard calibration source of ^{137}Cs normalized in area. The photopeaks and Compton continuum features typical of the source are clearly visible, and the relative amount of counts in the two features indicates the lower photopeak efficiency of the $LaBr_3$ compared to the NaI due to its smaller size. The superior energy resolution of the $LaBr_3$ is also evident.

The *Scionix Ltd.* PMTs used on STEFF were modified by the manufacturer to be more resistant to high-rate saturation effects by switching the input voltage polarity, extending the capacitor chain and reducing the resistor chain between the dynodes, and removing the capacitor on the PMT output [21]. Examples of testing of the new PMT performance at high rates are presented in Ref. [21]. The need for these modifications arose due to the differences between ILL and n_ToF, where the latest STEFF campaigns took place. A further description of the fission rates and gamma-ray flux at n_ToF are presented in Chapter 5.

3.1.4 Gas-filled Detector Principles

STEFF features several gas-filled chambers: MWPC STOP detectors and Bragg detectors (BD), i.e. ionization chambers with a coaxial anode orientation. Typical gas-filled detectors rely on ionization caused by charged particles to produce electron ion pairs, which may be used to form a signal. In the case of STEFF, FFs or electrons ejected from timing foils undergo a series of collisions with gas molecules. The signal is produced through collection of the resulting electrons and, in the case of STEFF BDs, is proportional to FF energy, although there are several effects that need accounting for when considering the signal. Such effects include non-ionizing excitations of the gas molecules

during the collision, capture of ejected electrons by ions (called recombination), and possible electron exchange between the gas and the FF.

The general process of stopping of charged particles in a medium is described by the Bethe-Bloch formula given in Eq. (3.2) [98]. Note that the Bethe-Bloch formula does not perform as well for stopping of ions in the FF velocity range compared to faster ions, see Chapter 4 for detail.

$$\frac{\mathrm{d}E}{\mathrm{d}x} = -\rho\frac{2KZ}{A\beta^2}\left[\ln\left(\frac{2m_e c^2\beta^2}{I\left(1-\beta^2\right)}\right) - \beta^2 - \frac{C}{Z} - \frac{\delta}{2}\right], \tag{3.2}$$

where

$$K = \frac{4\pi N e^2}{m_e c^2}. \tag{3.3}$$

In the Bethe-Bloch formula, $^{\mathrm{d}E}/_{\mathrm{d}x}$ is the differential energy loss (often referred to as the stopping power or, more accurately, stopping force), ρ is the medium density, Z is the medium atomic number, A is the medium atomic mass, β is the fragment velocity ($^{v}/_{c}$), m_e is the mass of an electron, e is the electron charge, and I is the mean excitation potential. The $^{C}/_{Z}$ term is used for lower energy collisions, when lower electron orbitals are screened by higher orbitals. The $^{\delta}/_{2}$ term is a relativistic correction.

The effects of recombination are reduced by increasing the electrode potential inside the chamber. Five regions of operation of gas-filled chambers are defined in [90] based on the electrode potential. These regions are shown in Figure 3.5.

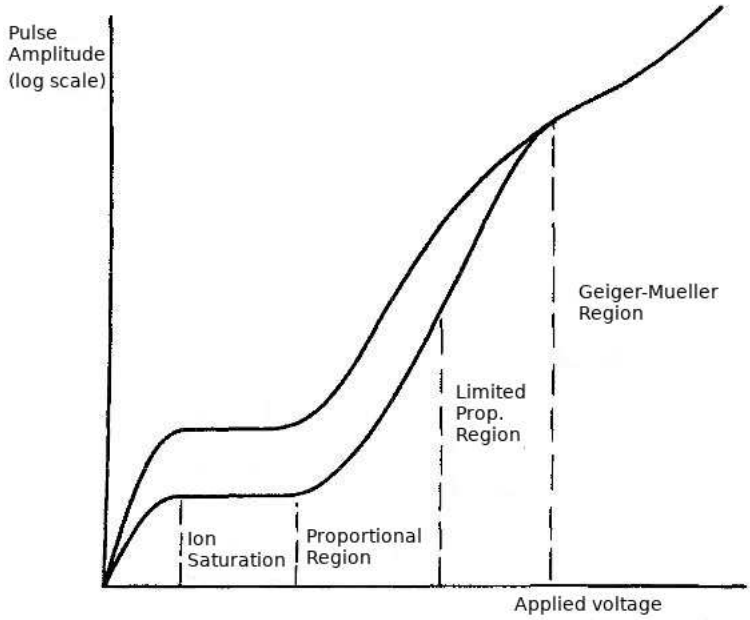

FIGURE 3.5: A diagram of regions of operation of gas-filled detectors based on the applied voltage adapted from [90]. The diagram is divided into five regions by vertical dashed lines. The five regions are: the recombination region, the ion saturation region, the proportional region, the limited proportionality region, and the Geiger-Mueller region. The two lines represent the effect of doubling the energy deposition inside the gas. All gas-filled chambers discussed in this work are operated in the proportional region.

In the first region, the potential is too low to prevent recombination. An increase in the potential results in reduction of recombination, meaning that the electrodes collect nearly all the charge released in ionization. Further increases in the potential accelerate the released charges to a sufficient drift velocity to cause multiplication. Multiplication is a process whereby primary electrons produced in ionization events are accelerated towards electrodes and cause further ionization by colliding with medium atoms. In this region, the height of the pulse collected on the electrodes is approximately proportional to the initial (pre-multiplication) charge. Increase in potential past this region results in loss of the linear relation of pulse and initial ionization. In the Geiger-Mueller region, any proportionality is lost. This loss occurs due to multiplication processes becoming dominant over the initial ionization events. In this voltage range, multiplication releases charges until the amount of ions released offsets the electrode potential below the threshold for further multiplication. All the signals collected by the electrodes then result in same pulse height. Further increase in voltage causes breakdown arcs to spontaneously occur in the detector volume [98].

The process of charge multiplication in a chamber takes the form of an avalanche, where newly-released electrons are accelerated by the field, potentially causing further ionization. This process is called a Townsend avalanche [99] [90]. Fractional increase in the free electron number is given in the Townsend equation as

$$\frac{\mathrm{d}n}{n} = \alpha \mathrm{d}x. \tag{3.4}$$

The Townsend equation provides information on the increase in the number of free electrons $\mathrm{d}n$ over a distance $\mathrm{d}x$. The two quantities are related by the Townsend coefficient α, which is specific to a particular gas used in the chamber, and also depends on the gas pressure. Below the multiplication threshold potential $\alpha = 0$. If the electric field is constant inside the detector, which is the case for the STEFF MWPCs, the Townsend coefficient is a constant. MAGBOLTZ [100] simulations calculate a value $\alpha = 407$ in the MWPCs for isobutane gas.

3.1.4.1 Fill Gases

Unsurprisingly, a critical choice in designing a gas-filled detector is the fill gas. There are a number of fill gases frequently used, such as isobutane (iC_4H_{10}), P-10 (90% argon and 10% methane), CF_4, and argon [98]. There are a variety of factors that are important when considering the choice of a fill gas for a given gas-filled detector's purpose. A parameter of particular importance is the average ionization energy W. The values of this parameter for several gases are summarized in Table 3.1. The choice of parameters for the work presented here has to be made so as to maximize the signal amplitude in order to maximize the detector energy resolution and make any features in the signal formation process more identifiable.

TABLE 3.1: List of the average ionization energies W for a variety of typical fill gases. The values are taken from Ref. [98].

Gas	W (eV)
isobutane	26
P-10	30
CF_4	54
Ar	25

Average ionization energy determines the number of electrons produced in ionization during FF stopping, which in turn determines the amplitude of the signal (although electron re-absorption probability for a given gas will also affect this). Of the typical gases listed in Table 3.1, isobutane and argon have the lowest average ionization potentials, and stand out as the natural fill gas candidates. Fig. 3.6 shows a modeled number of electrons produced by a charged particle ionizing various gases as a function of the number of electrons in a molecule. It is evident from the figure, that isobutane provides the greatest electron yield, far in excess of argon. This is reconciled with the W considerations above by considering the screening of the lower electron orbitals by the electrons in higher orbitals, reducing the likelihood of their ionization.

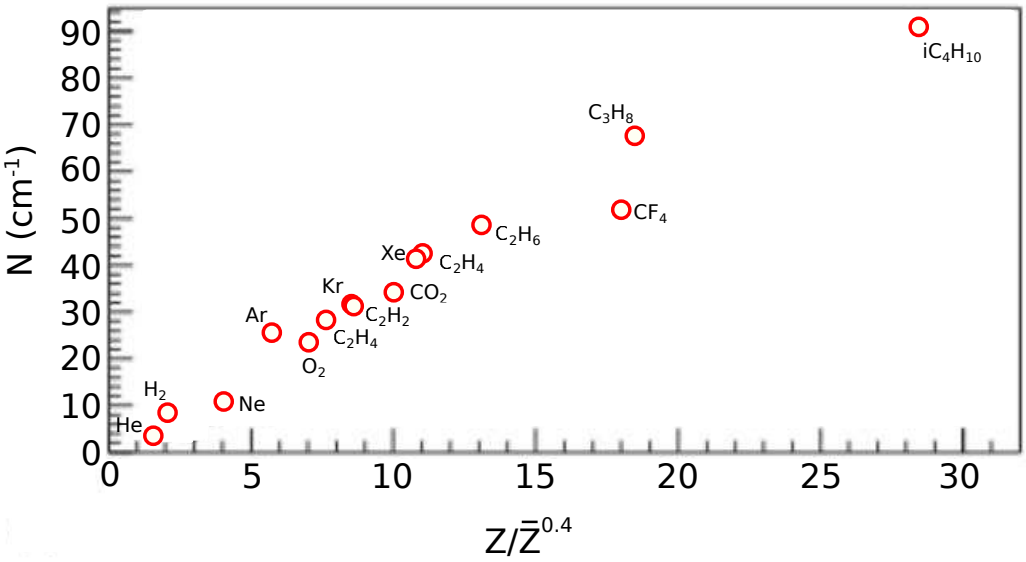

FIGURE 3.6: A plot of simulated number of electrons produced per unit range by charged particle ionization in various fill gases, adapted from Ref. [101]. The x-axis of the plot is a fitted ratio of the total number of electrons in a molecule Z divided by a power of the average number of electrons per atom in the molecule $\bar{Z}$. Ref. [101] provides comparison of their model with experimental results, which are found to agree.

Following the above considerations, all the gas-filled detectors on STEFF are operated with isobutane, although future experiments may consider other gases due to a health and safety issue of isobutane's flammability.

3.1.5 Multiwire Proportional Counters

MWPCs were first proposed in 1968 by G. Charpak with his colleagues [102], an invention that earned him a Nobel Prize [103]. MWPCs consist of a gas-filled chamber with an anode represented by a plane of thin wires stretched in parallel. The multiplication region, i.e. the region where the field is high enough to cause multiplication, is relatively small, meaning it does not span the volume of the chamber. Instead, it is cylindrically symmetric and centered around the wire [102]. A diagram of the field shape around a wire is shown in Figure 3.7.

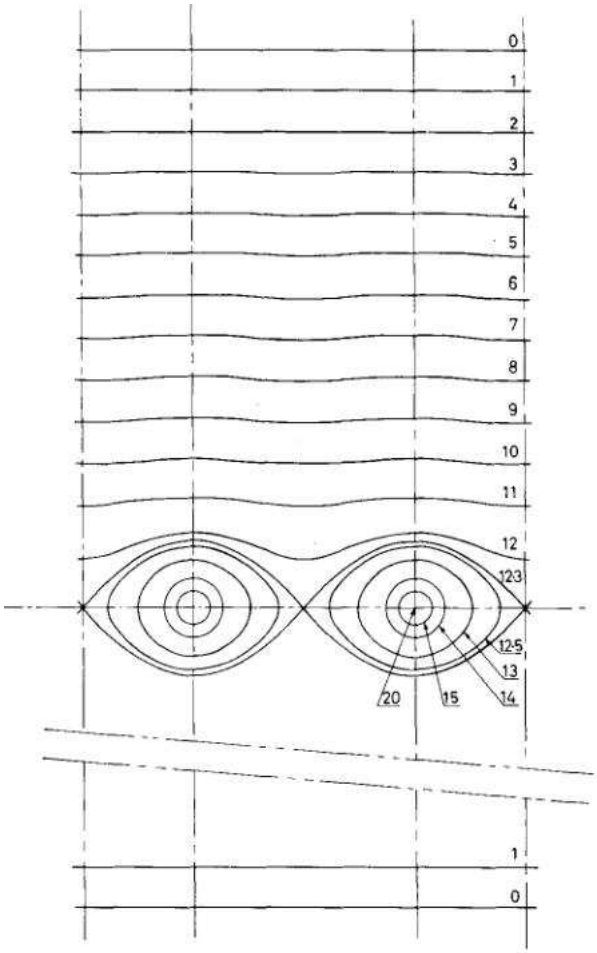

FIGURE 3.7: The shape of equipotential lines for an electric field around two wires in a multiwire proportional counter [102]. The centre of one of the wires is indicated by field line number 20, which is effectively a point.

The primary electrons drift towards the wire closest to the location of ionization, and upon entering the multiplication region accelerate sufficiently to start an avalanche. A Monte Carlo simulation result for an avalanche around an anode wire is shown in Figure 3.8.

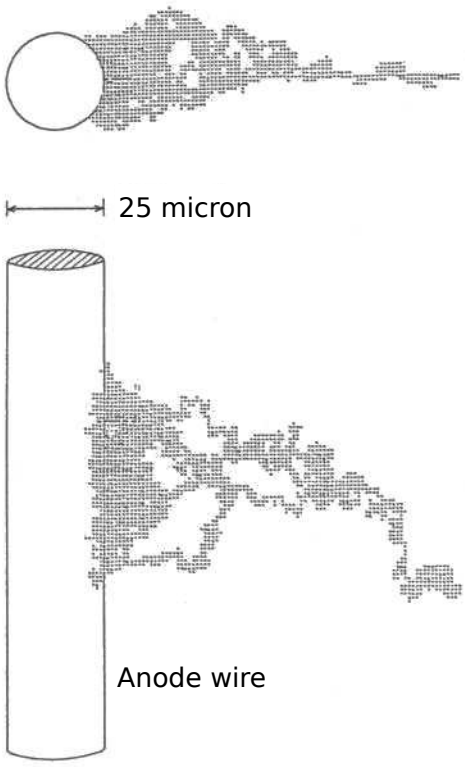

FIGURE 3.8: A schematic representation of a Monte Carlo simulation result for an electron avalanche around an anode wire [104]. Shading represents electron density.

3.1.5.1 STEFF MWPC STOPs

The STOP detectors in the main arms' ToF sections are made of a 0.2 μm indium-coated formvar window resting on a wire grid at a potential of -9 kV, acting as a SEE foil, an electrostatic mirror grid and a stack of two MWPC planes with a cathode plane. The arrangement is shown in Fig. 3.9 with cathode plane removed for visibility. As a secondary electron is emitted from the SEE foil, it travels through an electrostatic mirror, which deflects the electrons towards the MWPC planes. Unlike the START electrostatic mirror, the STOP mirrors have two acceleration regions both at a potential of -18 kV: one formed by the diagonal wire grids and the second region formed by two wire planes at the top of the electrostatic mirror. The additional acceleration is needed to ensure that the electrons have enough energy to pass through a 0.9 μm Mylar window that separates the gas of the MWPCs from the vacuum of the ToF section. The 45° angle of the electrostatic mirror relative to the emission foil reduces the path the electrons emitted at the bottom of the foil traverse before being deflected, while increasing the now-deflected electrons' path towards the gas window. The effect is reversed for the electrons emitted at the top of the foil, so they travel a longer distance towards the mirror, and then a shorter distance towards the window. Thus, the mirror's angle serves to normalize the distances all the backscattered electrons travel, improving the signal time characteristics. Furthermore,

the initial acceleration of electrons towards the electrostatic mirror results in reduction of the signal timing width caused by a distribution of initial electron velocities. As the backscattered electrons' velocities increase, the distribution of velocities is compressed, resulting in a narrow pulse with better time characteristics.

The gas inside the MWPC stack is isobutane at a pressure of 9.0 mbar. The arrangement of the wire grid stack is shown in Fig. 3.10 (note that the diagram is upside down compared to how the MWPCs are placed inside STEFF). The wire grids are soldered and glued onto 50×15 cm PCB planes. The first wire grid that the electrons encounter is the cathode held at a -600 V potential and is comprised of 50 μm gold-coated tungsten wires at 1 mm pitch and stretched length-wise. The next wire grid is an anode held at ground potential and subdivided into 4 electrically-connected banks of wires for position sensitivity. The anode wires are 20 μm thick gold-coated tungsten wires at a pitch of 1 mm, stretched perpendicularly to the wires of the cathode grids. The cathode and the anode grids are attached to a cathode plane made of copper, which also had a -600 V potential applied to it. The separation of all the layers forming the stack is 3.2 mm and all the layers are not electrically coupled to each other.

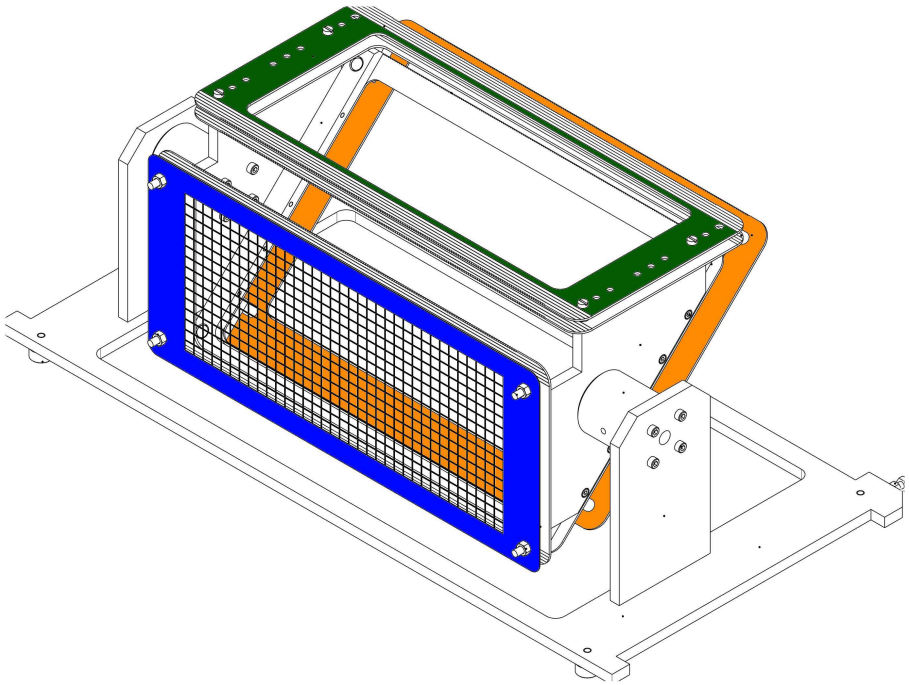

FIGURE 3.9: A diagram of the entire assembly for one of the two MWPC STOP detectors on STEFF. The SEE foil support is shown in blue along with the mesh that supports the foil. The electrostatic mirror plane position is shown in orange. The position of the anode wire plane is shown in green. The diagram omits the cathode plane that is layered above the MWPC wire grids for visibility.

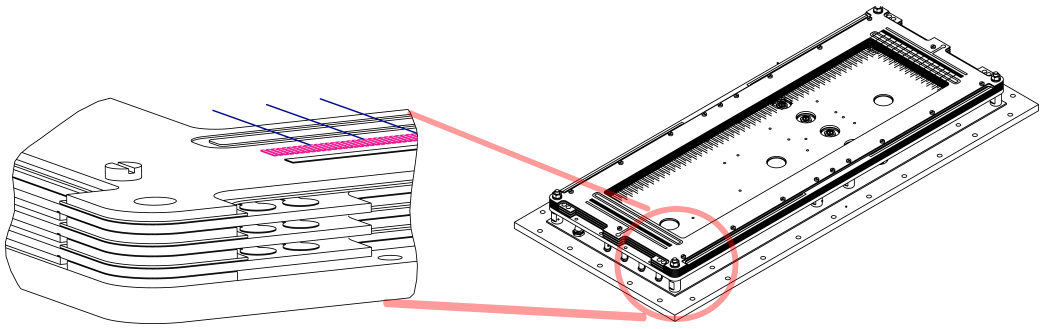

FIGURE 3.10: A diagram of the MWPC planes arrangement. The inset shows an expanded view of one of the assembly corners for greater visibility of the stack of anode and cathode grids. Pads onto which the wires are soldered are shown in magenta. Examples of wire orientation for the anode planes is shown with dark blue lines.

3.1.5.2 STEFF Bragg Chambers

There are four Bragg chambers that terminate each of the four STEFF arms and result in a total geometric efficiency of 134 mSr (the main arms cover 30 mSr and FiFIs cover 37 mSr each). While FiFI Bragg and FiFI Hipps BDs are identical, the construction of Bragg BD, Hipps BD and the FiFIs is different. The schematic diagrams of each type of BD is shown in Figs. 3.11. The Bragg BD operates at 70 mbar isobutane pressure and a 1200 V potential, while the Hipps and FiFI BDs operate at 100 mbar pressure with 900 V potential. The Bragg BD is 20 cm deep, and the Hipps and FiFI BDs are 15 cm deep. The depth of the chamber here is measured from the entrance window (0.9 μm of aluminized Mylar) to the Frisch grid. The diagrams of the Bragg and Hipps arms including the BDs are shown in Figs. 3.12 and 3.13 respectively.

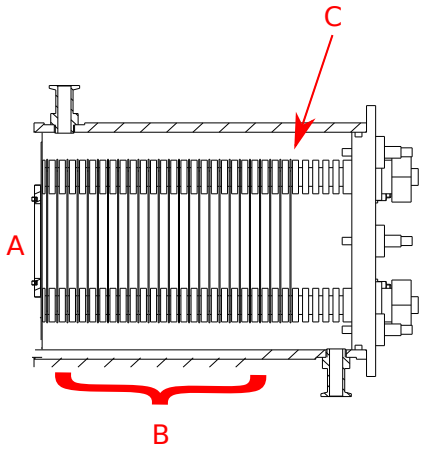

FIGURE 3.11: A schematic diagram of the structure of a FiFI BD. Letter A indicates the location of the entrance window foil, B shows the guiding rings and C shows the position of the Frisch grid and the anode.

The Frisch grids are used in the Bragg chambers in order to shield the anode from the electromagnetic fields of electrons and ions as they form while the FF is stopping. Positive ions are swept by the electrostatic field towards the window, which acts as a

cathode. The electrons that are formed at the start of the FF track exist in the volume of the BD for longer than the electrons formed at the end of the FF track. Therefore an unshielded anode, beside accumulating varying amounts of ion signal, would collect the signal from the early electrons for longer than from the later electrons, leading to non-linearity of the final BD signal depending on the track length. A Frisch grid acts as shield, preventing the induced electron signal from reaching the anode until the electrons drift past the grid, and blocking the signal from the ions. The electrons are accelerated to their full velocity almost immediately upon forming, which means that they travel with the same drift velocity as they pass by the grid, taking the same time to traverse the grid-anode space, leading to a linear signal. STEFF Frisch grids are made of 20 μm wires stretched at a pitch of 2 mm, 1 cm above the anodes.

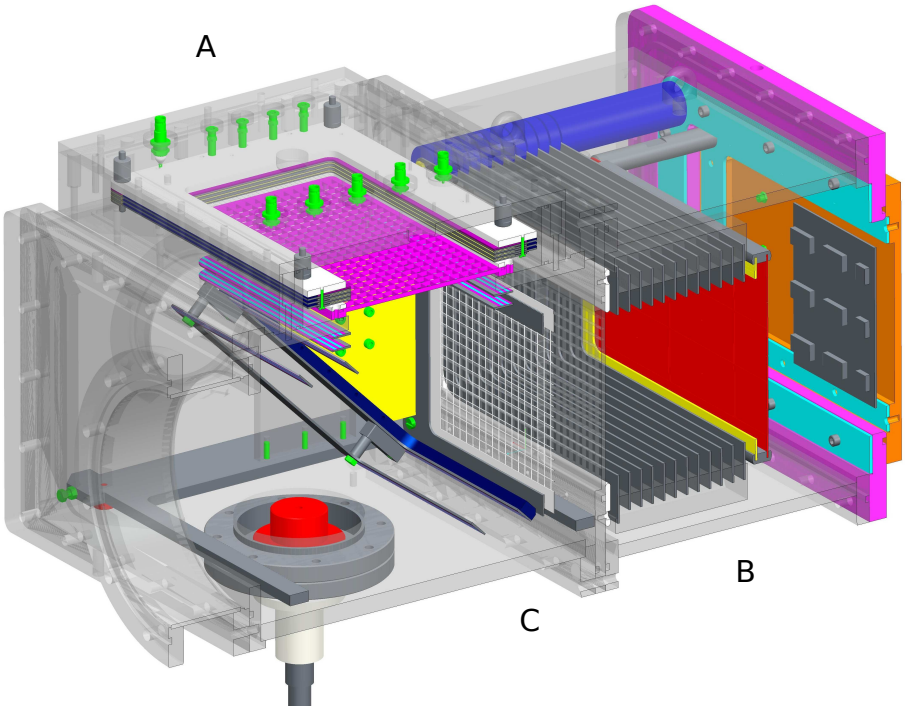

FIGURE 3.12: A false-colour diagram of the position of Bragg arm BD relative to STOP. Letter A denotes the position of the MWPC STOP volume, letter B marks the position of the BD and letter C shows the location of the window (shown as a grey mesh) separating the two. Inside the BD there is a series of repeating grey planes that represent the guiding rings, followed by a yellow plane that holds the Frisch grid. The red plane behind it is the anode.

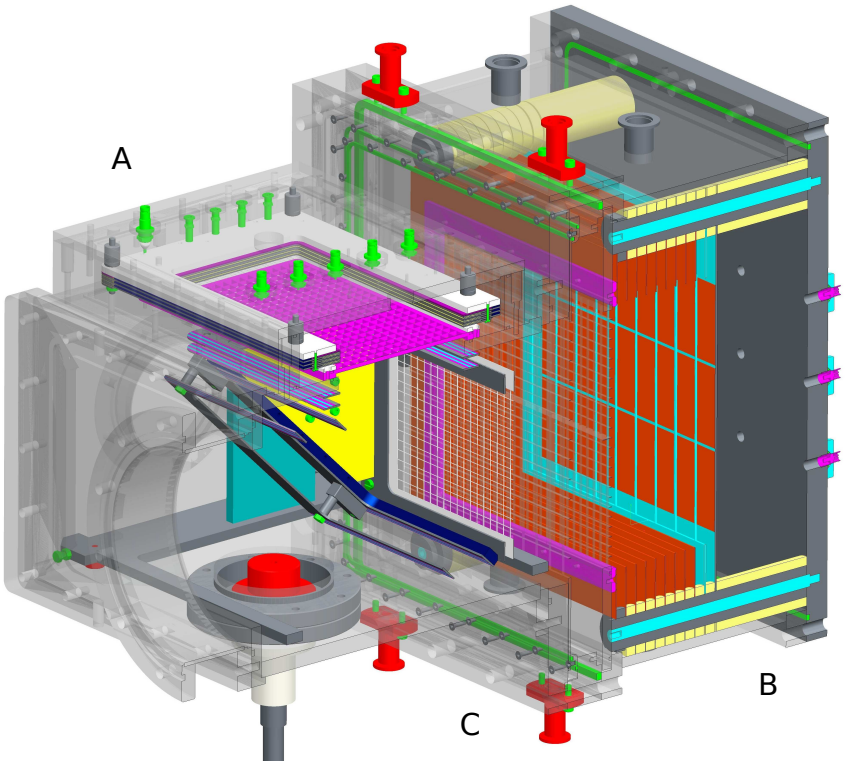

FIGURE 3.13: A false-colour diagram of the position of Hipps arm BD relative to STOP. Letter markers are the same as for Bragg in Fig. 3.12. The grey mesh at point C shows the position of the Mylar window between the BD and STOP. The orange planes inside the BD represent the guiding rings, and the positions of the Frisch grid and the anode are shown as light blue planes.

The anodes in the two main arms of STEFF are segmented into 15 parts, arranged in a 3×5 grid of pads. Each pad has the dimensions of 98×48 mm with 2 mm space between the pads. The anodes in the FiFI arms are not segmented and are circular with a diameter of 8 cm. Furthermore, each BD contains guiding rings space at intervals of 1 cm that increase in potential in even steps up to the Frisch grid potential (800 kV in the Hipps arm and 1100 kV in the Bragg arm). These rings are used to ensure the field that draws electrons towards the anode is uniform across the chamber length, and preventing the electrons from hitting the sides of the volume and getting grounded.

Chapter 4

FiFI Characterization at Lohengrin

The fission process is driven by the electromagnetic repulsion of the protons, and therefore knowledge of the atomic numbers of the FF is critical for modeling the dynamics of fission. Moreover, beta decay models and subsequent fission product chemical properties are dependent on the proton number, and therefore good understanding of this aspect of fission is very important to reactor operation and nuclear waste management. Given the broad applicability of the data on charge yields in fission, it is not surprising that a multitude of experiments have been conducted with the aim of extracting these data.

A common type of atomic number measurement of fission fragments is through gamma- or X-ray spectroscopy [105] [106] [107] [108]. Measurements of such decays allow unambiguous identification of the nuclear species, provided the level scheme of the observed fission fragment is known, a condition that precludes identification of some of the more exotic fission fragments. Another common type of Z-measurements is ΔE-E spectroscopy, whereby a fragment interacts with a pair of detectors, such as silicon [109], losing some of its kinetic energy (ΔE) in one detector and the remainder (E) in another. A plot of these two measured quantities then produces lines corresponding to the Z of the incident FF, although the FF are separable by charge only up to an upper limit of $Z \approx 42$ using this method [110]. An improvement on this limitation has been made at Lohengrin by using calorimetric low-temperature detectors for energy measurements and varying thicknesses of silicon-nitride foils to obtain energy loss [111]. The upper limit was moved up to $Z \approx 52$ using such a detection setup, which still precludes measurements of many atomic numbers found in fission, which in the case of ^{235}U(n,f) go up to 60 and beyond [112].

Gas-filled detectors may be used for incident ion atomic number identification as well by means of a method called Bragg Curve Spectroscopy (BCS) [113]. An ion entering a volume of gas with energies greater than a few MeV/amu loses energy in accordance with the Bethe-Bloch formula shown in Eqn. 3.2. The majority of the energy is lost at the very end of the ion range, producing a characteristic peak, known as the Bragg peak, the position of which allows for unambiguous identification of the incident ion's atomic number. This method of ion identification has been broadly used [114] [115], particularly for studies of fission in inverse kinematics [116], whereby a heavy nucleus (such as an actinide) is accelerated at a light target and undergoes fission following particle exchange with the target, as opposed to direct kinematics, where a neutron (or some other particle) impinges on a stationary heavy nuclear target. An example of charge yield spectrum from an inverse-kinematics measurement of ^{236}U (^{235}U+n compound system) is shown in Fig. 4.1, although the comparability of measurements in inverse kinematics and in neutron-induced fission has been a topic of debate, due to questions of which nuclear states are populated in the two reactions [117]. The reason for the use of BCS in ion beam identification and fission in inverse kinematics is the aforementioned applicability condition of the measured ion having energies of a few MeV/amu or greater. For example, inverse kinematics measurements discussed in Ref. [118] employed ionization chambers for identifying FF with energies of ≈1 GeV, i.e. ≈10 MeV/amu. If the ion velocity is lower, as is the case for the FF in fission in direct kinematics (≈1 MeV/amu), a Bragg peak does not form, and the majority of the FF energy is lost in the beginning of its path in the detector volume, rather than the end. A plot of energy loss profiles simulated in SRIM-2013 [119] for a ^{90}Kr nucleus (a common fission fragment) at 1.5 GeV (≈17 MeV/amu) and at a typical light fission fragment energy of 90 MeV is shown in Fig. 4.2.

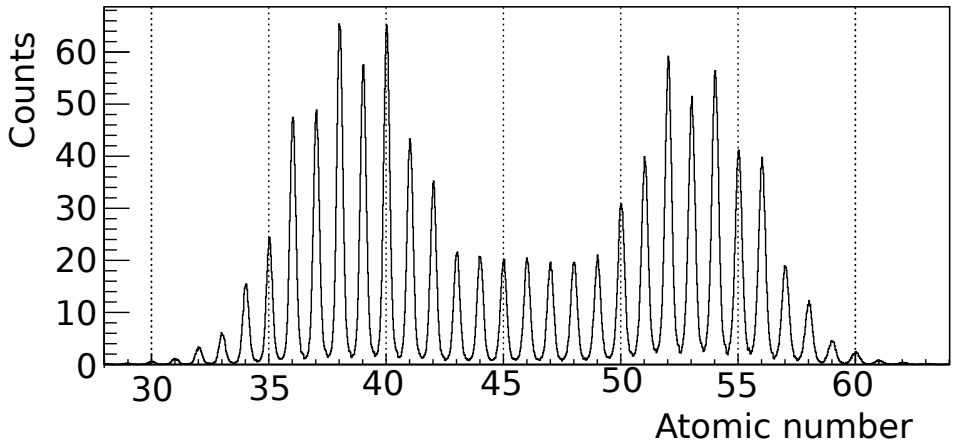

FIGURE 4.1: A spectrum showing isotopic yields from ^{236}U fission measurements in inverse kinematics at average excitation energy of 12 MeV [120].

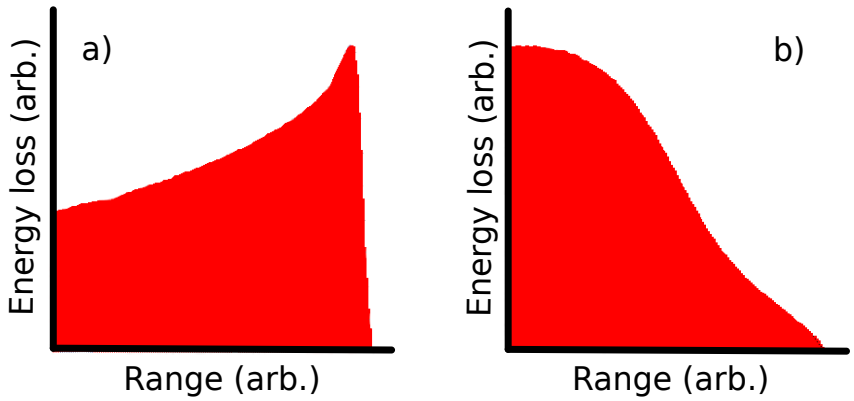

FIGURE 4.2: Profiles of average energy loss with range inside an isobutane volume by a ^{90}Kr with kinetic energies of a) 1.5 GeV and b) 90 MeV, simulated for 100 ions in SRIM. The energy loss profile in a) shows a characteristic Bragg peak, the position of which is related to ion Z. The 90-MeV fragment energy loss profile is typical for FF and shows no peaks, making charge extraction difficult.

Since many fission experiments in direct kinematics rely on gas-filled detectors (2E2v spectrometers STEFF, SPIDER and FALSTAFF mentioned previously are just a few examples), a method of using the energy loss of FF to provide indications of the FF atomic number within the relevant energy range would be highly beneficial for fission studies in general and subsequently help address fission theory and nuclear industry needs for charge yields. The results of an experimental effort at extracting energy loss-related parameters from FF ionization traces to examine the response of a Bragg detector to varying atomic numbers is presented here and have also been published in [121].

4.1 Fission Fragment Stopping in Gas

The change in the energy loss profile at sub-Bragg peak energies occurs as a consequence of the so-called 'effective charge' problem, which was identified shortly after the discovery of fission. As a heavy nucleus undergoes fission, some of its electrons are taken up by the fragments and others are stripped, resulting in fragments that are partially ionized, with a typical ionic charge of ∼20 [122]. As the partially-ionized fission fragment enters the gas volume of a Bragg detector, it interacts with the medium molecules in a series of complicated interactions, which involve electron exchange, polarization and screening. All these effects contribute to distortion of the atomic number 'seen' by electrons into the so-called effective charge Z_{eff}, which changes their binding energy. Calculating ranges and stopping powers that depend on the effective charge has been a long-standing problem in physics due to the dependence of multiple effects on both the medium and the projectile, requiring considerable amount of measurements. An early method of calculating Z_{eff} was proposed by Niels Bohr in 1948 [123], by considering

relative electron and ion velocities. Bohr suggested that as the ionized projectiles slow down, the electrons with orbital velocities slower than the FF velocity v are stripped and the resulting effective charge can be written as

$$Z_{eff} = \frac{v}{v_0} Z^{\frac{1}{3}}, \tag{4.1}$$

where v_0 is the Bohr velocity (2×10^8) cm/s. Typical FF velocities are ≈4-6 times greater than v_0 [124]. Furthermore, Bohr proposed dividing the stopping power of the medium for the ions into two contributions: electronic and nuclear stopping. The somewhat-misleadingly named nuclear stopping accounts for all the ion's energy loss caused by interactions of the ion with the atoms of the medium as a whole, such as non-ionizing elastic scattering, whereas electronic stopping accounts for interactions of the ion with individual electrons in the medium, such as ionization and electron exchange.

Further work on extracting effective charges was primarily focused on accumulating sufficient experimental data [125] and producing empirical approximations to Z_{eff} [126]. A considerable breakthrough has been made in stopping theories by J. Lindhard, M. Scharff and H.E. Schiøtt [127], who over the course of ten years formulated the LSS theory, named after them. LSS theory inherits Bohr's division of stopping into nuclear and electronic contributions to calculate stopping powers and ranges of any particles in any medium [127] within an accuracy of a factor of three [128]. The theory was formulated relying primarily on fission fragment stopping data, and takes a statistical approach to produce several integral equations for ion energy loss [127] and range [129], but does not address the effective charge problem [130]. A method of calculating the effective charge Z_{eff} for an ion in an ionization state q has been proposed by W. Brandt and M. Kitagawa [131], whereby Bohr's consideration of electron velocity relative to that of the fragment was modified to compare electron velocities to the Fermi velocity of the medium. Thus calculations based on the Z_{eff} estimates such as Brandt-Kitagawa can be used in conjunction with the LSS theory to perform stopping calculations.

As the fragments slow down, they exchange electrons with the atoms in the medium. A 1972 review of experimental evidence available at the time by H.-D. Betz [124] suggests that heavy ions in the fission fragment velocity range during a single collision with the atoms in the medium are likely to either pick up single electrons or lose several electrons at once. Exchange of electrons proceeds until the ion reaches an equilibrium charge, and further interactions with the medium by the ion proceed at or around the equilibrium charge. Gas separators rely on charge equilibration to produce beams of known isotopic composition. An empirical method of calculating such equilibrium charges was proposed by Betz in 1966 [132] using the formula

$$\frac{Z_{eff}}{Z} = 1 - Cexp(-\delta\beta/\alpha), \tag{4.2}$$

where

$$\delta = Z^{-\gamma}. \tag{4.3}$$

C and γ are coefficients fitted to the data for particular projectile and target gas combination, Z is the atomic number of the projectile, α is the fine structure constant and β is the ion velocity divided by the speed of light. If $C = 1$ and $\gamma = 2/3$, multiplication of Eqn. 4.2 by Z yields the effective charge proposed by Bohr.

The velocity dependence of stopping power can be divided into different regions as shown in Fig. 4.3. The figure shows qualitative plots of stopping power $-dE/dx$ for low- and high-Z ion energy-to-mass ratio E/A adapted from [133]. The stopping power variation is roughly divided into 4 regions, which will be described in reverse order to reflect gradual energy loss of an ion in a medium. Region IV ions are relativistic and obey Bethe-Bloch equation in their stopping. In region III, charge is exchanged by the ion and the medium and ionization of target atoms occurs. When ions slow down into region II, their charge is equilibrated. In region I, ions slow down through nuclear stopping, a process that does not produce ionization electrons.

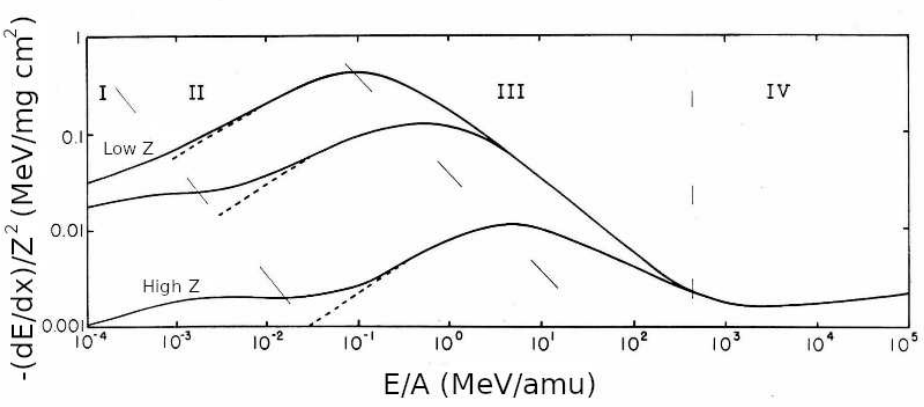

FIGURE 4.3: A qualitative plot of low- and high-Z ions' stopping power $-dE/dx$ as a function of E/A [133]. The plot is subdivided into 4 regions. Region I is dominated by nuclear stopping and produces little ionization. Region II represents electronic scattering of an ion at an equilibrated charge state. Region III is dominated by charge exchange and ionization effects. Ions in region IV are relativistic and the scattering in this region can be described by the Bethe-Bloch formula.

4.2 Lohengrin

The Institut Laue-Langevin in Grenoble is a common facility for measuring fission mass [59] [134] and charge yields [109] [111] due to its high neutron flux research reactor. As the reactor name suggests, it is optimized to produce high fluxes of neutrons reaching up to 1.5×10^{15} neutrons s^{-1} cm^{-2} in the center [135]. The facility features more than 40 instruments, which use neutrons from the reactor to perform experiments for a variety of scientific fields of research. Of particular interest to this work is PN1 Lohengrin. Lohengrin is a mass separator, which functions as a FF velocity selector using two magnets. Only one other separator like Lohengrin, called HIAWATHA [136], has been built in the University of Illinois at Urbana-Champaign, USA, but was decomissioned along with its reactor in 2004 after ceasing operations in 1999.

Fig. 4.4 shows an overview of the Lohengrin structure. Lohengrin's fission fragment source is a target foil of fissile material placed inside the reactor at the entrance of the PN1 beamline, which is 0.5 m from the reactor core [137]. The flux at that position is $\approx 5 \times 10^{14}$ neutrons s^{-1} cm^{-2}. The targets at Lohengrin are typically deposited onto 0.2 mm thick titanium backing [137] with a thickness of fissile material of a few tens to a few hundred $\mu g/cm^2$, further covered with a tantalum foil with a thickness of 40 $\mu g/cm^2$ [138]. As the fragments leave the target they pass through a dipole selector magnet, which selects fragments by their A/q (mass to ionic charge) ratio, and then through an electrostatic deflector, which selects fragments based on their E/q ratio, i.e. the ratio of their kinetic energy to ionic charge. The FF mass resolution typically achieved at Lohengrin is $A/\Delta A \approx 950$ and a typical energy resolution is $E/\Delta E \approx 350$ [137]. The total flight time of FF through Lohengrin ranges between one and two microseconds [138], a time that is shorter than the typical beta decay timescale (a few microseconds or greater [30]), meaning that the focal plane at the end of the beamline provides secondary fragments. Since the selection of the secondary fragments comprising the beam is based on their masses and kinetic energies, the resulting beam consists of fragments traveling at the same velocity, but with different masses. Furthermore, the selection is performed based on ionic charge, resulting in mass selections typically containing several isobars. A typical spectrum of FF energies is shown in Fig. 4.5 with several clearly-separated peaks corresponding to fragments with a $A/q = E/q = 4$ Lohengrin setting and demonstrating the remarkable ease of identifying fragments at Lohengrin.

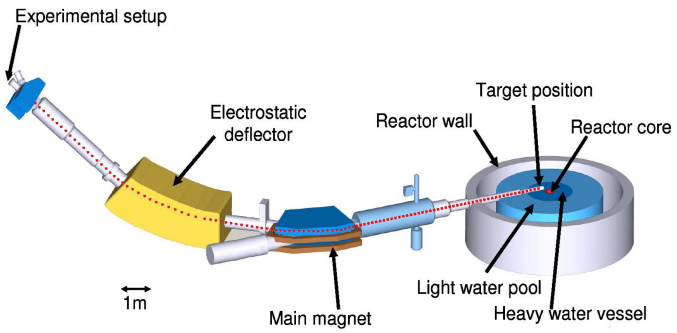

FIGURE 4.4: A diagram showing the layout of Lohengrin adapted from [137]. Shown are the interior of the reactor, the target position, the two magnets that perform FF selection and the area where experiments can be installed. The red dotted line indicates the trajectory of FF through Lohengrin.

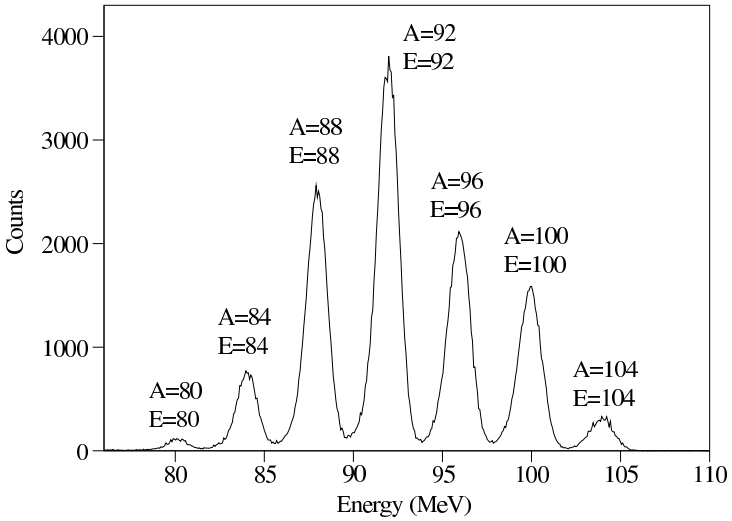

FIGURE 4.5: A spectrum of FF energies measured at the Lohengrin focal plane for a $A = 80$ amu, $q = 20$, $E = 80$ MeV setting, with the peak mass and energy identification shown.

4.3 FiFI at Lohengrin

A campaign of measurements at Lohengrin was performed in 2016 over the course of 12 days (and two more days for assembly/disassembly) using a Bragg detector identical to the FiFI BDs on STEFF. A schematic diagram of the set-up is shown in Fig. 4.6 and a photo of FiFI mounted at the focal plane of Lohengrin is shown in Fig. 4.7. For simplicity, this Bragg detector will be also referred to as FiFI throughout this chapter. The principal difference between FiFI used at Lohengrin and the ones on STEFF is the addition of two timing detectors similar to the MCP STOP assemblies on STEFF. These detectors were separated by a 1 metre-long time-of-flight section to provide velocity measurements. The aim of the experiment was twofold: the primary aim was to investigate the response of

the BD to varying FF atomic numbers, and the secondary aim was to investigate charge-changing collisions inside Lohengrin. Lohengrin is a perfect facility for atomic number investigation, since as described earlier in this chapter the effective charge depends on velocity and atomic number, and the velocities at Lohengrin are known very precisely, and can therefore be effectively 'fixed'. The isobaric composition is also quite well known based on existing yields measurements, so for any known mass the dominant Z contributions can be identified. Lohengrin is held at a $\approx 10^{-6}$ mbar vacuum, and therefore there remains a low possibility ($\sim 10^{-4}$) that some FF may collide with residual gas atoms, resulting in charge state alteration, and thus contributing contaminants to the beam. This low possibility of contamination if not significant for the majority of the Lohengrin beams, however it may have a measurable impact on yields measurements in the symmetry region of the fission mass distribution [139]. Such contaminants have a velocity that is expected to be ≈2% different from the rest of the beam, and the time-of-flight section of FiFI was added to investigate this effect.

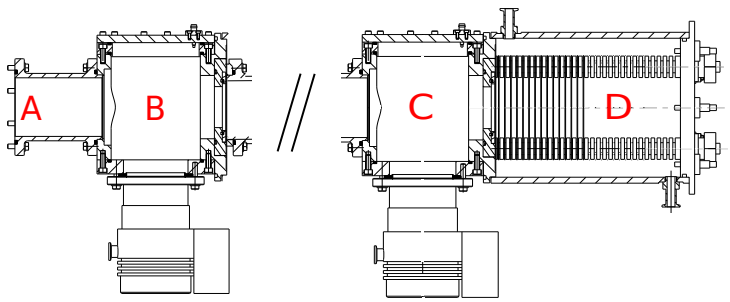

FIGURE 4.6: A schematic diagram of the FiFI arm used at Lohengrin in 2016. Point A marks beam entry point. Volumes B and C show the positions where MCP timing assemblies are inserted. The assemblies are constructed identically to Fig. 3.2. Below each of the two volumes there is a vacuum pump, and the two volumes are separated by 1 metre-long flghtpath, which has been omitted in this schematic for clarity. Volume D is the Bragg detector.

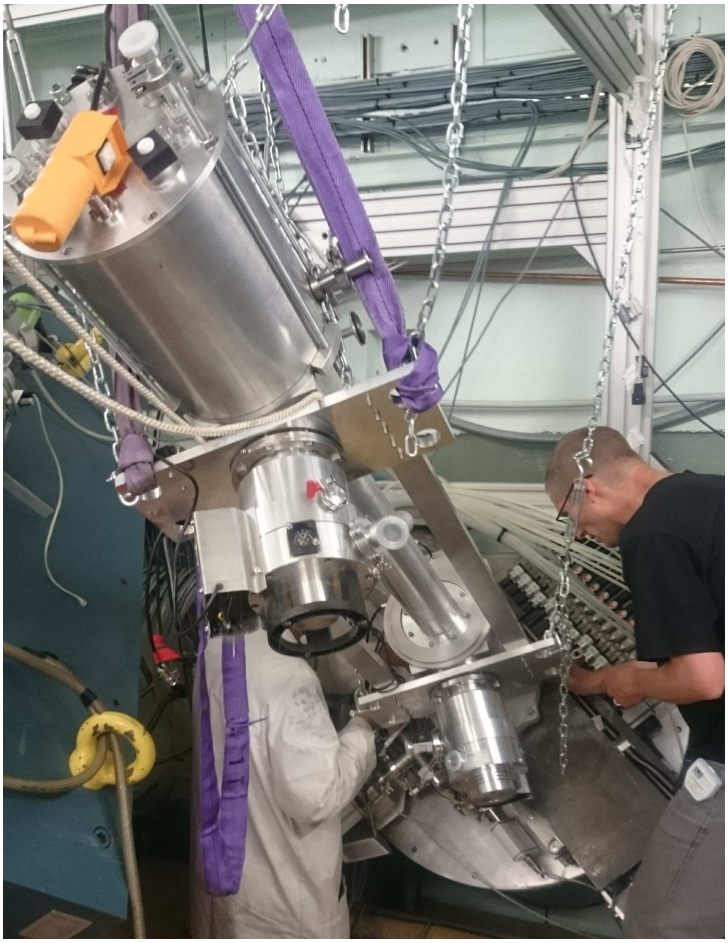

FIGURE 4.7: A photo of FiFI being mounted at the focal plane of Lohengrin.

During the campaign FiFI was operated at 10^{-6} mbar vacuum in the ToF section and at 100 mbar isobutane pressure in the BD. The MCPs were operated at 2000 V and the electrostatic mirrors at 4000 V. The timing foils manufactured for the experiment were made of ≈300 nm thick formvar, which was aluminized to a thickness of ≈370 Å. The aluminization of the foil was performed using an evaporator and verified using a precision scale, which provided a sub-1% uncertainty on the average thickness. The window separating the BD from the ToF section was made of Mylar with a thickness of 0.5 μm, and deposited onto a steel colimator, which matched the dimensions of the Lohengrin beam at the focal plane, i.e. a 4×0.8 cm rectangular slit. The BD anode was set to 1400 V and the Frisch grid to 1200 V. The gas inside the chamber was circulated at a rate of 14 mbar L s^{-1}. The signals from the BD were processed using Cooknell EC572 charge-sensitive preamplifiers and the waveforms were recorded using CAEN V1724 ADCs.

As the campaign started, it was quickly noted using the online monitoring system that the FF energy resolution inside the BD was of the order of a few MeV, considerably below the expected <1 MeV. The energy distortion was determined to be caused by

the timing foils. An uneven coating of aluminium resulted in straggling of the FF, and causing a spread in the energy loss in the foils, and therefore in the final deposited energy in the gas volume. An example of an energy spectrum for identical Lohengrin settings to Fig. 4.5 before the foil removal is shown in Fig. 4.8, clearly demonstrating the degraded energy resolution.

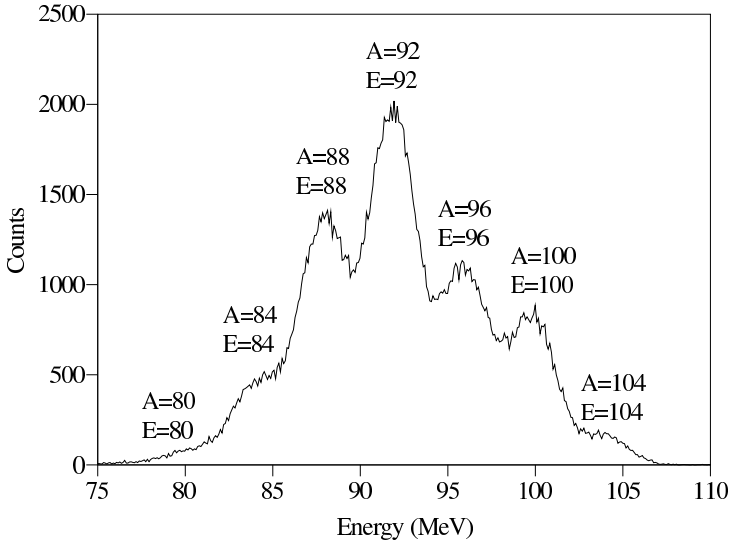

FIGURE 4.8: A spectrum of FF energies measured at the Lohengrin focal plane for a $A = 80$ amu, $q = 20$, $E = 80$ MeV setting, with the peak mass and energy identification shown. The spectrum was taken before the removal of the timing foils, showing degraded energy resolution compared to Fig. 4.5.

The identification and investigation of the resolution degrading, removal of the foils and the subsequent return of the system to a working vacuum have taken up a considerable amount of time, resulting in the final analysis focusing on the data collected over a span of only two days. Consequently, there was a lack of measurements used in the analysis for the heavy mass region, and the removal of the foils naturally prevented the use of the ToF section, thus precluding any investigation of charge-changing inside Lohengrin.

4.4 Data Processing

Over the course of the measurement campaign 250 GB of data were accumulated and 200 combinations of Lohengrin settings were used, however only 60 of those were performed following the foil removal. From these 60 settings, 40 were selected for the final analysis, while the remaining 20 were either in the symmetry region and had insufficient statistics, or the Lohengrin magnets had not finished re-configuring after settings changes, subsequently compromising reliability of the beam composition.

The data were read into and analyzed using Manchester in-house fission event analysis software called GAVSORT [140], which is written in C with a TK/TCL frontend and

capability for creating and managing databases written in MariaDB [141]. The software allows users to create custom files called 'user sortfiles' for reading and processing data. The sortfile that was written for the campaign discussed in this chapter, read in Frisch grid and anode traces recorded during the experiment and applied a sequence of digital filters to the anode signal with the aim of extracting various signal properties. Typically when ion stopping is investigated, e.g. using Bragg peak spectroscopy, the two immediately apparent observables of interest are range in the medium and energy loss. Following the same reasoning, the goal in processing Lohengrin data was extraction of signal parameters related to these two quantities. Data processing aimed to identify the energy deposited by the fragment in the BD through ionization Q_{max}, and the maximal slope of the anode signal, proportional to the maximum energy loss by a fragment, ${}^{dQ}/_{dt}|_{max}$. Furthermore, another parameter of interest extracted alongside the energy-related parameters is t_{10-90}, or the risetime of the signal from 10% to 90% of its maximal amplitude, which can be related to FF range if the electron signal drift velocity is known. A diagram of the parameters of interest demonstrated with an anode trace is shown in Fig. 4.9. The filter sequence is shown in Fig. 4.10 along with the final observables extracted from them. Each filter's operation and effect are described below.

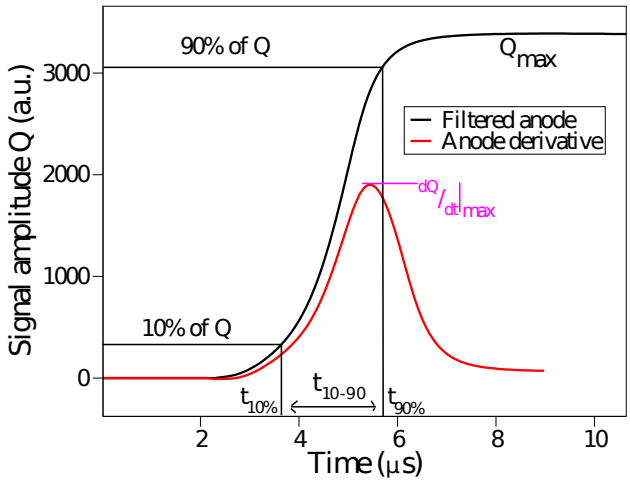

Figure 4.9: A filtered anode signal averaged over >1000 FF from one of the Lohengrin runs shown alongside its derivative. Parameters of interest extracted from the signal are shown. Q_{max} represent the maximum amplitude, ${}^{dQ}/_{dt}|_{max}$ represents the maximum slope, $t_{10\%}$ shows the time of the signal crossing 10% of its maximal amplitude, and $t_{90\%}$ shows the 90% amplitude crossing.

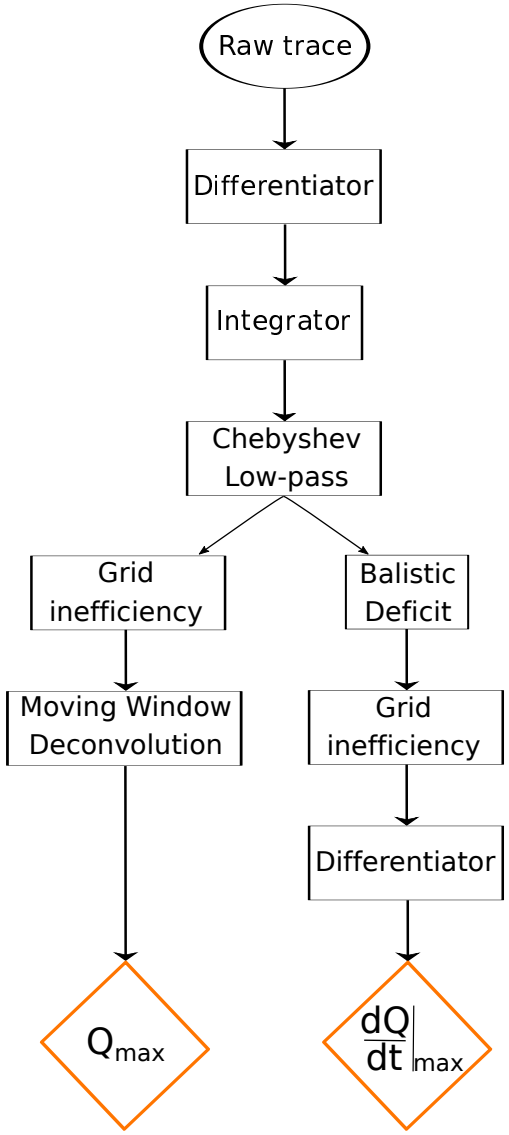

FIGURE 4.10: A flowchart showing the sequence of digital filters that were applied to anode signals with the aim of extracting maximum energy loss and the total deposited energy in the BD.

4.4.1 Differentiator

The first filter applied to an anode trace is the differentiator, which is used to filter out low-frequency noise (such as ground loops) below some cut-off frequency f, and to set the signal baseline to zero. The filter is recursive, and a point along the differentiated trace $^{dQ}/_{dt}$ at index i can be described in terms of two points along the raw trace Q and the previous differentiated point $^{dQ}/_{dt}[i-1]$ using the following expression [142]:

$$\frac{dQ}{dt}[i] = \frac{1+e^{-2\pi f}}{2}\big(Q[i]-Q[i-1]\big) + e^{-2\pi f}\frac{dQ}{dt}[i-1], \tag{4.4}$$

for

$$f = \frac{1}{2\pi x}, \tag{4.5}$$

where x is the time window in channels over which differential is calculated. The resulting differentiated trace is shown in Fig. 4.11 alongside the initial unfiltered pulse.

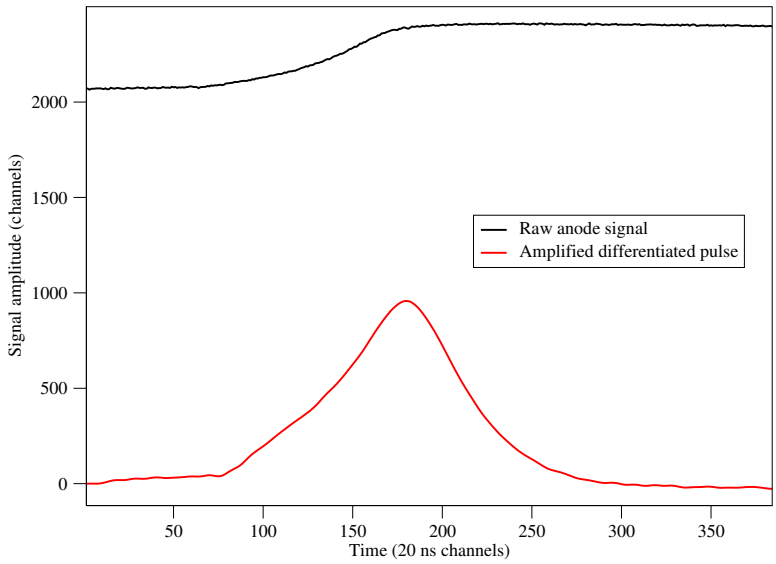

FIGURE 4.11: An unfiltered anode trace is shown in black alongside a differentiator trace in red.

The functioning of a differentiating filter depends strongly on the frequency parameter, which, if set too wide, can remove the signal entirely, and conversely a very narrow setting would merely reproduce the input signal frequencies, resulting in no filtering. The differentiated pulse shapes for a variety of frequency settings are shown in Fig. 4.12 alongside an anode pulse that has already been filtered for noise for comparison. It is evident from the plot that the smaller f is (i.e. the wider the time window for filtering is), the more similar the differentiated pulse is to the anode pulse, and no filtering is being done. Conversely, for larger f less signal is preserved. Since the differentiated amplitude ${}^{dQ}/_{dt}|_{max}$ is the value of particular interest taken from the differentiator, a plot similar to Fig. 4.12 is shown for reference in Fig. 4.13, showing the trend of reduction in ${}^{dQ}/_{dt}|_{max}$ with increasing f.

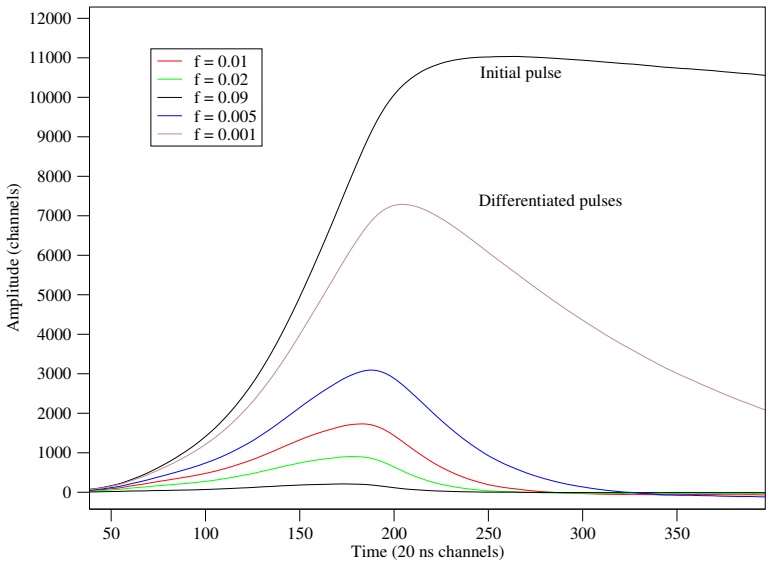

FIGURE 4.12: A plot showing the initial anode pulse in black and a series of differentiated pulses for a variety of frequency settings demonstrating the effect of the frequency on the differentiator.

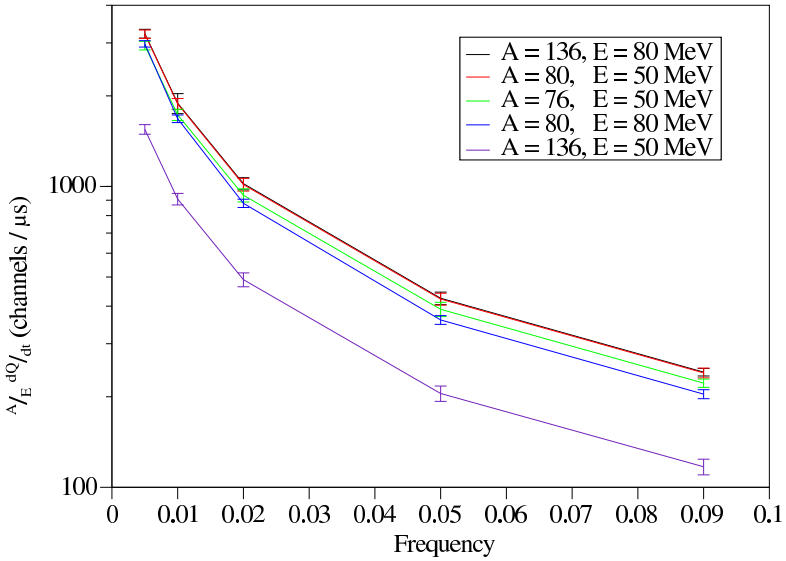

FIGURE 4.13: The maximum amplitude of the differentiated pulse $^{dQ}/_{dt}|_{max}$ shown as a function of differentiator frequency.

An intermediate range of f values was chosen for further investigation by considering the width of the anode signal risetime (≈150 channels). The differentiating window should be appreciably smaller that the anode risetime, so as not to distort the detail of energy loss during stopping. A plot of several f values in the chosen range is shown in Fig. 4.14 for several fragments with a similar velocity. It is evident from the plot that within the chosen range, the separation of fragments is fairly insensitive to f, and subsequently a value of 0.01 (16-channel window) was chosen.

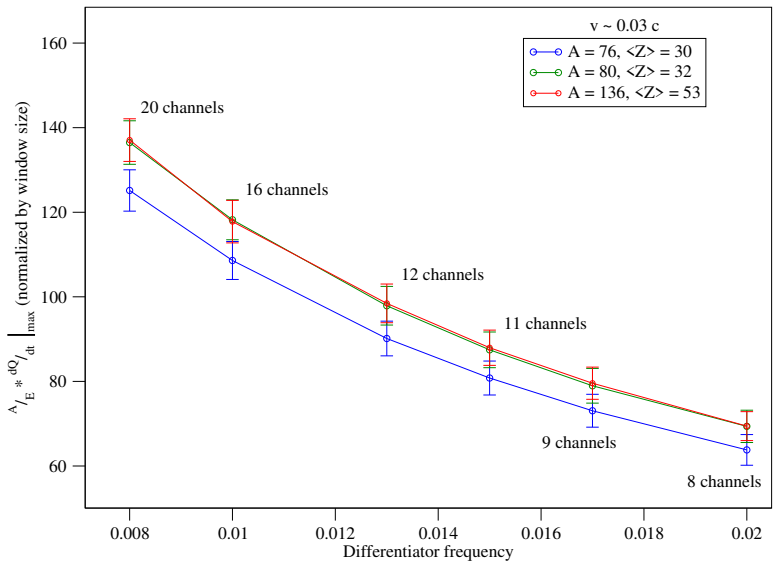

FIGURE 4.14: The maximum amplitude of the differentiated pulse $^{dQ}/_{dt}|_{max}$ shown as a function of differentiator frequency for several different fragments at the same velocity.

4.4.2 Integrator

The integrating filter is considerably simpler than the differentiator, as it simply does a running sum of $^{dQ}/_{dt}[i]$ values over the length of the differentiated pulse. The recursive formula for the filter's functionality can be written as

$$Q[i] = \frac{dQ}{dt}[i] + \sum_{j=1}^{i-1} \frac{dQ}{dt}[j]. \tag{4.6}$$

The resulting pulse is an amplified version of the raw anode pulse without the noise that has been removed at the differentiator stage. An example of the resulting pulse along with the initial raw anode pulse from Fig. 4.11 is shown in Fig. 4.15.

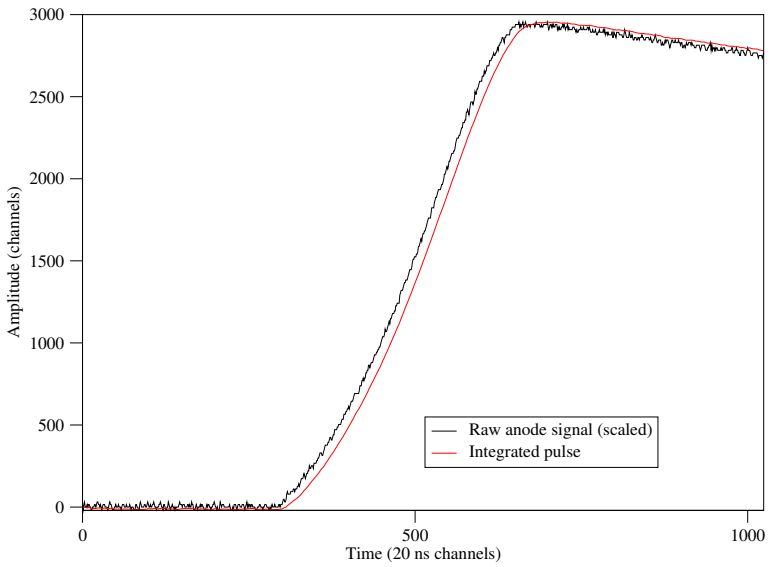

FIGURE 4.15: A scaled initial raw anode trace with zeroed baseline for visibility shown in black alongside a trace that has undergone differentiator and integrator filtering in red. The filtered trace has had the low-frequency noise contribution filtered out and has also been amplified by a factor of ≈16.

4.4.3 Chebyshev Filter

Following the application of the high-pass filtering, a Chebyshev low-pass filter was used. Low-pass filters are used to remove high-frequency contributions to the pulse, such as radio-frequency noise. The settings of the filter has been adapted from Ref. [142]. Low-pass Chebyshev filter settings include three parameters: cut-off frequency, ripple and pole. Cut-off frequency represents a frequency threshold beyond which the contributions to the pulse are suppressed by the filter. A plot of frequency response of a typical Chebyshev filter is shown in Fig. 4.16 [142]. The plot shows a sharp reduction (called 'roll-off') in amplitude contributions (shown as a percentage on the y-axis) beyond the cut-off frequency of 0.2. The functionality of the Chebyshev filter is a trade-off between the sharpness of the roll-off and ripple. Ripple can be seen as wave-like structures before the roll-off, and each ripple structure represents exaggerated contribution of a given frequency, which is undesirable. Ripples can be present in either the passband or the stopband (i.e. frequency range where contributions are retained or filtered out), corresponding to either Type 1 (used in this work) or Type 2 Chebyshev filters. Ref. [142] recommends a ripple of 0.5% (a very small contribution to noise compared to a typical Bragg detector signal, where noise levels of a few percent of Q_{max} are typical). Since ionization signals are very slow (typically a few microseconds), a low cut-off frequency of 0.1 was set.

The Chebyshev filter pole is a more complicated parameter, which is described in detail in Ref. [142]. In simple terms, a filter has a transfer function, which defines for a

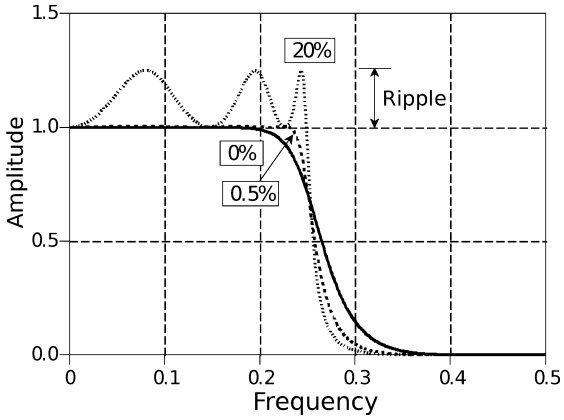

FIGURE 4.16: A plot of Chebyshev filter frequency response for several different ripple settings and a cut-off frequency of 0.2. Figure adapted from Ref. [142].

given input frequency what its contribution in the output will be. The function is typially expressed as a ratio of two complex polynomials, and therefore the transfer function's zeroes correspond to numerators being equal to zero, and poles occur when the denominator is zero. By defining the poles and zeroes of a filter, one can define the transfer function. i.e. the action of the filter. An increase in the number of poles allows for a more complicated transfer function with a faster roll-off, so a maximum 6-pole setting suggested by Ref. [142] was chosen. A trace that has been processed with a Type 1 6-pole Chebyshev filter with the aforementioned ripple and cut-off frequency settings is shown in Fig. 4.17, and a comparison of the trace in the vicinity of the maximal amplitude following integration with and without Chebyshev filtering is shown in Fig. 4.18. The latter plot shows clearly the reduction in high-frequency components of the pulse, with only slowly-varying components remaining.

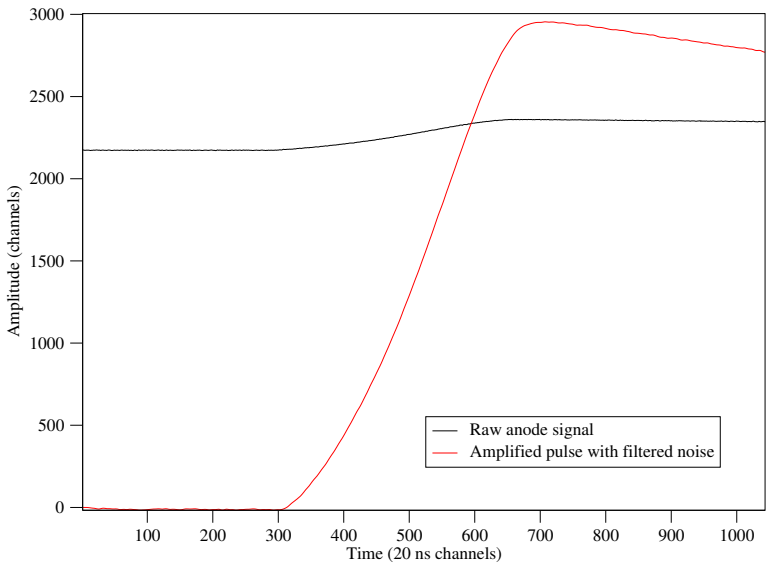

FIGURE 4.17: An initial raw anode trace shown in black alongside a trace that has undergone differentiator and integrator filtering and subsequent Chebyshev filtering in red. The latter trace has had the high-frequency noise contribution filtered out, which can be seen by comparing the peaks of the filtered pulse in this figure and Fig. 4.15.

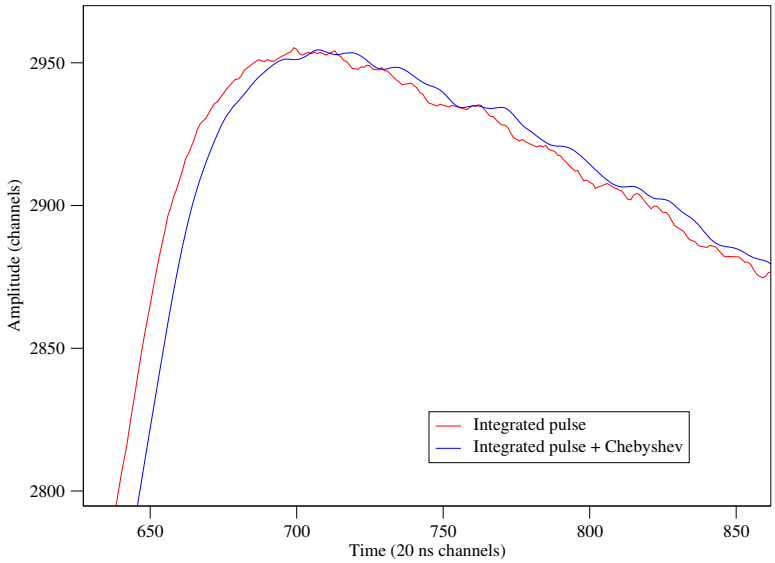

FIGURE 4.18: A demonstration of the effects of a Type 1 6-pole Chebyshev filter. Shown in red is the peak of a differentiated-integrated pulse prior to application of the Chebyshev filter. The peak of the same pulse following Chebyshev filtering is shown in blue with a notable reduction in high-frequency noise.

4.4.4 Ballistic Deficit Correction

STEFF and FiFI BD signals are processed using charge-sensitive preamplifiers, which integrate signal from the electrons present in the space between the anode and the grid as they drift towards the anode. The preamplifier has a time decay constant, which determines the rate at which the exponential decay of a collected signal is discharged from

the preamplifier (for Cooknell EC572 preamplifiers used on FiFI, time decay constant is 50 μs). Signal decay occurs throughout the collection of the signal, resulting in a cumulative pulse height deficit across the trace. If the signal collection time for various signals is similar, this pulse height loss is not significant, since it will be an approximately constant fraction for all the collected signals [90]. FF, however, arrive at a variety of masses, velocities and charge states, resulting in a large variation in stopping time inside the gas, and subsequently considerable variation in electron drift time (the signals collected during the Lohengrin campaign showed drift time of $\approx$1.8 μs with a variation of $\sim$20% for various FF).

The variation in drift time necessitated a correction, which was applied using the ballistic deficit filter, which restore the maximum amplitude of a pulse and removes the preamplifier decay tail. The filter function in calculating an element $Q_{bd}[i]$ of a ballistic deficit corrected trace can be written as

$$Q_{bd}[i] = Q_{bd}[i-1] + Q[i] - Q[i-1] + f_{BD}Q[i]. \tag{4.7}$$

Here, f_{bd} is a ballistic deficit filter frequency setting based on the preamplifier decay constant. The frequency setting used throughout this work for the ballistic deficit filter is 0.0004, which approximately corresponds to $1/\tau$, where τ is the mean preamplifier decay time, which is 2275 ns in the case of this work. A comparison of a trace before and after the filter is shown in Fig. 4.19.

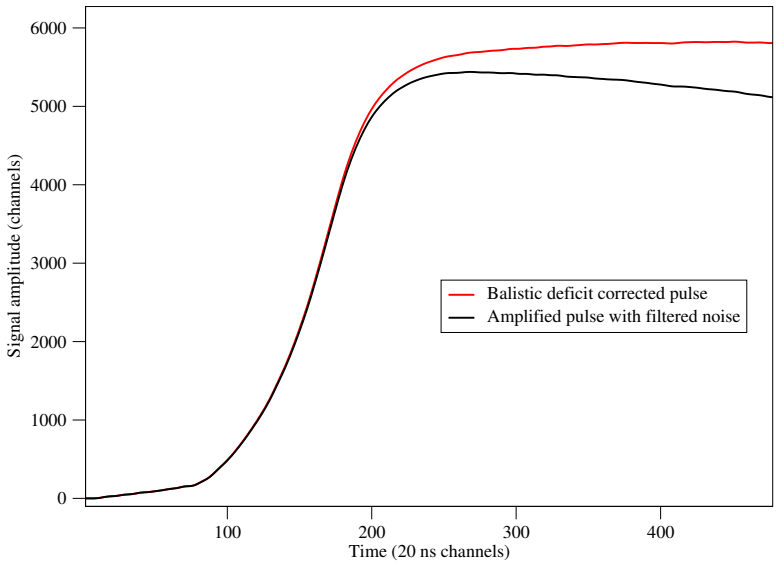

FIGURE 4.19: A comparison of a trace, which has been filtered with a differentiator, integrator and a Chebyshev filter, shown in black, with a red trace, showing the restoration of the signal's amplitude distribution by a ballistic deficit filter.

4.4.5 Moving Window Deconvolution

The ballistic deficit filter corrects the entire pulse for the preamplifier decay, making it useful for extracting ${}^{dQ}/_{dt}|_{max}$, which originates from the pulse rising edge. However, it is less reliable for extracting Q_{max}, which is the peak of the pulse, a value which can fluctuate depending on noise remaining after the filtering. The ballistic deficit correction does not filter out the remaining noise, and an alternative method of addressing the pulse height deficit caused by the preamplifier decay is used in the form of the Moving Window Deconvolution (MWD) filter [143]. The MWD filter, as the name suggest, uses an averaging window, making it less sensitive to any noise, and the peak of the MWD pulse corresponds to Q_{max} corrected for pre-amplifier decay. MWD filter can be written as

$$Q_{mwd}[i] = Q[i] - Q[i-m] + \frac{1}{\tau * \bar{Q}}, \tag{4.8}$$

where m is the width of the averaging window in channels (250 in the case of this work), and $\bar{Q}$ is a running sum of averaged windows expressed as

$$\bar{Q} = \bar{Q} + \frac{Q[i] - Q[i-m]}{m}. \tag{4.9}$$

An example of a trace produced by MWD along with the output trace of a ballistic deficit filter are shown in Fig. 4.20.

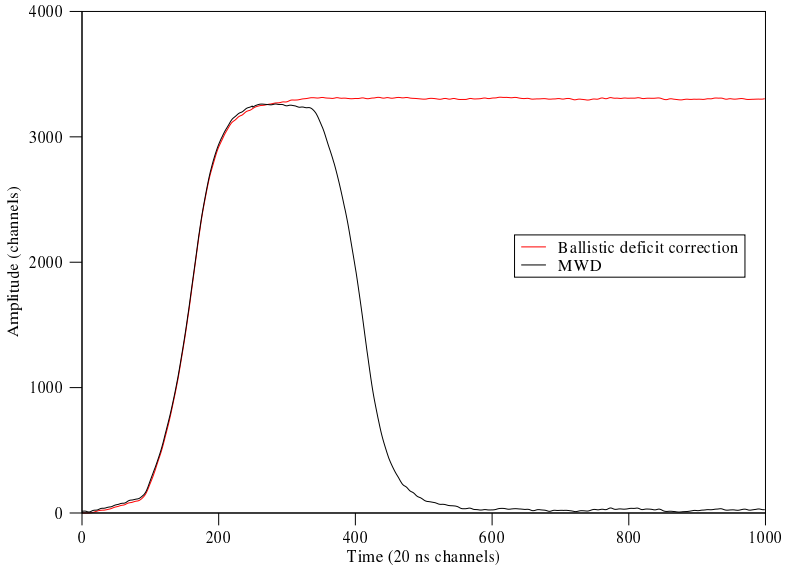

FIGURE 4.20: A comparison of a trace following ballistic deficit correction (in red) and MWD (in black).

4.4.6 Frisch Grid Inefficiency Correction

Another effect that may alter extracted Q_{max} of a trace is the Frisch grid inefficiency. Section 3.1.5.2 discusses the shielding of a BD anode by the grid, a task with an associated efficiency which depends on the grid geometry [144]. Since Frisch grids in the case of all the BDs in this work are grids of wires (mesh configurations are also frequently used [145]), the spacing between the wires determines how much signal from the electron cloud following FF stopping is leaked through, resulting in excess in the signal amplitude and subsequently overestimation of deposited energy. A method has been prescribed by Göök *et al.* [144] for correcting the leakage during pulse-shape analysis stage using the expression

$$Q_{corr}[i] = \frac{Q[i] + \sigma Q_c[i]}{1 - \sigma}, \tag{4.10}$$

where $Q_{corr}[i]$ is an element of the corrected anode trace, σ is the inefficiency parameter, and Q_c is an element of the cathode signal, which is dominated by the ion signal and gets subtracted to compensate for the ion signal leaking onto the anode. The BD on FiFI is not configured for collection of the cathode signal, as the ions are grounded using the gas window, so the cathode signal was reconstructed using the method prescribed in Ref. [146], which consists of summing the Frisch grid and anode signals and then multiplying the result by -1 to represent the opposite polarity of the cathode signal to the grid and the anode. The calculation of σ was complicated by insufficient baseline collection time set in the ILL DAQ for the anode signals during the Lohengrin campaign, so the parameter was determined in Manchester after the Lohengrin campaign to be 8.8% based on FiFI measurements using a ^{252}Cf source [147]. No changes to the BD have been implemented between the two campaign and the grid investigation.

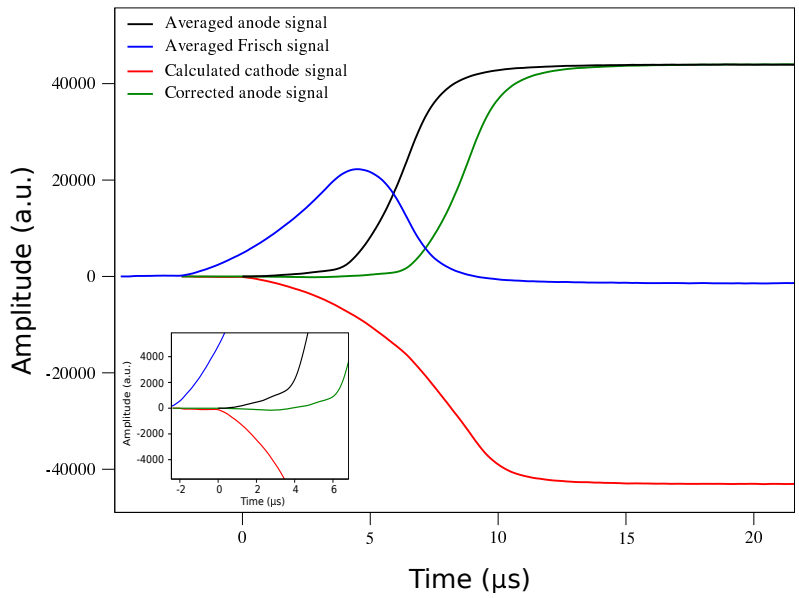

FIGURE 4.21: A comparison of a raw anode signal in black with a grid inefficiency corrected signal in green. The reduction in grid leakage contribution is shown in the inset for visibility. The Frisch grid signal (in blue) and the reconstructed cathode signal (in red) are both shown as well.

4.5 Data Analysis

Filtered traces have been written into a MARIADB database using GAVSORT, and the database allowed compilation of the data into matrices. The matrices were produced on a run-by-run basis and contained traces for anode and grid as rows and maximal filtered anode amplitude (i.e. detected energy) as columns. That allowed the use of clean energy spectra, where the FF masses are easily identified as shown in the example in Fig. 4.5, to cut mass/energy gates to retrieve anode and grid traces averaged over all the FF that were included in the gate. This process could perhaps be more easily understood graphically, as shown in Fig. 4.22. The intensity of Lohengrin beams allowed for substantial averaging, with a typical gated trace being averaged over ≈8000 FF in a narrow energy gate of ≈300 keV.

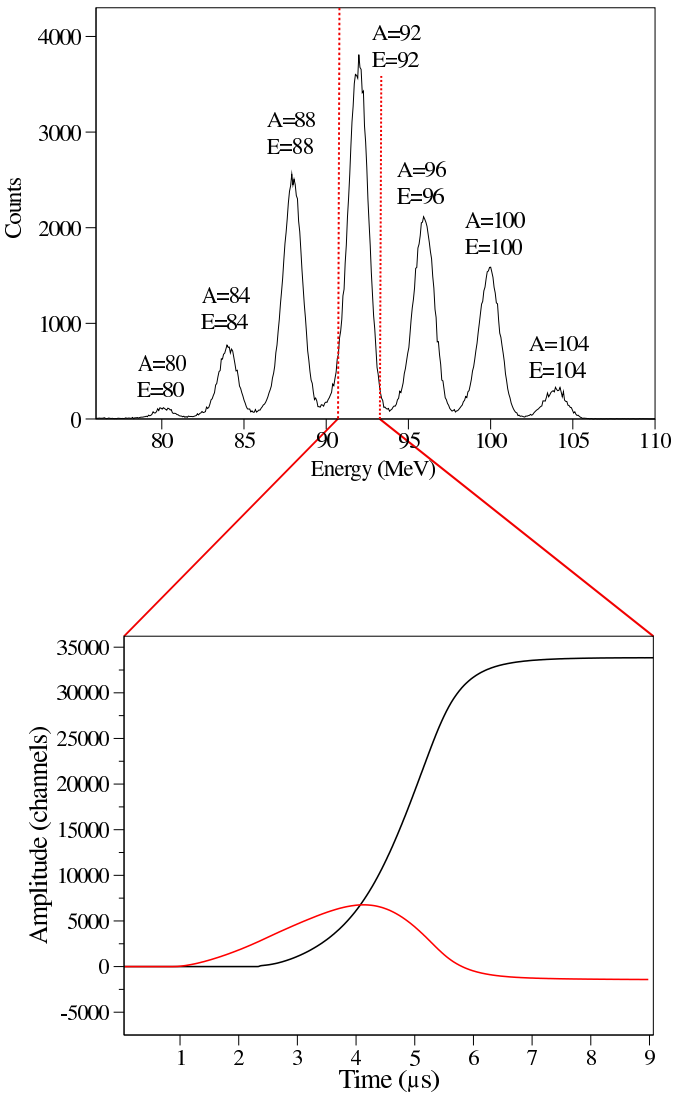

FIGURE 4.22: A graphical representation of the process of energy gating for retrieving averaged anode and Frisch grid traces.

4.5.1 Defining Parameters

Once the averaged traces were retrieved, the parameters of interest (Q_{max}, ${}^{dQ}/_{dt}|_{max}$ and t_{10-90}) described earlier in Fig. 4.9 were extracted from them. Due to the averaging over a large number of signals, it was deemed acceptable to interpolate linearly between the data points in order to increase precision of the timing related variables ${}^{dQ}/_{dt}|_{max}$ and t_{10-90}.

The Mylar gas window used during the Lohengrin campaign was not aluminized and subsequently was not grounded, which led to charge accumulation during the campaign and introduced gain drift into the signal. The drift of the energy peaks was monitored using dedicated GAVSORT functions during data processing and was found to be not significant over the course of a single Lohengrin run (runs were typically brief, lasting

≈20 mins), however the position of the various mass/energy peaks between runs with the same settings changed considerably. The effect is demonstrated in Fig. 4.23, showing that the effect is less significant over shorter time intervals, but becomes considerable over the course of days.

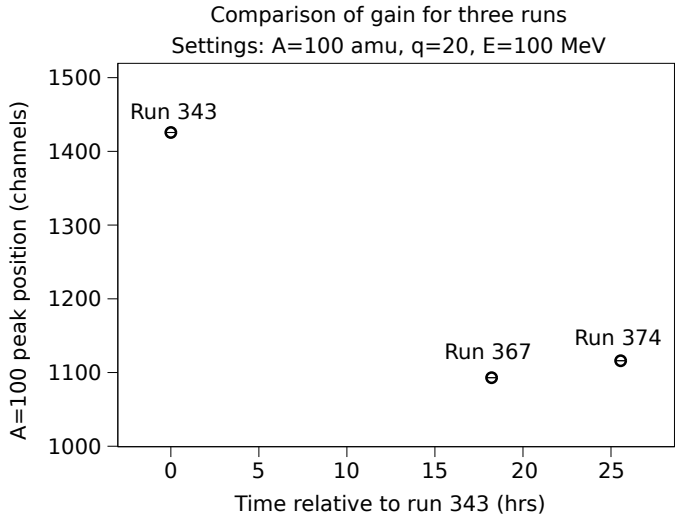

FIGURE 4.23: Drift in BD gain tracked using three runs with the same Lohengrin settings (A=100 amu, q=20, E=100 MeV). The position of the A=100 amu peak is shown in channels with an uncertainty represented by the square root of the number of counts in the peak. The x-axis shows time in hours relative to the first of the three runs.

Detector gain has a defining effect on energy measurements, so if FF energy loss, represented by ${}^{dQ}/_{dt}|_{max}$, was to be considered for investigating the influence of atomic number on BD signals, a gain drift correction would be necessary. Such a correction was accomplished by considering the other energy-dependent parameter that would suffer from gain drifts similarly, i.e. Q_{max}, and combining it with energy loss into a single parameter defined as

$$\epsilon = \frac{{}^{dQ}/_{dt}|_{max}}{Q_{max}}. \tag{4.11}$$

Since Q_{max} is a measure of FF energy deposited in the BD, the division by this parameter introduces dependence on FF mass and velocity into ϵ. Furthermore, the energy deposited in the ionization chamber will not be the same as the kinetic energy of FF in Lohengrin, since the FFs will lose energy in the gas window. These considerations led to modification of ϵ by the FF kinetic energy to shape the final parameter for energy loss consideration, defined as

$$\epsilon' = \frac{A(v_{corr})^2}{2}\epsilon, \tag{4.12}$$

where v_{corr} is FF velocity corrected by FF energy loss in the window. The form of the parameter raises two considerations: the method for correcting velocity, and the implications of dividing Q_{max} by kinetic energy. The velocity correction was implemented using SRIM-2013 [128] simulations of energy loss. SRIM is known to provide only approximate values of stopping for FF due to its reliance on LSS formalism [128], and a further discussion of SRIM is provided later in this chapter. SRIM accuracy was deemed acceptable for calculating a correction factor, however, since no velocity was corrected by more than 13% (the case for the slowest, heaviest FF), and most of them were corrected by less than 5%. SRIM is considered accurate to within 20-30%, resulting in an uncertainty of a few percent on the final energy loss parameter, which is still acceptable compared to typical energy loss models.

The division of Q_{max} by kinetic energy may seem redundant at a glance, however considering the origins of the two provides insight into the effect of the division. Q_{max} is linearly proportional to the energy deposited in the BD through ionization, while the kinetic energy it is divided by is calculated on the bases of Lohengrin settings and SRIM, thus representing the energy one expects. The ratio of the two will therefore represent any BD energy loss effects that are not ionization of isobutane. These effects, such as charge exchange and polarization, are all dependent on the effective charge of the FF, and therefore contain information of interest to the investigation.

Since the range is proportional to inertial mass, a modification has also been applied to the risetime parameter, however since it is insensitive to gain, the risetimes were simply normalized in mass to form a new parameter τ defined as

$$\tau = \frac{t_{10-90}}{A}. \tag{4.13}$$

4.5.2 Fitting the Data

The two parameters chosen for investigation, ϵ' and τ, were calculated for all the FF in the light and heavy fragment data. Since both of the parameters are expected to be dependent on FF velocity and Z, plots of the results were made against the Lohengrin velocity setting v, considered henceforth as a fraction of the speed of light in vacuum c for simplicity. For each mass an average atomic number $\bar{Z}$ was assigned based on the JEFF-3.1 database [112] by considering 7 isobars with the highest yield and taking a yield-weighted average of them. All the mass settings used in the analysis were predominantly composed of one FF Z with small contributions by near-Z isobars (standard deviation in charge assignment was $\sigma_{\bar{Z}} \approx 0.2$). A plot of the results is shown in Fig. 4.24.

The uncertainties on τ and ϵ' were calculated based on uncertainties in the total deposited energy σ_E and uncertainty in energy loss σ_{dE}, while the <1% uncertainties in the FF velocities and masses selected by Lohengrin were considered negligible. σ_E was calculated as the standard deviation of the Gaussian fit to mass peaks divided by $\sqrt{N}$, where N is the number of counts in the energy gate, from which average waveforms were extracted. σ_{dE} is uncertainty in identifying the maximum derivative of the rising edge of the anode trace, which depends on energy resolution, maximum derivative was calculated and was taken as σ_E divided by the maximum derivative, i.e.

$$\sigma_{dE} = \frac{\sigma_E}{\frac{dQ}{dt}|_{max}}. \tag{4.14}$$

Since ϵ' is the ratio of energy loss to total energy, its uncertainty was calculated in quadrature based on σ_E and σ_{dE} as follows:

$$\sigma_{\epsilon'} = \sqrt{\left(\frac{\sigma_{dE}}{t_{max}}\right)^2 + \left(\frac{dQ/dt|_{max}\ \sigma_E}{t_{max}^2}\right)^2}. \tag{4.15}$$

Here, t_{max} is the time of anode trace derivative maximum.

The uncertainty in τ is similar to the uncertainty in maximum derivative, as it relies on identification of points along the trace, i.e. the positions the 10% and 90% of maximum amplitude. The identification relies on energy resolution in identifying the position of the maximum, and therefore the uncertainty in τ is written as

$$\sigma_\tau = \sigma_E \sqrt{\left(\frac{1}{dQ/dt|_{10\%}}\right)^2 + \left(\frac{1}{dQ/dt|_{90\%}}\right)^2}. \tag{4.16}$$

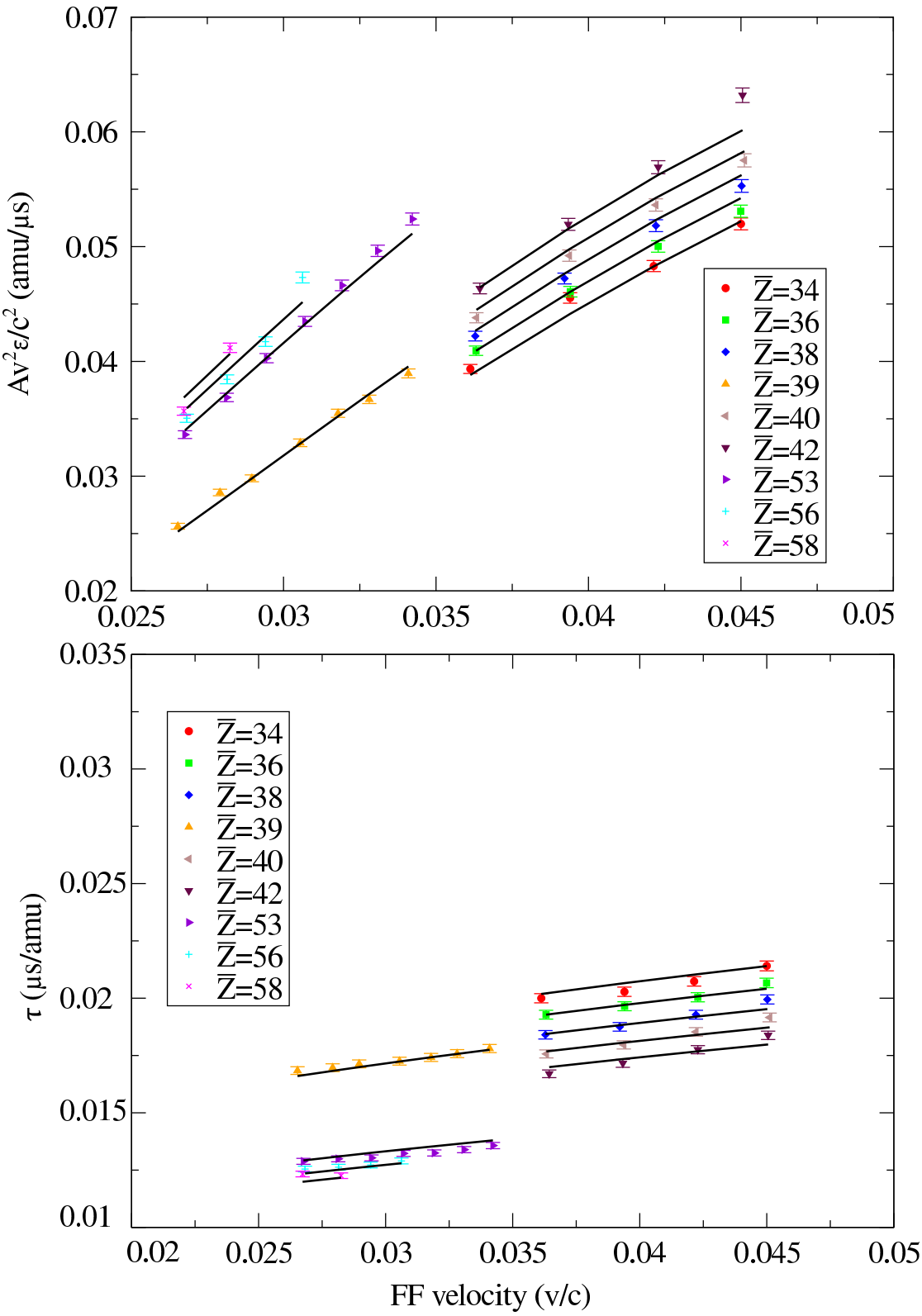

FIGURE 4.24: A plot of measured ϵ' and τ values against Lohengrin velocity setting. Dashed lines show fit results.

The data were fitted with a function in order to examine the behaviour of ϵ' and τ with $\bar{Z}$. The functional form was taken to be some power dependence of the parameters on v and $\bar{Z}$, since both energy loss and range were expected to go to zero if the initial velocity is zero, a condition that power dependence satisfies. The simplest functional form then is of the form

$$f_1(v, \bar{Z}) = a\bar{Z}^{\alpha}v^{\beta}, \tag{4.17}$$

where a, α and β are fitted parameters. The fit converged with a reduced chi-squared of ≈2 for τ and ≈9 for ϵ'. In an effort to improve the poor agreement of the fit with ϵ', two following modified forms of the function f_1 were considered:

$$f_2(v, \bar{Z}) = a\bar{Z}^{\alpha}v^{\beta+\gamma\bar{Z}}, \tag{4.18}$$

and

$$f_3(v, \bar{Z}) = a\bar{Z}^{\alpha+\gamma v}v^{\beta}. \tag{4.19}$$

In both of these new fitting functions, fitting parameter γ is added with one of the two fitted variables in order to represent the variation in charge with velocity, since the two are not independent. Fitting form f_2 resulted in worse reduced chi-squared of ≈4 for τ and ≈11 for ϵ' and therefore any further inquiry with it was discontinued. Fitting form f_3 improved the ϵ' fit, which converged with $\chi^2_{red.}$ ≈4, but it made virtually no difference to the fit to τ, and therefore the simpler form f_1 was retained for that parameter. The dashed lines in Fig. 4.24 show the final fits to the data: form f_1 for τ and form f_3 for ϵ'. The final values of the fitting parameters are shown in Table 4.1.

TABLE 4.1: Fitting parameters extracted from fits of function f_1 to τ and of function f_3 to ϵ'.

Fit parameter	τ	ϵ'
a	0.90 ± 0.04	173 ± 169
α	-0.82 ± 0.02	1.30 ± 0.08
β	0.27 ± 0.02	3.37 ± 0.29
γ	-	-14.2 ± 2.2

The introduction of γ parameter in function f_3 resulted in covariance issues between constants a and γ, leading to an uncertainty in excess of 100% in a.

4.5.3 Comparison with SRIM-2013

All the various $\bar{Z}$ and v combinations shown in Fig. 4.24 have been simulated in SRIM to compare the toolkit used commonly in research and industry to the experimental results. Extracted values of τ and ϵ' for SRIM results are shown in Fig. 4.25 along with the experimental values.

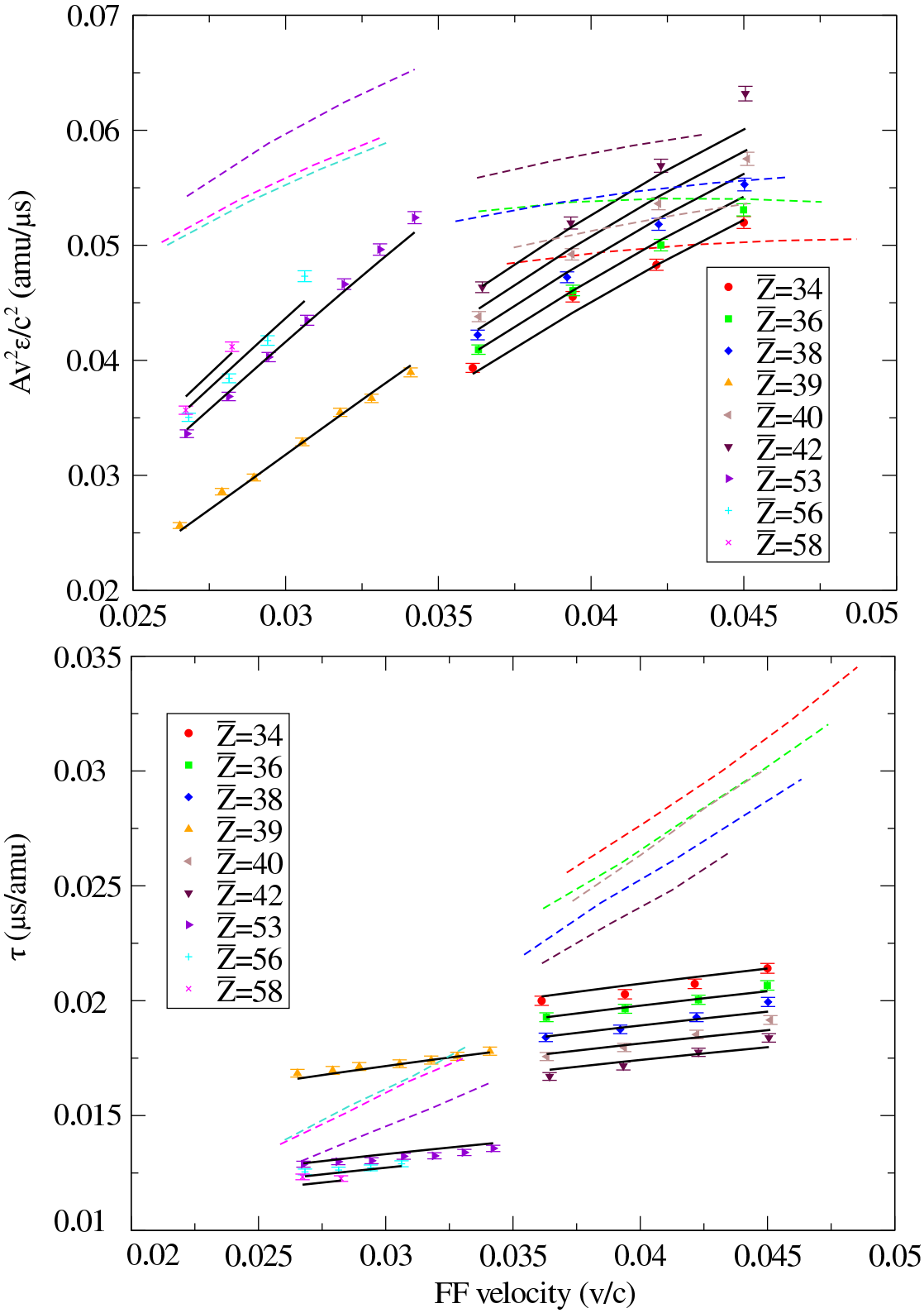

FIGURE 4.25: A copy of Fig. 4.24 with added simulation results from SRIM-2013 shown in coloured dashed lines. Colours for the SRIM simulations and the corresponding fragments in the data are indicated with the same colour.

The SRIM results show some agreement in trends and values for the heavy fragment results and approximately correct values for the light fragments for the ϵ' parameter, however there is no agreement between SRIM and data in either trends or values of τ. The exact cause of discrepancies between SRIM and data is hard to pinpoint, however SRIM simulated the starting FF as stripped, and equilibrating the charge inside the gas, whereas Lohengrin FF arrive with a certain ionic charge q, which is altered by the window.

An investigation of FF ranges and energy losses predicted by SRIM and data available at the time had been conducted by Filliatre *et al.* [148] in 2013. Simulated ranges were found to be overestimated by 10-20% and energy loss was underestimated by up to 23% compared to the results for range measured by M. Pickering and J.M. Alexander [149] and energy loss measurements by M. Forte *et al* [150]. The current data show the opposite effect to the previous results, whereby energy loss-like parameter is overestimated, while the range-like parameter is also overestimated. This warrants further investigation, since the two values are related. A numerical integration of the form

$$Range = \int_{E_0}^{0} \frac{-1}{dE/dx(Z,v)} dE \approx v_d A\tau \approx \frac{-v_d A Q_{max}}{E_0} \int_{v}^{0.1v} \frac{v^3}{\epsilon'(\bar{Z},v)} dv, \tag{4.20}$$

was attempted, where ϵ' and Q_{max} have been calibrated from charge to energy, E_0 is the Lohengrin energy setting corrected for the energy loss in the window, and v_d is the electron drift velocity in BD. The drift velocity was determined for a BD with identical field and gas configuration to FiFI, and was found to be 3.119±0.068 cm/μs [151]. The result of the integral was found to vary greatly depending on the choice of the final velocity of the FF, which suggests that the fit cannot be safely extrapolated far beyond the range of values over which it has converged. For this reason, a non-zero final velocity was chosen as 10% of the initial velocity, resulting in an agreement between $A\tau$ and the integral of ≈20%.

A direct comparison of the energy loss parameter with the results of Forte *et al.* is difficult, since the experiment in the earlier work averages energy loss over FF range, whereas the work here extracts only the maximal energy loss. A comparison with the data of Pickering and Alexander is also complicated by differing definitions of range, since in their work FF from a ^{252}Cf source entered a volume of gas and were swept perpendicularly onto a foil, and the position of various FF along the strips of foil was identified using gamma-ray spectroscopy. The present work does not consider the total range, since for pulse-shape analysis routines the resulting range values would be very sensitive to the definition of the beginning and end of the electron signal deposition onto the anode, a parameter which is difficult to quantify. This difference in range definition

however does not prevent a general comparison of the data, and a plot of reduced ranges (range divided by gas density, 0.233±0.001 μg/cm^3) from Pickering and Alexander's work and the current work are shown in Fig. 4.26.

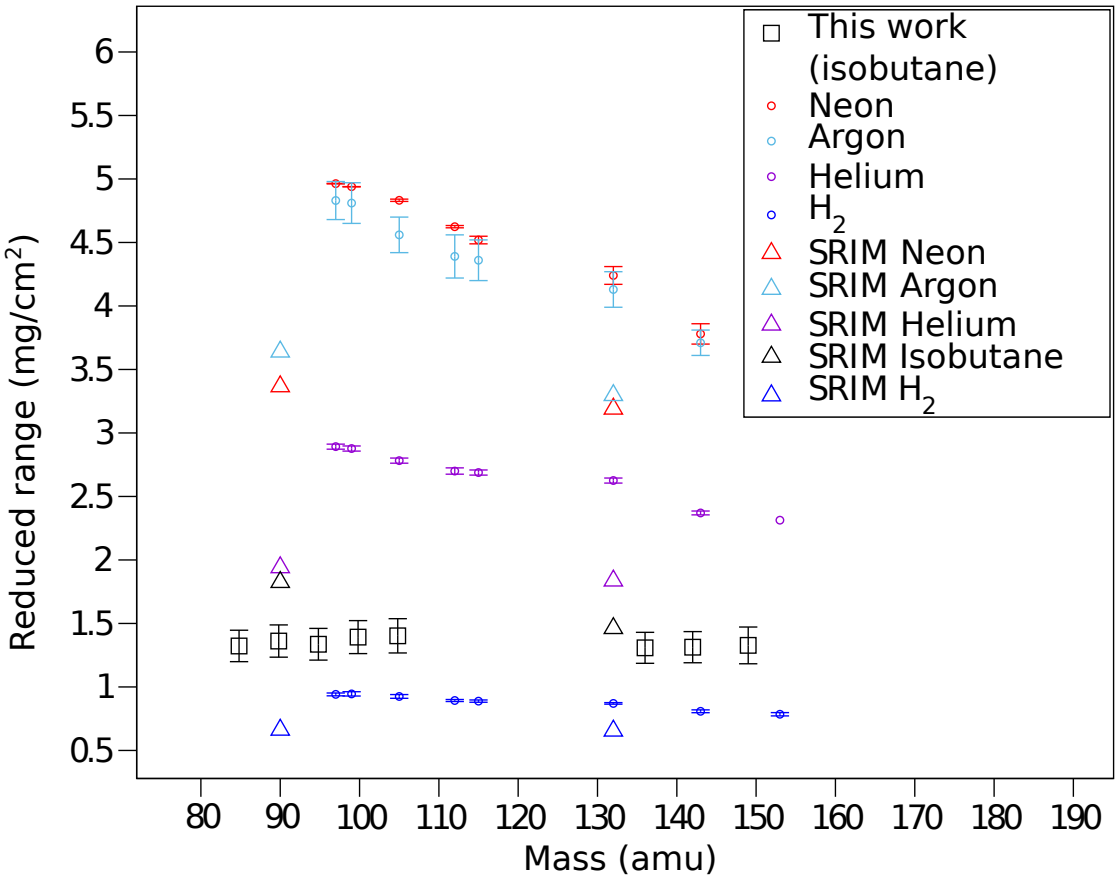

FIGURE 4.26: A comparative plot of FF ranges determined in Ref. [149] and the current work. A comparison of the simulation results calculated using SRIM-2013 is also shown.

A full comparison of the results could be potentially achieved by considering a scaling parameter to compensate for the difference in range definition. Nonetheless, the overall arrangement of the various fill gases considered in Ref. [149] and this work is confirmed by SRIM (with the exception of argon and neon), although the values between the two experimental results and SRIM still disagree. The current data also shows much less variation in range with mass than the previous data. Several possible factors affecting the measurement of range in this work have been identified: incorrect estimate of the drift velocity, diffusion of charge in the volume of the detector, and risetime distortion due to filters.

The drift velocity measurement has been made for a different ionization chamber filled with isobutane and with the same reduced field as FiFI during the Lohengrin campaign. The drift velocity was determined using the time between the leading edge of the Frisch grid signal and its minimum, i.e. the time the charge is sensed in the chamber and the

time all of it crosses the grid, having traversed the entire depth of the chamber's active volume. The determined velocity has been found to be consistent with the literature values and MAGBOLTZ simulations for the reduced field settings and the details of the work can be found in Ref. [151].

Charge diffusion has also been previously addressed using MAGBOLTZ [77] for STEFF Bragg arm ionization chamber, which has the same reduced field as the experiment presented in this chapter. Charge was calculated to spread by ≈0.3 cm for a typical fragment. Ranges of fragments in this work have been measured as ∼5 cm, meaning that the ionization electrons traverse ∼9 cm to reach the anode. Resulting charge diffusion then contributes ≈3% spread in risetimes. Assuming that electrons spread isotropically, this effect will average out, contributing to the measured uncertainties, but not to the risetime measured from an averaged pulse.

4.5.3.1 Filter Correction

Noise-correcting filters (differentiator, integrator and Chebyshev filters) were tested using a pre-filtered pulse. Such a pulse was chosen, since it would be smoother than a raw data pulse, and therefore allow for easier measurement of pulse height, and therefore 10%-90% risetime. The pulse was compressed by factors of 0.5-1.5 in steps of 0.1 to produce artificial pulses with different risetimes. Each of the compressed pulses had its t_{10-90} measured, and then was processed with the noise-correcting filters to extract post-filter t_{10-90}. A plot of the resulting filtered 10%-90% risetimes against their pre-filter counterparts for each degree of compression is shown in Fig 4.27 along with the linear fit. The linear fit was then used as a correcting formula which decreased the range values by ≈5%.

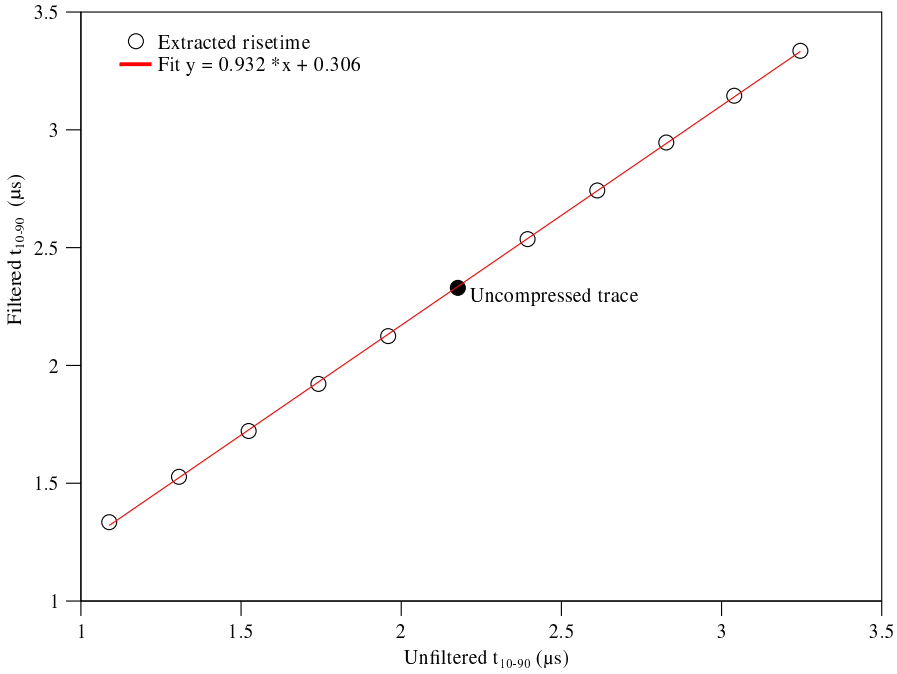

FIGURE 4.27: A plot of filtered signal 10%-90% risetime against pre-filtered t_{10-90} for signals compressed by a factor of 0.5-1.5 in steps of 0.1. The linear fit is shown in red along with the resulting equation, and the value for the uncompressed signal is indicated with a filled circle.

The range data were corrected using the fit formula and the resulting corrected versions of Figs. 4.25 and 4.26 are shown below in Figs. 4.28 and 4.29 respectively. The new fit parameters are tabulated in Table 4.2, and the reduced chi-squared of the fit remained ≈2. It is evident from the figures that the correction for filter effects does not explain the differences in the present experimental data and SRIM..

TABLE 4.2: Fitting parameters extracted from fits of function f_1 to τ following the filter effect correction.

Fit parameter	τ
a	0.80 ± 0.04
α	-0.77 ± 0.02
β	0.32 ± 0.02

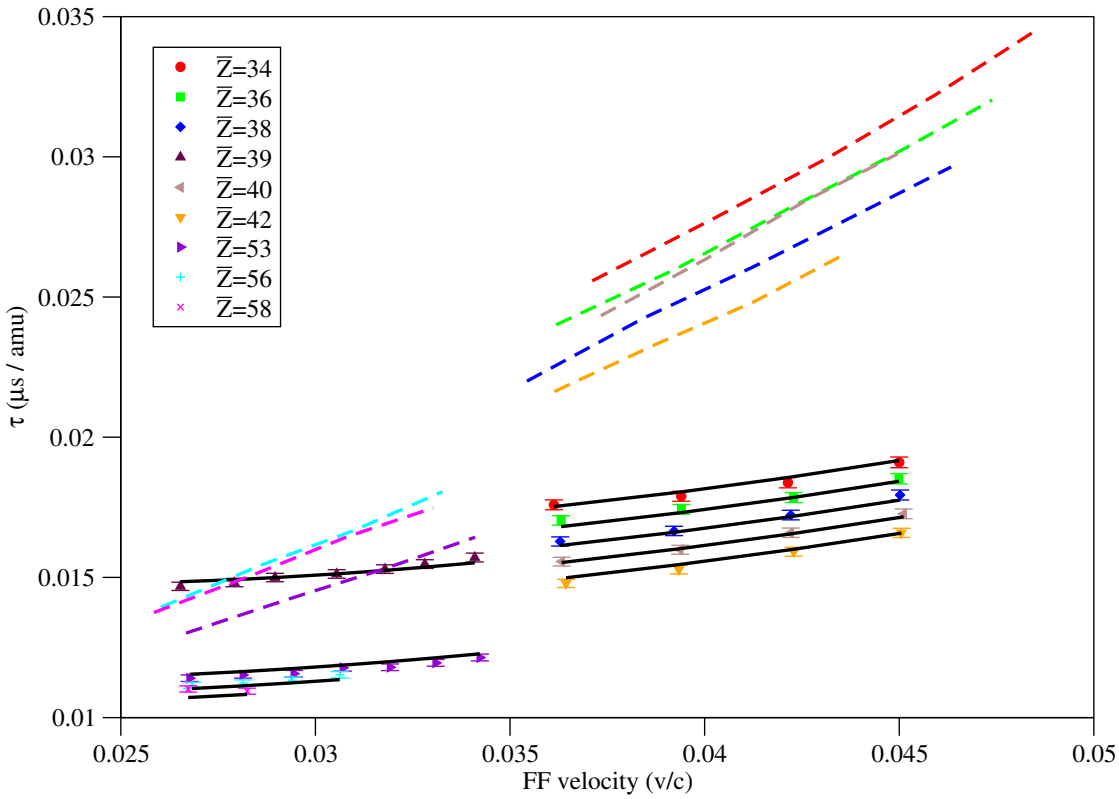

FIGURE 4.28: A copy of the right panel of Fig. 4.25 with a filter-effect correction applied. The colours of the SRIM simulations for specific fragments are matched to the colours of the measured results.

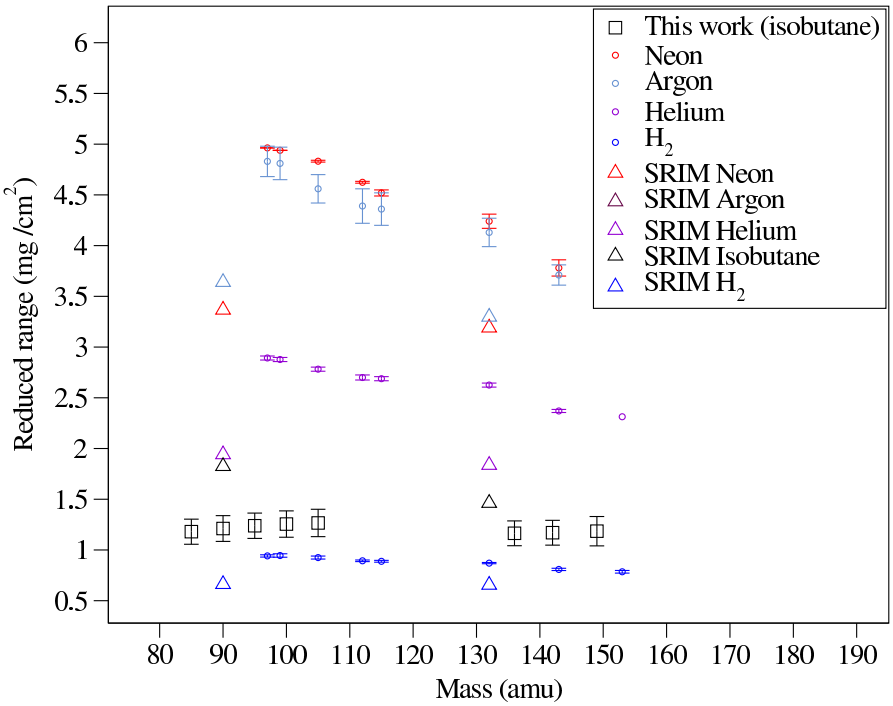

FIGURE 4.29: A copy of the right panel of Fig. 4.26 with a filter-effect correction applied.

4.6 Conclusion

An experiment was performed at Lohengrin, whereby various FF with various average atomic numbers $\bar{Z}$ have been identified, and the ionization traces extracted from FiFI BD were processed with digital filters to extract three parameters from averaged mass-gated pulses: maximal energy, maximum energy loss and risetime. These were fitted in powers of $\bar{Z}$ and v for future BD calibration. The results have also been compared to SRIM, which was found to be in considerable disagreement and also to previous results, which showed agreement in trends. Possible contributions to the differences between the measured results and the literature values have been considered and accounted for. The results presented in this chapter have been published in Nuclear Instruments and Methods A [121] and a follow-up proposal for examining the response of the BD for more heavy and symmetry-region FF for different fill gases, as well as a further investigation of charge-changing collisions in Lohengrin, has also been accepted by ILL for the summer 2020 reactor cycle. Additional data from the follow-up experiment will provide further values for range and energy loss measurements for the FF stopping studies, and offer a new set of calibration parameters for common BD fill gases.

Chapter 5

^{235}U Campaign and Data Processing at n_ToF

5.1 Neutron Time-of-Flight Facility

As mentioned previously, STEFF has been used at n_ToF to perform two experiments on ^{235}U fission products. The n_ToF Facility is a neutron spallation source located at CERN, built following a proposal by Rubbia *et al.* [152] and operating since 2001 [153]. The facility provides beams of neutrons covering a wide energy range from thermal to 1 GeV [154]. For its operations, the facility relies on proton beams from the CERN Proton Synchrotron (PS), which is part of the LHC acceleration chain. The 20 GeV/c proton pulses from the PS are sent out every 1.2 s to a number of experimental facilities around CERN. Some of the proton pulses are sent to the East Area Experimental Hall of CERN, which have different beam requirements from n_ToF. The beams redirected back from the East Area are referred to as 'parasitic', and are less intense than the beams sent directly to n_ToF, which are called 'dedicated'. Dedicated pulses have a higher number of protons, $\approx 7\times10^{12}$ protons per pulse (ppp) compared to $\approx 3\times10^{12}$ in the parasitic pulses, as well as a more consistent time distribution: both have an r.m.s. pulse length of $\approx$7 ns, although the parasitic pulses may show small variations depending on the proton use in the East Area [155]. PS proton pulses are frequently referred to as 'bunches', which is the term that will be used throughout this work.

The neutrons are produced by spallation when the proton beam impinges on a 1.3 tonne lead target encased in aluminium [156] [157], yielding $\approx$300 neutrons per incident proton [158]. Spallation involving a 20 GeV proton is a complicated process involving product nuclei populated at very high energies and relatively low angular momenta (due to parton interactions) compared to reactions using beams of heavier projectiles

[159]. The spallation process is shown schematically in Fig. 5.1. The dynamics of spallation can be modeled in two steps by first considering the projectile interactions within the volume of the target nucleus and then by examining the de-excitation of the residual nucleus [160] [159]. In the high-energy regime of up to a few GeV [161], the first step can be modeled using the Intranuclear Cascade Model (ICM), which treats the projectile interaction as a series of quasi-independent nucleon-nucleon and pion-nucleon interactions within the nuclear medium [161]. Note, that in the case of the very high-energy PS 20 GeV/c beam further extension has to be applied to the ICM to account for the parton interactions [162]. The cascade of interactions can produce particles, such as pions and kaons [158], and also leads to knock-out reactions, where protons and neutrons are removed from the nucleus [161]. Within ICM, the cascade is typically propagated until the total energy of the particles that compose the cascade falls below some threshold or the cascade timespan has exceeded the time it would take for a nucleus to thermalize [159]. Once the cascade has stopped, the residual nucleus may de-excite by emitting photons, neutrons, protons or even clusters of nucleons (which can be treated as highly-asymmetric fission [159]). The nucleus can also fission, although this process is hindered by particle emission in a manner similar to multichance fission [159]. Furthermore, multi-fragmentation can occur, whereby the residue dissociates into a number of light- and medium-mass nuclei [161].

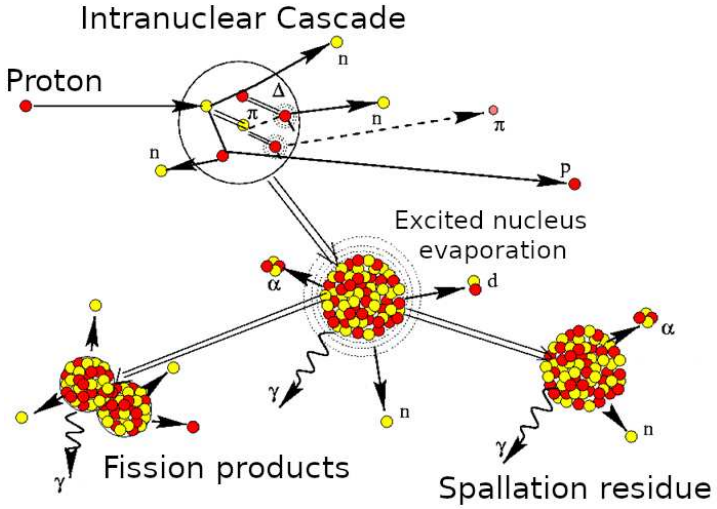

FIGURE 5.1: A diagram of the main stages in the process of spallation. The diagram shows a proton incident onto a heavy nucleus, causing an intranuclear cascade leading to a production of several different particle types, including neutrons. The remaining excited nucleus then de-excites by cluster, particle or photon emission, leading to a residue, which can undergo fission or break up further by emitting particles, fragments or photons [163].

The lead target discussed in this work is a cylinder, that is 40 cm long and 60 cm in diameter [158]. The target is cooled by 1 cm of water and has a 4 cm thick exchangeable

additional layer of moderator [157], which can be de-mineralized water or a water solution with a ≈1.28% admixture of H_3BO_3 [158]. The boron in the solution is ^{10}B, and it is useful due to its high thermal neutron absorption cross-section, ≈3860 barn for (n,α) reaction with a thermal neutron in JEFF-3.3 [11], which serves to reduce the thermal neutron contribution to the flux and moreover through dilution reduces the probability of neutron capture in hydrogen in water, a reaction that may produce a 2.223 MeV gamma ray with a cross-section of ≈16.7 barn [11], which contributes to gamma background [158]. Borated water is only applied to the forward face of the target, precluding its use for background reduction for STEFF (the position of STEFF relative to the target is described below). The orientation of the target and the moderator layers are shown in Fig. 5.2 along with the directions of the two neutron beamlines introduced below.

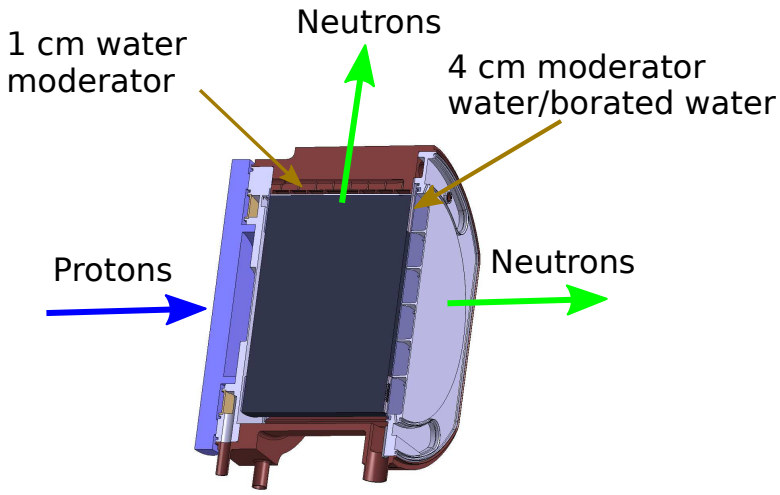

FIGURE 5.2: A schematic of the orientation of the lead spallation target cylinder relative to the proton beam. Two layers of moderator as well as the two neutron beamline directions are indicated. Adapted from [164].

The additional layers of moderator can only by added to the side of the circular face of the target that is opposite of the beam entry point, but not to the target sides. When the current spallation target, the second one to be used at n_ToF, was installed in 2008, the facility only had one beamline, Experimental ARea 1 (EAR1), and the moderator is positioned to face it. Since then, in 2014 a new beamline has been constructed, named EAR2. The orientation of the two beamlines relative to the proton beam and the target is shown in Fig. 5.3. Since STEFF to date has only been used in EAR2, the details of EAR1 are omitted in this thesis.

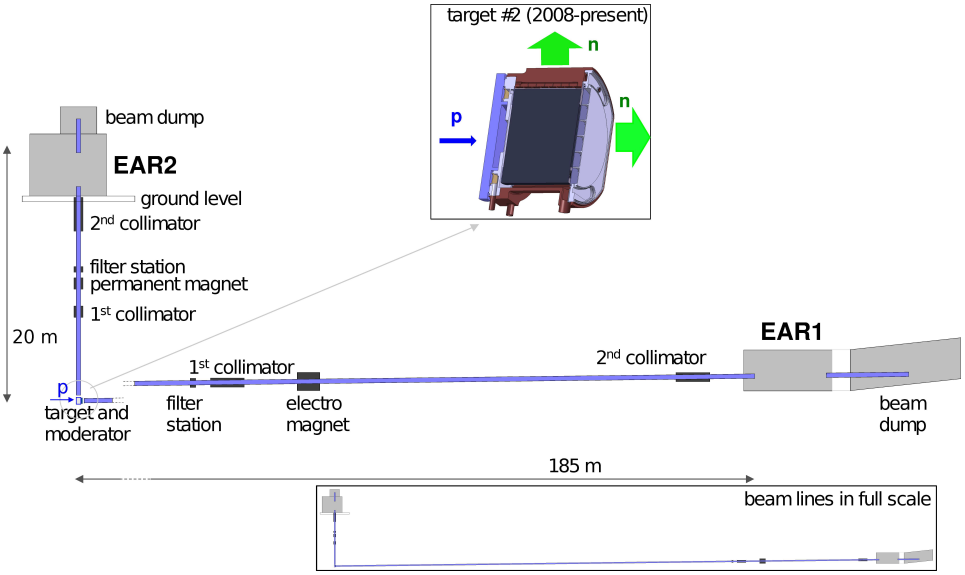

FIGURE 5.3: A diagram of the layout of the n_ToF Facility lead target and the two beamlines, EAR1 and EAR2, along with their main components. The inset at the top of the diagram shows the orientation of the spallation target relative to the proton beam and also the direction of flight of the neutrons in the two neutron beamlines (while overall spallation neutron emission occurs in all directions, and is forward-peaked relative to the proton beam). The inset in the bottom shows the scale of the two beamlines. Adapted from [158].

EAR2 beamline points vertically upwards from the target and has a length of ≈20 m [156]. This beamline has a sweeping magnet and two collimators. The magnet is located 10.4 m above the target and is composed of 168 radiation-resistant Sm_2Co_{17} blocks arranged to produce a 0.287 Tm dipole magnetic field around a 1.134-meter section of the beamline. Immediately after the magnet lies the filter station, where filters for attenuating gamma-rays or filtering specific neutron energy ranges can be inserted into the beam. The first collimator is located 7.4 m above the lead target and is a meter-long iron cylinder with a 20 cm inner diameter. The second collimator is 15.04 m above the target and is 3 m long. It is a vacuum vessel with an outer diameter of 680 mm and its volume is subdivided into 4 sections, each of which is chicane-shaped. The first 2 m of the second collimator is made of iron, followed by 60 cm of borated polyethylene (B-PE) and concluded by 40 cm of boron carbide (B_4C). The second collimator can be set to either a wide or a narrow setting, depending on the experimental flux requirements. The wide setting produces an opening of 70 mm, and the narrow settings reduces it to 20 mm. Following the second collimator, the beamline enters a room where experiments can be mounted on the beamline coming out of the floor and connected to the further beamline coming down from the ceiling, which leads to the beam dump. The beam dump is housed on the roof of the EAR2 building. The 400×400×400 mm^3 core of the beam dump is made of B-PE, which slows and absorbs beam neutrons as well as neutrons that backscattered in the beam dump. The core contains a hole with a diameter of 340 mm and depth of 250

mm, into which the final section of the beamline is inserted. The core is surrounded by 1600×1600×1600 mm^3 volume of iron for absorbing fast neutrons and gamma rays. The final layer of shielding is made of concrete and has the dimensions of 3200×3200×2400 mm^3 [156].

Due to its proximity to the spallation target, EAR2 has superior neutron flux compared to EAR1. Fig. 5.4 shows neutron flux as a function of neutron energy for the two areas. The higher thermal flux at EAR2 is the result of the lack of borated water moderator available for that area. As for the neutrons, the shorter flightpath of EAR2 means that background radiation in that experimental area is also greater. Of particular importance to STEFF is the gamma-ray background. The gamma background time distributions for EAR2 are shown in Fig. 5.5 along with the neutron time-of-flight.

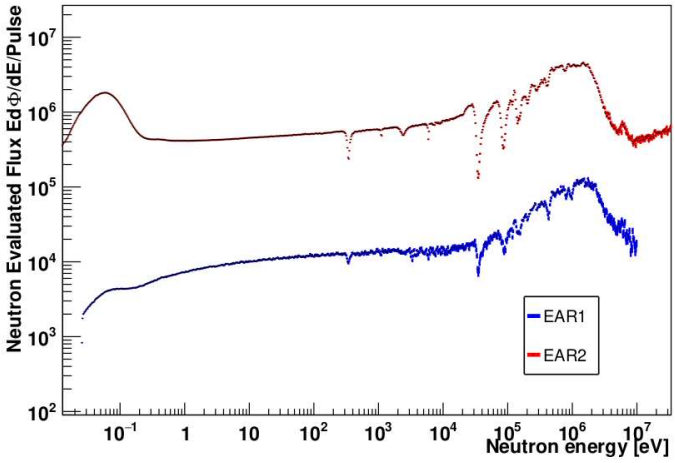

FIGURE 5.4: Comparison of neutron flux at EAR1 (blue) and EAR2 (red) at the n_ToF Facility [158]. Note the considerable increase in flux in EAR2, in particular at near-thermal energies. Also shown are absorption dips at neutron energies above 10^3 eV from elastic scattering reactions with trace ^{55}Mn in the target shielding, and above 10^4 eV from (n,γ) reactions with ^{27}Al, which is a major component of the material surrounding the target.

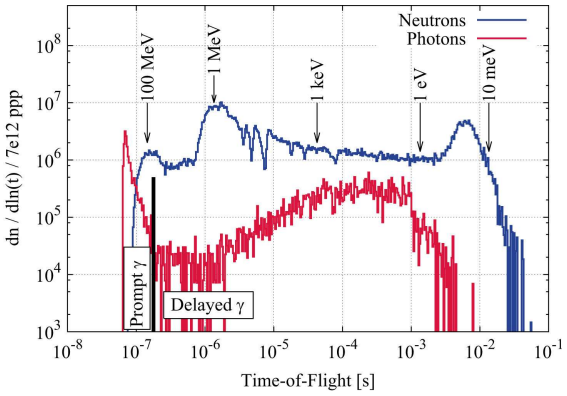

FIGURE 5.5: A simulated time distribution of gamma-ray background at EAR2 [156]. The contributions from prompt spallation gamma rays and delayed gammas originating from post-spallation de-excitation are indicated. Also shown is the neutron time-of-flight distribution with arrows indicating some neutron energies for reference.

The proximity of EAR2 to the spallation target has several downsides. Firstly, the shorter flightpath means that the neutron energy resolution is lower at EAR2, since neutrons traveling at different velocities have less time to separate from one another within the pulse. Secondly, fast neutrons are also less spatially separated from the fast spallation products, in particular gamma-rays. When spallation occurs at n_ToF, a large burst of spallation photons travels down the beamlines accompanied by further photons emitted from the surrounding materials by charged particles and neutrons. This radiation burst is called a 'γ-flash', and it has the effect of saturating most detectors that are in its way, and the fast neutrons accompanying the photons may also eject charged particles from detector materials via (n,p) and (n,α) reaction channels, further contributing to detector suppression. Depending on detector type, this results in a period of paralysis of varying duration, where saturated detectors cannot accept any new signals. A typical pulse shape of a γ-flash signal in a NaI detector is shown in Fig. 5.6 along with a zoomed-in trace of a signal from the same crystal immediately after the γ-flash, showing a featureless spectrum in Fig 5.7. A recovered response of a NaI crystal in the thermal region ($\sim$10 ms after spallation) showing a number of gamma-ray signals with a typical pulse shape is shown in Fig. 5.8.

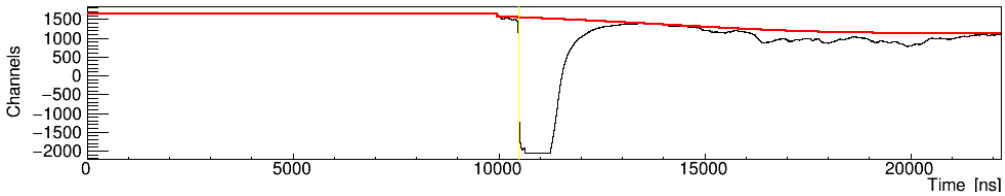

FIGURE 5.6: An example of γ-flash effects demonstrated by an unprocessed NaI signal. The x-axis is time in nanoseconds and y-axis is signal amplitude in arbitrary units. Black line shows the NaI signal trace. The large signal spike is γ-flash arriving at STEFF and saturating the detector. Red line marks the fitting routine's estimate of the baseline and yellow line marks the identified time of the γ-flash using 20% CFD on the saturated signal. The $\sim$11 μs time of the γ-flash signal is typical of dedicated bunches.

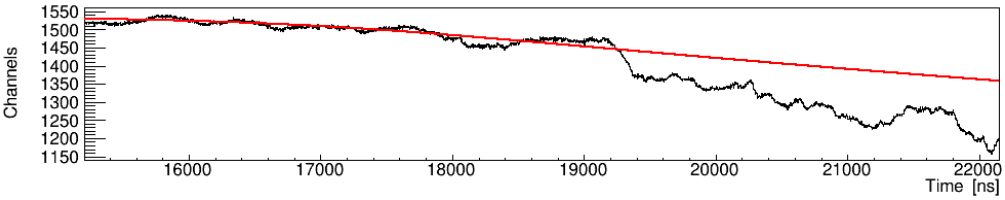

FIGURE 5.7: NaI scintillator signal following the γ-flash shown in Fig. 5.6. The response is suppressed by saturation and shows no discernible features.

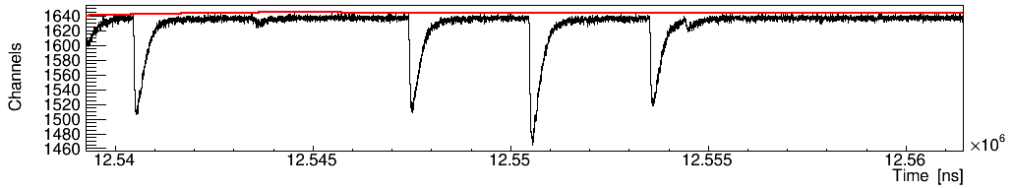

FIGURE 5.8: An example of a NaI response in the thermal neutron time-of-flight region ($\sim 10^7$ ns after spallation). Unlike Fig. 5.7, four prominent pulses with a characteristic NaI pulse shape appear in the spectrum.

5.1.1 n_ToF Data Processing

Data writing in the n_ToF data acquisition (DAQ) system is triggered from the pick-up (typically referred to as PKUP) signal, a wall current monitor detector which uses the current induced by the proton beam in the beamline walls to measure the intensity of the proton pulse and signal the arrival of the proton bunch at the lead target. Once the data acquisition has been triggered by the PKUP, it begins recording data streams from any detectors set in the DAQ for the next 32 ms. Detectors at n_ToF can be configured with a zero-suppression setting, which when set represents the amount of time data streams should be opened for if the detector signal passes a certain threshold. Alternatively, it can be set to 0, so that DAQ writes 'raw' data for the entire 32 ms window. The digitizing of detector output at n_ToF can be done using several different ADC cards, and the work presented here involves the use of four ADCs: one SP-device model ADQ412 and three SP-device model ADQ14 (the cards are 12- and 14-bit respectively). The digitizers are specified for each detector in the DAQ control along with the dynamic ranges, pre- and post-samples, rates etc. Once the digitizers convert the analog input into a digital trace, the data are timestamped and transferred to the CERN Advanced Storage (CASTOR) facility, where all the streams are written to magnetic tape for secure storage.

Stored data are subdivided into runs, with a single run representing the DAQ being set to start and then, typically after 4 hours of data collection, stopped. The duration of a run varies depending on whether the experiment is running as planned, availability of proton beams, DAQ performance etc. Each run is further subdivided into segments. A segment represents 20 proton bunches, meaning that every 20 bunches DAQ sends the data to CASTOR, which prevents significant data loss if an error occurs late into a run.

After storage on CASTOR, the data can then be retrieved using a Linux-based interface called LXPLUS. The interface provides utilities for 'staging' data, i.e. re-converting it from tape storage to digital traces, and then downloading it in .RAW.FINISHED format. The staging process can be slow (up to several days of waiting time), depending on the volume of data requested and on current demand from other users. n_ToF data can be converted from raw format (binary stream) into a format accepted by ROOT [165],

CERN C++-based histogramming and data management software. The conversion is done using a C++ code called RAW2ROOT, which relies on n_ToF libraries NTOFLIB to interpret the binary stream and the headers. The code provides an interface, which reads the raw data and accepts a customizable text file called USERINPUT as input. This text file provides various settings for processing of different detector streams. The RAW2ROOT code contains a class called DETECTOR, which can be set to accept various derived class implementation files using USERINPUT by specifying the derived class's name after the name of a detector, the output of which should be processed. For example, a large number of n_ToF experiments including STEFF rely on the Pulse-Shape Analysis (PSA) derived class of DETECTOR, which is used for extracting signal parameters, such as amplitudes and times. When USERINPUT is set to 'PSA', RAW2ROOT sets DETECTOR class's definitions to be implemented from the PSA C++ routine. More details about the functioning of the PSA routine can be found in [166]. The interaction of the C++ files comprising RAW2ROOT is shown in Fig. 5.9. The final output of RAWR2ROOT is a ROOT file, which contains a list of all the fit results for all the detectors processed with PSA.

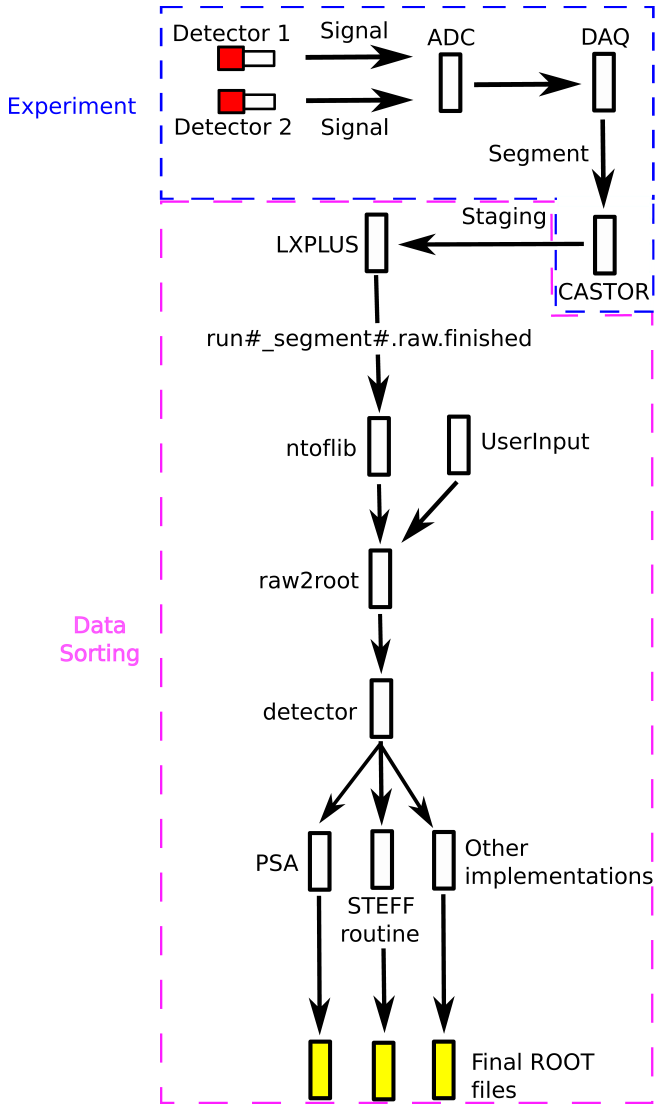

FIGURE 5.9: A diagram outlining processing of a detector signal into ROOT files. The blue dashed box shows the data writing part, which occurs during the experiment, while the pink dashed box shows the data sorting component, which converts stored experimental data into a format fit for analysis. The detector signals are written by DAQ to CASTOR and can be 'staged' onto LXPLUS for access in .RAW.FINISHED format. The resulting raw data files can be read using NTOFLIB libraries, which pass the data to RAW2ROOT codes. These codes use a text file called USERINPUT to inform them which derived class of DETECTOR class to use, which guides how the signals are processed. The final result is a ROOT file containing processed signals.

5.2 2016 Campaign Data Processing

The 2016 campaign of ^{235}U measurements with STEFF was allocated 30 days of beam-time and received 1.53×10^{18} protons on target. The ^{235}U target used during the campaign was 81 mm in diameter with a thickness of 100 μg/cm^2, composed of 93% enriched $^{235}UO_2$. Uranium was electroplated onto a supporting backing of 0.7 μm-thick aluminium. A photograph of the target is shown in Fig. 5.11. The target was aligned inside STEFF as shown in Fig. 5.10, i.e. at 45° relative to the neutron beam facing FiFI Bragg arm entrance. This meant that the FF would have to pass through some additional material due to the target angle to get into the main arms, but would have the clearest path into the FiFI Bragg arm. This alignment also precluded the use of FiFI Hipps arm, since the target holder faced in that direction, so FiFI Hipps STOP, Frisch grid and anode were excluded from data analysis.

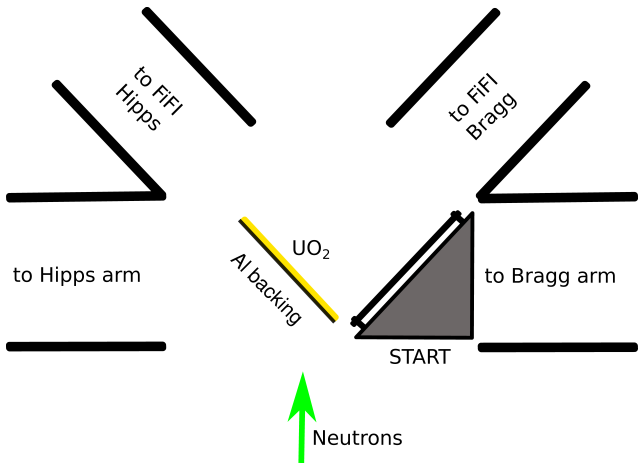

FIGURE 5.10: A diagram of the orientation of uranium target inside STEFF during the 2016 campaign.

FIGURE 5.11: A photograph of the uranium target used in STEFF during the 2016 campaign at n_ToF. The yellow deposit is uranium oxide deposited onto aluminium foil, which is mounted onto the target holder. The uneven surface of the foil occurred due to the unusually large diameter of the target for the thin target support clamps. The foil developed wrinkles when the clamp was tightened.

The analysis of the first n_ToF campaign using STEFF in 2015 was complicated by the large data volumes collected (≈500 TB). The details of the processing of the data are presented in [21]. The target for the 2016 campaign was considerably larger (the target in 2015 was 33 mm in diameter), and a large second collimator in EAR2 (70 mm opening) was used, so a considerable increase in data volumes was expected. However, the campaign in 2015 relied only on zero-suppression in the DAQ to perform data cuts, but otherwise it ran in an essentially triggerless fashion (except for the PKUP trigger to DAQ), so in order to reduce the amount of data that was stored, a second-level trigger (Master trigger) was implemented, that would suppress DAQ writing unless a signal from any of the four Frisch grids on STEFF is registered. The grids are used to create a Master trigger signal which indicates that there has been a fission event and opens the DAQ channels for recording over an interval of 30 μs with pre- and postsample durations relative to the Master depending on the detector type. If a second Master trigger was set off during the 30 μs window, the window would be extended to 60 μs. The second-level trigger method prevented the DAQ from acquiring data over the entire 32 ms window typical to n_ToF, or recording signals from background gamma rays or spontaneous emission in the timing detectors, when there has been no fission within a few microseconds, thus reducing the final data volume. The configuration of electronics for producing Master triggers is discussed in [77]. The windows set for recording various detector signals were broad (e.g. 2.2 μs window was set for NaI compared to few hundred nanosecond typical signal width). The window size was chosen to be large due to poor timing resolution of the Frisch grids caused by the requirement for electron current to drift across a large fraction of the depth of the BD and by varying ranges of the FF in

gas. Ultimately, the campaign accumulated a total dataset of 68 TB on CASTOR, which is a considerable data volume compared to many n_ToF experiments, but nonetheless significantly smaller than the 2015 campaign.

RAW2ROOT code is well-suited for experimental set-ups with fewer detectors and smaller data size than in a STEFF experiment, due to its approach to data segment processing. When a segment file is passed to it, each detector's stream is read and processed, and no reading of any other detector stream is implemented during this time. This feature disallows correlation of various detectors into a single event during the reading, which has to be done subsequently in ROOT. For a spectrometer such as STEFF featuring many detectors, this is a major complication. This single-stream property of RAW2ROOT led to a further complication, since STEFF BD signals required different filters to the ones offered in PSA. For that reason, existing derived classes of DETECTOR class were unsuitable for the BD signals, which had to be written out as a raw pulse for future processing in Manchester using filters discussed in the previous chapter. An entire 30 ms trace recorded for each BD, however, would constitute a very large amount of data, most of which would consist of baseline and/or pre-amplifier decay. Due to all the complications listed above, a two-step approach was adopted for processing STEFF data on the servers at CERN using RAW2ROOT.

In the first step, following a calibration of the PSA fitting parameters inside USERINPUT, PSA analysis was performed on all the detectors that were not inside the BDs including Master signal traces. For the second step, a list of all the Master trigger times was extracted for every bunch from PSA processing in step 1 and fed into a custom DETECTOR implementation written specifically for STEFF processing, called STEFFDETECTOR, which would extract traces containing BD signals from the full 30 μs traces. The resulting cut trace will henceforth be referred to as a 'waveform' and the STEFFDETECTOR derived class will be referred to as 'waveform routine'. The process is outlined below in Fig. 5.12, and a list of all the STEFF detector types, the routines used and the sampling settings for the DAQ is given in Table 5.1.

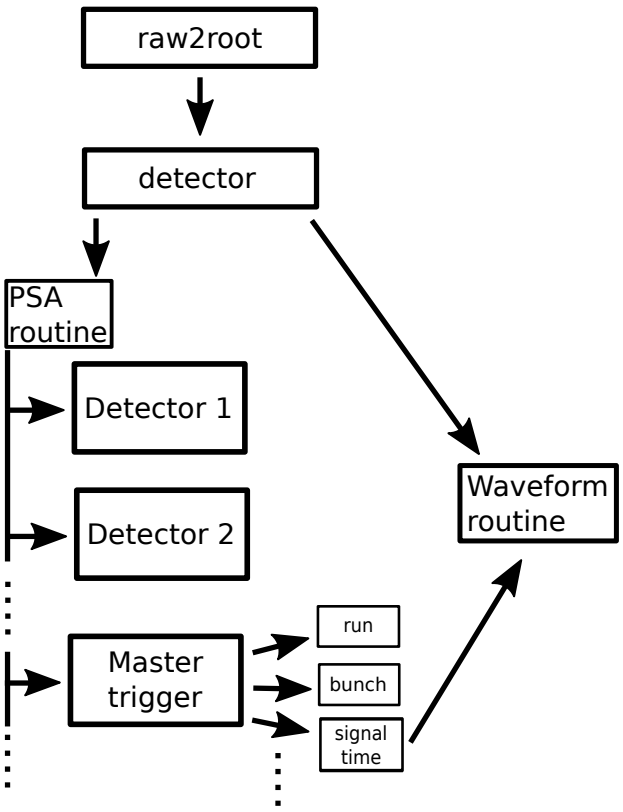

FIGURE 5.12: A diagram representing the steps of producing the inputs necessary for the waveform-processing derived class of the DETECTOR class in RAW2ROOT. RAW2ROOT is first run with the PSA routines to produce a list of Master trigger times, which is then fed into the second round of processing with RAW2ROOT for extracting BD signal waveforms based on Master trigger time. The internal structure of the PSA-processed ROOT files is described in greater detail below in Subsection 5.2.1.

TABLE 5.1: A list of STEFF detector types and RAW2ROOT routines used for their processing, as well as sampling rates (in megasamples per second) and pre- and post-sample settings.

Detector type	Routine	Sampling rate (MS/s)	Presamples	Postsamples
Pick-up	PSA	1800	1024	1024
Master trigger	PSA	1800	1024	1024
START	PSA	1800	16200	1800
STOP MWPC	PSA	1800	16200	1800
NaI	PSA	450	9000	900
$LaBr_3$	PSA	450	9000	900
FiFI Bragg STOP	PSA	1800	18000	18000
Bragg arm Frisch grid	Waveform	125	2500	30000
Bragg arm anode pads	Waveform	125	2500	30000
Hipps arm Frisch grid	Waveform	112.5	2250	20000
Hipps arm anode pads	Waveform	112.5	2250	20000
FiFI Bragg arm Frisch grid	Waveform	1000	10000	750000
FiFI Bragg arm anode	Waveform	1800	18000	72000

Once the waveforms and the PSA-processed signals have been collected, they were transferred to Manchester and re-correlated into individual fission events, which were then stored and processed using GAVSORT for storage in a MariaDB database for final analysis. The full outline of all the milestones involved in the processing of the 2016 STEFF Campaign at n_ToF are shown in Fig. 5.13.

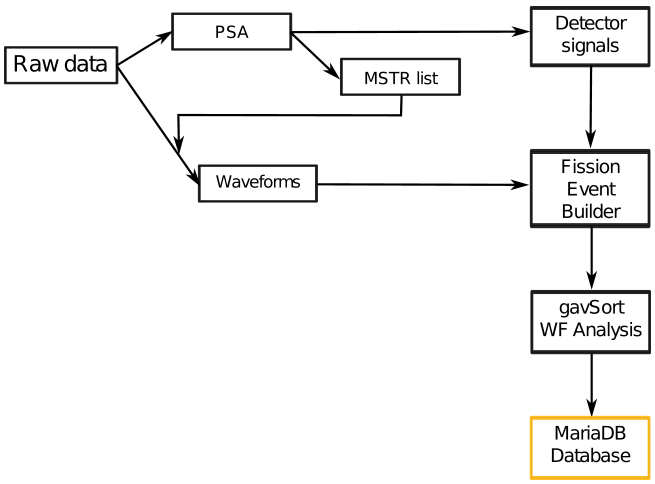

FIGURE 5.13: An outline of the steps involved in extracting raw data traces from n_ToF. The steps are as follows: processing the non-BD signals with the PSA routine, feeding the Master trigger time output of the PSA routine to the waveform routine, extracting the BD signal waveforms, re-correlating waveforms with the PSA-processed signals, reading them into gavSort, and storing all the data in a MariaDB database.

5.2.1 PSA Routine Results

The PSA routine relies on signal derivative threshold crossings to identify the presence of a pulse, and then it may be set to either attempt a fit or to directly extract signal amplitude and area. The fitting for the STEFF campaign was done using default PSA quadratic fitting (only the peak of the signal is fitted with a parabola) for all the detectors except for the scintillators, which were fitted using a set of averaged pulse shapes, which were produced for each detector type i.e. $LaBr_3$ or NaI, during the campaign in 2016. Once the pulse is fitted, a number of variables is extracted from the fit and from the DAQ that help identify signal origin and time the signal within the campaign. The extracted variables are then written to a ROOT file. The variables and their meaning are shown in Table 5.2.

TABLE 5.2: A list of variables written into ROOT files by PSA routines with an explanation of their meaning.

TBranch name	Meaning
RUNNUMBER	Number of the run as recorded by the DAQ
SEGMENT	Number of the segment in the run
BUNCHNUMBER	The number of the proton bunch within a run
PULSEINTENSITY	Proton beam intensity, used for identifying whether the bunch was parasitic or dedicated
DETN	Detector ID starting at zero used for identifying individual detectors, e.g. NaI entry with DETN = 1 is NaI crystal 2
TFLASH	The time of the γ-flash relative to PKUP signal time identified by PSA using the routine's dedicated γ-flash identifying functions
TOF	The time of the signal relative to PKUP identified by PSA routine using 20% CFD
AMP	Maximum amplitude of a signal, measured by PSA routine by fitting a Gaussian around the peak within a signal trace
AREA	Integrated area under the signal following background subtraction
FWHM	Full-width half-maximum of the signal

5.2.2 Waveform Routine

The waveform routine's purpose is to use Master trigger times and proton bunch numbers to identify and cut signal traces from the STEFF BDs in such a way, that some baseline, signal risetime and some preamp decay is preserved in the final cut waveform. A pictorial diagram of the process is shown in Fig. 5.14.

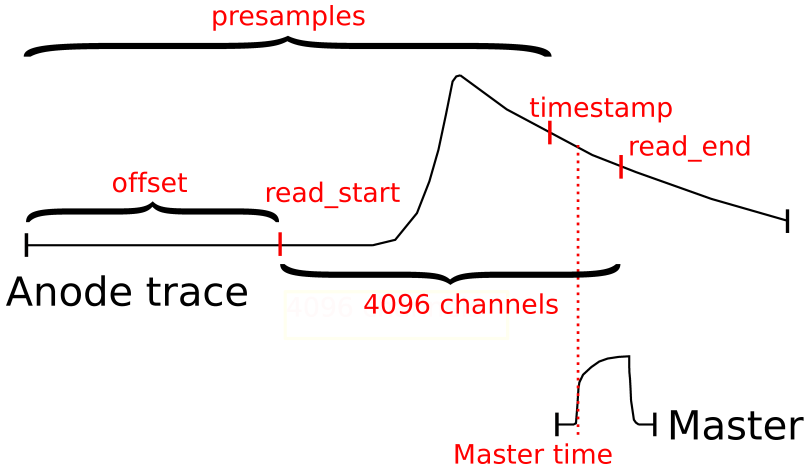

FIGURE 5.14: An outline of a typical raw anode pulse showing its position in time relative to a Master trigger, and indicating all the variables involved in cutting of a waveform out of a full trace. The times and signal widths and amplitudes are not shown to scale. The diagram shows the Master time as a 20% CFD of a Master trigger. A timestamp is asigned by the DAQ when the full trace is written, and lies a short time before or after the Master trigger time depending on the ADC card used. The trace begins a certain number of presamples before the timestamp time. READ_START and READ_END variables are calculated using a user-defined OFFSET for timing the position of the signal within the trace.

Master signals are compared to signal timestamp, which corresponds to the time when the DAQ channel for the detector in question has been triggered for writing. The time of the first bin in the trace is offset from the timestamp by a certain number of presamples, that were set in the DAQ individually for various detectors before the campaign. A list of presample lengths and ADC channel widths in time are given below in Table 5.3.

TABLE 5.3: A list of STEFF BDs along with their presample and ADC time channel widths for the 2016 campaign.

Detector type	Presamples (channels)	ADC channel width (ns / channel)
Bragg Frisch grid	2500	8
Bragg anodes	2500	8
Hipps Frisch grid	2250	8.88889
Hipps anodes	2250	8.88889
FiFI Bragg Frisch grid	10000	1
FiFI Bragg anode	18000	0.55556

There are several effects that are considered during the waveform cutting. BDs in different arms of STEFF were processed on different ADCs, which meant that there

will be small constant offsets due to Master triggers originating from four Frisch grids on STEFF. These offsets were extracted from PSA processing of Master signals coming from the four Frisch grids and taking the time difference of each Master channel relative to Master channel 1, which corresponded to the ADC associated with the Bragg arm's Frisch grid. The results of this are shown in Table 5.4.

TABLE 5.4: A list of offsets of time offsets in the arrival of Master triggers used in the campaign. The times are listed relative to one of the Bragg arm Master signal time, referred to as MSTR1.

Master channel	Time offset relative to MSTR1 (ns)
MSTR2 (Hipps arm)	-200
MSTR3 (FiFI Bragg arm)	-48
MSTR4 (FiFI Hipps arm)	182

Furthermore, every time a new bunch arrives, the n_ToF DAQ is configured to set the timestamp to zero and start taking data 10 μs earlier for the first Master trigger, than for the rest. This setting is a DAQ property, that is in place to ensure that n_ToF detector output streams always capture γ-flash. This feature is not of essential importance to the BDs, since faster detectors rely on γ-flash for timing, but the BD time resolution is too low to rely on it. Nonetheless, a 10,000 ns offset was added for every event where TIMESTAMP variable is set to zero.

The offsets are combined with the number of presamples and the timestamp to calculate READ_START, i.e. the expected position of the signal within the full trace. Prior to calculating READ_END, the final channel of the cut trace, all the BD channels in the full trace were averaged over a detector-dependent window to compress the length of the waveform. The averaging window widths in channels are listed for all the detector types in Table 5.5.

TABLE 5.5: A list of widths of averaging windows in channels of the original full trace used for compressing cut traces into final waveforms used for analysis.

Detector type	Averaging window width (channels)
Bragg Frisch grid	4
Bragg anodes	4
Hipps Frisch grid	4
Hipps anodes	4
FiFI Bragg Frisch grid	16
FiFI Bragg anodes	16

Once averaging was applied, READ_END was set 4096 averaged channels following READ_START. The final ROOT file produced by RAW2ROOT is a list of all the detectors processed by the waveform routine, arranged in a similar fashion to PSA-produced files, however each BD entry in the list stores timing information and a 4096 channel array containing the waveform, rather than fit information.

5.2.3 Fission Event Builder

The first stages of STEFF data analysis, i.e. staging, PSA and waveform cutting, focused on bringing the data to Manchester and resulted in ≈6 TB of data, reducing the total volume by ≈90%. The data were still split over various detectors in an uncorrelated fashion, and therefore a dedicated package, called Fission Event Builder (FEB), was developed for the purpose of re-packaging the data into fission events.

FEB is centered around a C++ code called Data_Proc, which assembles fission events within a single run. A flowchart of its functionality is shown in Fig. 5.15. The code functions by storing all the PSA-processed data in memory and correlating them based on signal amplitude cuts and time windows set for each detector relative to the Master channel 1. An example of a time window setting for START and Master channel 1 is shown in Fig. 5.16, and a full list of amplitude and time cuts for all the detectors is given in Table. 5.6. The waveform data are too large to store in memory, and therefore the code checks which BD detectors are missing (since some anode pads were not active for all the runs) and creates a look-up table within the waveform ROOT file for quick access to the data. Once all the PSA events are correlated into fission events and stored in memory, they are written out to a correlated data ROOT file, and the waveforms are added to the output during the writing stage.

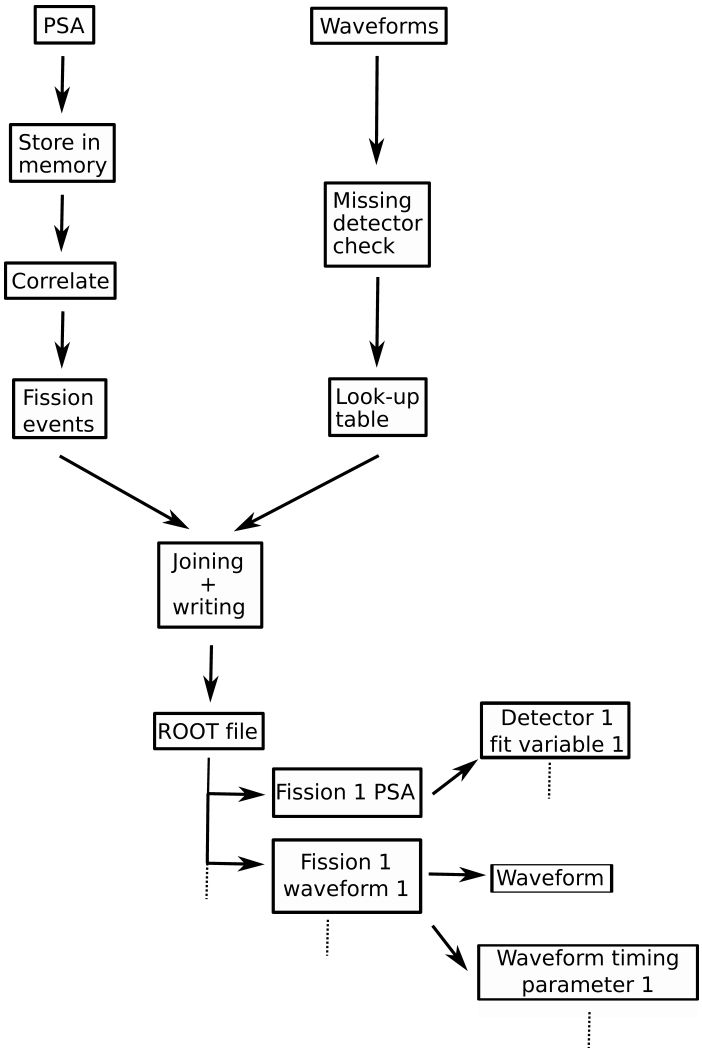

FIGURE 5.15: A flowchart of PSA and waveform correlation into packaged fission events by the DATA_PROC code. The code reads and correlates all the PSA-processed signals around Master triggers based on time and amplitude cuts. Then it creates a look-up table of all the waveform entries with their times and while writing out the PSA-processed events adds the waveforms into the final ROOT file after the PSA, relating them to each other with a fission event index ('Fission 1' in this diagram).

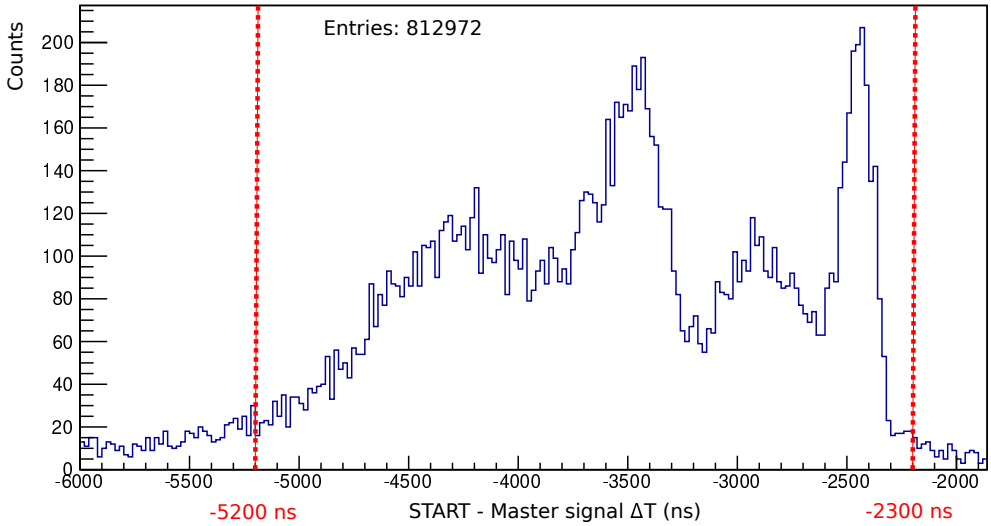

FIGURE 5.16: Time difference distribution of all the START signals relative to Master channel 1 within each bunch for an entire run. The spectrum shows a clear pair of double-hump structures, originating from either Bragg or Hipps Master signals triggering the DAQ (the structure on the left with the longer time scale corresponds to Hipps). Each double-hump structure represents either light or heavy fragment time of flight to each of the two main arms' BDs. There is a START signal amplitude cut of 3000 channels used for this spectrum. Red dashed lines represent the position of the final time cut used for fission event building: between -5.2 and -2.3 μs before Master channel 1.

TABLE 5.6: A list of amplitude cuts and selections in time relative to Master channel 1 for all the PSA-processed detectors. The amplitudes are given in channels for accuracy (dynamic ranges of the ADCs used for each detector can be accessed in the n_ToF DAQ run logs) and times are given in nanoseconds. Some MWPC wire banks have positive and negative amplitude cuts, due to the possibility of preserving signals induced in them by other wire banks, which can be used for positioning of the electron cloud inside the MWPC. Some of these banks will have two time cuts corresponding to positive and negative amplitude cuts.

Detector	Time cut (ns)	Amplitude cut (channels)
START	-5200 to -2300	3000
Bragg STOP anode bank 1	-5500 to -1700	100
Bragg STOP anode bank 2	-5300 to -1800	±50
Bragg STOP anode bank 3	-5500 to -1900	-50
Bragg STOP anode bank 4	-5100 to -1600	-50
Bragg STOP anode bank 5	-5000 to -2200 -5000 to -1800	±50
Hipps STOP anode bank 1	-3200 to -2000 -5000 to -2100	100 / -50
Hipps STOP anode bank 2	-4800 to -2000 -5000 to -1800	50 / -100
Hipps STOP anode bank 3	-5000 to -2000 -4500 to -1700	±50
Hipps STOP anode bank 4	-5000 to -2000	±50
Hipps STOP anode bank 5	-5000 to -1700	50
NaI	-9000 to -1300	0
$LaBr_3$	-9000 to -1800	0
FiFI Bragg STOP	-5000 to 0	0
PKUP	0	1000

The final output ROOT file contains a list of all the fission events. Each fission event occupies several entries, the first of which contains the PSA-processed data, followed by two entries for each waveform: one entry contains the waveform and the other all the timing information for the waveform. All the entries can be identified as belonging to the same fission event based on an index assigned by the code.

The final data volume following DATA_PROC did not get reduced, but increased to ≈8 TB from the initial 6 TB, due to unfolding of the waveforms from a large single array of all the waveforms to individual arrays for each fission event. This data structure's storage inefficiency was deemed acceptable, due to its more intuitive file structure and easier handling when interfacing with GAVSORT in the next step of STEFF data processing.

5.2.4 Database

Once GAVSORT was set up for compatibility with ROOT, a database of experimental results was written out from the FEB output. The processing took two weeks and resulted in a ≈1 TB database, meaning that the STEFF data processing pipeline yielded a ≈70-fold reduction in data volume. Reduction in volume following the FEB output processing came from rejection of waveforms containing noise, more compact packaging of waveforms as binary data, and a tighter cut being placed on PSA events relative to fast-timing detectors, which was not possible during the fission event building stage, since at that point all the PSA signals only shared slow Master signals.

During the processing, the data were divided into 6 'trigger types'. Each trigger type identifies fission events with particular fast-timing signal combination, that allow quick selection of events based on the quality of the timing signal the user can expect. The triggers are tabulated below in Table 5.7. For all the trigger types, a 250 ns cut was applied to all the PSA events relative to the fast-timing signal. Furthermore, a 64 PSA-signal cut was placed on any fission event, since MARIADB does not allow dynamic lengths for database rows. Unused slots for fission events with fewer PSA-processed signals were filled with dash ('-') characters. This cut has proven to be generous, as shown in Fig. 5.17, since none of the events in either dedicated or parasitic pulses had more events than 64 (typically there was ≈20 PSA events).

TABLE 5.7: A list of trigger types chosen for the database and their numbering. Trigger types effectively represents presence or absence of fast-timing detectors, allowing for quick selection of fission events with particular timing resolution possibility.

Trigger type number	Timing detectors present in the fission event
1	START and either (or both) MWPC detectors
2	Both MWPCs with or without START
3	START with either main arm anode
4	Hipps MWPC with either main arm anode
5	Bragg MWPC with either main arm anode
6	FiFI Bragg STOP with FiFI Bragg anode

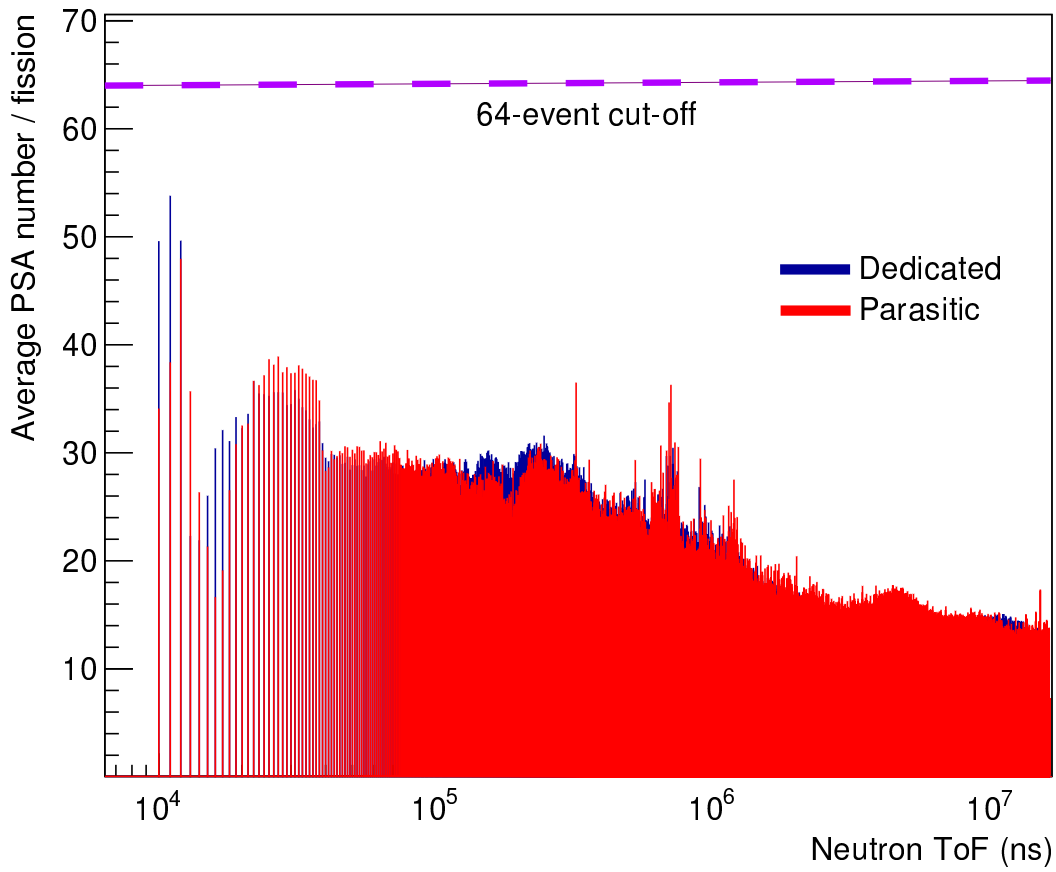

FIGURE 5.17: Number of PSA events per fission for dedicated (blue) and parasitic (red) pulses. 64-event cut is shown in purple and demonstrates that none of the fission events would have been affected by the cut-off. The plot features only the PSA events that were accepted based on fast-timing detector cuts in gavSort, since following Master time cuts in FEB the events in the 10^4 ns timing range featured up to ≈400 PSA events.

The database rows represent individual fission events, and 431 columns contain several fission event properties, PSA signal properties for up to 64 PSA signals, several properties for each waveform, and the unfiltered waveforms themselves stored as binary large objects (BLOBs). Furthermore, a sum signal comprising the gainmatched anode pads in each of the two main arms was constructed and stored. The addition was done by identifying the anode pad with the largest signal, and adding only the neighboring anode pads (not including diagonal neighbors). Addition of all the non-neighbor anode pads was rejected, due to amplification of noise levels in the sum signal caused by anode pads which have no FF signal. A summary of all the main column types of the database are listed in Table 5.8.

TABLE 5.8: A list of unique types of columns in the database. Repeating column types, such as those for each of the PSA events, have been omitted. Character '#' represents a number, which ranges from 0 to 63 for PSA events, and 0-15 for BD anodes, indicating individual events (anode pad 0 is the sum trace). Only Bragg arm waveform columns are shown for brevity.

Column name	Column content
Fission event information	
N	Number of the fission event (unique identifier)
RunNumber	Run number in the n_ToF DAQ
TRG	Trigger type (see Table 5.7)
BunchNumber	Number of the proton bunch within a run
PulseIntensity	The intensity of the proton pulse as measured by PKUP
PSA information	
Type#	A character identifying the STEFF detector (e.g. 'L' is $LaBr_3$)
TRG#	Trigger type
Det#	Detector number (e.g. '10' for NaI crystal 10)
E#	Signal amplitude
T#	Signal time
Waveform information	
BraggE	Amplitude of the anode sum signal
BraggToF	CFD timing of the anode sum signal
BraggE#	Signal amplitude of an individual anode pad
BraggA	BLOB containing the anode traces
BraggG	BLOB containing the grid trace

5.3 Conclusion and Future Improvements

A STEFF experiment with a wide collimator and a large ^{235}U target has been conducted at n_ToF in 2016 with the aim of collecting large number of data on fission fragments and prompt fission gamma rays. A data pipeline has been constructed for the experiment as part of the work presented in this thesis, featuring a sequence of codes for transferring STEFF experimental data from the n_ToF DAQ to Manchester and storing the transferred data in a convenient MARIADB database, which now contains ≈5.8 million fission events. The pipeline has reduced the data volume by a factor of ≈70. Data processing took a total of 1.5 years across all the stages, a time that included considerable amount of code testing and troubleshooting, and therefore will be significantly faster with a pre-existing codebase. A considerable improvement in processing time can also be reached by excluding reliance on USB disks for transferring data to Manchester, and processing the data on the clusters at CERN to reduce disk I/O. Furthermore, a cluster with 100+

GB of RAM could potentially be used for the fission event building stage. Waveforms were read in and written out for each fission event individually for the project presented here, which resulted in a large amount of I/O between the code and the disks. Test with reading all the waveforms for each run into memory before fission event building has been conducted, and resulted in 3× faster processing. If a cluster with large RAM capacity is not available, making runs shorter in time during the conduct of future STEFF experiments could result in run files with smaller waveform quantities, that could fit into more conventional memory sizes. Once a database is built, experimental data can be processed relatively quickly (the campaign presented in this work can be read and analyzed in full from the database in the span of ≈7 hours). A graphical reference of approximate processing times and data volume changes at various stages of the pipeline are presented below in Fig. 5.18.

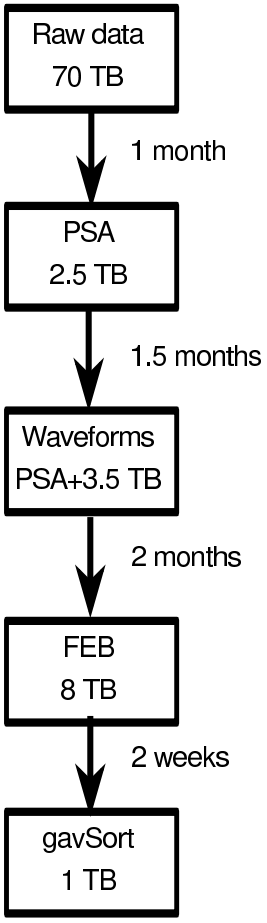

FIGURE 5.18: A timeline of approximate processing times and total data volumes at various stages of the STEFF data pipeline presented in this work.

Chapter 6

^{235}U Gamma-ray Measurement Results with STEFF

6.1 Prior STEFF Gamma-ray Measurements

Following the ILL and the 2015 n_ToF campaigns of ^{235}U PFG measurements using STEFF, there has been an unresolved question of loss of gamma-ray efficiency between the two experiments. PFG multiplicity measurements are performed by counting the number of gamma rays, called event fold, for each fission event, which then can be converted to multiplicity by accounting for the detector effects in a process called deconvolution. The details of deconvolution of the ILL data can be found in Ref. [20]. During the analysis of the 2015 n_ToF campaign, an excess of fold-0 events, i.e. fission events with no measured gamma rays, has been identified relative to the ILL campaign. The fold distributions of the two campaigns are shown in Fig. 6.1. The n_ToF data exhibit considerably fewer events with fold of 2 or more, and the ratio of fold-1 to fold-0 is $\approx$1.3 for ILL data, and around 1 for the n_ToF measurement. Since ILL PF1B beamline offered a considerably lower gamma-ray background and did not expose detectors to stresses such as the γ-flash characteristic to n_ToF, the difference in the fold distributions suggests that there may be effects contributing to the loss of gamma ray detection efficiency in the measurements at n_ToF. The details of the effort to identify the causes of the discrepancy are discussed in this chapter based on the data from the 2016 STEFF campaign at n_ToF, which had better statistics than the 2015 campaign due to larger target and collimator, as well as the benefit of a $LaBr_3$ crystal for reference.

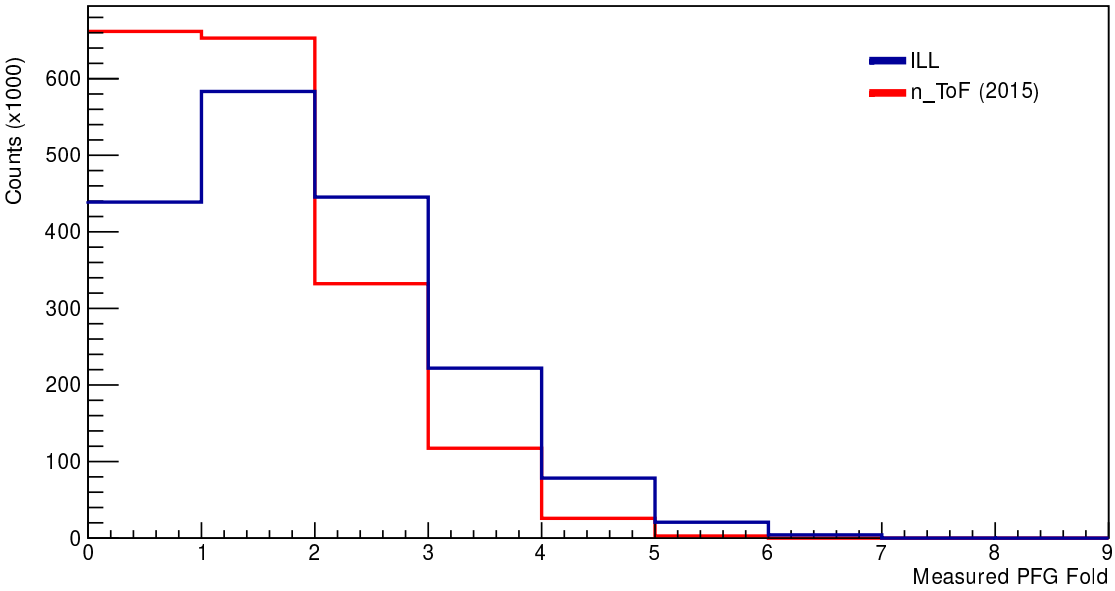

FIGURE 6.1: PFG fold distributions from the ILL (blue) and the 2015 n_ToF (red) ^{235}U PFG measurement campaigns. The data are normalized in area to ILL data.

6.2 Gamma-ray Data Time Cuts and Calibration

STEFF data from the 2016 n_ToF campaign are based on detector events cut using a wide Frisch grid-based time windows, and hence in order to extract fission gamma-ray measurement results, it is necessary to identify when the fission happened within the time window. The time of fission, $t_{fission}$, may then be used to set narrow time gates on various STEFF detectors. Fast-timing detectors were designed to be used for precise measurements of $t_{fission}$, and time distributions of START signals relative to MWPC STOP signals can be used to extrapolate FF time-of-flight backwards from the START signal to identify $t_{fission}$. Examples of such time distributions for the Bragg and Hipps arms are shown in Fig. 6.2. The signals from the various wire banks of the Bragg and Hipps MWPCs were aligned relative to Bragg anode bank 2 and Hipps anode bank 1 respectively by fitting the distributions with double or triple Gaussians (depending on the contributions from ringing) and taking time offsets based on the centroids of the light fragment peak. Table 6.1 lists the extracted time differences.

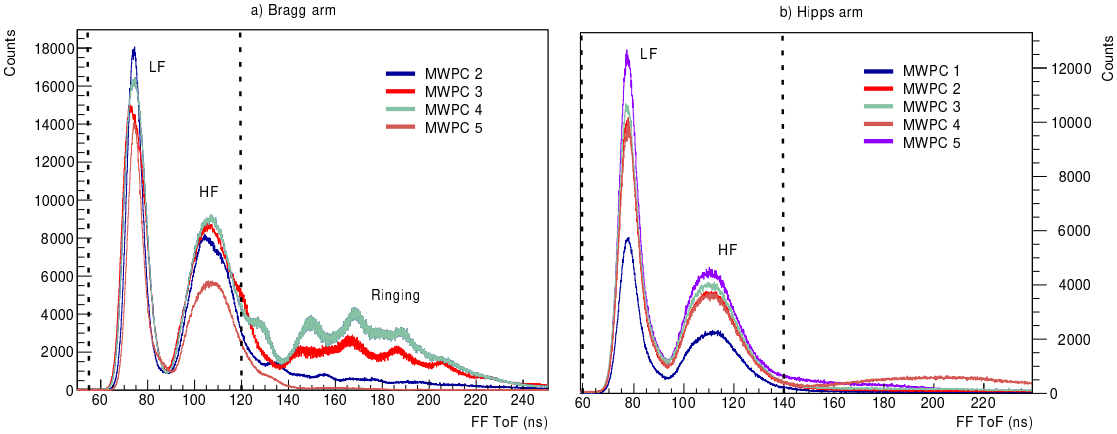

FIGURE 6.2: Spectra of differences in signal time between Bragg MWPC (left) and START, and Hipps MWPC (right) and $t_{fission}$ calculated based on the Bragg arm signals. The peaks corresponding to the light and heavy fragment groups are indicated with LF and HF respectively. Longer time-scale signals caused by electronic ringing following the main signal in some of the MWPC wire banks are also indicated. Dashed lines indicate time cuts used for gating on fission events; the time cut for the Hipps arm was only used for extracting second fragment velocity, but was not used for gamma-ray correlation.

TABLE 6.1: List of time offsets of the MWPC wire banks in Bragg and Hipps arms relative to Bragg anode bank 2 and Hipps anode bank 1.

MWPC wire bank	Time offset (ns)
Bragg MWPC3	-0.7
Bragg MWPC4	-5.3
Bragg MWPC5	-3.8
Hipps MWPC2	3.8
Hipps MWPC3	4.3
Hipps MWPC4	1.2
Hipps MWPC5	-18.7

Time cuts were chosen for the Bragg arm around the double-hump structure originating from the light and heavy fission fragments (since Hipps arm ToF calculation requires a cut on the Bragg arm in order to extract $t_{fission}$, no cuts were imposed based on the Hipps arm ToF distribution for the gamma-ray data analysis). For the Bragg arm the window was between 50 and 120 ns for the difference in START and STOP signals. Using known distance from the START foil center to the Bragg MWPC emission foil (732 mm), the velocity of the fragment was calculated. A plot of FF velocities in the two main arms is given in Fig. 6.3 (Hipps arm velocity was calculated based on Hipps STOP foil distance relative to the target center, 878 mm). The calculation of the velocity distribution was performed prior to Schmitt calibration [167], which is used to calibrate energy and timing for FF measurements. The calibration requires FF energy information, and since STEFF BD anode gainmatching has not been completed , preliminary offsets were added to FF ToF (-10 ns for the Bragg arm and -15 ns for Hipps) in order to account for

START-STOP timing differences originating from differing methods of signal formation and experimental electronics. The preliminary offsets were determined calculated based on comparison with existing ^{235}U FF velocity measurements [168]. In order to improve timing resolution of the Bragg STOP signals, all the anode pad signals within 1 ns of each other were averaged. The identified velocities were then used to calculate the time it would take the FF to travel from the center of the target to the START detector based on target center to START emission foil center distance of 152 mm, and the calculated time was then subtracted from the START signal time to obtain $t_{fission}$.

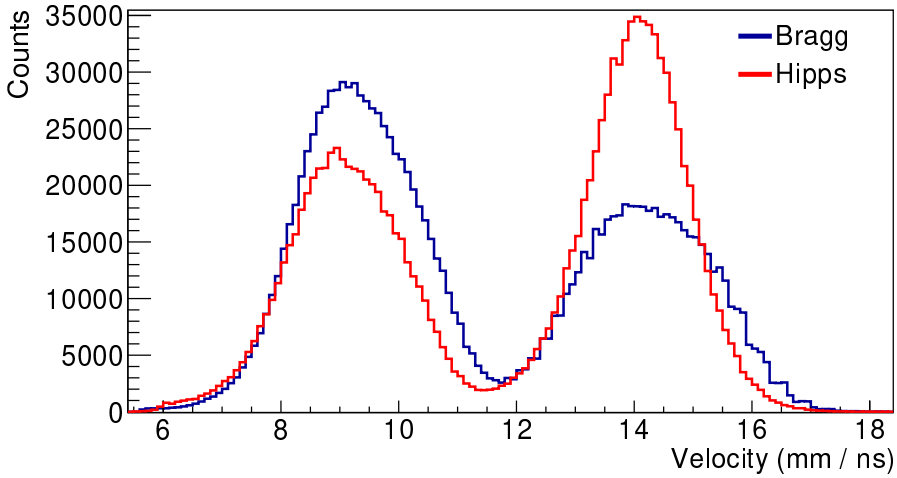

FIGURE 6.3: A distribution of FF velocities calculated by dividing the distance between STOP SEE foil and START foil by the fragment ToF. Bragg arm distribution is shown in blue and Hipps arm in red.

Scintillator signal times can be compared to $t_{fission}$ to obtain time cuts on their signals in order to separate fission gamma-rays from the majority of the background introduced into the database by the wide Frisch grid time gates. Plots of scintillator signal times relative to $t_{fission}$ show flat background with a peak originating from fission gamma-rays. The position of the fission peak in scintillator timing spectra can be used to find time offsets between individual scintillators relative to each other, which have all been normalized to NaI crystal 1. The offsets were verified using a ^{60}Co calibration source, which produces two gamma rays with 1173- and 1332-keV energies separated in time by ≈0.7 ps [169], by correlating one of the two gamma rays in all the scintillators relative to the second gamma ray in NaI 1. Time offsets were applied to the scintillator signal timing and a spectrum of $t_{fission}$ distribution summed for all the NaI crystals was produced alongside a similar spectrum for the $LaBr_3$ crystal. The two distributions are shown in Fig. 6.4, and all the individual time offsets are listed in Table 6.2.

TABLE 6.2: A list of coefficients for the quadratic energy calibration of each scintillator, as well as timing offsets relative to NaI crystal 1.

Scintillator	Quadratic coeff.	Linear coeff.	Constant coeff.	Time offset (ns)
NaI 1	0.00202	13.1	-36.1	-19.01
NaI 3	0.00302	14.6	-81.4	4.02
NaI 5	-0.00300	15.0	-73.2	-3.58
NaI 6	-0.00366	13.3	-110.3	4.43
NaI 7	-0.00038	14.7	-51.2	2.61
NaI 8	-0.00552	14.6	-123.7	3.77
NaI 9	-0.00251	12.7	-91.4	-0.73
NaI 10	-0.00448	14.1	-85.5	3.67
NaI 11	-0.00372	13.9	-106.3	8.53
NaI 12	-0.00432	13.8	-79.7	3.42
$LaBr_3$	0.00203	15.2	31.1	8.87

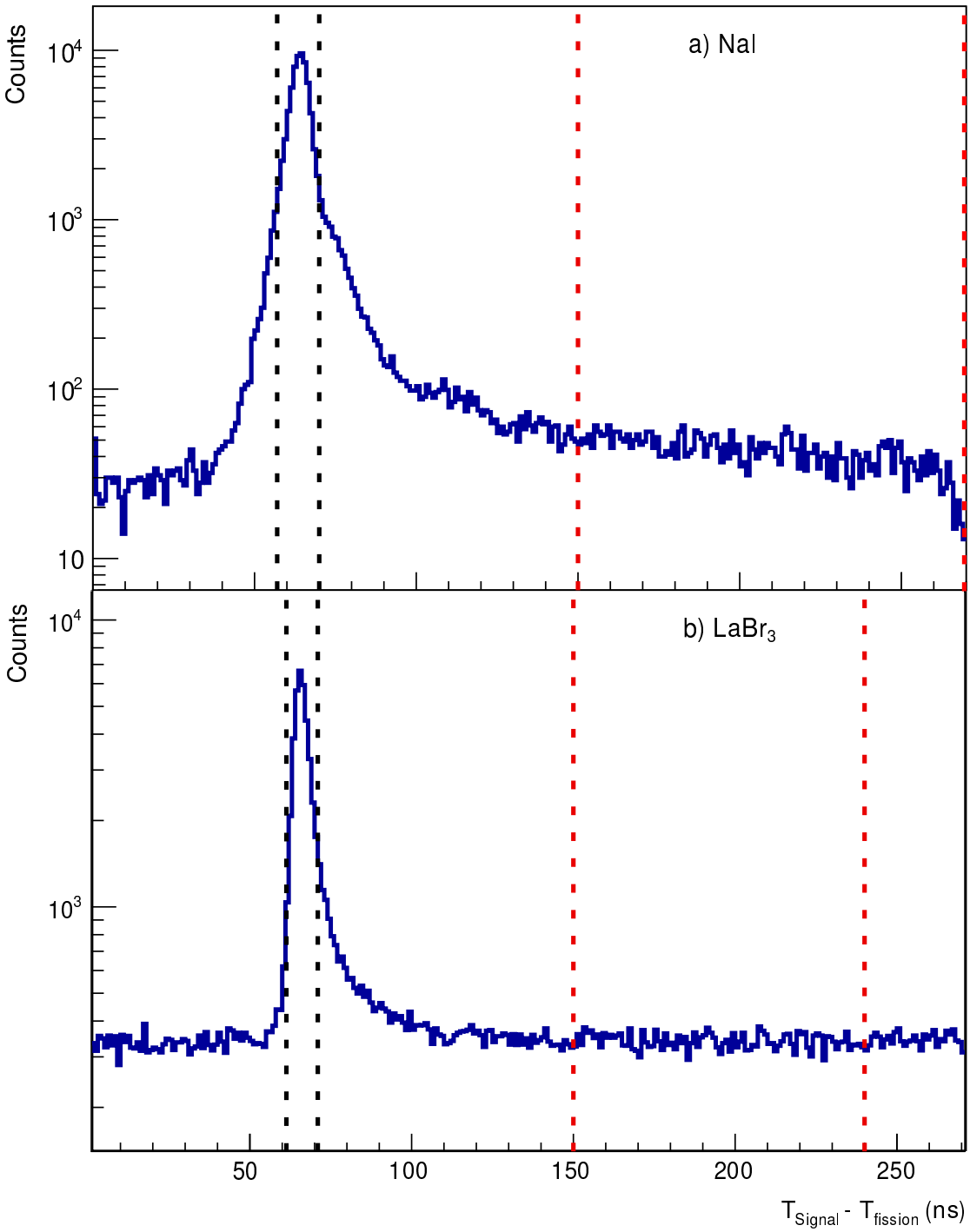

FIGURE 6.4: Time offset in nanoseconds of a) NaI signals and b) $LaBr_3$ signals relative to the time of fission. Time cuts for fission gamma-ray identification are shown in black dashed lines: 58-70 ns for NaI and 62-71 ns for $LaBr_3$, chosen to be symmetric around the peak while avoiding the prompt neutron contribution (seen as an asymmetric bump at longer time scales due to neutron speeds being lower than c). The centroid of the NaI distribution is 63.4 ns with a FWHM of 8.4 ns, and the centroid of the $LaBr_3$ distribution is 65.6 ns with a FWHM of 5.9 ns. Red dashed lines show background time cuts: 150-270 ns in NaI and 150-240 ns in $LaBr_3$. Background time cuts are ten times wider than the fission gate to allow for increased background statistics to produce average background spectra and fold distributions.

Table 6.2 also shows coefficients for the energy calibration of each scintillator crystal. The calibrations were performed using ^{60}Co, ^{137}Cs, ^{88}Y and ^{241}Am^{9}Be sources. Since the calibration sources cover a large energy range (661 to 4438 keV), a quadratic calibration fit was used, although it can be seen from Table 6.2, that the quadratic coefficients were always small. A typical calibration plot exemplified by NaI crystal 1 is shown in Fig. 6.5.

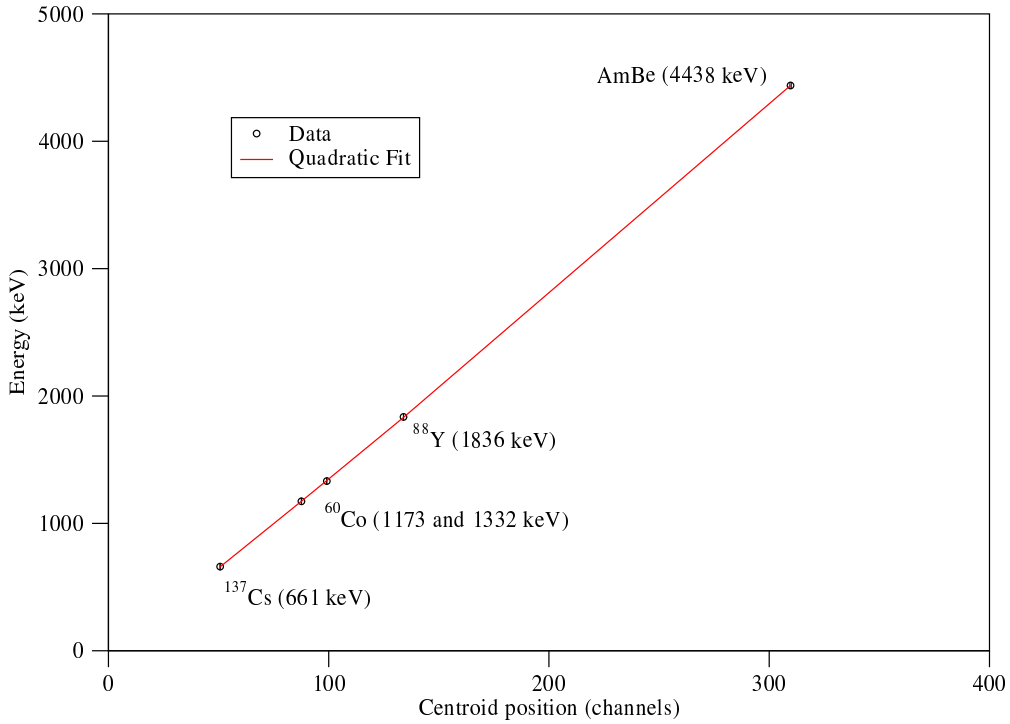

FIGURE 6.5: Energy calibration of NaI crystal 1 showing gamma-ray energies plotted against photopeak centroids. Red line shows quadratic fit used to relate channels in the scintillator spectra to the incident gamma-ray energies.

A further time cut was imposed on the data during the analysis based on the Master trigger times. Time differences between consecutive Master signals in the thermal energy region were calculated to ensure there was only one signal per fission event to avoid introducing gamma-ray events from the same fission more than once into the analysis. Since fission events are independent of one another, i.e. a nucleus undergoing fission does not influence the probability of other nuclei in the target undergoing fission, fission probability should follow Poisson statistics, which means that the probability of a fission event occurring in a certain interval after the previous event should follow exponential decay. The Poisson distribution expectation is approximate when applied to fission distribution at n_ToF, since fission rate is not constant due to change in flux and energy of neutrons, however the approximation can be made over short time scales. Fig. 6.6 shows a plot of the calculated time differences, which indeed do follow exponential decay as shown in the inset. However, structures at short time scales are evident and imply

that there is some correlation between the events written into the database. The double-peak structure at ≈4 μs was attributed to double-triggering from the two main arms of STEFF. While the time-of-flight differences of the FF in the two arms should be on the order of 10 ns, the signal formation time differences in the Frisch grids (the source of Master triggers) will be of the order of a microsecond, due to different ranges of the two fragments and the slow electron cloud drift, resulting in considerable difference in signal CFD crossing times in the two arms. A third peak-like structure is also visible in Fig. 6.6 at ≈5 μs, attributed to discriminator double-triggering in the Master trigger electronics. Since Frisch grid signals are bipolar (due to electron cloud first inducing signal on one side of the grid, then drifting past the wires and inducing signal on the other side of the grid), the discriminator may be triggered by the rising edge of the Frisch grid signal as expected, and then get triggered again by the rising edge of the preamplifier decay following the change in polarity of the incoming signal. The contribution to the fission events considered during the analysis by such fictitious triggers was avoided by imposing a 14 μs dead time in Master triggers and resulting in rejection of ≈17% of the Master triggers.

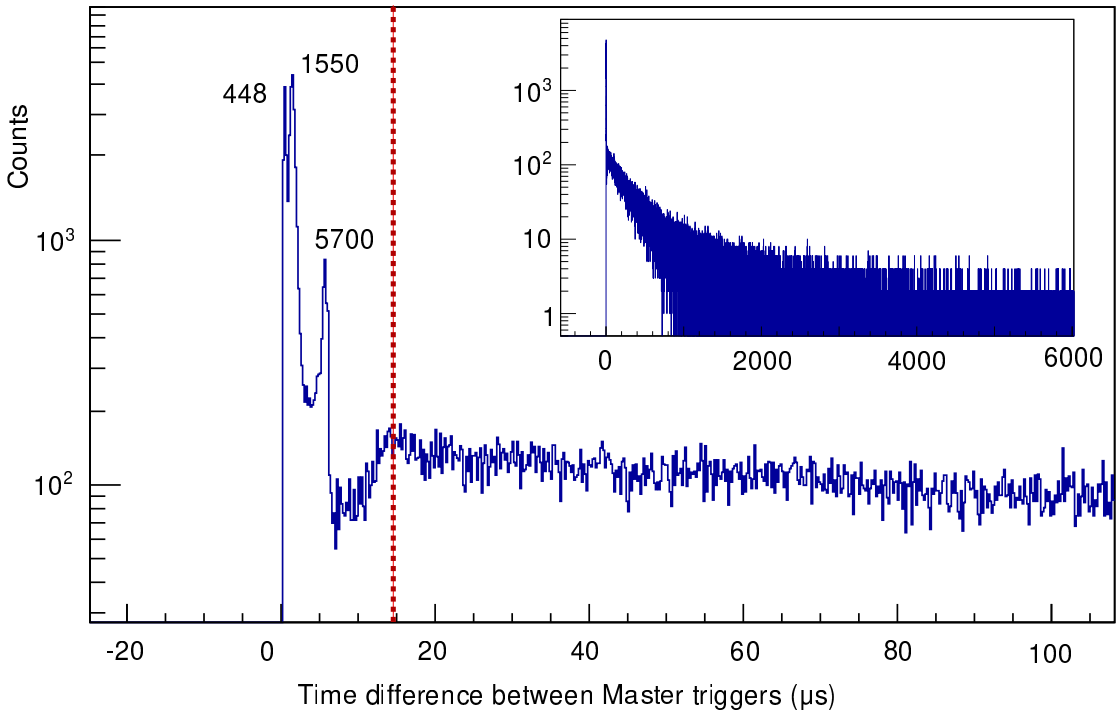

FIGURE 6.6: Calculated time differences between consecutive Master triggers in microseconds (only triggers corresponding to events at neutron energies below 1 eV were included). The inset shows a large time scale of 6000 μs and the main plot shows expanded view of the shorter timescales of <100μs. Several structures are evident at time differences shorter than ≈14 μs and their centroids are indicated. The events associated with these structures were removed from the analysis by imposing a dead time of 14 μs, shown as a dashed red line.

6.3 Scintillator Gain Effects

Verifying scintillator stability and quantifying any gain fluctuations is crucial in analysing gamma-ray data spanning the whole STEFF campaign. The background gamma rate at the n_ToF Facility is high, in particular in the region of the γ-flash as well as around thermal neutron energies, and many scintillator PMTs are known to saturate in such environment, resulting in extended periods of dead time. A series of measurements have been performed using one of the STEFF NaI detectors prior to the 2015 campaign on samples of ^{197}Au in order to characterize the behaviour of the detectors in EAR2. ^{197}Au has a known resonance at 4.9 eV with (n,γ) cross-section of $\approx$27,000 barn [11]. Therefore, when neutrons at that energy are absorbed, a large increase in gamma-ray flux is expected in the scintillators around the target. By using two samples, a thin and a thick one (with diameters of 20 and 10 mm, and thicknesses of 0.1 and 1 mm respectively), changes in NaI response could be observed at the resonance for an increase in count rate produced by the thick target compared to the thin one. The top panel of Fig. 6.7 shows the resulting counts as a function of incident neutron energy. At lower count rates associated with the thin sample, the plot clearly shows a sharp resonance peak, however detector suppression is evident in the thick sample results, where instead of a resonance peak, the detector measured counts show a trough. The bottom panel of the plot shows count rate in that neutron energy region for the thick sample, and the drastic reduction in counting efficiency after count rates of >1 MHz is evident.

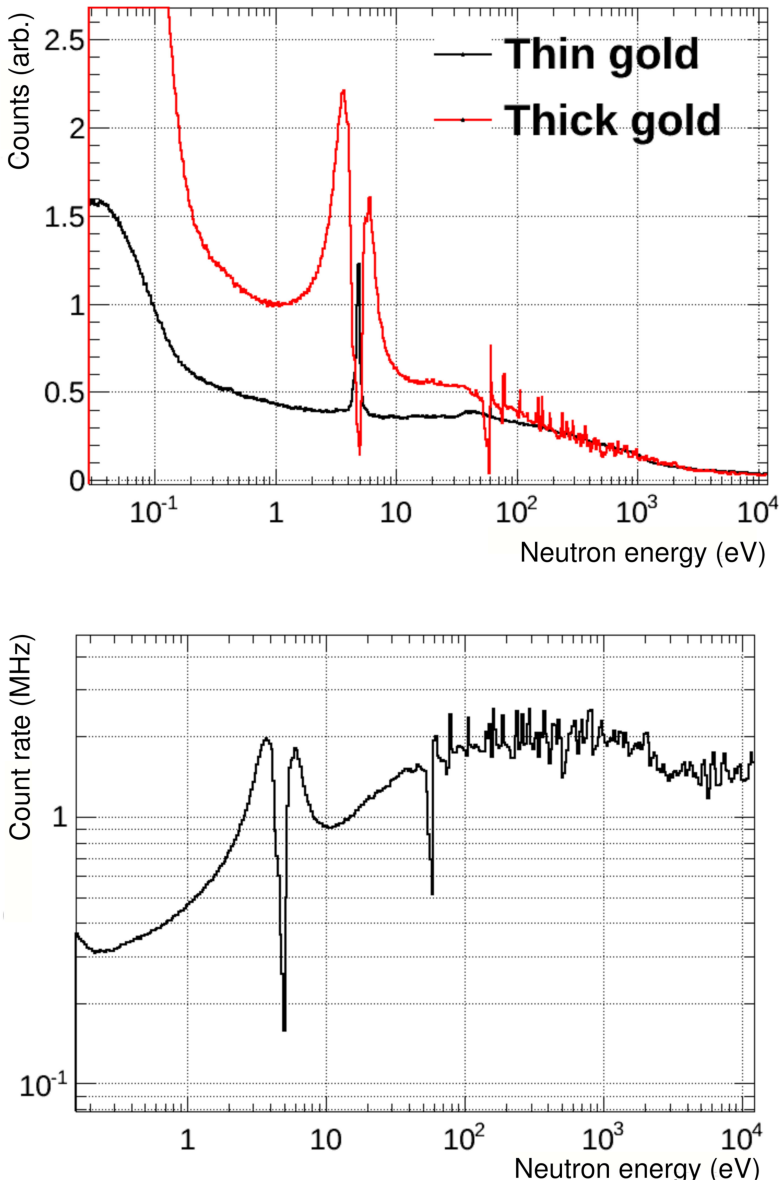

FIGURE 6.7: Top panel: comparison of gamma-ray counts as a function of incident neutron energy for the thin (black) and thick (red) ^{197}Au samples. The detector saturation effects are evident at the 4.9 eV resonance in the thick sample data. Bottom panel: count rate as a function of incident neutron energy for the thick sample. This panel also shows reduced counting efficiency at the 4.9 eV resonance.

A full description of count rate effect characterization during the 2015 campaign can be found in Ref. [21]. An important result of the gold test was the identification of saturation effects at ≈1 MHz rates and subsequent modification of the PMTs in the NaI scintillators used on STEFF (also detailed in Ref. [21]). The modifications were performed by the manufacturer and resulted in restoration of the sharp resonance peak for the thick gold sample. Note, that $LaBr_3$ scintillators have also been modified prior to being loaned to the STEFF team. In the case of $LaBr_3$, the modifications constituted the outer glass container of the PMT being given an 'HA treatment', whereby the glass

cover around the photocathode is covered in insulating black paint preventing leakage signal from forming between the cathode and the grounded glass [170].

A further investigation into the count rate effects was conducted after the PMT modifications using a ^{22}Na source by varying the distance between the source and the scintillators and observing the drift of the photopeak position [21]. The results of the investigation are shown in Fig. 6.8, demonstrating increase in gain with increase in count rate. During the testing of the NaI crystal, it was also determined similarly to the results obtained from gold, that the crystal becomes saturated at around 1 MHz rates, and the gain reduces sharply, causing the photopeaks to become indistinguishable. The $LaBr_3$ crystal, on the other hand, shows steady increase in gain at rates up to 1.4 MHz.

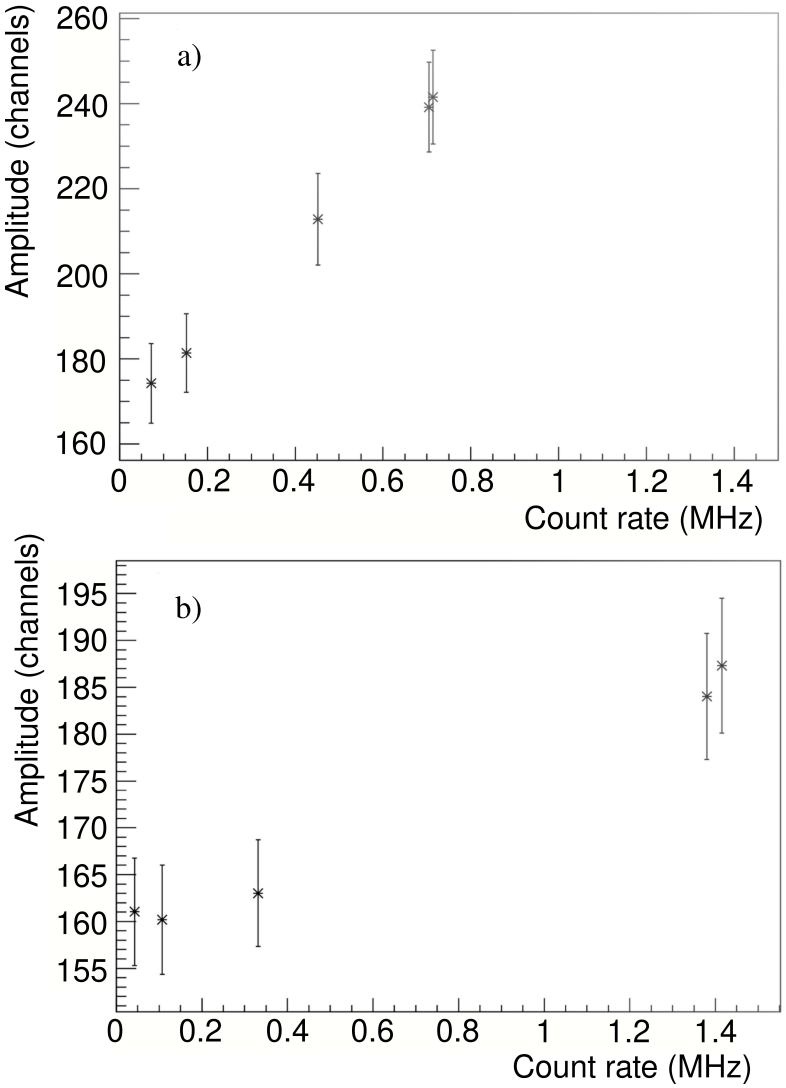

FIGURE 6.8: Change in ^{22}Na 1275-keV gamma-ray photopeak position at varying count rates based on the source proximity to a) NaI and b) $LaBr_3$ scintillator.

Indeed, the effect of increasing count rate resulting in the PMT gain increase followed by a decrease is known although not fully understood [171]. Fig. 6.9 shows the effect in

qualitative terms. The reductive effect can be explained by space charge accumulation [90], whereby incident light deposited into the photomultiplier at a high rate produces electrons, while the electron cloud associated with the previous light pulse is still inside the volume of the PMT. This results in the anode 'seeing' less of the new pulse's charge, as it is obscured by the previous pulse. Rosen and Chromey [171] discuss in detail the effects of PMT fatigue, which may also result in similar gain variations, although fatigue is typically a cumulative effect over long periods of PMT operation. Fatigue is not very well understood [171], however a number of explanations have been proposed, including ejection of material from the dynodes by incident electrons [172], charging up of the insulators between the dynodes [173], oxidation-induced Malter effect (formation of positive charge on the dynode surface following electron ejection, and resulting in electrons being pulled to the surface from the interior of the dynode) [174], or oxidation of dynodes resulting trapping of ejected electrons [175].

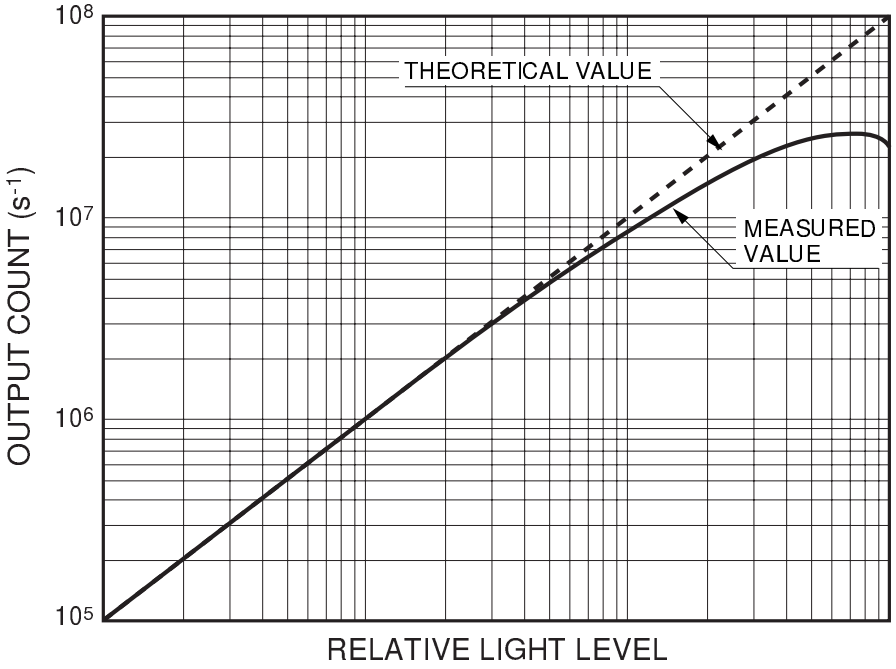

FIGURE 6.9: A qualitative demonstration of decrease in counting efficiency of a PMT for large quantities of incident light due to reduction in gain at particularly high count rates. Figure adapted from [170].

A further consideration concerning STEFF scintillator gain lies with the detector 'history effect' associated with the γ-flash. PMTs are known to exhibit light hysteresis [170], an effect whereby the incident light is changed in a drastic manner, resulting in a rapid change of anode current, producing a non-linear gain change of the PMT to incident radiation. Fig. 6.10 shows a qualitative representation of the effect. For the detectors operating at n_ToF, the γ-flash constitutes a large step-like increase in gamma rays incident on the detectors, resulting in large bursts of light in the PMTs, as shown in Fig. 5.6. The subsequent saturation of the detectors and light hysteresis require

long signal recovery times, which may extend into the neutron time-of-flight regions of low background gamma count rate. For this reason, it is important to consider post-gamma flash time when investigating scintillator performance at n_ToF, and not simply instantaneous count rate.

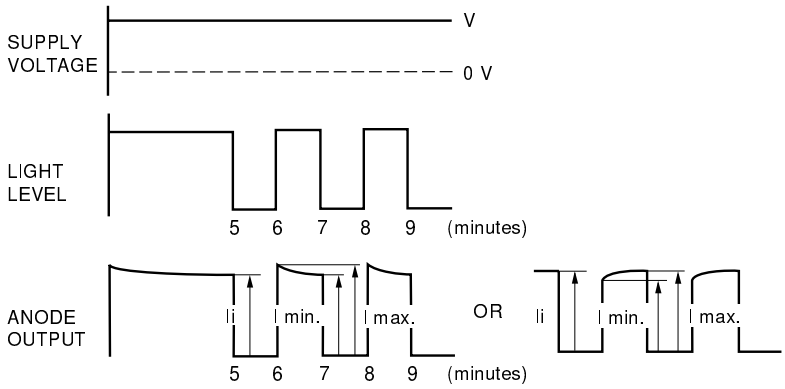

FIGURE 6.10: A qualitative description of light hysteresis effect in PMT. The top panel shows constant voltage applied to the PMT set to some value V. In the second panel, light input into the PMT is shown, varying in a step-like way every minute, which results in step pulses in the anode output in the bottom panel. Note the shape of the anode output current, which may show under- or overshoots, called 'light hysteresis'. The effect is shown here on the scale of minutes, and it is unclear whether it will be present and to what extent on the millisecond scales of the neutron pulses. Figure adapted from [170].

6.4 Quantifying the NaI Gain Variations

Fig. 6.11 shows NaI signal PSA fitting quality reduction for shorter neutron time-of-flight regions for a dedicated proton bunch by comparing fits in regions of increasing count rate (the count rate is approximately 200 kHz for the top panel and approximately 1 MHz for the bottom panel). Fig. 6.12 shows measured count rate as a function of neutron ToF in both NaI and $LaBr_3$ scintillators for dedicated and parasitic bunches. The details on how to convert between the neutron time-of-flight and energy for n_ToF experiments in EAR2 can be found in Ref. [157] (note that the flightpath length for the calculation used for this work is 19.85 m found by observing the resonances in the START detector rates and matching them to the known neutron resonance energies, specifically 1.14, 11.7 and 19.3 eV, as well as matching the position of the EAR2 flux maximum at ≈40 meV). It is evident from the two figures, that as count rates get higher, the PSA fits struggle to reproduce the spectrum due to pile-up, which results in uncertainty in baseline estimation. In the bottom panel one can clearly see signal pile-up (e.g. at 7346×10^3 ns), where pulses become hard to resolve even by eye.

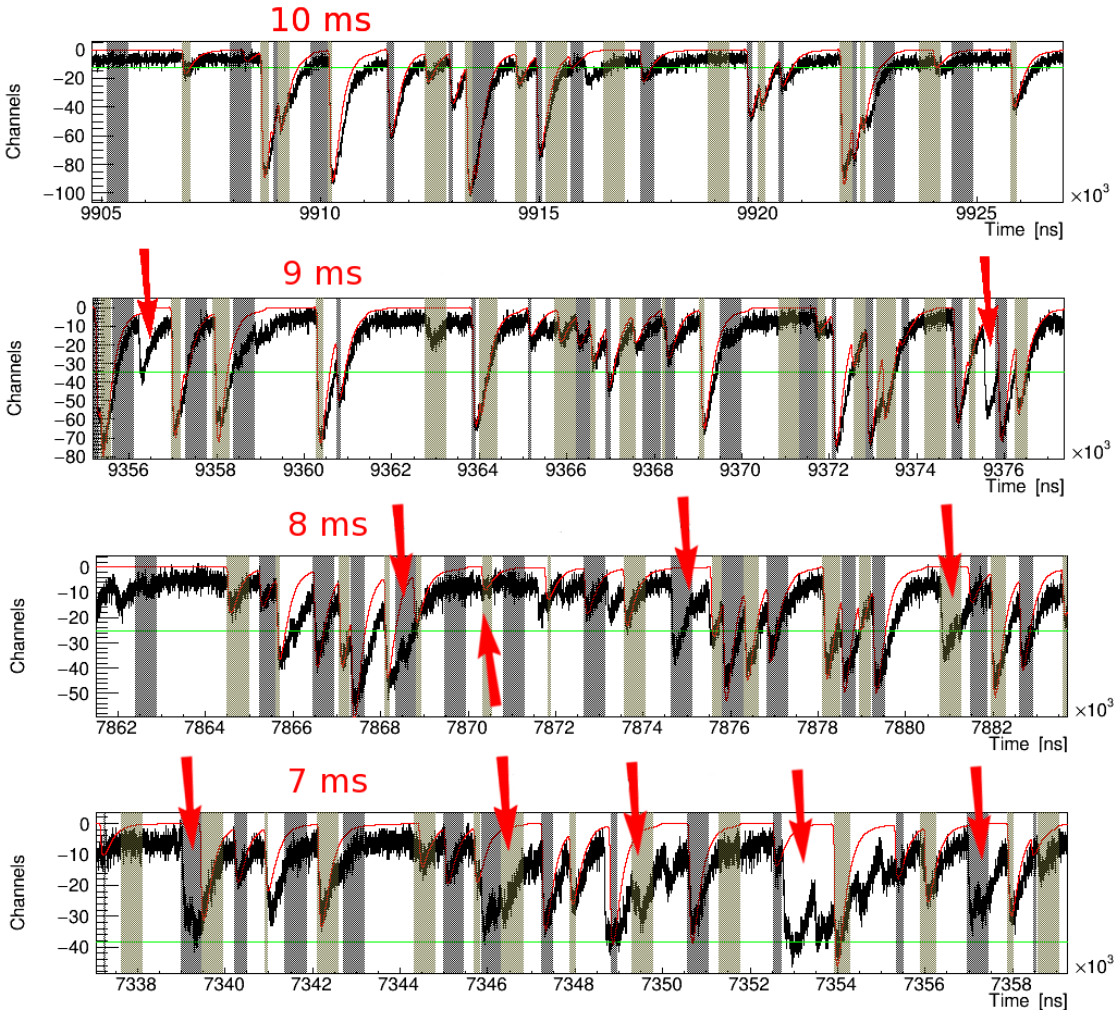

FIGURE 6.11: Signals fitted by PSA routine originating from NaI crystal 8 at varying neutron time-of-flight timescales: 10, 9, 8 and 7 ms (top to bottom), corresponding to neutron energies of approximately 0.02, 0.025, 0.03 and 0.04 eV respectively. Black line shows signal with zeroed baseline, red line shows fit, and green line shows amplitude threshold. Horizontal axis shows the timescale and vertical axis is signal amplitude. Red arrows indicate instances where PSA routine failed to accurately reproduce the signal. It is evident that in lower neutron time-of-flight regions the fitting gets progressively less reliable.

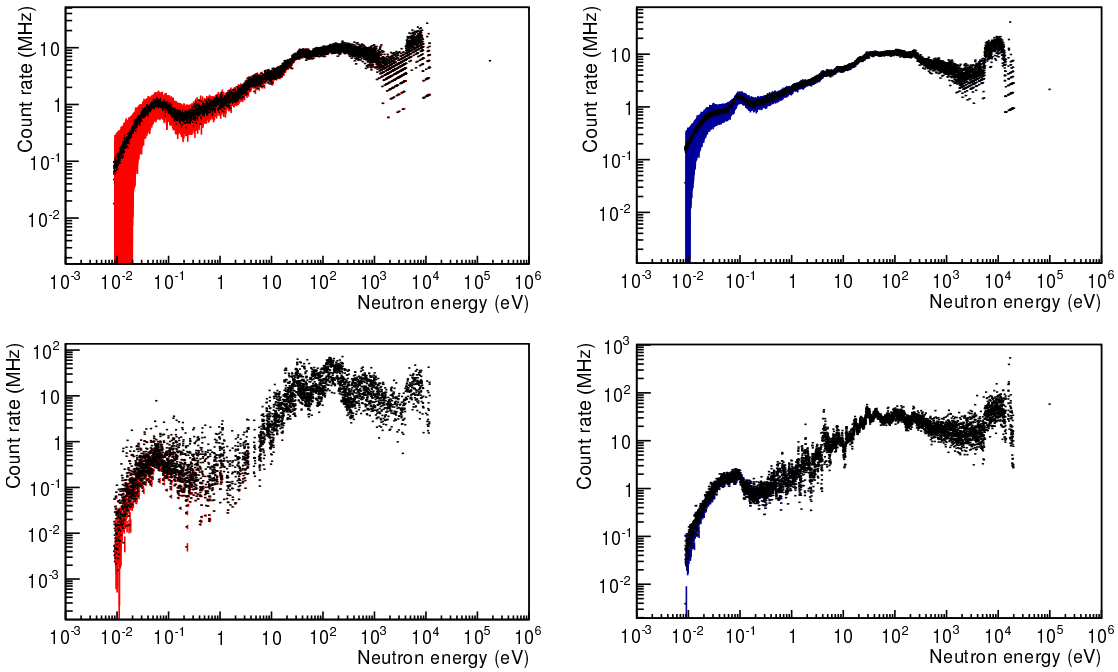

FIGURE 6.12: Estimated count rates in NaI crystal 1 (top two panels) and $LaBr_3$ (bottom two panels) for dedicated (blue error bars) and parasitic (red error bars) bunches. Note the two regions where count rates exceed 1 MHz: γ-flash region and at near-thermal energies (0.04-0.06 eV depending on pulse type). In these regions stated count rates are approximate due to signal saturation resulting in difficulty of estimating real count rates. All the count rates except for the $LaBr_3$ dedicated pulse one were calculated for STEFF runs without the uranium target and with no Master triggering. The $LaBr_3$ dedicated count rate was calculated by multiplying the parasitic count rates for each neutron energy bin by the ratio of dedicated-to-parasitic count rates in NaI scintillator 1.

Due to the fitting quality deterioration, the γ-ray data analysis was restricted to regions of 10^7 ns in neutron time-of-flight or greater for sodium iodides. No complications in fitting were observed for $LaBr_3$ signals around the thermal and epithermal regions, and therefore the cut-off for analysis of $LaBr_3$ signals was set at 1 eV neutron energy ($\approx$1.5 ms neutron time-of-flight), just before the ^{235}U resonance at $\approx$1.14 eV [11]. Fission in the resonance region is likely to originate from different nuclear states populated by the neutron compared to thermal/epithermal energies, which may result in different γ-ray spectra, and therefore data corresponding to the neutron resonances were not mixed with the analysis of the thermal/epithermal fission data.

In order to investigate gain variation further, matrices were produced for each bunch type and each of the 12 scintillators. The matrices contained rows corresponding to neutron time-of-flight binned in 12 μs bins and columns containing gamma-ray energy spectra (separate matrices were produced for fission-gated spectra and for background-gated spectra). These matrices could be used to perform background-subtraction gated on gamma-ray spectra at specific neutron energies and thus examine the evolution of fission spectrum as a function of neutron energy and pulse type (thus making it effectively a function of count rate) for both scintillator types. A visualization of one such matrix is shown in Fig. 6.13 for NaI crystal 1 background-subtracted gamma-ray spectra in the neutron time-of-flight region of 10-28 ms. Examples of spectral shape differences at different neutron times-of-flight are given in Fig. 6.14, comparing gamma-ray spectra for NaI at 10 and 28 ms and for $LaBr_3$ at 10 and 20.8 ms (higher ToF regions were not used for $LaBr_3$ due to low statistics).

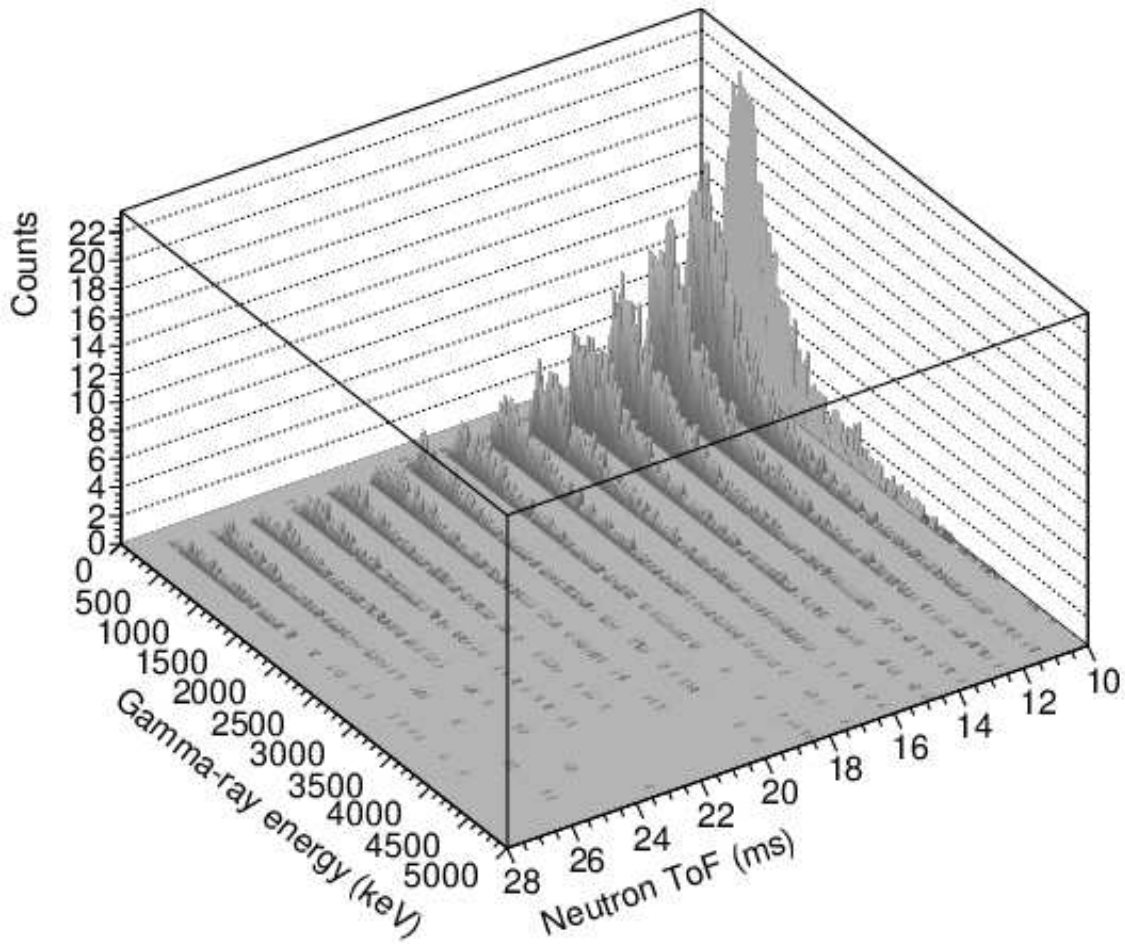

FIGURE 6.13: An example of a matrix of background-subtracted NaI scintillator 1 gamma-ray spectra for various neutron ToF gates. The spectra show reduction in count rate at higher neutron ToF and are useful for examining the evolution of the spectral shape for gain variation.

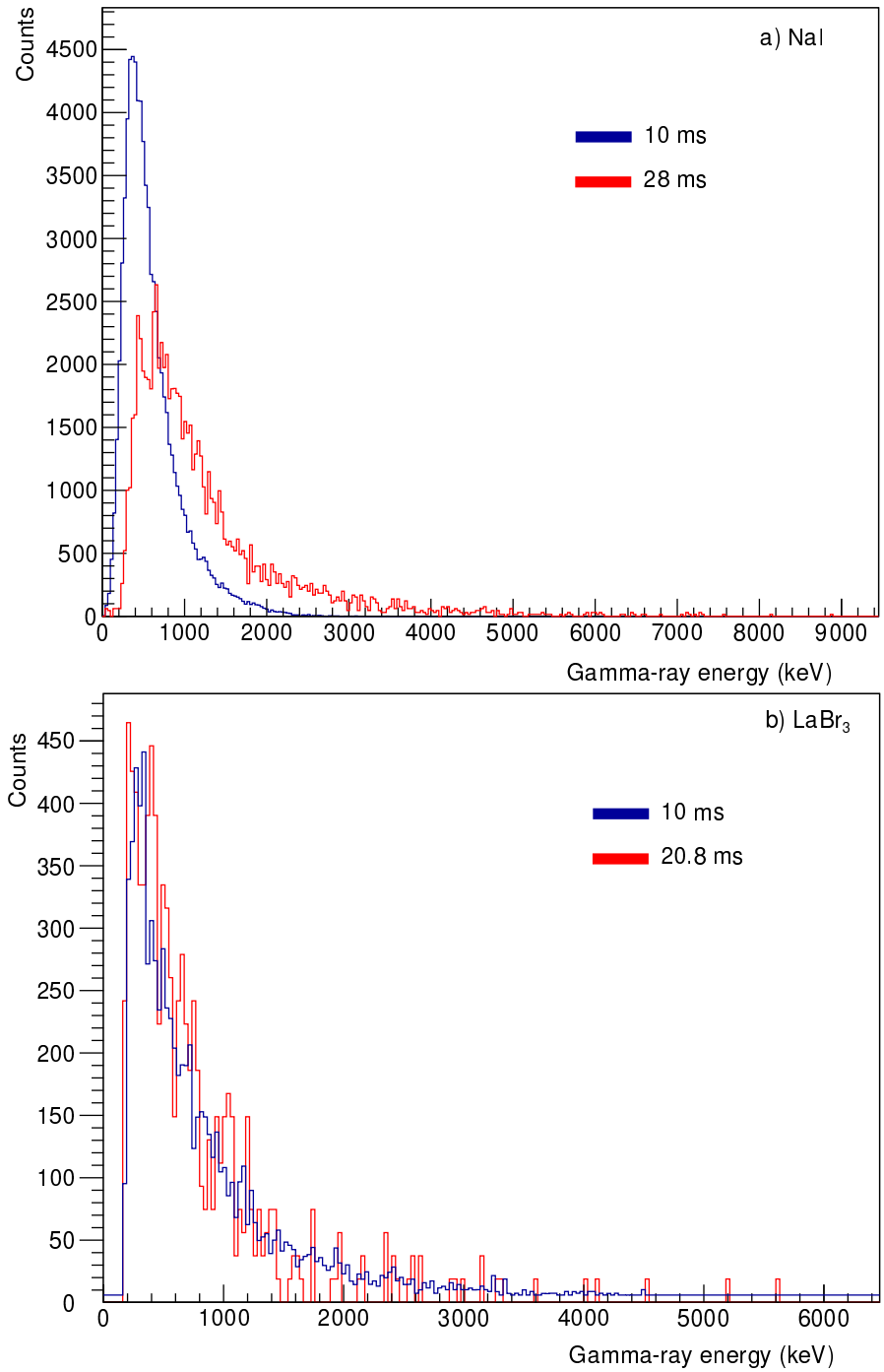

FIGURE 6.14: Comparison of gamma-ray spectral shape for a) NaI at 10 ms (blue) and 28 ms (red) neutron time-of-flight and b) $LaBr_3$ at 10 (blue) and 20.8 ms (red) neutron time-of-flight. The NaI spectra show a clear difference, whereas the $LaBr_3$ data are in reasonable agreement. The spectra are normalized in area to the 10 ms data for each crystal type.

Fission gamma-ray spectra feature gamma-rays originating from a large range of nuclei in different populated states and contain a large contribution from statistical E1 transitions. For these reasons along with the relatively poor NaI energy resolution, NaI PFG spectra discussed in this work do not feature any distinct peaks (as can be seen in Fig. 6.14), the change in the position of which would facilitate gain change investigation. Instead, fission gamma-ray spectra are effectively continuous, and the lack of any peaks masks gain effects. The shape of the spectrum, however, is expected to be the same across the thermal and epithermal range, based on the assumption that sub-electronvolt changes in energy will not have a substantial effect on the populated fission states. Thus the shape of the spectrum itself can be used as a monitor of gain, and can be analyzed as a function of neutron ToF. $LaBr_3$ spectra appear to be very similar for the two ToF cuts presented above, but the NaI spectra show major difference in shape, whereby the energies appear compressed at lower ToF values, suggesting gain drift. As part of STEFF scintillator gain investigation, two useful spectral shape parameters were identified and investigated based on the gamma-ray data. These parameters are root-mean-squared value of gamma-ray energy above the peak (henceforth RMS) and half-width half-maximum of the distribution (henceforth $HWHM$). A typical spectrum demonstrating the method of extraction of these parameters is shown in Fig. 6.15.

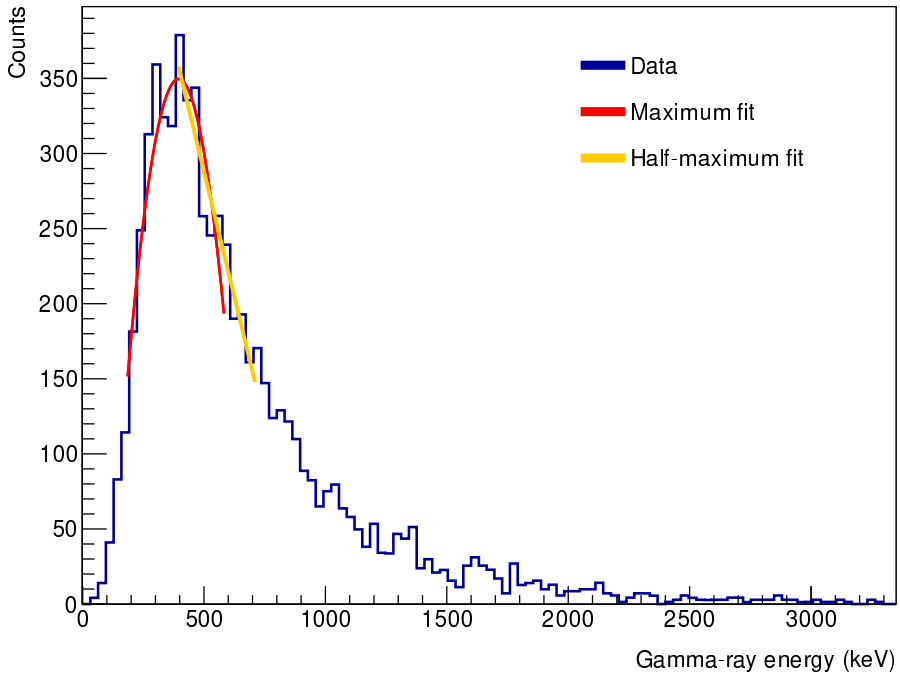

FIGURE 6.15: An example of a gamma-ray spectrum originating from NaI crystal 9 for neutron times-of-flight between 12.4 and 13.6 μs for dedicated bunches. The red line shows a parabolic fit for extracting the energy at which the maximum of the distribution occurs, and the yellow line shows the linear fit around the position of the half-maximum. Half-maximum position is estimated based on parabolic fit to the maximum and the final $HWHM$ value is extracted from fitting. These two fits are used to extract spectral features used to characterize the distribution.

The peak of the distribution is fitted with a parabola (in red) to identify the maximum spectral amplitude and the energy at which the maximum occurs E_{max}, which is then used for the calculation of the two aforementioned parameters. RMS can be calculated as

$$RMS = \sqrt{\frac{\sum\limits_{E>E_{max}} N_E(E - E_{max})^2}{N}}, \tag{6.1}$$

where E is the gamma-ray energy of a given energy bin, N_E is the number of events in bin E, and N is the total number of gamma-rays with energy greater than E_{max} in the spectrum.

$HWHM$ is a simpler parameter to express, as it is simply the difference between the energy corresponding to the half-maximum of the distribution (on the high-energy side of the peak) found from the linear fit and E_{max} found from the parabolic fit. The two parameters are useful in different ways: RMS is more sensitive to high energy tail of the distribution, and therefore describes how high in energy the spectrum goes, while $HWHM$ is the width of the distribution, describing how quickly the energy of the measured gamma rays 'drops off'.

All the collected spectra for all the neutron time-of-flight regions of interest were fitted, and the two parameters were calculated. The spectra were summed for all the sodium iodides to improve statistics. The average value of each of the two fitted parameters for each pulse and crystal type was found for neutron times-of-flight greater than 20 ms, and the ratios of the parameter values for each neutron energy bin to the average were plotted. The resulting distribution of RMS and $HWHM$ values is shown in Fig. 6.16, where they are grouped by bunch and crystal type, and Fig. 6.17, where they are grouped by fitted parameter and crystal type.

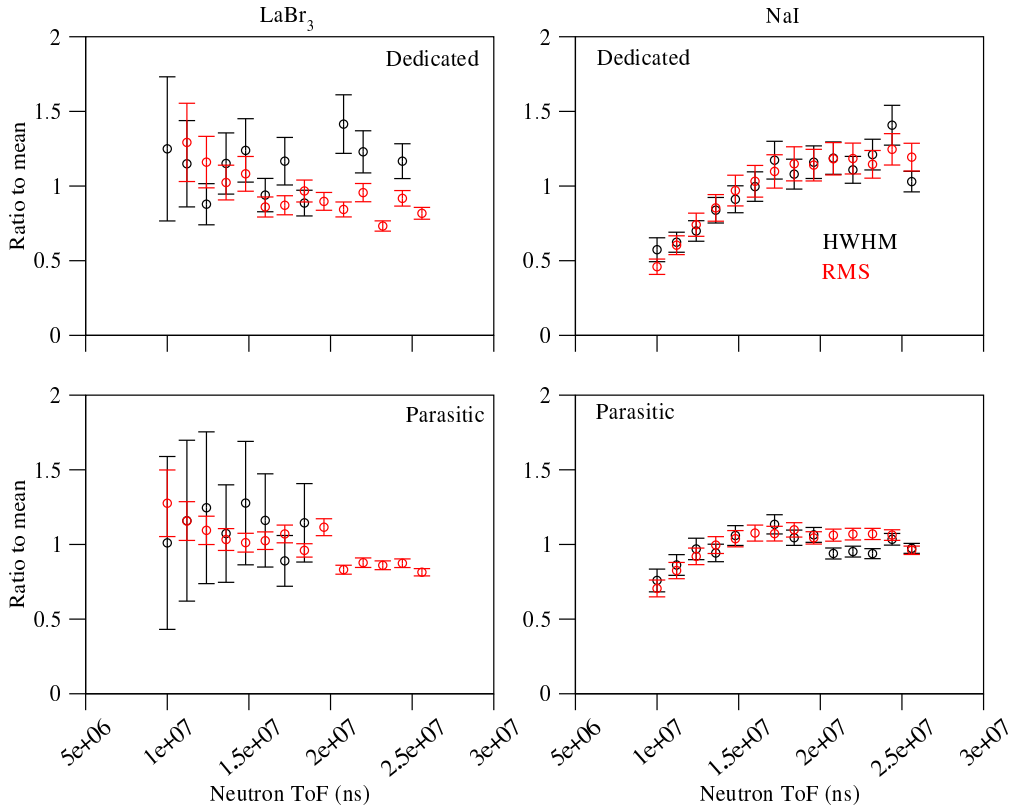

FIGURE 6.16: A plot of the $HWHM$ (black) and RMS (red) fitted parameters grouped by crystal and bunch type as a function of neutron time-of-flight for comparison of the parameter variation.

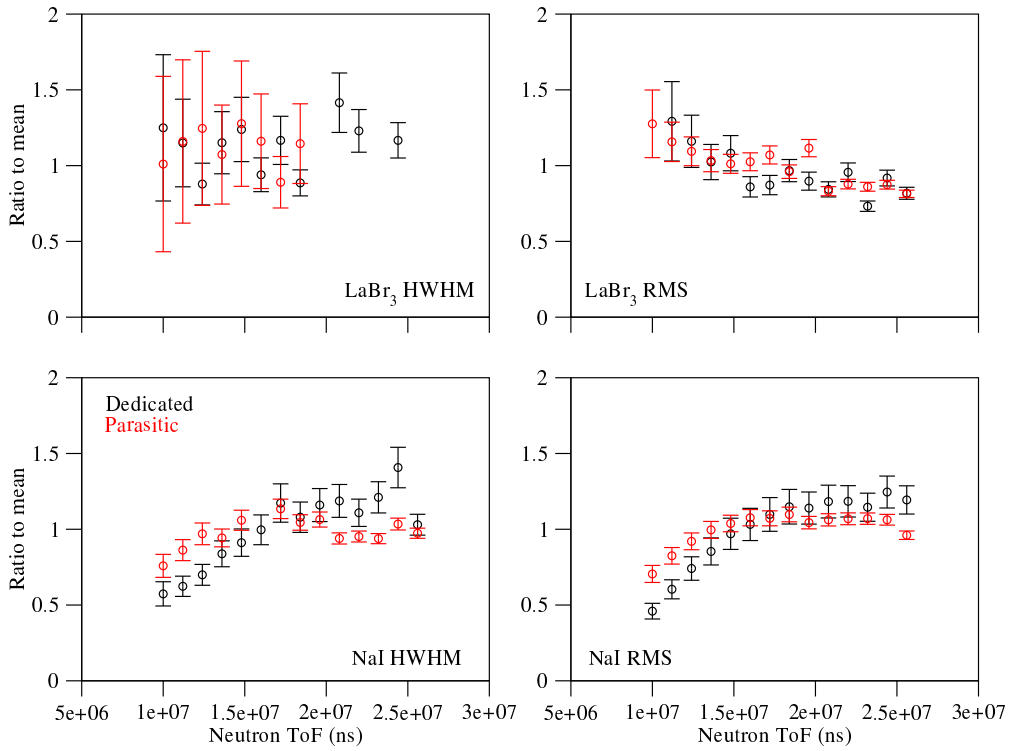

FIGURE 6.17: A plot of the $HWHM$ and RMS fitted parameters grouped by crystal and parameter type as a function of neutron time-of-flight for comparison of differences in bunches (and therefore count rates). Dedicated bunches are shown in back and parasitic in red.

The uncertainties on the RMS results were calculated using Eqn. 6.2 and the uncertainties on the $HWHM$ values were calculated using Eqn. 6.5. The RMS uncertainty is the more complicated one and can be expressed as

$$\frac{\sigma_{RMS}}{RMS} = \sqrt{\left(\frac{\sigma_{num}}{num}\right)^2 + \left(\frac{\sigma_{den}}{den}\right)^2}, \tag{6.2}$$

where σ_{num} is the numerator (num) uncertainty and σ_{den} is the denominator (den) uncertainty, and the numerator and denominator refer to the contents of the square root in Eqn. 6.1. The denominator uncertainty is simply the uncertainty in N, and can be expressed as $^{E_{max}}/_{N}$. The uncertainty in the numerator is composed of two parts: the uncertainty due to N_E and the uncertainty in the fitting of E_{max}. The two components can be written as

$$\sigma_{N_E} = \sum_{E>E_{max}} \frac{(E - E_{max})^2}{N_E} \tag{6.3}$$

and

$$\sigma_{E_{max}} = \sum_{E>E_{max}} (2N_E(E_{max} - E)). \tag{6.4}$$

The components of the final RMS uncertainty are covariant. For example, if due to the uncertainty in the fit the peak position was identified lower by one energy bin than the 'true' position, the iterative procedure that sums all the bins above the maximum will be missing a bin. Such covariances have not been accounted for in the formulae given above.

The uncertainty on $HWHM$ can be calculated as

$$\frac{\sigma_{HWHM}}{HWHM} = \sqrt{\left(\frac{\sigma_{E_{half}}}{E_{half}}\right)^2 + \left(\frac{\sigma_{E_{max}}}{E_{max}}\right)^2}, \tag{6.5}$$

where E_{half} is the energy at the half-maximum position in the spectrum and $\sigma_{E_{half}}$ is the uncertainty in identifying the energy. E_{max} uncertainty is calculated the same way as in the equation 6.4, while $\sigma_{E_{half}}$, can be calculated as

$$\sigma_{E_{half}} = E_{half}\frac{\sigma_m}{m}, \tag{6.6}$$

where m is the slope of the linear fit and σ_m is the fit uncertainty for the slope calculated by ROOT.

Similarly to RMS, the uncertainty in $HWHM$ contains covariant quantities. Namely, change in the estimate of E_{max} will result in shifting of the fitting window for the linear fit used to identify E_{half}, which will change the fit and subsequently m.

6.5 NaI Gain Correction Results

The scaling of the extracted $HWHM$ and RMS by the average value of each respective parameter for neutron times-of-flight greater than 20 ms, where the parameters exhibit little variation, was done in order to produce a fractional correction parameter for the spectral shape as a function of neutron time-of-flight. Each of the two parameters was fitted with a function of the form

$$f(ToF) = 1 - e^{A - B \times ToF}, \tag{6.7}$$

where A and B are fitted parameters. In the case of the parasitic $HWHM$ parameter, the first constant (1) also had to be set as a fitted coefficient for the ROOT fitting routine to converge. The results of the fits are shown in Fig. 6.18 and the resulting coefficients and reduced chi-squared values are tabulated in Table 6.3. Since at higher neutron energies gamma-ray spectra show compression, the extracted functions from the fits are used to correct signal amplitude based on ToF, resulting in a greater amplitude at lower ToF, where the count rates are higher. The energy of a gamma ray that could be distinguished from background by PSA routine settings used for STEFF analysis is ≈150 keV. This threshold value is then increased by the correction, and the resulting minimal energies for different corrections are also tabulated alongside the fit parameters. The increase in gamma-ray energy threshold means that the final NaI spectra do not feature the maximum of the PFG energy distribution, which has previously been measured in the 100-200 keV range [14].

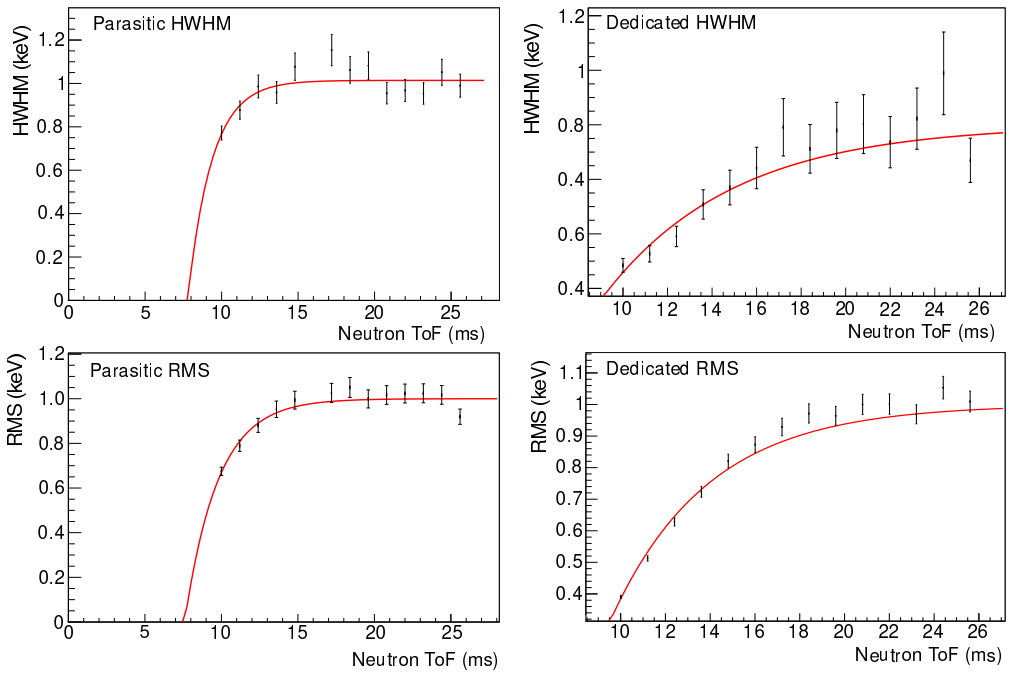

FIGURE 6.18: A plot of the evolution of the spectral $HWHM$ and RMS fitted parameters as a function of neutron time-of-flight. The fits to the trace (black) are shown in red. Green line shows minimal amplitude cut-off.

TABLE 6.3: Fitted parameter, gamma-ray energy thresholds and reduced chi-squared values for the $HWHM$ and RMS fits.

Fit type	A	B (ns^{-1})	$\chi^2_{red.}$	Minimal γ-ray energy (keV)	Notes
Parasitic $HWHM$	5.0±3.0	(-6.4±2.9)×10^{-7}	1.12	200	First coeff: 1.01±0.02
Dedicated $HWHM$	1.09±0.24	(-1.71±0.22)×10^{-7}	1.09	330	-
Parasitic RMS	3.50±0.68	(-4.60±0.66)×10^{-7}	0.96	230	-
Dedicated RMS	1.82±0.08	(-2.30±0.08)×10^{-7}	2.7	400	-

A comparison of the corrected background-subtracted NaI gamma spectra along with the uncorrected spectra are shown in Fig. 6.19 and Fig. 6.20 for the parasitic and dedicated pulses respectively. Both correction parameters have produced visibly more consistent spectral shapes that are considerably less dependent on the incident neutron energy. Unsurprisingly, $HWHM$ parameter performed better at restoring the spectral width, although the spectra show different maximal amplitudes, while RMS did better at restoring the maximal amplitude of the distribution at the expense of width consistency.

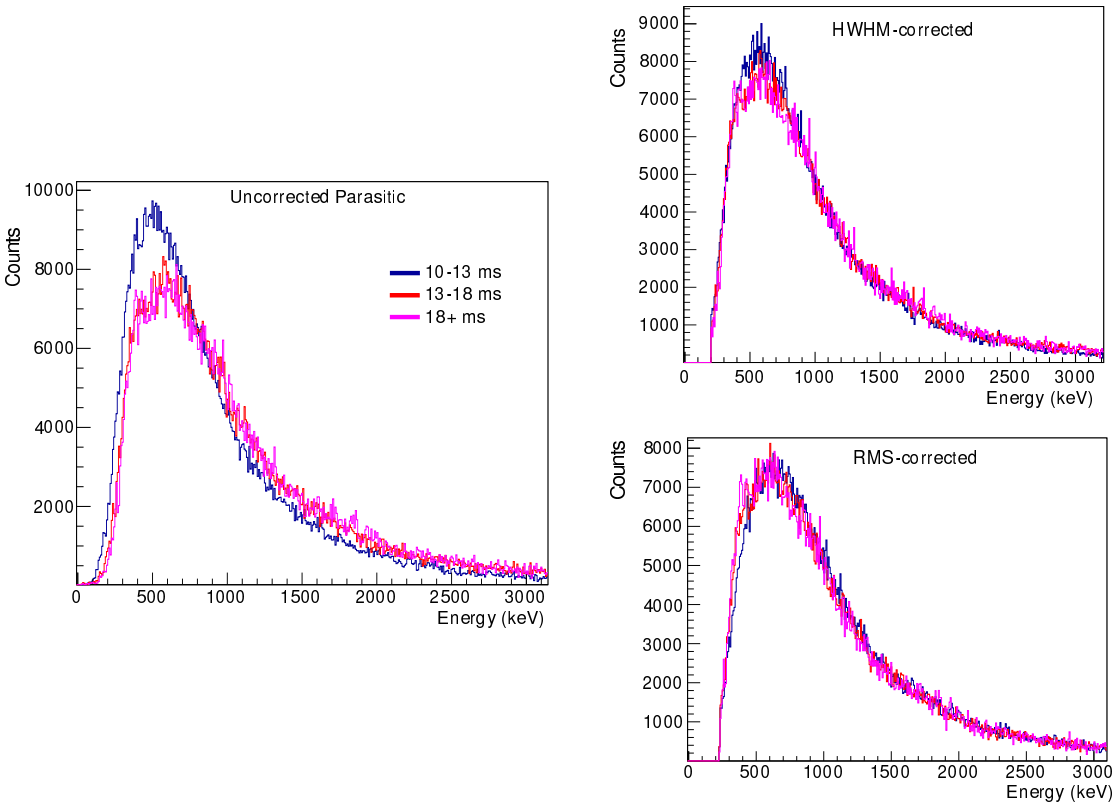

FIGURE 6.19: A comparison of the background-subtracted fission gamma-ray spectra without corrections (left) and with $HWHM$ (top) and RMS (bottom) corrections for parasitic pulses. The spectra are shown for three neutron ToF bins (10-13, 13-18 and 18+ ms). All the spectra are normalized in area to the 10-13 ms cut.

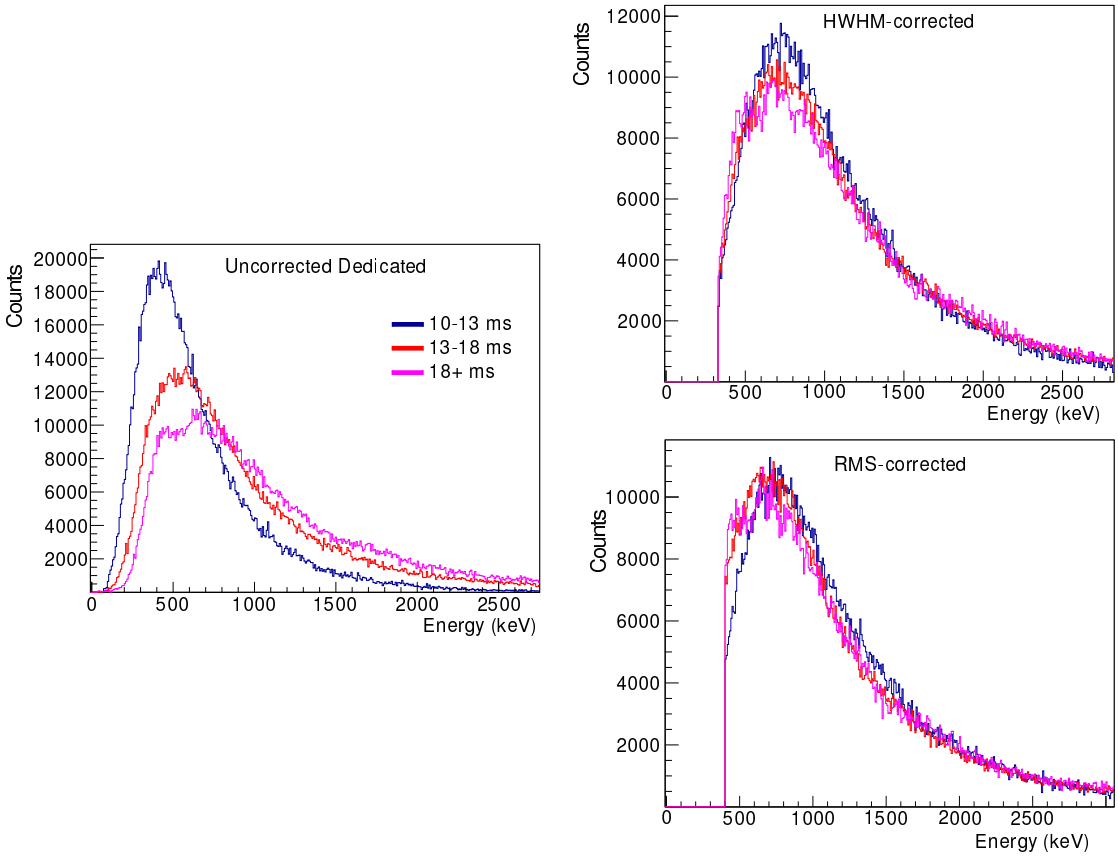

FIGURE 6.20: A comparison of the background-subtracted fission gamma-ray spectra without corrections (left) and with $HWHM$ (top) and RMS (bottom) corrections for dedicated pulses. The spectra are shown for three neutron ToF bins (10-13, 13-18 and 18+ ms). All the spectra are normalized in area to the 10-13 ms cut.

A comparison of the $HWHM$-corrected NaI spectra are shown overlayed with the results from measurements performed at ILL in 2014 in Fig. 6.21. The spectra are normalized in area between 1.5 and 5 MeV gamma-ray energies and appear to be in overall agreement for that energy region, however the distributions disagree for lower energies, peaking at different points, and also disagree above 5 MeV. The n_ToF measurements for both pulse types appear to lose lower energy gamma rays and have a lower number of gamma rays above 5 MeV.

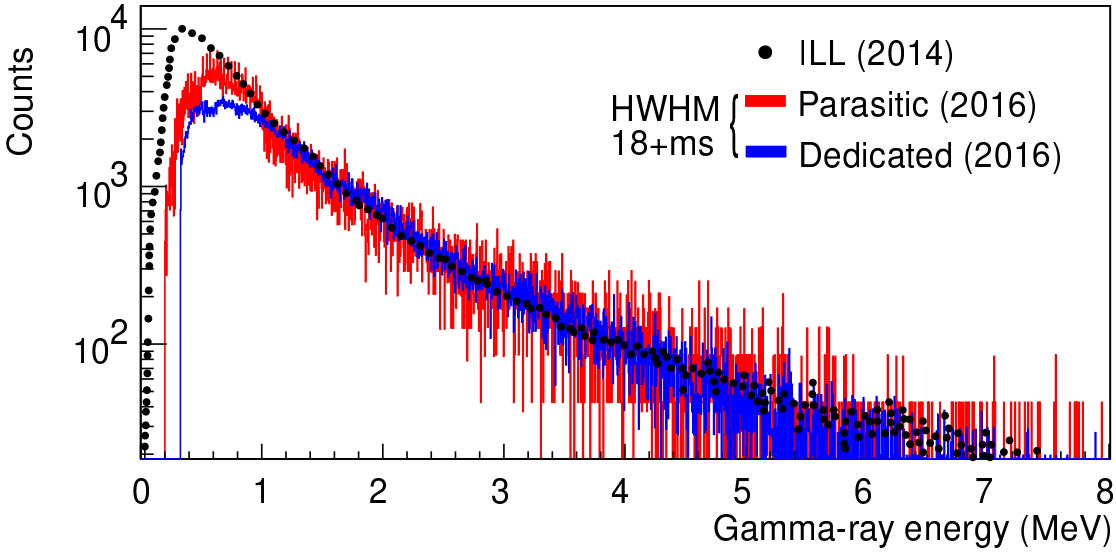

FIGURE 6.21: Overlayed gamma-ray spectra collected at ILL and n_ToF. The ILL spectrum presented here is the measured spectrum, i.e. a spectrum not corrected for detector effects such as Compton scattering probabilities. The n_ToF data are normalized in area to the ILL results in the 1.5-5 MeV range. n_ToF spectra for both pulse types have been collected only in the 18+ ms ToF range and have undergone $HWHM$ correction.

6.6 PSA Fit Quality Investigation

An investigation of the fits to the raw data using the PSA routines was conducted with particular focus on the fitting of the low-amplitude signals. A miscalibration of the time limit parameter, used as duration over which PSA performs dedicated γ-flash baseline estimation instead of operating with the user-defined baseline settings, was identified for the NaI PSA configuration (the parameter was set to 10^9 ns, whereas a considerably more well suited value of $3{\times}10^6$ ns was found during the re-investigation). This excessively large time limit size resulted in the baseline estimation failing for signals that are far removed from the γ-flash (most importantly in the 10 ms region used in the present analysis). The chosen baseline setting works well in the high count-rate regions of the data, and when the PSA settings were optimized at the beginning of the data processing campaign, the quality of the fits in these regions was emphasized without

the appreciation of the extent of gain variations in the detectors themselves. The $LaBr_3$ fits were also re-examined, but appeared to be calibrated well at least for all count rate regions below 1 eV neutron energy. Screenshots of the fits are shown in Fig. 6.22. It is evident from the fit visualization that the baseline in NaI signals is underestimated by approximately 8 channels, resulting in the routine missing a real signal (which is missed by the improved fit as well, but due to low amplitude cut-off as intended), as well as introducing three artificial signals.

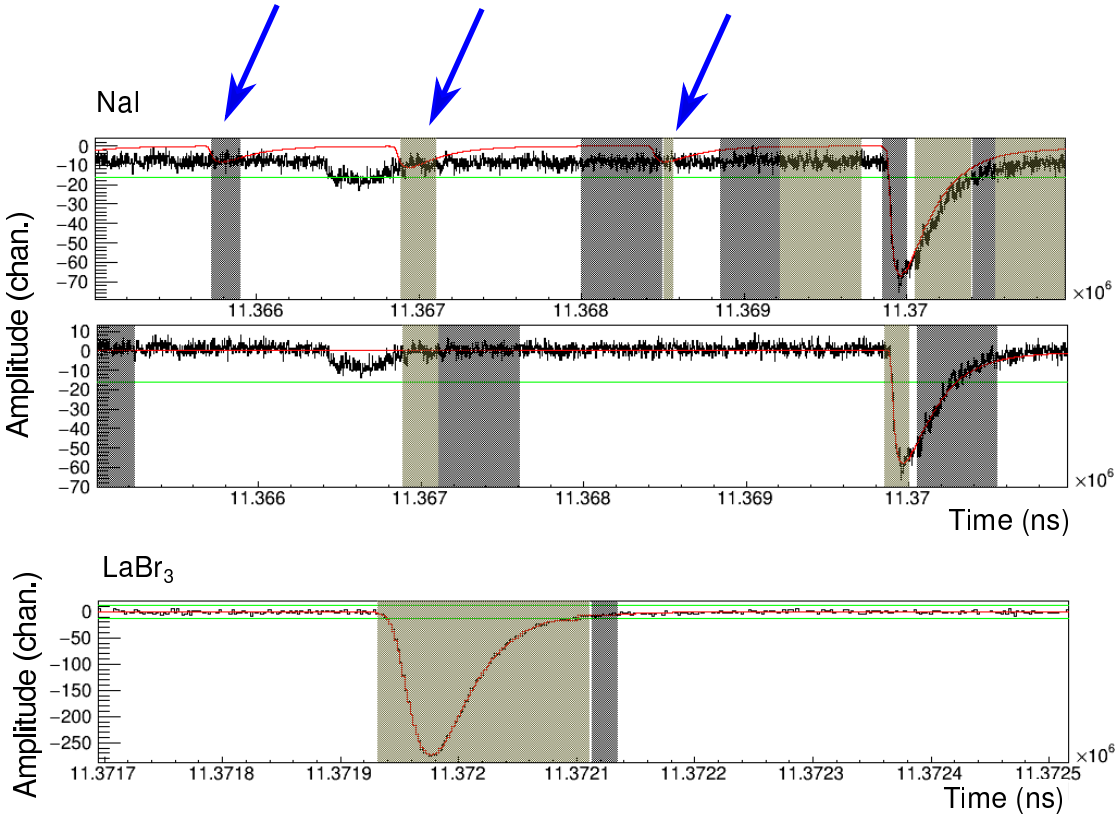

FIGURE 6.22: Visualization of PSA fits for both scintillator types used on STEFF. NaI signals with the original fit used during fission event building are shown in the top panel. An improved fit for the same trace segment is shown beneath it. Bottom panel shows PSA fit for a $LaBr_3$ signal evidencing the good quality of both the baseline estimation and the signal fitting. Blue arrows indicate artificial signals resulting from poor baseline estimation.

Following the identification of approximately 8 channel underestimation of the baseline an investigation was conducted to assess the behaviour of the fits for signals of various amplitudes and at different neutron energies. Unfortunately, during the initial PSA processing in 2016, PSA routines did not offer chi-squared calculation for each pulse, which is a functionality that has since been implemented and will benefit future STEFF data processing. The underestimation of baseline results in fits with greater amplitude, at least partially contributing to the lack of observed low-energy fission gamma rays. On the other hand, the introduction of artificial signals is unlikely to affect the fission

spectra significantly, since such signals are unlikely to coincide with a narrow fission time gate in coincidence with the fast-timing detectors.

In order to assess the baseline underestimation, the NaI PSA settings were improved (only by changing the step size variable) and a run of NaI data was re-processed with the old parameters and then with the new, the latter data set serving as a reference. The comparison of the signal amplitudes was performed using all the signals within the chosen run (run 204893), i.e. both background gamma rays and fission gamma rays. Gating on fission gamma-rays would require a full round of re-processing of the data into fission events, which is a time-consuming process, while fitting errors are unlikely to affect fission gamma rays any differently to the background ones. A comparison of the resulting original and new fit amplitude spectra for the two proton pulse types are shown in Fig. 6.23. The fits for both pulse types appear to agree reasonably well for gamma ray energies above 1 MeV, however there is a considerable increase in low-energy gamma-rays for the original fit settings. This is likely caused by the combination of overestimation of pulse amplitude due to background underestimation and the introduction of the artificial signals.

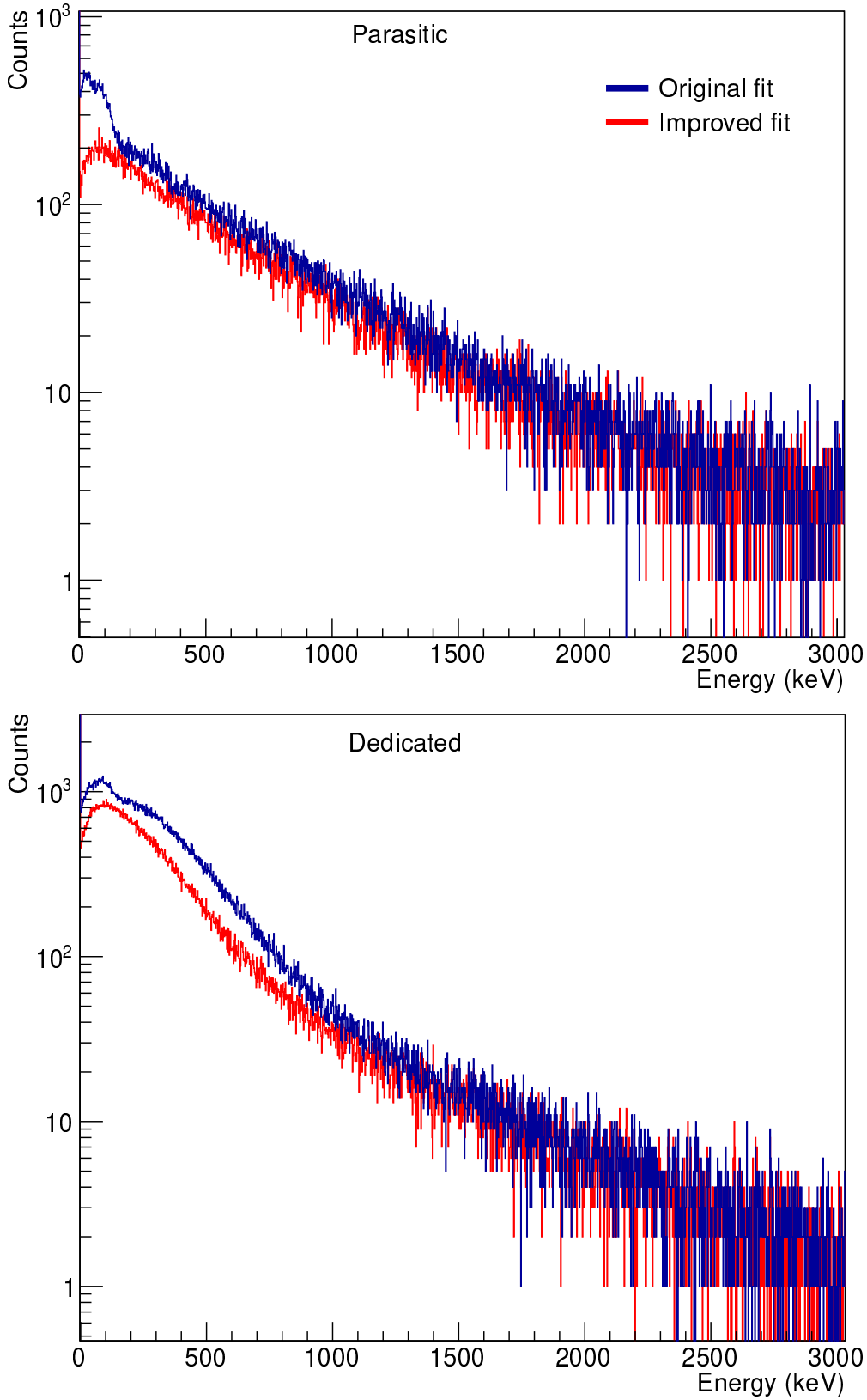

FIGURE 6.23: A comparison of the amplitude spectra of all the fitted gamma rays for one run using original PSA fit settings (blue) and new settings (red). The parasitic pulse data are shown in the top panel and the dedicated in the bottom panel.

In order to quantify the fitting defects, gamma-rays from the improved fits were matched to the their original fit counterparts using ROOT, by requiring that gamma rays originate from the same proton bunch and are identified within 5 ns of each other, accounting for the drift in CFD crossing due to amplitude changes. Distributions of amplitude differences between improved and original fit signals were then plotted to investigate the effect of count rate (by means of neutron time-of-flight gates), minimal amplitude cut, and signal pileup on the fit performance. The effect of the neutron ToF cut is shown in Fig. 6.24. The centroid of the dedicated data is approximately -8 channels with a standard deviation of 4 channels, while the centroid of parasitic data lies at -7 channels with the same standard deviation as the dedicated data. All the ToF cuts appear consistent within one standard deviation, although the lowest ToF cut (in black) has a large peak at 0 channel difference, indicating agreement of the two data sets. This occurs due to the baseline setting in PSA, which sets the baseline at higher count rate regions, where signal baseline does not fully restore following pulses, resulting in similar fitting by both parameter sets. Due to this effect, further PSA investigations were conducted for neutron ToF greater than 2.5 ms.

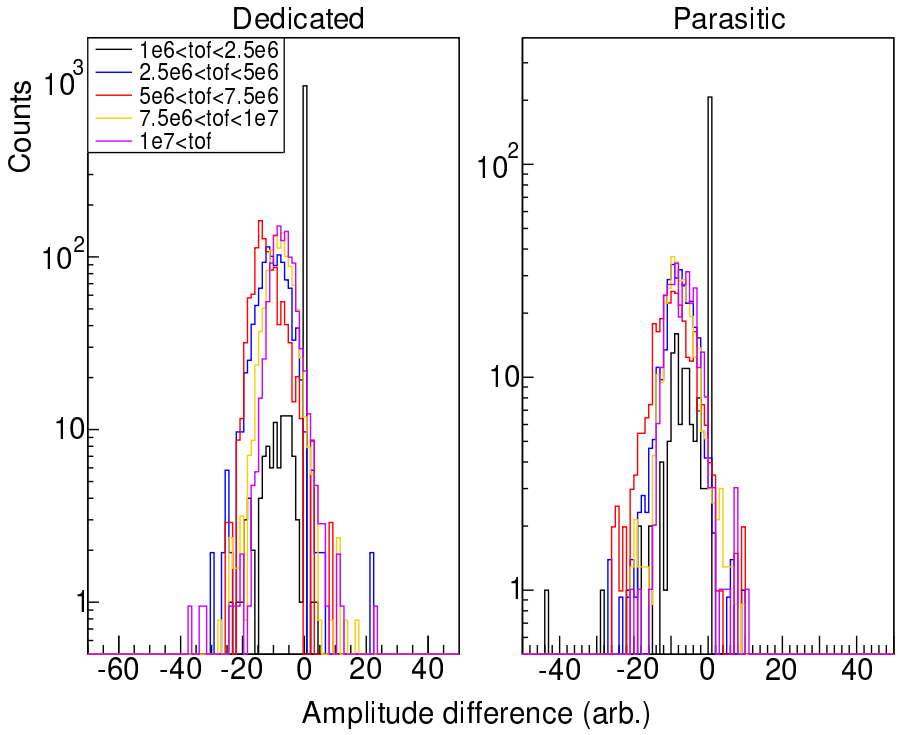

FIGURE 6.24: A comparison of the amplitude spectra for both proton pulse types (dedicated on the left and parasitic on the right) for different neutron ToF cuts in NaI crystal 2.

Fig. 6.25 shows the effect of setting a different minimum amplitude gates on the two data sets during their correlation in ROOT on the amplitude differences in the spectra. Fig. 6.26 shows the amplitude differences for signals with *pileup*1 PSA variable set to 0 and 1. *pileup*1 represents PSA routine's attempt at estimating the pileup with a value

of 0 meaning that no pileup was identified, value of 1 meaning that the signal starts or ends above a set threshold, and -1 meaning that the signal starts or ends below a set threshold. The threshold was set to 10 channels for both PSA fit data. Neither the change in minimal amplitude nor the imposition of a *pileup*1 flag value resulted in a significant change in amplitude differences, suggesting that neither neutron ToF, nor amplitude cut or pile-up affect the performance of the baseline estimation significantly. Furthermore, the effect seems consistent regardless of which NaI crystal is selected, as shown in Fig. 6.27.

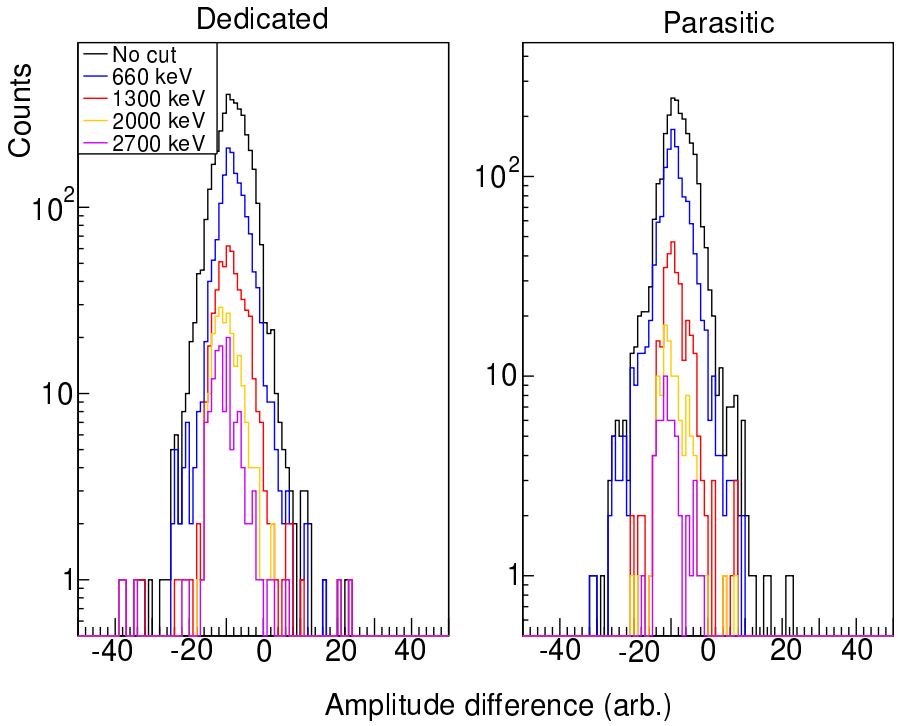

FIGURE 6.25: A comparison of the amplitude spectra for both proton pulse types (dedicated on the left and parasitic on the right) for different minimal amplitude cuts in NaI crystal 2.

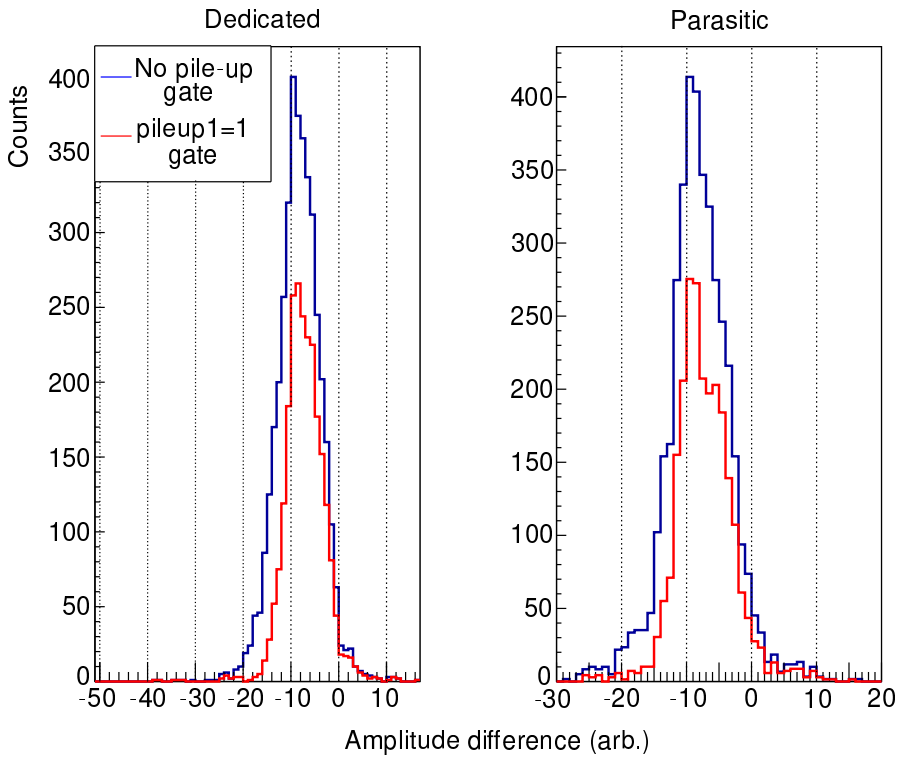

FIGURE 6.26: A comparison of the amplitude spectra for both proton pulse types (dedicated on the left and parasitic on the right) for different *pileup*1 settings (0 in blue, 1 in red) in NaI crystal 2.

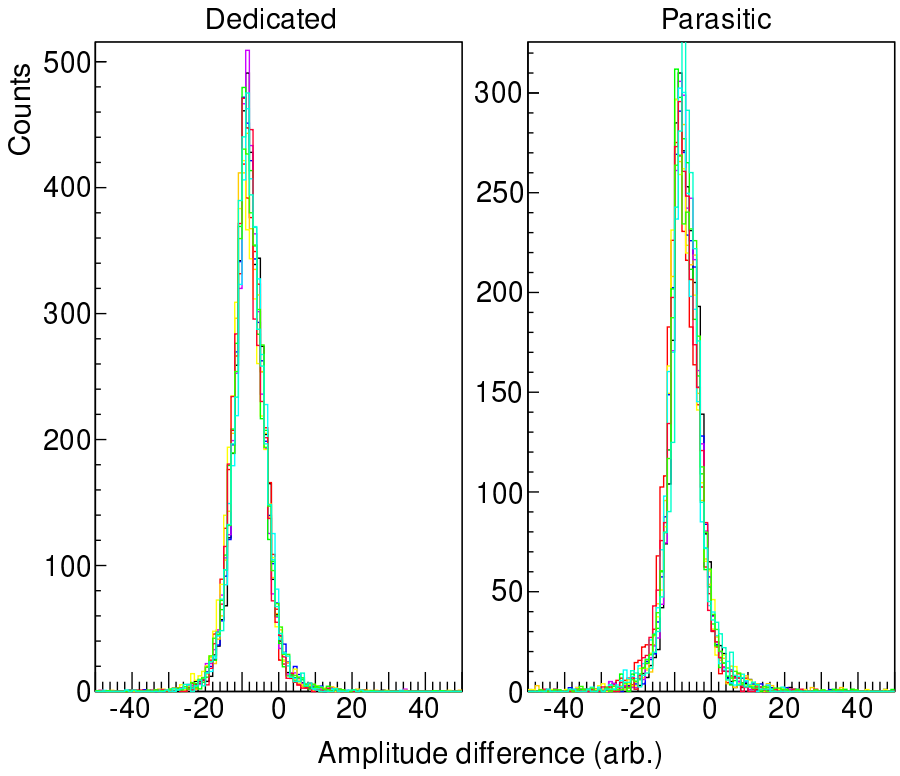

FIGURE 6.27: A comparison of the amplitude spectra for both proton pulse types (dedicated on the left and parasitic on the right) for different NaI crystals.

Based on the consistency of the amplitude differences for all the signals, a plot of amplitude difference for all neutron ToF greater than 2.5 ms has been constructed for each pulse type summed for all the NaI crystals to investigate a constant offset to apply to each signal in the analysis. The centroids are -8.13 with a standard deviation of 4.09 for both pulse types, corresponding to an offset of 92-112 keV depending on the crystal. The calibration source data PSA fits used for energy calibration did not have the same variations in the count rate, allowing for an accurate determination of the baseline, and therefore did not suffer from an offset during fitting. For that reason, energy calibrations did not take the offset into account despite having the same PSA settings, and the fission energy spectra were re-compiled with all the signals reduced by 8.13 amplitude channels. The results of the 8-channel correction are shown for the parasitic and dedicated pulse in Figs. 6.28 and 6.29 respectively.

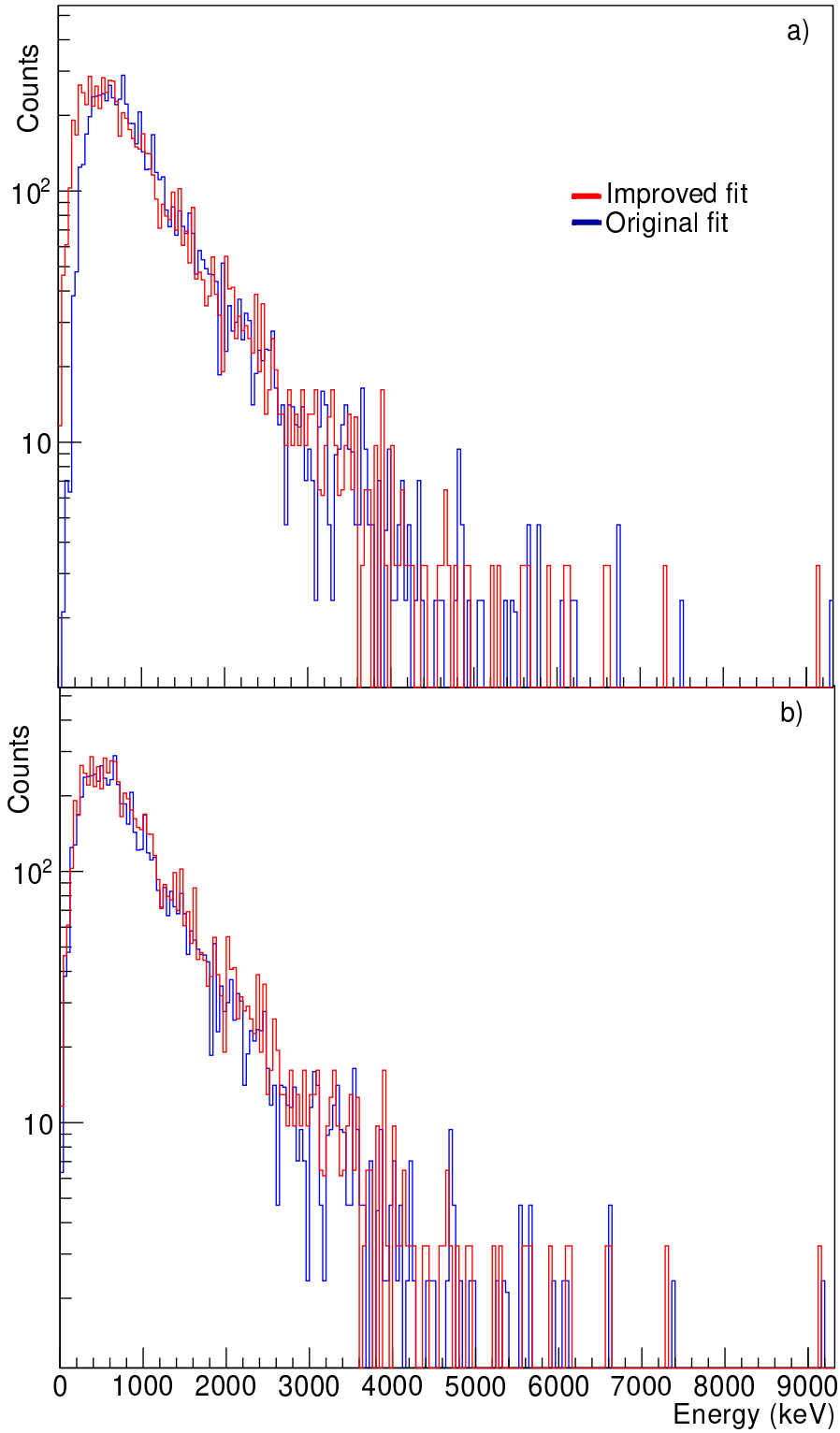

FIGURE 6.28: A comparison of the gamma-ray energy spectra for $HWHM$-corrected parasitic pulse data a) before and b) after applying the 8-channel offset. The improved fit data are shown in red and the original fit is shown in blue. The data are normalized in area.

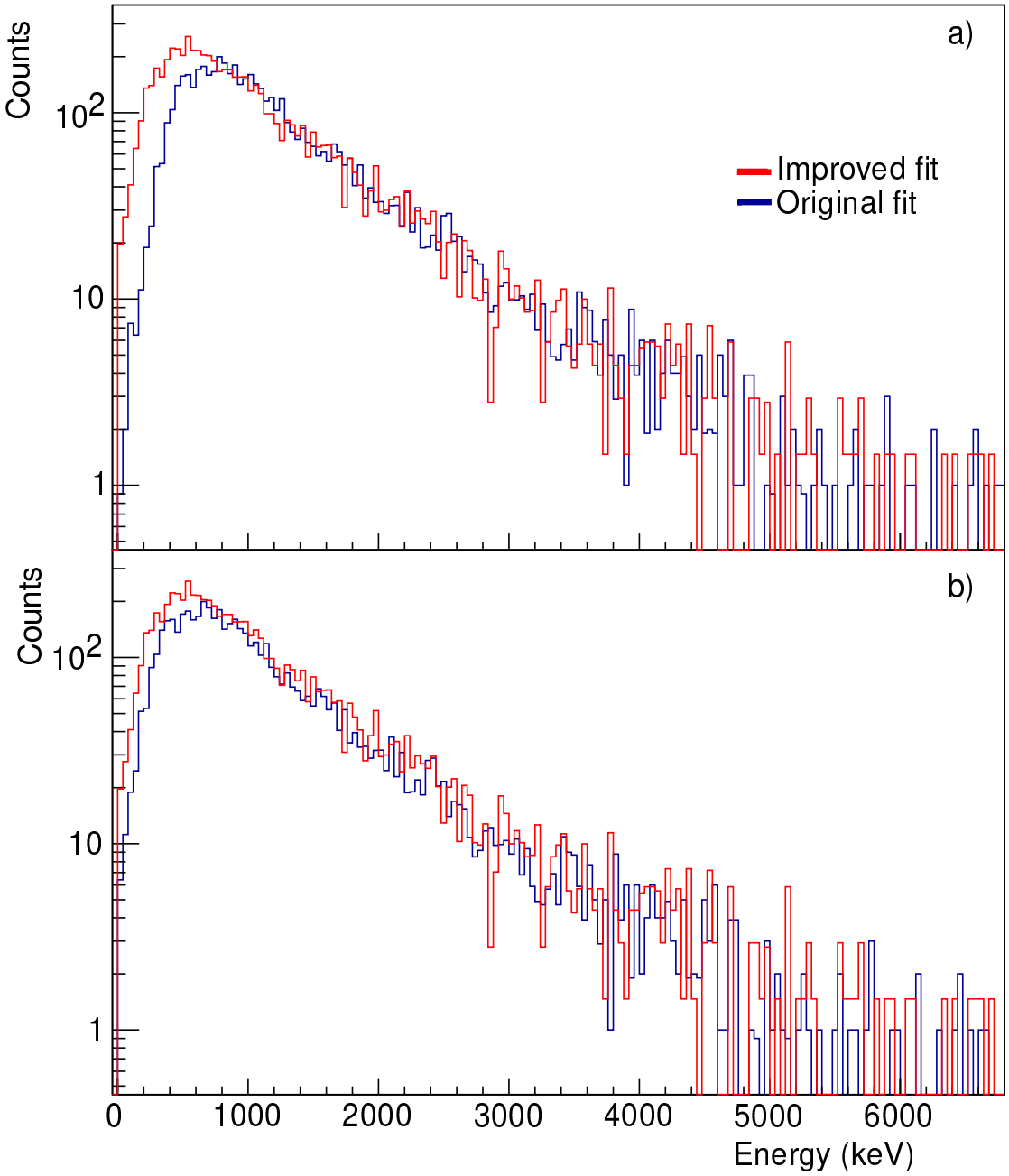

FIGURE 6.29: A comparison of the gamma-ray energy spectra for $HWHM$-corrected dedicated pulse data a) before and b) after applying the 8-channel offset. The improved fit data are shown in red and the original fit is shown in blue. The data are normalized in area.

Shifting the spectra by 8 channels appears to bring the overall shape of the energy spectra to general agreement with the improved fit data. An example comparing the ILL data to a shifted spectrum is shown in Fig 6.30. It is evident that there are still a lot of low-energy and high-energy counts missing, but it is difficult to estimate how many signals were lost due to baseline misidentification by simply looking at PSA fits (and therefore correct the spectrum) due to the introduction of artificial signals. In

order to accurately estimate the loss of fission gamma-rays in the PSA routine, a full re-correlation of newly-fitted NaI data with the fast-timing detectors is required.

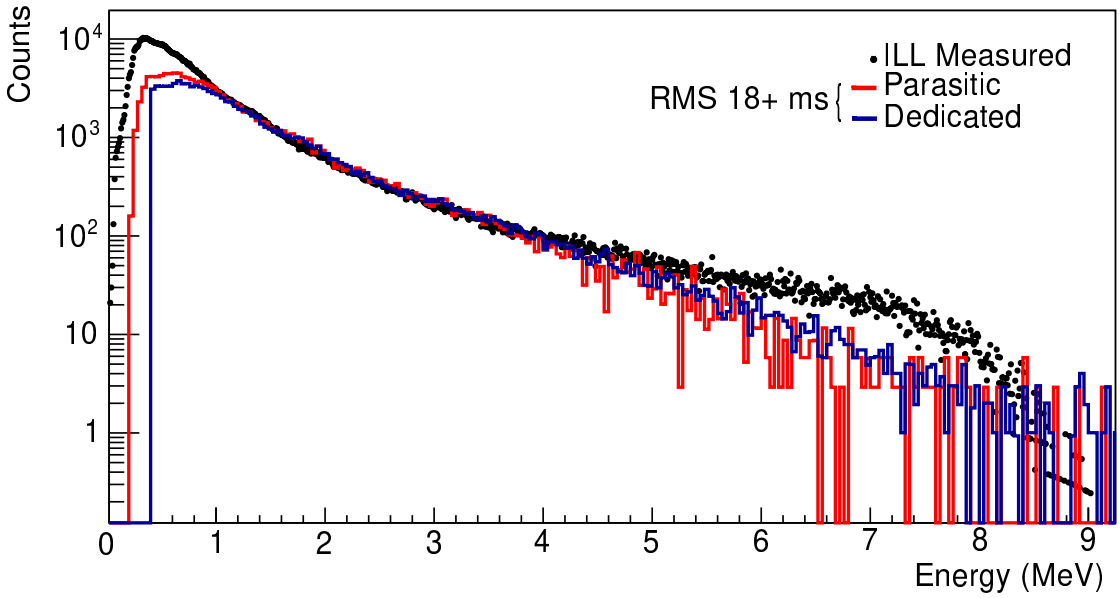

FIGURE 6.30: A comparison of the ILL measured PFG spectra to the measured n_ToF PFG spectra for *RMS*-corrected parasitic (red) and dedicated (blue) pulse data in the 18+ ms neutron ToF range with *RMS* shape correction applied. The n_ToF data have been corrected for fitting errors by 8 amplitude channels.

Background-subtracted fold distributions for the 2016 data were produced following the method described in Ref. [21]. Fig. 6.31 shows the fold distribution in the 2016 data for both pulse types compared to the previous results. The new fold distributions shown are gated on 18+ ms neutron ToF and feature contributions from the artificial pulses introduced by the fitting. The data from this work have not undergone neutron signal subtraction. There is an evident excess of fold-0 events in the dedicated data (fold-1 to fold-0 ratio is ≈ 0.93), and the parasitic data are in relative agreement with the 2015 data in the low-fold side of the distributions (fold-1 to fold-0 ratio of $\approx$1.00), but feature more high-fold events.

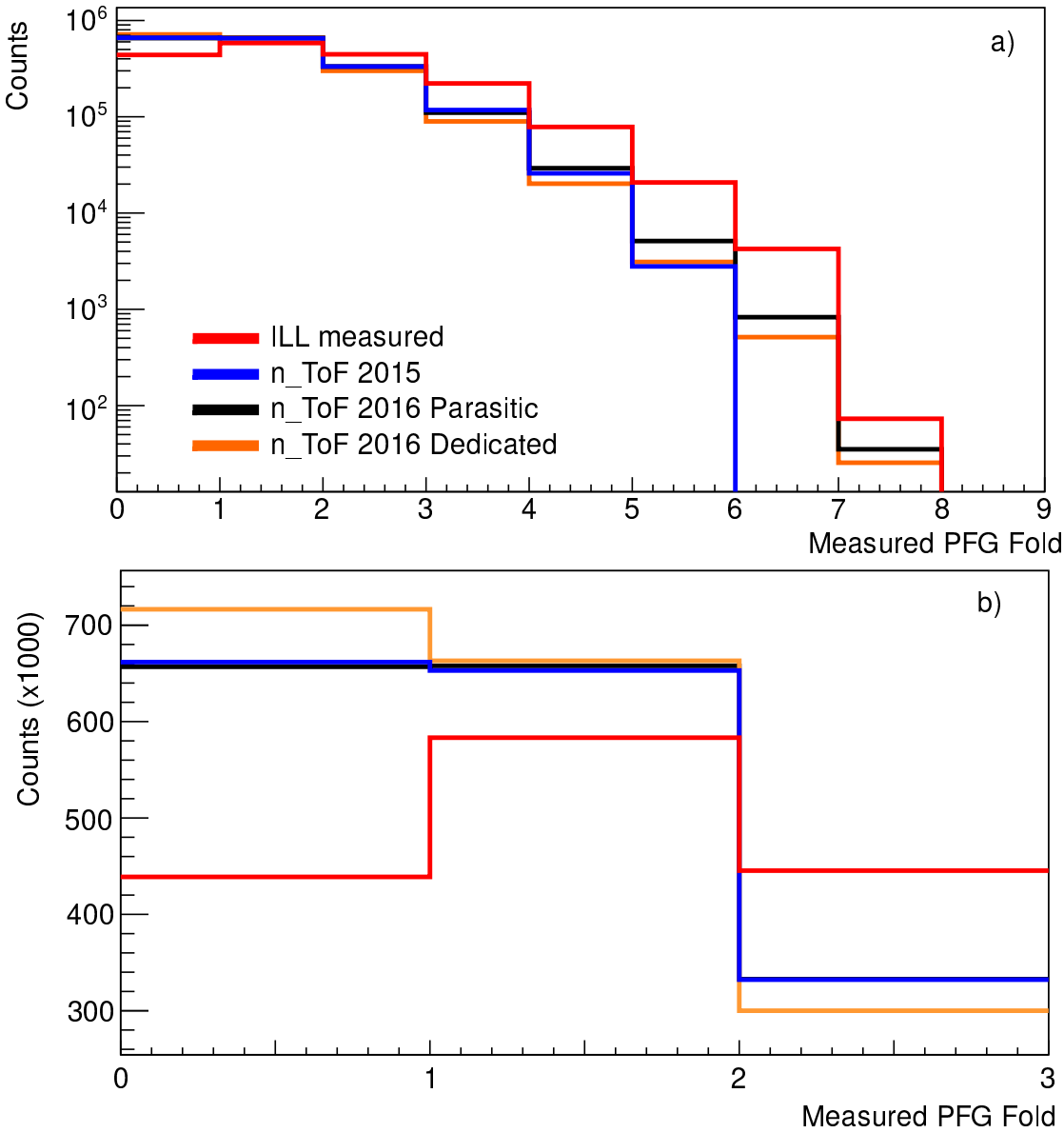

FIGURE 6.31: A comparison of the PFG fold distributions in Fig. 6.1 with the results of the work presented in this chapter. Panel a) shows expanded view of the entire fold distribution, while panel b) shows enhanced view of the low-fold segment of the plot. ILL data are shown in red, n_ToF 2015 data are shown in blue, the parasitic distribution from the 2016 data is shown in black, and the dedicated pulse data are shown in orange. All the distributions are normalized in area to the ILL data.

6.7 $LaBr_3$ Gain Investigation

6.7.1 Count rate correction

As was shown in Fig. 6.8, based on calibration source investigation $LaBr_3$ detector is expected to exhibit gain fluctuations with increasing count rate like NaI, however the change is expected to be linear in count rate. A linear fit was produced based on ^{22}Na count rate effect investigation data with a slope of 20.1±4.9 and an intercept of 157±4 ($\chi^2_{red.}$ ≈7). The linear fit was used to calculate expected amplitude as a function of count rate, however count rate information is not available directly from fission event data in the database, so count rates were calculated as a function of neutron energy. In order to perform the calculation, a 9^{th} order polynomial has been fitted to the parasitic and dedicated count rates in $LaBr_3$ shown in Fig. 6.12 in the thermal to 1 eV neutron energy range. The fits are shown in Fig. 6.32 and the fit coefficients are listed in Table 6.4.

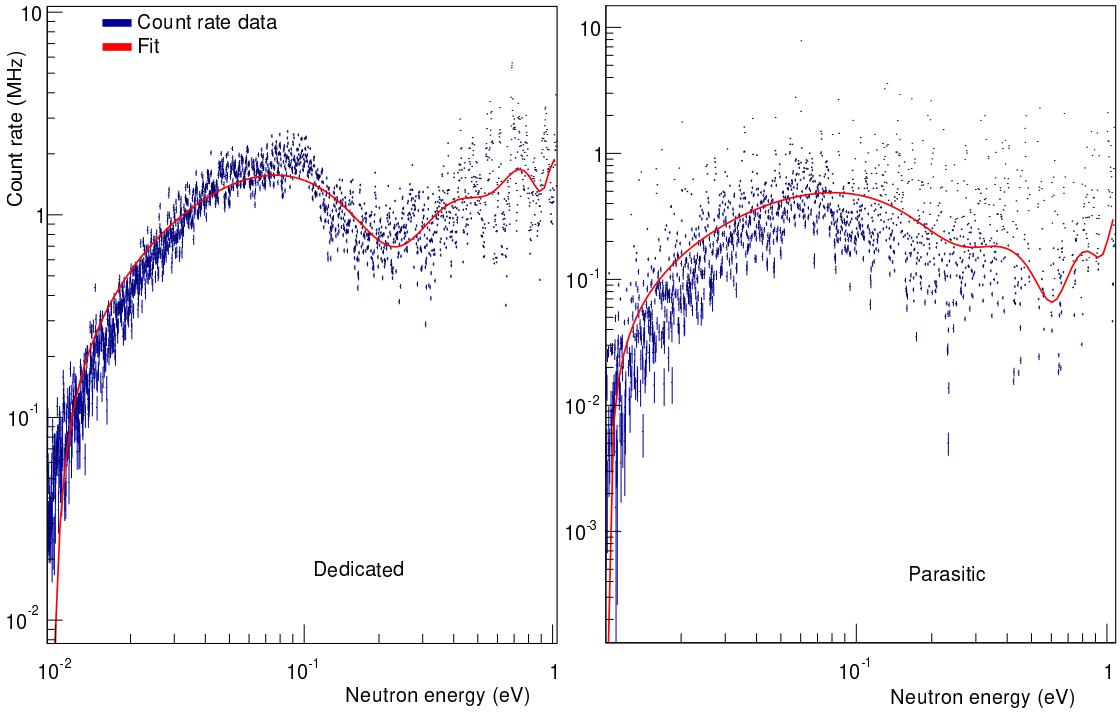

FIGURE 6.32: Polynomial fits to $LaBr_3$ count rates for dedicated (left) and parasitic (right) pulses in the thermal to 1 eV incident neutron energy range. The fits are shown in red and the data in blue.

TABLE 6.4: Fit parameters for the 9^{th} order polynomial fits to $LaBr_3$ count rates for both pulses types.

Coefficient order and units	Dedicated fit	Parasitic fit
0 (MHz)	-0.672±0.002	-0.211±0.001
1 (MHz / eV)	76.3±0.2	23.0±0.05
2 (MHz / eV^2)	-897±4	-265±1
3 (MHz / eV^3)	4440±31	1350±7
4 (MHz / eV^4)	-10400±100	-3650±30
5 (MHz / eV^5)	9130±360	5370±70
6 (MHz / eV^6)	6740±580	-4000±110
7 (MHz / eV^7)	-21400±500	869±95
8 (MHz / eV^8)	16400±300	562±47
9 (MHz / eV^9)	-4650±60	-266±10

Neutron energy was calculated based on the time of each $LaBr_3$ signal, and was used as an input to the count rate calculation, which was applied for all signals corresponding to neutron energies below 1 eV. The calculated count rate was then used in the linear fit in order to correct the amplitude for the count rate-induced gain effect. The effect of the correction is demonstrated in Fig. 6.33.

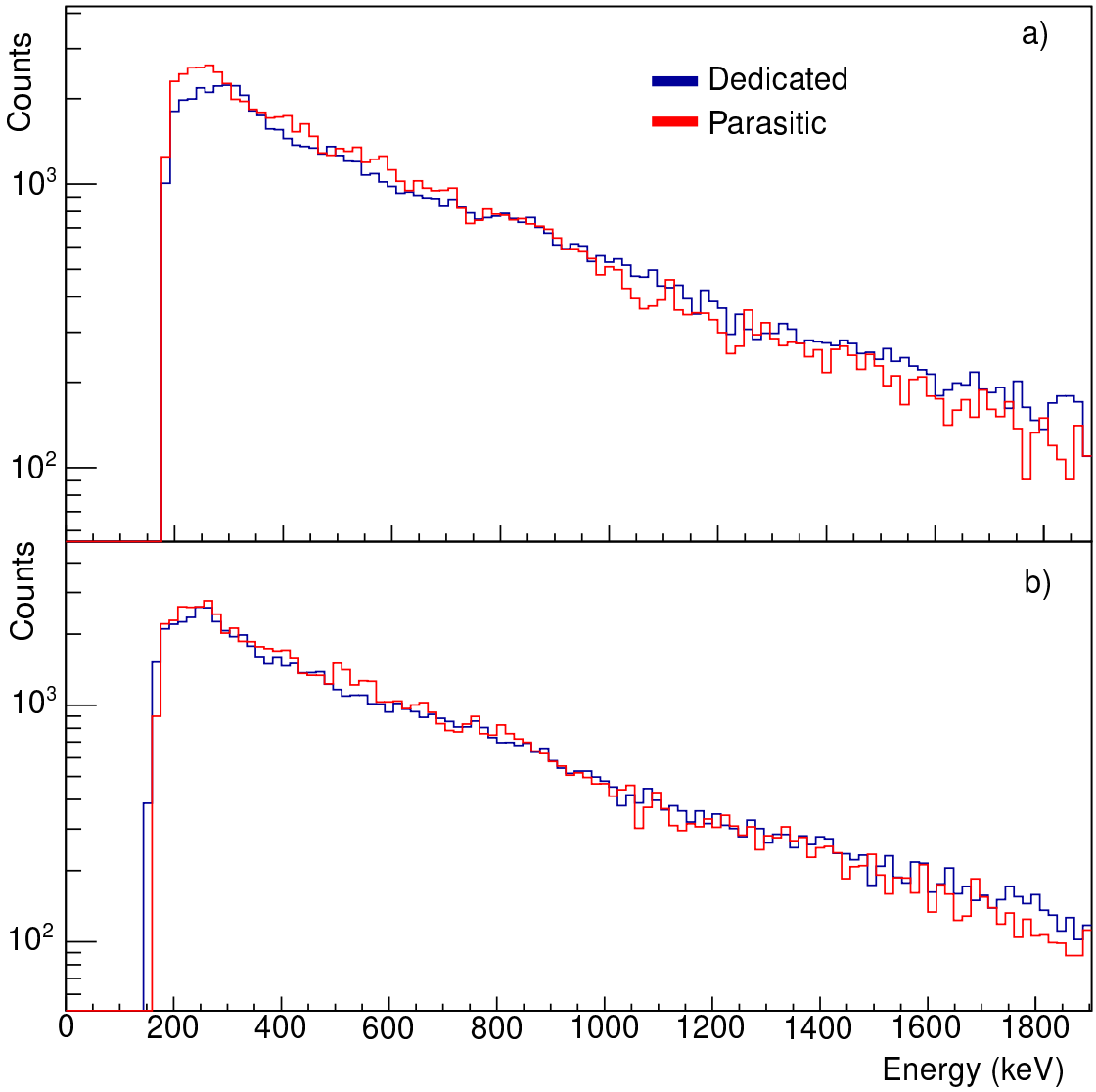

FIGURE 6.33: A comparison of the uncorrected (a) and corrected (b) parasitic and dedicated background-subtracted fission-gated spectra from the $LaBr_3$ detector. Count rate correction has resulted in a closer agreement in the peaks of the parasitic and dedicated fission spectra.

6.7.2 Background peak correction

A further gain correction was implemented in $LaBr_3$ spectra based on the background spectra which featured a single peak, unlike the smooth background spectra in NaI detectors. A comparison of the background spectra between the parasitic pulses in $LaBr_3$ and NaI detector 1 is shown in Fig. 6.34, and the peak visible in the $LaBr_3$ spectrum is presented more clearly in Fig. 6.35.

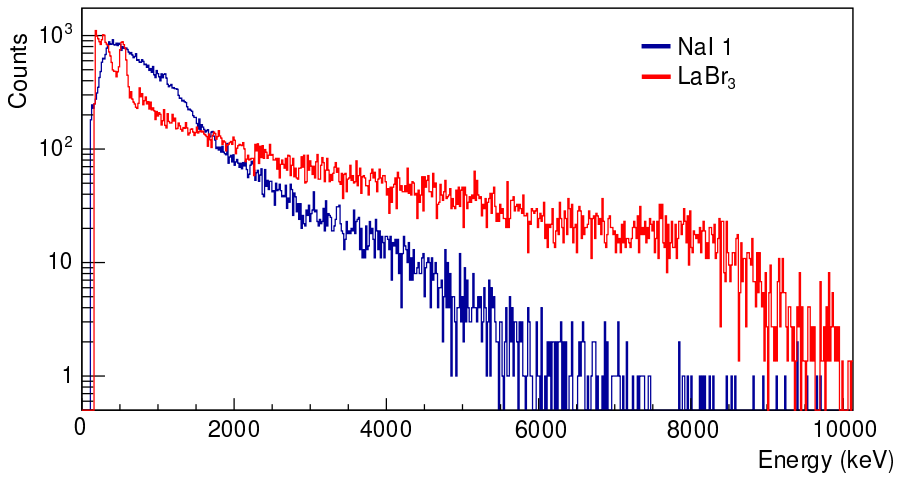

FIGURE 6.34: A comparison of the parasitic background spectra between $LaBr_3$ and NaI detector 1. Unlike the smooth NaI spectrum, there is a single peak-like structure in the $LaBr_3$ spectrum at ∼500 keV.

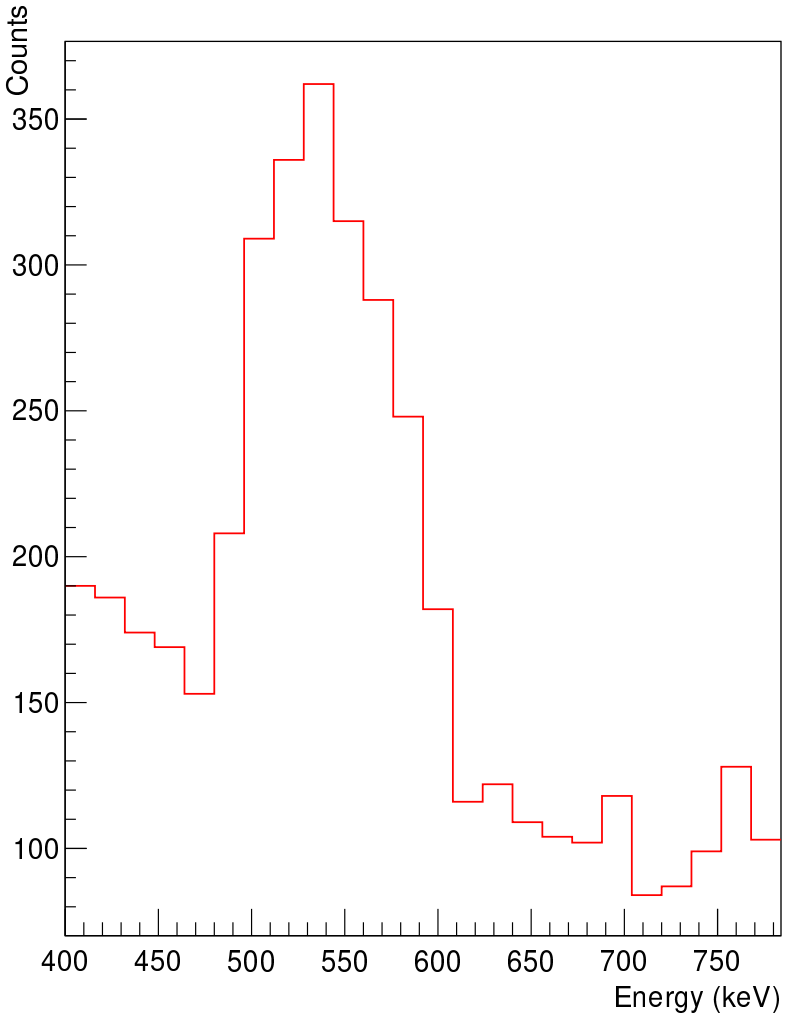

FIGURE 6.35: An enhanced view of the peak in the $LaBr_3$ background spectrum visible in Fig. 6.34.

In an effort to investigate the behaviour of the peak as a measure of gain, as well as to

determine its origin, the position of the peak was tracked in different neutron time-of-flight regions for each proton pulse type. A plot of several time-of-flight cuts for both pulse types is presented in Fig. 6.36. Following the count rate correction based on ^{22}Na source data, parasitic $LaBr_3$ spectra were considered gain corrected, and indeed the peak position appears stable across all ToF cuts. The position of the peak drifts with ToF in the dedicated pulses despite the prior correction, and appears at a higher energy than in parasitic, suggesting more complicated gain effects likely based on the more intense rates and background of the dedicated pulses.

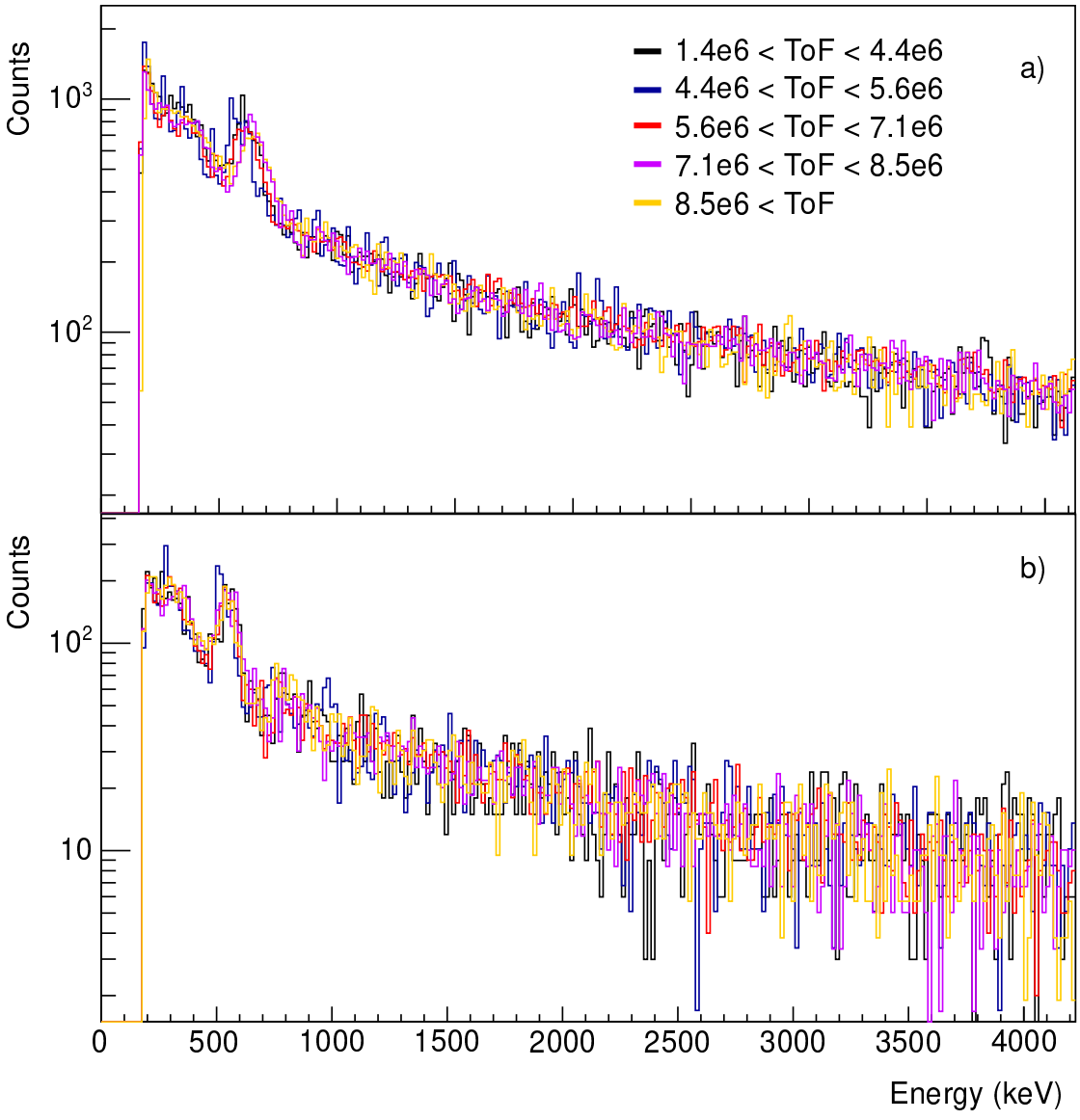

FIGURE 6.36: Plots of a) dedicated and b) parasitic background spectra for different neutron ToF cuts.

The position of the peak was fitted with a Gaussian on a linear background, and peak positions for each pulse type were plotted as a function of neutron ToF (in ns) to produce

a gain correction for the parasitic pulses. A typical fit is shown in Fig. 6.37, and the resulting peak position distribution is shown in Fig. 6.38.

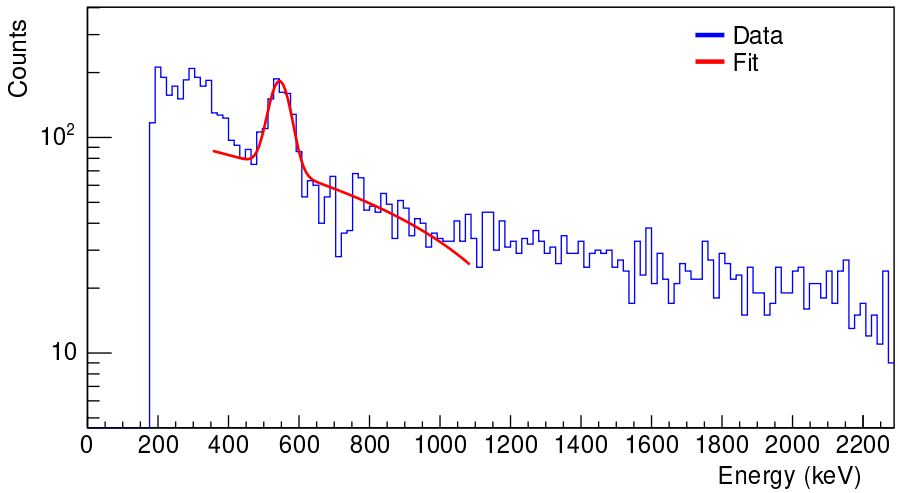

FIGURE 6.37: An example of a Gaussian fit on linear background fit for the background gamma-ray spectrum in a parasitic pulse with a neutron ToF cut of 5.6 to 7.1 ms.

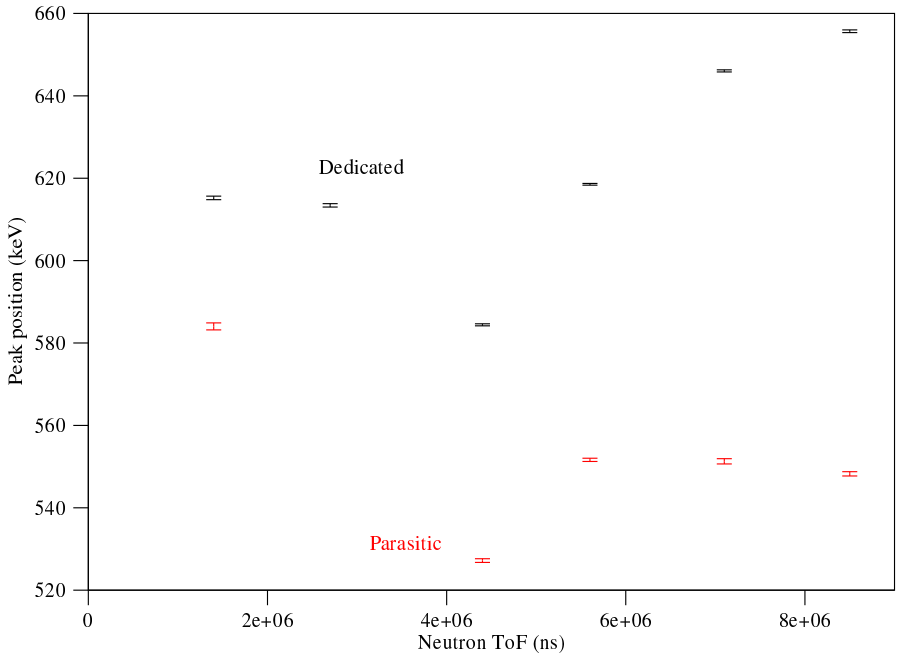

FIGURE 6.38: A distribution of peak centroids obtained from Gaussian fits to different neutron ToF cuts to both proton pulse types. Plotted uncertainties represent peak standard deviation divided by the square root of peak area. Peak position in the 2.7 ms ToF cut is omitted in the parasitic distribution, as it was combined with the 1 ms cut to improve statistics for fitting. The data points for both pulse types in the 5.5 ms cut exhibited unusual skewness, whereby the peak width was approximately the same as in the other cuts, but the peak maximum was skewed towards low energy.

Based on the data presented in Fig. 6.38, a correction was produced by taking the ratio of the peak positions in the dedicated pulses to parasitic, producing correction coefficients as a function of neutron ToF. The coefficients were fitted with a linear fit, which was used to calculate a multiplicative correction factor applied to the calibrated dedicated

$LaBr_3$ spectra. The fit is shown in Fig. 6.39 and the resulting background and fission gamma-ray spectra are shown in Fig. 6.40. It is evident from the background spectrum, that the peak positions in the two pulse types are in considerably better agreement following the correction. It is worth noting, that the post-correction reduction in gain has moved some signals below the 10-channel miminum PSA threshold corresponding to ≈180 keV gamma-ray energy, and for spectra summed across large timespans with count rate variations such as the one in Fig. 6.40 the threshold should be reapplied to the dedicated spectrum to produce the final measured PFG energy spectrum. The counts shifted below the threshold are retained in the spectrum shown here for demonstration of the gain correction effect only, and the proper threshold can be seen in the figure for parasitic data.

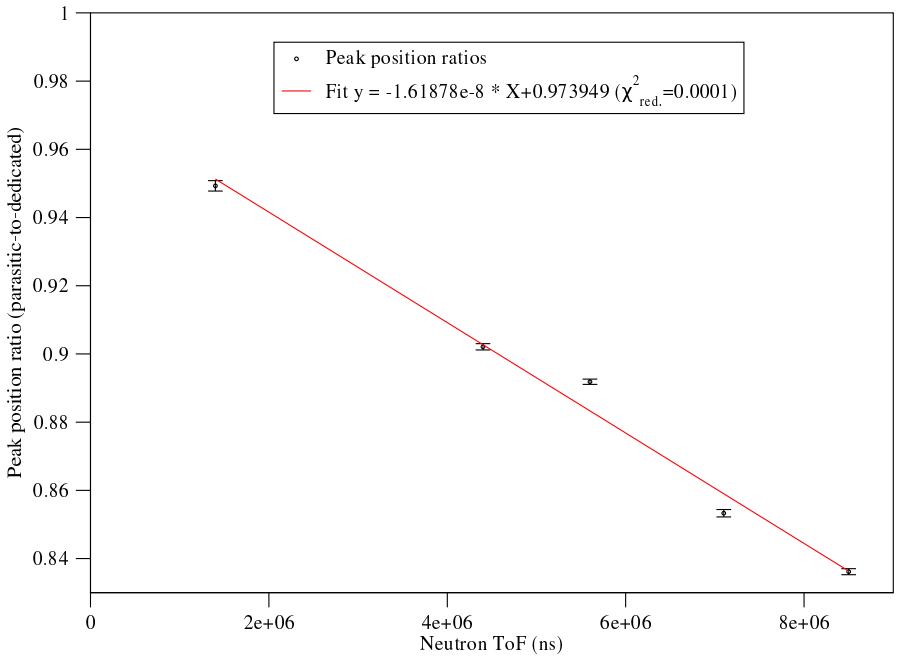

FIGURE 6.39: A distribution of dedicated-to-parasitic ratios in background peak positions for several neutron time cuts shown in black. A linear fit is shown in red.

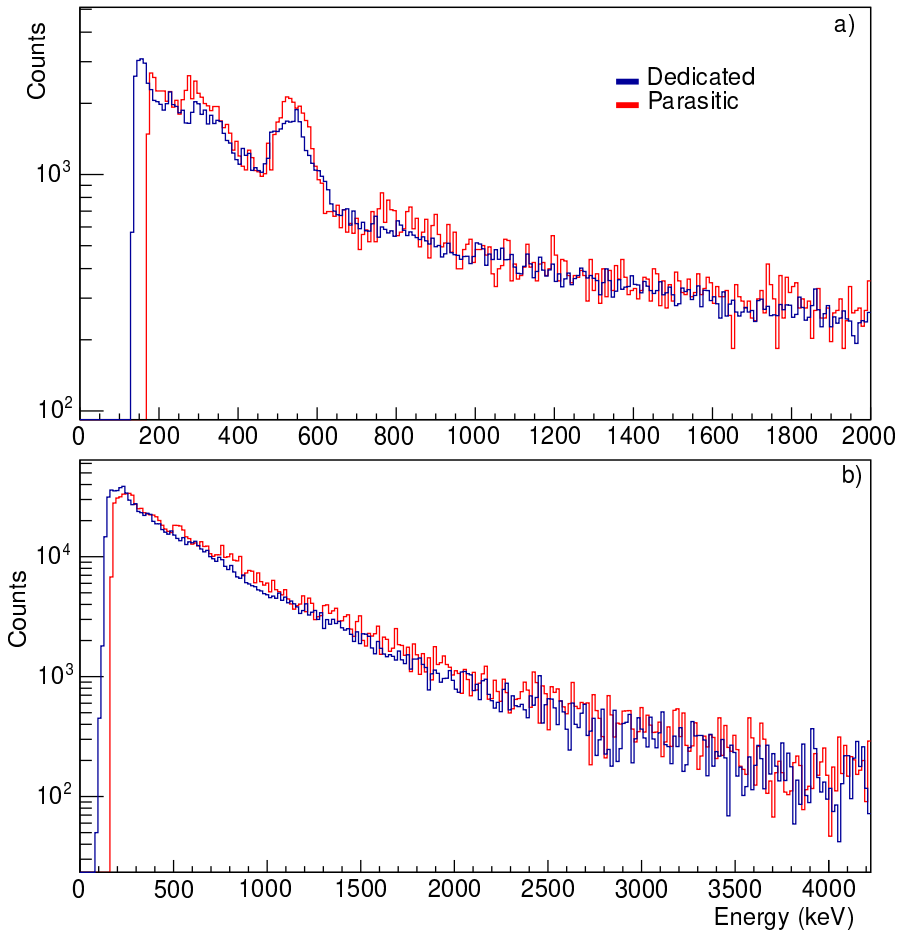

FIGURE 6.40: $LaBr_3$ a) background and b) fission gamma-ray energy spectra following gain correction based on the background peak position. Dedicated pulse data are shown in blue, and parasitic in red.

Throughout the analysis of the background peak presented here, it has been assumed that the peak corresponds to the same physical effect in both proton pulse types. Since the structure only appears in the $LaBr_3$ spectra and not in NaI indicates that there is some $LaBr_3$-specific activity producing the peak, rather than it being associated with the in-beam or STEFF structural components. A natural first guess at the origin of the structure is the internal activity in the detector produced by β decay of ^{138}La discussed previously in this work. The peak structure is quite broad (FWHM≈50 keV) compared to the resolution of a $LaBr_3$ scintillator, which may indeed suggest broadening due to the varing energy deposited by the β particle in coincidence with a gamma ray. Calibration source spectra have been used to investigate the possibility of internal transitions of the detector producing the peak-like structure. Source spectra normalized in time are shown in Fig. 6.41, and clearly indicate which of the peaks correspond to the internal activity in lanthanum, since the rates are approximately constant on the timescales of calibration spectrum collection.

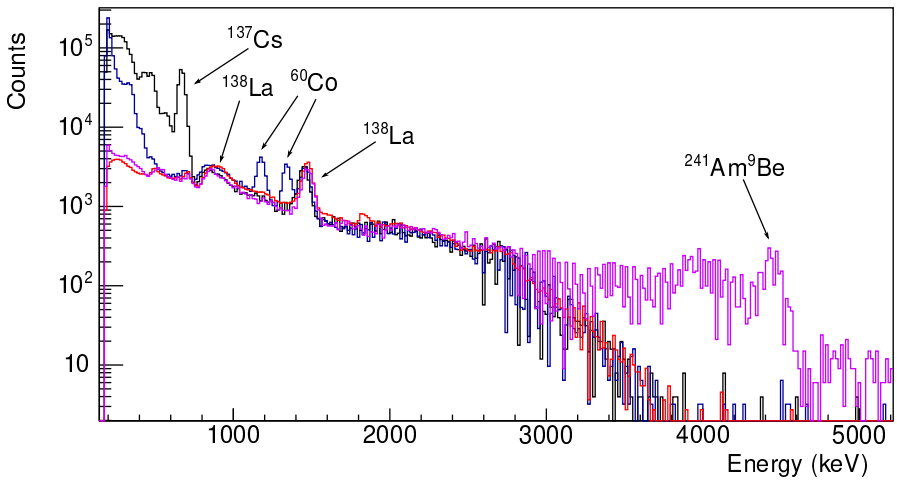

FIGURE 6.41: Overlapped ^{137}Cs, ^{60}Co and ^{241}Am^{9}Be source spectra normalized in collection time. The two internal transitions of ^{138}La are indicated alongside the prominent calibration source peaks.

The first ^{138}La peak is the 789-keV β^- decay, and shows characteristic broadening caused by the beta particle scattering. The shape exhibited by the peak is dissimilar to the one observed in the background. Moreover, due to the ease of identification of internal transitions in lanthanum-138, the energy calibration of the detectors may be tested. The spectra presented above have been calibrated using the calibration function derived from them, and the peaks are positioned within 7 keV of the known transition energies (with the exception of the AmBe 4436-keV transition which was underestimated by 10 keV), confirming the overall accuracy of the calibration, and making it unlikely that the background peak observed in the 500-600 keV range is actually the 789-keV transition. A considerable reduction in gain could indeed shift the peak position by 200 keV, however the peak position does not show recovery from gain reduction in the parasitic pulses (as seen in NaI), and appears to be stable overall. Further possibility of detector gain shifting due to damage has also been examined by comparing the position of the ^{88}Y peaks from calibrations before and after the STEFF campaign, and the peak position in the spectra does not change, suggesting that the detector was not damaged during the campaign in a way that would reduce gain.

Another possibility for a peak-like structure to occur in $LaBr_3$ is a neutron capture reaction occurring in the constituent elements of the detector (i.e. ^{138,139}La, ^{79,81}Br, and ^{140,142}Ce dopant). Neutron capture can lead to prompt gamma emission, a formation of a metastable state, which emits a gamma ray at some later time following capture, or a formation of a compound nucleus that is unstable against beta decay, producing a beta scattering-broadened peak from gamma decay following the emission of a beta particle. These scenarios were investigated using data evaluated in ENDF [10] and Ref. [176]. A clear way of testing neutron capture as a source of the peak would be to examine the

behaviour of the peak at varying neutron energies, in particular at the resonance energies of the various nuclei comprising the detector, however PSA fits to the $LaBr_3$ data are unreliable at neutron energies beyond ≈5 eV, below the majority of intense resonances of the nuclei in question.

For the scenarios listed above, the peak could in fact be an overlap of several gamma rays originating not from a single event types, but some combination of them. A simple such combination of processes would involve a 511-keV gamma ray originating from annihilation of a β^+ particle originating from ^{138}La or ^{80}Br (a product of neutron capture on naturally-occurring ^{79}Br in the detector). Another gamma ray in the energy range of ≈550-600 keV would then be required to explain the breadth of the peak. There are several candidates for such gamma rays. Firstly, ^{82}Br, produced by neutron capture with a cross-section of ≈6.5 b [11] on ^{81}Br, resulting in a 554-keV gamma ray following β^- decay to 2.648 MeV state of ^{82}Kr. Secondly, a gamma decay of ^{81}Br following excitation of the nucleus, which produces 566 keV gamma-ray from $3/2^-$ state directly to ground state. Similarly there are 544- and 553-keV transitions from $7/2^-$ state in ^{79}Br, and 569- and 576-keV transitions in ^{138}La from the 2^+ and 2^- states respectively. ^{138}Ba, β^+ product of ^{138}La, has a 547-keV gamma-ray decay, but it's originating from a state with energy of 2.446 MeV, above β^+-populated energy state of 1436 keV. ^{140,142}Ce isotopes in the crystal, ^{138}Ce (populated by β^- decay of ^{138}La), and ^{139}La do not have such low-energy gamma-rays with high intensities in low excitation states, which are the ones more likely to be populated in the decays following thermal neutron capture.

While there are many transitions listed above which may contribute to the peak, none of them are transitions to ground state directly from states populated by their respective reactions. This means that one would expect other gamma rays from their decay band to have a comparable intensity. Such transitions would subsequently appear in the spectra alongside the peak already observed, provided sufficient $LaBr_3$ efficiency in their respective energy regions, a condition which some of the candidate transitions satisfy. For example, the 554-keV transition originating from ^{82}Br has a cross-section of 0.838 b, and the same parent nucleus has a 776-keV transition with a cross-section of 0.990 b [176], which is not seen in the spectra. It is possible, however, that other materials, such as constituent elements of the PMT, contribute as well.

Despite the lack of a clear origin, the peak-like structure was deemed a good gauge of detector gain. Following the gain corrections, measured fold distributions for $LaBr_3$ were calculated. Since a single $LaBr_3$ crystal was used, during the narrow fission time window the fold can only take values of 0 or 1, and multiple hits will likely result in pile-up and subsequently a detected fold of 1. The ratio of fold 1 to fold 0 is ≈0.0438 for the dedicated pulses and ≈0.0385 for parasitic. A measured gamma-ray energy spectrum summed for

both pulse types is presented in Fig. 6.42. Both the folds and the energy spectra were produced for 1 eV maximum neutron energy, and have no gamma-ray energy thresholds applied beyond the 10 channel PSA fitting threshold corresponding to ≈184 keV. Note, that the gain corrections will have reduced the 184-keV energy threshold in the spectra to varying extents depending on the count rate and pulse type, but it has to be re-applied in the final STEFF PFG measurements with $LaBr_3$. The need to re-apply the thresholds arises, because the signals in the higher count-rate regions will have been corrected more and have been added to the energy spectrum shown below, while the gamma-rays with similar energies will have been rejected in PSA for lower count rate regions (which undergo less gain correcting). Thus at gamma energies below 184 keV the yield of gamma-rays is not reliable in the summed spectrum. The lower energy signals were retained in the plots presented here for demonstration of the gain correction effect only.

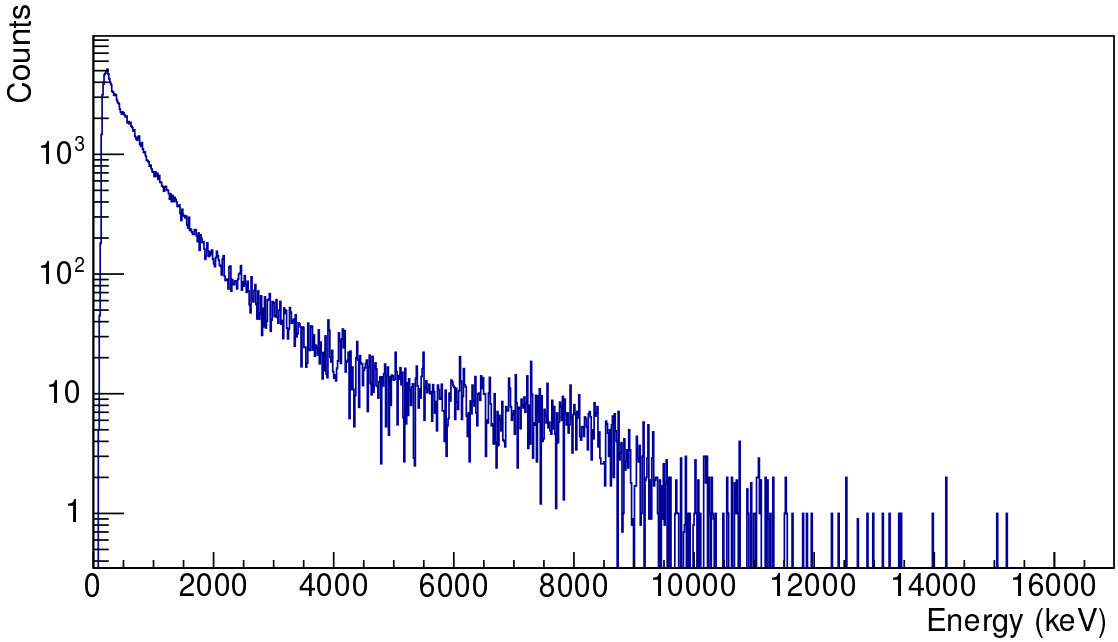

FIGURE 6.42: Measured $LaBr_3$ fission gamma-ray energy spectrum summed over both proton pulse types and corrected for gain drift.

6.8 Conclusion

Following the database construction for the 2016 n_ToF ^{235}U measurement campaign, the gamma-ray data were analyzed to extract measured PFGS and fold distributions. A series of corrections were devised for correcting for count-rate effects in NaI signals for neutron ToF greater than 10 ms for both the dedicated and parasitic proton pulse types. The corrections resulted in consistent spectral shape for all neutron ToF regions above 10 ms for each of the two pulse types, although small differences in the energy and fold

distributions between the pulse types remain. The resulting measured gamma-ray energy spectra have been compared to those measured during the ILL campaign. The spectra agree in the 1-4 MeV energy range, but disagree in the lower- and higher-energy regions. It is worth noting, that the deconvolved ILL energy spectra also show lack of low-energy gamma-rays compared to the existing data such as Oberstedt *et al.* [14], and only agree with them in the 1-3 MeV range, while observing a lack of low-energy gamma rays, but an increase in the high energy counts. The increase in high-energy counts in the spectra measured at ILL can also be investigated relative to the Makii *et al.* measurements [22], and the n_ToF spectra can be used for similar analysis after multiple-hits subtraction is performed. As part of the work presented here, calibrated and gain-corrected $LaBr_3$ energy and fold spectra have also been produced following investigation of the detector gain, and may shed light on both the disagreements with prior data (as measurements in Ref. [14] have been partially performed with $LaBr_3$ detectors) and on losses of NaI signals in the low-energy end of the gamma-ray spectrum.

In order to resolve fully the discrepancies between the existing STEFF measurements as well as with the previous data, several further steps are necessary. Firstly, the measured ILL data need to be re-visited to verify fold distributions with difference gamma-ray energy gates in order to identify more precisely the region where the n_ToF and ILL data agree using energy-gated fold distributions. Once a minimal reliable energy threshold for the n_ToF data has been identified based on fold agreement, the NaI and $LaBr_3$ spectra in that region require neutron signal subtraction, multiple hit subtraction and deconvolution as described in Ref. [20]. Deconvolution requires completion of GEANT4 [177] simulations of STEFF, which are currently undergoing testing by the Manchester fission group.

Blank page

Chapter 7

Conclusion

Following the 2016 STEFF campaign of ^{235}U(n,f) measurements of fission fragments and gamma rays, a data pipeline has been constructed. The pipeline is based on pre-existing libraries and pulse-shape analysis routine at n_ToF, which are used to convert the experimental data into ROOT format. A new routine has been written for RAW2ROOT, which extracted ionization traces. An event-building program has then been produced and tested for correlating individual detector signals into packaged fission events. The GAVSORT sorting program has been adapted to produce a MARIADB database from ROOT data for convenient access to the experimental results. The pipeline resulted in 70-fold data size reduction and allows for processing of the entire campaign in ≈7 hours.

The constructed database was then used to gate on fission gamma-rays using fast-timing detectors and investigate count rate effects on STEFF scintillators as a function of proton pulse type and neutron energy. Corrections have been developed to account for the saturation of the scintillators and corrected spectra have been assessed with reference to the 2014 STEFF campaign at ILL, which did not suffer from the saturating effects affecting NaI scintillators (background gamma-ray intensity, γ-flash) inherent to measurements at n_ToF. The spectra for the two campaigns agreed in the intermediate gamma-ray energy range (≈1-4 MeV), and the disagreement at lower energies has been attributed to poor signal fitting. A corrected set of fitting parameters for future STEFF experiments has been produced.

The performance of the PSA fitting routine has been investigated, and for the rates involved with the large STEFF target and large EAR2 collimator was found to be reliable for NaI detectors in the $\lessapprox$1 eV neutron energy range, and for $LaBr_3$ in the $\lessapprox$5 eV range. NaI signals were corrected to match the signals in the parasitic pulses for count rates of less than ≈200 kHz, which appears to be the maximum count rate for which the detector gain variations can be approximated as linear, and should form

the neutron ToF region of particular priority for fitting optimization and analysis in future STEFF measurements at n_ToF. The spectra and fold distributions presented in the current work are based on ≈911,000 fission events, which were extracted from the $\approx 5 \times 10^6$ fission events in the MariaDB database following cuts on the neutron time-of-flight, Master trigger timing and START-STOP coincidences.

An experiment has been conducted at ILL using FiFI Bragg detector in order to examine the response of the detector to varying fission fragment masses and atomic numbers. A calibration function based on ionization signal trace risetimes and amplitudes has been proposed, which could be used for extraction of fragment masses and atomic numbers. A comparison has been drawn to SRIM-2013 simulations, assessing the discrepancies between the simulations and the results of the experiment. The results of the work using FiFI at ILL have been published in Ref. [121].

7.1 Future work

7.1.1 STEFF

The 2016 experimental data have so far resulted in a set of background-subtracted energy spectra. These spectra still require neutron-induced signal subtraction as well as multiple hit subtraction deconvolution. The details of how these operations are applied to STEFF can be found in the analysis of the ILL campaign [20]. The simulations for producing the detector response matrix, used for accounting for interactions of the gamma rays at various energies with STEFF (for example by Compton scattering), are currently being tested in GEANT4. Deconvolution is a critical step used for converting observed spectra into the final fission parameters, such as photon multiplicity or average PFG energy. Following deconvolution, the combined results of the STEFF ^{235}U campaigns are planned for publication.

The results of the scintillator response examination based on the 2016 STEFF campaign suggest far superior stability of the $LaBr_3$ scintillators in the n_ToF EAR2 environment. Unlike NaI scintillator, the $LaBr_3$ detectors did not show significant saturation regardless of pulse type and neutron energy range (excluding regions near gamma-flash). For this reason, any future STEFF experiments at n_ToF should be conducted with as many $LaBr_3$ crystals as can be obtained. A further test of these detectors can be conducted using the data available from the 2019 ^{239}Pu campaign, which used two clusters of three $LaBr_3$ crystals. The plutonium campaign was conducted with the narrow n_ToF EAR2 collimator, and could therefore also provide a further test of the NaI detectors, as the saturation effects should be less drastic. Since it is unlikely that the detectors operated

in the count rate regions where the gain drift is linear, the method for correcting the signals proposed in this work may prove beneficial in the analysis of that dataset and perhaps future STEFF experiments.

Fission fragment waveforms have also been stored in the MariaDB database, but have not been analyzed as part of this work. Their analysis is ongoing, performed by a PhD student in Manchester, currently focused on gain-matching the anode pads in the two main arms of STEFF. Based on gain-matching coefficients, summed traces will be constructed, representing the entire ionization signal. Such summed traces can be used for extracting the kinetic energy of the fragments entering the detector volume, which in turn can be combined with the ToF measurements to produce mass spectra. Following completion of mass calculations, a calibration for atomic number extraction developed as part of this work may be applied.

7.1.2 FiFI

A proposal [178] has been accepted by ILL for a follow-up experiment using FiFI with improved timing foils for measurements of charge-changing effects inside Lohengrin and testing the atomic number calibration presented in this work for several fill gases. Following the 2016 experiment at Lohengrin, foil-making techniques in the Manchester fission group have been refined and have resulted in thinner Mylar foils (estimated to be $<$ 100 nm thick based on foil colour). Time permitting, running Lohengrin beams with identical settings for both timing detectors, as well as only START detector and then only STOP detector would allow for an accurate characterization of timing resolution of the new foils, as well as determination of smearing effects of each foil individually. A characterization of these foils will inform further developments of FiFI work and, likely, STEFF as a result.

A collaboration has been proposed between the Manchester fission group and the fission group at the Uppsala University in Sweden. The collaboration will aim to combine silicon detectors used on VERDI with the time-of-flight section of FiFI to investigate the plasma delay time in silicon as a function of fragment mass, energy and atomic number at Lohengrin. FiFI ToF section will serve as an absolute time reference for the comparison with Si signal timing. The proposal for the measurement [179] is currently awaiting decision by the ILL Scientific Council with the plan for the experiment to take place immediately after the 2020 FiFI run.

Blank page

Bibliography

[1] O. Hahn and F. Strassmann, Die Naturwissenschaften **27**, 11 (1939).

[2] L. Meitner and O.R. Frisch, Nature **143**, 239 (1939).

[3] Argonne National Laboratory, Early Exploration - Reactors Designed by Argonne National Laboratory, http://www.ne.anl.gov/About/reactors/early-reactors.shtml, 2016, Accessed: 19.05.2017.

[4] European Nuclear Society, Nuclear Power Plants, Worldwide, https://www.euronuclear.org/info/encyclopedia/n/nuclear-power-plant-world-wide.htm, 2017, Accessed: 19.05.2017.

[5] World Nuclear Association, Nuclear Power in the World Today, http://www.world-nuclear.org/information-library/current-and-future-generation/nuclear-power-in-the-world-today.aspx, 2019, Accessed: 25.02.2020.

[6] I. Pioro *et al.*, *Handbook of Generation IV Nuclear Reactors*, 1 ed. (Woodhead Publishing, 2016).

[7] World Nuclear Association, Generation IV Nuclear Reactors, http://www.world-nuclear.org/information-library/nuclear-fuel-cycle/nuclear-power-reactors/generation-iv-nuclear-reactors.aspx, 2019, Accessed: 25.02.2020.

[8] K.S. Krane, *Introductory Nuclear Physics* (John Wiley & Sons, Inc., 1988).

[9] World Nuclear Association, Fast Neutron Reactors, http://www.world-nuclear.org/information-library/current-and-future-generation/fast-neutron-reactors.aspx, 2020, Accessed: 11.03.2020.

[10] D.A. Brown *et al.*, Nucl. Data Sheets **148**, 1 (2018).

[11] Evaluator: R.W. Mills, Neutron-induced Fission Product Yields, https://www.oecd-nea.org/dbdata/jeff/jeff33/downloads/JEFF33-nfy.asc, 2017, Accessed: 28.01.2019.

[12] G. Rimpault *et al.*, Physics Procedia **31**, 3 (2012).

[13] OECD HEA, NEA Nuclear Data High Priority Request List, HPRL, http://www.oecd-nea.org/dbdata/hprl/hprlview.pl?ID=421, 2006, Accessed: 09.05.2017.

[14] A. Oberstedt *et al.*, Phys. Rev. C **87**, 051602(R) (2013).

[15] A. Oberstedt *et al.*, Phys. Rev. C **90**, 024618 (2014).

[16] R.W. Peelle and F.C. Maienschein, Phys. Rev. C **3**, 1023 (1971).

[17] F. Pleasonton, R.L. Ferguson and H.W. Schmitt, Phys. Rev. C **6**, 1023 (1972).

[18] V.V. Verbinski, H. Weber and R.E. Sund, Phys. Rev. C **7**, 1173 (1973).

[19] C.Y. Wu, Total Prompt Gamma-ray Emission in Fission of ^{235}U, ^{239,241}Pu, and ^{252}Cf, in *14th International Conference on Nuclear Reaction Mechanisms*, 2015.

[20] E.S. Murray, *Measurement of Prompt Gamma-ray Energy Distribution and Multiplicity of ^{235}U Following Thermal Fission Using STEFF*, PhD thesis, Nuclear Physics Group, School of Physics and Astronomy, The University of Manchester, 2015.

[21] J.A. Ryan, *Measuring the Energies and Multiplicities of Prompt Gamma-ray Emissions from Neutron-induced Fission of ^{235}U using the STEFF Spectrometer*, PhD thesis, Nuclear Physics Group, School of Physics and Astronomy, The University of Manchester, 2017.

[22] H. Makii *et al.*, Phys. Rev. C **100**, 044610 (2019).

[23] M.D. Chadwick *et al.*, Nucl. Data Sheets **107**, 2931 (2006).

[24] I. Tsekhanovich *et al.*, Phys. Lett. B **790**, 583 (2019).

[25] V.K. Utyonkov *et al.*, Phys. Rev. C **92**, 034609 (2015).

[26] N. Vassh *et al.*, J. Phys. G **46**, 065202 (2019).

[27] N. Bohr and J. Wheeler, Phys. Rev. **56**, 426 (1939).

[28] C.F. v. Weizsäcker, Zeitschrift für Physik **96**, 431 (1935).

[29] A. deShalit and H. Feshbach *Theoretical Nuclear Physics Volume I: Nuclear Structure* Vol. 1 (Wiley Library Classics, 1990).

[30] C. Wagemans, *The Nuclear Fission Process* (CRC Press, 1991).

[31] E.K. Hyde *The Nuclear Properties of the Heavy Elements III Fission Phenomena* Vol. 3 (Prentice-Hall, Inc., 1964).

[32] B.M. Aleksandrov *et al.*, Sov. At. Energy **28**, 462 (1970).

[33] R. Vandenbosch and J.R. Huizenga, *Nuclear Fission* (Academic Press, 1973).

[34] M. Mac Innes, M.B. Chadwick and T. Kawano, Nuclear Data Sheets **112**, 3135 (2011).

[35] A. Sen *et al.*, Phys. Rev. C **96**, 064609 (2017).

[36] E.K. Hulet *et al.*, Phys. Rev. C **40**, 770 (1989).

[37] S.M. Polikanov and other, ZhETF **44**, 804 (1963).

[38] S.G. Nilsson, Kgl. Dan. Vd. Selsk., Mat.-Fys. Medd. **29**, 1 (1955).

[39] V.M Strutinsky, Nucl. Phys. A **95**, 420 (1968).

[40] B. Slavov and A. Faessler, Z. Physik **271**, 161 (1973).

[41] P. Möller *et al.*, Nature **409**, 785 (2001).

[42] K.-H. Schmidt and B. Jurado, Rep. Prog. Phys. **81**, 10 (2018).

[43] P. Möller and S.G. Nilsson, Physics Letters **31B**, 283 (1970).

[44] S. Finch *et al.*, Phys. Rev. C **98**, 014608 (2018).

[45] A.C. Shotter *et al.*, J. Phys. G: Nucl. Phys. **2**, 769 (1976).

[46] A.A. Kotov *et al.*, Phys. Rev. C **74**, 034605 (2006).

[47] K.-H. Schmidt *et al.*, Nucl. Phys. A **665**, 221 (2000).

[48] E. Kolbe, K. Langanke and G.M. Fuller, Phys. Rev. Lett. **92**, 111101 (2004).

[49] H. Feshbach, C.E. Porter and V.F. Weisskopf, Phys. Rev. **96**, 448 (1954).

[50] N.C. Shu *et al.*, Chinese Physics C **39**, 054101 (2015).

[51] K. Hirose *et al.*, Phys. Rev. Lett. **119**, 222501 (2017).

[52] S. Pommé and C. Wagemans, Nucl. Phys. A **587**, 1 (1994).

[53] F. Gönnenwein *et al.*, Phys. Lett. B **652**, 13 (2007).

[54] Yu. V. Pyatkov *et al.*, Phys. Rev. C **96**, 064606 (2017).

[55] P. Jesinger *et al.*, Eur. Phys. J **A**, 379 (2005).

[56] A.C. Wahl, Proc. Symp. on Physics and Chemistry of Fission Vol. 1, p. 317, Vienna: IAEA, 1965.

[57] K.F. Flynn *et al.*, Phys. Rev. C **5**, 1725 (1972).

[58] J. Kilman, M.G. Itkis and S. Gmuca, *Dynamical Aspects of Nuclear Fission* (World Scientific, 2008).

[59] I. Tsekhanovich *et al.*, Nucl. Phys. A **658**, 217 (1999).

[60] W. von Oertzen and A.K. Nasirov, J. Phys.: Conference Series **569**, 012040 (2014).

[61] U. Brosa *et al.*, Physics Reports **197**, 167 (1990).

[62] P. Siegler *et al.*, Nucl. Phys. A **594**, 45 (1995).

[63] A.C. Mueller and B.M. Sherrill, Annu. Rev. Nucl. Part. Sci. **43**, 529 (1993).

[64] N. Carjan and M. Rizea, Phys. Lett. B **747**, 178 (2015).

[65] R.W. Fuller, Phys. Rev. **126**, 684 (1962).

[66] N.V. Kornilov *et al.*, Nucl. Phys. A **789**, 55 (2007).

[67] A.S. Vorobyev *et al.*, Journal of Experimental and Theoretical Physics **125**, 619 (2017).

[68] A. Göök *et al.*, Phys. Rev. C **98**, 044615 (2018).

[69] I. Ahmad and W.R. Phillips, Reports on Progress in Physics **58**, 1417 (1995).

[70] K. Nishio *et al.*, Nucl. Phys. A **632**, 540 (1998).

[71] A.S. Vorobyev *et al.*, EPJ Web of Conferences A **8**, 03004 (2010).

[72] H. Nifenecker *et al.*, Nucl. Phys. A **189**, 285 (1972).

[73] O. Litaize *et al.*, EPJ Web of Conferences **169**, 00012 (2018).

[74] I. Tsekhanovich *et al.*, Phys. Rev. C **78**, 001301(R) (2008).

[75] J.A. Dare, *Development of the Spectrometer for Exotic Fission Fragments*, PhD thesis, Nuclear Physics Group, School of Physics and Astronomy, The University of Manchester, 2009.

[76] E.S. Murray *et al.*, Nuclear Data Sheets **119**, 217 (2014).

[77] S.G. Warren, *Development of the STEFF Detector for the Neutron Time of Flight Facility (n_TOF), CERN*, PhD thesis, Nuclear Physics Group, School of Physics and Astronomy, The University of Manchester, 2016.

[78] A. Oed *et al.*, Nuclear Instruments and Methods in Physics Research **219**, 569 (1984).

[79] M.O. Frègeau *et al.*, Nuclear Instruments and Methods in Physics Research A **817**, 35 (2016).

[80] M.O. Frègeau and S. Oberstedt, Physics Procedia **64**, 197 (2015).

[81] F. Tovesson *et al.*, EPJ Web of Conferences **62**, 05002 (2013).

[82] D. Doré *et al.*, Nuclear Data Sheets **119**, 346 (2014).

[83] A. Al-Adili, The VERDI Spectrometer - Opportunities and Challenges, in *Nuclear Data 2019 Conference, Beijing*, 2019.

[84] F. Tovesson *et al.*, EPJ Web of Conferences **146**, 04010 (2017).

[85] Q. Deshayes, FALSTAFF, An Apparatus to Study Fission Fragment Distributions: First Arm Results, in *Nuclear Data 2019 Conference, Beijing*, 2019.

[86] M. Vernassiere, Quantify the Effect of Target Orientation, Thickness, Homogeneity and Backing Thickness for an Experiment with the STEFF Detector, Rapport de Stage, Private Communications, 2016.

[87] K.E. Pferdekämper and H.-G. Clerc, Zeitschrift für Physik A **275**, 223 (1975).

[88] J. Bath, Foils for Secondary Electron Generation in Time-of-Flight Spectrometry, M.Phys. Report, Private Communications, 2019.

[89] Hamamatsu Photonics, *MCP (Microchannel Plate) and MCP Assembly*, 2016.

[90] G.F. Knoll, *Radiation Detection and Measurement* (John Wiley & Sons, Inc., 1979).

[91] Saint-Gobain Crystals, *NaI(Tl) and Polyscin® NaI(Tl) Sodium Iodide Scintillation Material*, 2016.

[92] Saint-Gobain Crystals, *Lanthanum Bromide and Enhanced Lanthanum Bromide*, 2017.

[93] Scionix Ltd., Scintillation light detection devices, https://scionix.nl/read-out/, 2019, Accessed: 05.07.2019.

[94] M. Moszyński *et al.*, Nucl. Instrum. Methods A **805** (2016).

[95] S.A. Payne *et al.*, IEEE Transactions on Nuclear Science **NS56** (2009).

[96] ORTEC, Ametec, *Lanthanum Bromide Scintillation Detectors*, 2015.

[97] P.R. Menge *et al.*, Nuclear Instruments and Methods in Physics Research A **579**, 6 (2007).

[98] F. Sauli, *Gaseous Radiation Detectors: Fundamentals and Applications* (Cambridge University Press, 2014).

[99] J.S. Townsend, Nature **62**, 11 (1900).

[100] S.F. Biagi, Nucl. Instum. Methods A **421**, 234 (1999).

[101] I.B. Smirnov, Nucl. Insturm. Methods A **554**, 474 (2005).

[102] G. Charpak *et al.*, Nuclear Instruments and Methods **62**, 262 (1968).

[103] About NobelPrize.org, The Nobel Prize in Physics, 1992, https : // www.nobelprize.org/nobel_prizes/physics/laureates/1992/, 2017, Accessed: 15.05.2017.

[104] M. Matoba *et al.*, IEEE Transactions on Nuclear Science **NS32**, 541 (1985).

[105] W. Reisdorf *et al.*, Nucl. Phys. A **177**, 337 (1971).

[106] G.S. Simpson *et al.*, Phys. Rev. C **81**, 024313 (2010).

[107] J.N. Wilson *et al.*, Phys. Rev. Lett. **118**, 222501 (2017).

[108] T. Materna *et al.*, EPJ Web of Conferences **146**, 04041 (2017).

[109] A. Singh *et al.*, IEEE Transactions on Nuclear Science **62**, 264 (2015).

[110] J.P. Bocquet, R. Brissot and H.R. Faust, Nucl. Instrum. Methods A **267**, 466 (1988).

[111] S. Dubey *et al.*, J. Low Tempt. Phys. **193**, 1257 (2018).

[112] A. Koning *et al.*, The JEFF-3.1 Nuclear Data Library, 2006.

[113] C.R. Gruhn *et al.*, Nucl. Instrum. Methods **196**, 33 (1982).

[114] J.M. Asselineau *et al.*, Nucl. Instrum. Methods **204**, 109 (1982).

[115] A. Oed, P. Geltenbort and F. Gönnenwein, Nuclear Instruments and Methods **205**, 451 (1983).

[116] E. Pellereau *et al.*, Phys. Rev. C **95**, 054603 (2017).

[117] A.N. Andreyev, K. Nishio and K.-H. Schmidt, Rep. Prog. Phys. **81**, 016301 (2018).

[118] M. Caamaño *et al.*, Phys. Rev. C **88**, 024605 (2013).

[119] J.F. Ziegler, M.D. Ziegler and J.P. Biersack, Nucl. Instrum. Methods B **268**, 1818 (2010).

[120] L. Grente *et al.*, EPJ Web of Conferences **122**, 01006 (2016).

[121] N.V. Sosnin *et al.*, Nucl. Instrum. Methods A **957**, 163397 (2020).

[122] N.A. Perfilov, Doklady Akademii Nauk USSR **28**, 426 (1940).

[123] N. Bohr, Kgl. Dan. Vd. Selsk., Mat.-Fys. Medd. **8**, 1 (1948).

[124] H.-D. Betz, Reviews of Modern Physics **44**, 12 (1972).

[125] B.L. Cohen and C.B. Fulmer, Nucl. Phys. **6**, 547 (1958).

[126] L.C. Northcliffe, Phys. Rev. **120**, 1744 (1960).

[127] J. Lindhard, M. Scharff and H.E. Schiøtt, Kgl. Dan. Vd. Selsk., Mat.-Fys. Medd. **33**, 14 (1963).

[128] J.F. Ziegler, J.P. Biersack and M.D. Ziegler, *SRIM: The Stopping and Range of Ions in Matter* (SRIM Co., 2008).

[129] J. Lindhard *et al.*, Kgl. Dan. Vd. Selsk., Mat.-Fys. Medd. **33**, 10 (1963).

[130] A. Guesmia *et al.*, Radiation Physics and Chemistry **96**, 205 (2014).

[131] W. Brandt and M. Kitagawa, Phys. Rev. B **25**, 5631 (1982).

[132] H.-D. Betz, Physics Letters **22**, 643 (1966).

[133] N.M. Denkin, *Stopping Power of Gases for Heavy Ions*, PhD thesis, California Institute of Technology, 1977.

[134] Y.K. Gupta *et al.*, Phys. Rev. C **96**, 014608 (2017).

[135] ILL - Neutrons for Society, Technical Characteristics - Description of the ILL High-flux Reactor, https://www.ill.eu/reactor-and-safety/high-flux-reactor/technical-characteristics/, 2019, Accessed: 16.09.2019.

[136] G. Diiorio and B.W. Wehring, Nucl. Instum. Methods **147**, 487 (1977).

[137] U. Köster *et al.*, Nucl. Instum. Methods A **613**, 363 (2010).

[138] P. Armbruster *et al.*, Nucl. Instum. Methods **139**, 213 (1976).

[139] A.G. Smith *et al.*, Digital Sub-Bragg-Peak Spectroscopy at Lohengrin, ILL Research Proposal, 2016.

[140] A.G. Smith, gavSort, http://nucpc100.ph.man.ac.uk/software.html, 2013, Accessed: 18.09.2019.

[141] MariaDB Foundation, MariaDB - Supporting Continuity and Open Collaboration, https://mariadb.org/, 2019, Accessed: 25.07.2019.

[142] S.W. Smith, *The Scientist and Engineer's Guide to Digital Signal Processing* (California Technical Publishing, 1997).

[143] V.T. Jordanov and G.F. Knoll, Nucl. Instrum. Methods A **345**, 337 (1994).

[144] A. Göök *et al.*, Nucl. Instrum. Methods A **664**, 289 (2012).

[145] A. Al-Adili *et al.*, Nucl. Instrum. Methods A **673**, 116 (2012).

[146] C. Budtz-Jørgensen *et al.*, Nucl. Instrum. Methods A **258**, 209 (1987).

[147] P. Van Den Eltzen and R. Varley, X-ray Emission from Fission Fragments, M.Phys. Report, Private Communications, 2019.

[148] P. Filliatre, C. Jammes and B. Geslot, Nucl. Instrum. Methods A **618**, 294 (2010).

[149] M. Pickering and J.M. Alexander, Phys. Rev. C **6**, 332 (1972).

[150] M. Forte *et al.*, Phys. Rev. B **14**, 956 (1976).

[151] S.A. Bennett *et al.*, Nucl. Instrum. Methods A **951**, 162846 (2019).

[152] C. Rubbia *et al.*, European Organization for Nuclear Research Report No. CERN/LHC/98-02, 1998 (unpublished).

[153] C. Borcea *et al.*, Nucl. Instum. Methods A **513**, 524 (2003).

[154] C. Guerrero *et al.*, Nucl. Data Sheets **119**, 5 (2014).

[155] M. Giovannozzi, R. Cappi and G. Métral, The Proton Beams for the Time-of-Flight Neutron Facility at the CERN-PS, in *7th European Particle Accelerator Conference*, 2000.

[156] C. Weiss *et al.*, Nucl. Instum. Methods A **799**, 90 (2015).

[157] C. Guerrero *et al.*, Eur. Phys. J **49**, 27 (2013).

[158] F. Gunsing *et al.*, Eur. Phys. J. Plus **131**, 371 (2016).

[159] J. Benlliure, *Spallation Reactions in Applied and Fundamental Research* (In: Al-Khalili J., Roeckl E. (eds) The Euroschool Lectures on Physics with Exotic Beams, Vol. II, Lecture Notes in Physics, vol. 700, Springer, Berlin, Heidelberg, 2006).

[160] R. Serber, Phys. Rev. **72**, 133 (1947).

[161] J.P. Bondorf *et al.*, Physics Reports **257**, 133 (1995).

[162] J. Lerendegui-Marco *et al.*, Eur. Phys. J. A **52**, 100 (2016).

[163] CEA, Modeling of Spallation Reactions, http://irfu.cea.fr/dphn/en/Phocea/Vie_des_labos/Ast/ast_visu.php?id_ast=2229, 2019, Accessed: 23.07.2019.

[164] F. Gunsing, Neutron-induced Reactions at the n_ToF Facility at CERN, in *Oslo Workshop 2011*, 2011.

[165] CERN, ROOT, a Data Analysis Framework, https://root.cern.ch/, 2017, Accessed: 31.05.2017.

[166] P. Zûgec *et al.*, Nucl. Instum. Methods A **812**, 134 (2016).

[167] H.W. Schmitt, W.E. Kiker and C.W. Williams, Physical Review **137**, B837 (1965).

[168] F. Shiraishi and M. Hosoe, Nucl. Instrum. Methods **107**, 493 (1973).

[169] E. Browne and J.K. Tuli, Nucl. Data Sheets for $A = 60$, 2013.

[170] Hamamatsu Photonics K.K., *Photomultiplier Tubes: Basics and Applications*, 3rd ed. (Hamamatsu Photonics K.K., 2007).

[171] W.A. Rosen and F.R. Chromey, The Astronomical Journal **90**, 139 (1985).

[172] F.H. Marshall, J.W. Coltman and L.P. Hunter, Review of Scientific Instruments **18**, 504 (1947).

[173] O. Youngbluth, Jr., Applied Optics **9**, 321 (1970).

[174] I. Cantarell and I. Almodóvar, The Review of Scientific Instruments **18**, 504 (1963).

[175] M. Yamashita, Review of Scientific Instruments **51**, 768 (1980).

[176] IAEA, *Database of Prompt Gamma Rays from Slow Neutron Capture for Elemental Analysis* (International Atomic Energy Agency, 2007).

[177] S. Agostinelli *et al.*, Nucl. Instrum. Methods A **506**, 250 (2003).

[178] N.V. Sosnin *et al.*, Investigation of Fission Fragment Atomic Number Response in Ionization Chamber Coupled to a Time-of-Flight Arm at Lohengrin, ILL Research Proposal, 2019.

[179] A. Al-Adili *et al.*, Investigation of the Plasma Delay Time Effect in PIPS Detectors for the Development of the VERDI Fission Spectrometer, ILL Research Proposal, 2020.